



**HAL**  
open science

# Ductile damage prediction in sheet metal forming processes

Zhenming Yue

► **To cite this version:**

Zhenming Yue. Ductile damage prediction in sheet metal forming processes. Materials and structures in mechanics [physics.class-ph]. Université de Technologie de Troyes; Universität Dortmund, 2014. English. NNT : 2014TROY0025 . tel-03358311

**HAL Id: tel-03358311**

**<https://theses.hal.science/tel-03358311v1>**

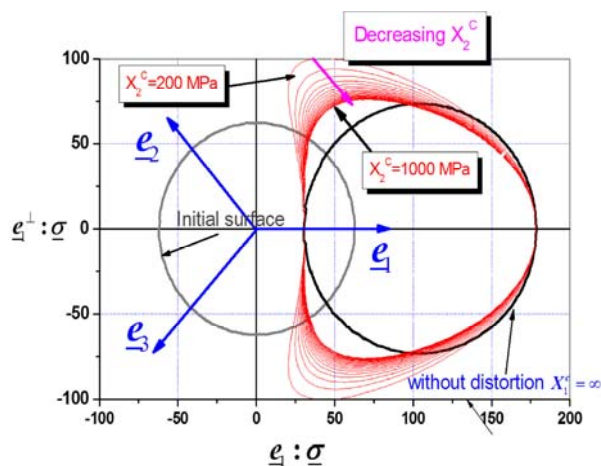
Submitted on 29 Sep 2021

**HAL** is a multi-disciplinary open access archive for the deposit and dissemination of scientific research documents, whether they are published or not. The documents may come from teaching and research institutions in France or abroad, or from public or private research centers.

L'archive ouverte pluridisciplinaire **HAL**, est destinée au dépôt et à la diffusion de documents scientifiques de niveau recherche, publiés ou non, émanant des établissements d'enseignement et de recherche français ou étrangers, des laboratoires publics ou privés.

Zhenming YUE

# Ductile Damage Prediction in Sheet Metal Forming Processes



**Spécialité :**  
Systèmes Mécaniques et Matériaux

2014TROY0025

Année 2014

Thèse en cotutelle avec Technische Universität Dortmund

---

---

# THESE

*pour l'obtention du grade de*

## DOCTEUR de l'UNIVERSITE DE TECHNOLOGIE DE TROYES Spécialité : SYSTEMES MECANIKES ET MATERIAUX

*présentée et soutenue par*

**Zhenming YUE**

*le 8 septembre 2014*

---

---

### **Ductile Damage Prediction in Sheet Metal Forming Processes**

---

---

#### JURY

M. A. MENZEL	PROFESSOR	Président
M. H. BADREDDINE	MAITRE DE CONFERENCES	Examineur
M. M. EKH	PROFESSOR	Rapporteur
M. P.-Y. MANACH	PROFESSEUR DES UNIVERSITES	Rapporteur
M. K. SAANOUNI	PROFESSEUR DES UNIVERSITES	Directeur de thèse
M. A. E. TEKKAYA	PROFESSOR	Directeur de thèse





# **Table of contents**

---

<b>Abstract</b> .....	<b>IV</b>
<b>Résumé</b> .....	<b>V</b>
<b>Abstrakt</b> .....	<b>VI</b>
<b>Main notations</b> .....	<b>VII</b>
<b>Introduction</b> .....	<b>1</b>
<b>Chapter I Theoretical Aspects</b> .....	<b>5</b>
I.1 Continuum mechanics and thermodynamics framework.....	7
I.1.1 Introduction .....	7
I.1.2 On kinematics of finite deformation: the strain measures and strain rates .....	7
I.1.3 Stress measures and stress rates .....	12
I.1.4 On the main conservation laws .....	14
I.1.4.1 Conservation of mass .....	14
I.1.4.2 Conservation of momentum or principle of virtual power .....	14
I.1.4.3 Conservation of energy or first principle of thermodynamics .....	15
I.1.4.4 Positivity of the entropy production or second principle of thermodynamics .....	15
I.1.4.5 Clausius-Duhem inequality.....	15
I.1.5 About the continuum damage mechanics (CDM) .....	16
I.1.5.1 Phenomenological aspects of the ductile damage .....	17
I.1.5.2 Mathematical representation of the ductile damage .....	18
I.1.5.3 Effect of ductile damage on the elastoplastic behavior of metals .....	18
I.1.5.4 State variables and effective state variables .....	19
I.2 Formulation of fully coupled elastoplastic-damage constitutive equations .....	20
I.2.1 Introduction.....	20
I.2.2 Overview of the distortional hardening without damage models .....	22
I.2.2.1 Barlat model.....	22
I.2.2.2 Feigenbaum and Dafalias model .....	23
I.2.2.3 Teodosiu model .....	23
I.2.2.4 Levkovitch and Svendsen model.....	24
I.2.2.5 François model.....	25
I.2.3 Formulation of the proposed fully coupled model .....	25
I.2.3.1 State variables and effective state variables .....	25
I.2.3.2 State potential and state equations.....	26
I.2.3.3 Yield function, dissipation potential and evolution equations.....	29
I.2.3.4 Thermodynamical admissibility .....	31
I.3 Forming limit curves for sheet metal forming (FLCs) .....	32
I.3.1 Introduction.....	32

I.3.2 About the construction of FLD curves .....	33
I.3.3 FLD curves from the M-K approach .....	35
I.3.3.1 A brief description of the M-K approach .....	35
I.3.3.2 Yield function and hardening law.....	37
I.3.3.3 Local necking definition .....	37
I.4 Conclusions .....	38
<b>Chapter II Numerical Aspects.....</b>	<b>39</b>
II.1 Introduction .....	40
II.2 Numerical implementation of the proposed model.....	40
II.2.1 Time and space discretizations of the IBVP .....	40
II.2.1.1 Strong and weak forms of the IBVP .....	40
II.2.1.2 Space discretizations of the IBVP .....	42
II.2.1.3 Time discretization of the IBVP .....	43
II.2.1.4 Global resolution scheme.....	44
II.2.2 Local integration scheme: state variables computation .....	46
II.2.3 Numerical treatment of contact with friction.....	56
II.3 Numerical Aspect of M-K approach.....	56
II.4 Conclusions .....	57
<b>Chapter III Experimental aspects and parametric study .....</b>	<b>59</b>
III.1 Introduction.....	60
III.2 Experimental procedure and results.....	60
III.2.1 Test materials.....	60
III.2.2 Experimental procedures .....	61
III.2.2.1 Uniaxial tensile tests (UT).....	61
III.2.2.2 In-Plane Torsion tests (IPT).....	67
III.2.2.3 Pre-Notched Tension tests (PNT) .....	69
III.2.2.4 Simple shear tests (SS).....	73
III.2.2.5 Combined loading tests (CL).....	74
III.2.2.6 Nakazima tests (NAK) .....	79
III.2.2.7 Cross section deep-drawing tests (CSD).....	82
III.3 Parametric study of the proposed fully coupled CDM models .....	85
III.3.1 Microcracks closure effects .....	85
III.3.2 Distortional parameters effects on the yield surfaces.....	86
III.3.3 Distortional parameters effect on damage evolution .....	97
III.3.4 Triaxiality ratio and Lode angle effect on damage evolution .....	98
III.4 Parametric study of M-K approach.....	101
III.4.1 Initial imperfection.....	101
III.4.2 Hardening laws .....	102
III.5 Conclusions .....	103
<b>Chapter IV Identification and validation of the proposed fully coupled CDM model and comparisons with FLCs approach.....</b>	<b>105</b>

IV.1 Introduction.....	106
IV.2 The identification methodology of fully coupled CDM model.....	106
IV.2.1 Elastoplasticity parameters identification .....	108
IV.2.2 Distortion parameters identification .....	110
IV.2.3 Ductile damage parameters identification.....	116
IV.3 Determination of FLD and FLSD for Al7020.....	124
IV.4 Nakazima tests simulation with fully coupled CDM model .....	125
IV.5 Cross section deep drawing tests (CSD).....	133
IV.6 Rectangular drawing tests (RD) .....	152
IV.7 Conclusions.....	157
<b>Conclusions and perspectives .....</b>	<b>159</b>
<b>Reference .....</b>	<b>163</b>
<b>Résumé extensif en Français .....</b>	<b>175</b>
<b>Umfangreiche Zusammengefasst in Deutch .....</b>	<b>199</b>
<b>Appendix A.....</b>	<b>225</b>

## **Abstract**

The objective of this work is to propose a “highly” predictive material model for sheet metal forming simulation which can well represent the sheet material behavior under complex loading paths and large plastic strains. Based on the thermodynamics of irreversible processes framework, the advanced fully coupled constitutive equations are proposed taking into account the initial and induced anisotropies, isotropic and kinematic hardening as well as the isotropic ductile damage. The microcracks closure, the stress triaxiality and the Lode angle effects are introduced to influence the damage rate under a wide range of triaxiality ratios. The distortion of the yield surface is described by replacing the usual stress deviator tensor by a ‘distorted stress’ deviator tensor, which governs the distortion of the yield surfaces. For comparisons, the FLD and FLSD models based on M-K approach are developed.

A series of experiments for three materials are conducted for the identification and validation of the proposed models. For the parameters identification of the fully coupled CDM model, an inverse methodology combining MATLAB-based minimization software with ABAQUS FE code through the Python script is used. After the implementation of the model in ABAQUS/Explicit and a systematic parametric study, various sheet metal forming processes have been numerically simulated. At last, through the comparisons between experimental and numerical results including the ductile damage initiation and propagation, the high capability of the fully coupled CDM model is proved.

## Résumé

L'objectif de ce travail est de proposer un modèle de comportement avec endommagement ductile pour la simulation des procédés de mise en forme de tôles minces qui peut bien représenter le comportement des matériaux sous des trajets de chargement complexes en grandes déformations plastiques. Basées sur la thermodynamique des processus irréversibles, les équations du comportement couplé à l'endommagement tiennent compte des anisotropies initiales et induites, de l'écroutissage isotrope et cinématique et de l'endommagement isotrope ductile. Les effets de fermeture des microfissures, de triaxialité des contraintes et de l'angle de Lode sont introduits pour influencer l'évolution de l'endommagement sous une large gamme de triaxialité des contraintes. La distorsion de la surface de charge est introduite via un tenseur déviateur qui gouverne la distorsion de la surface de charge. A des fins de comparaison, les courbes limites de formage sont tracées basées sur l'approche M-K.

Des essais sont conduits sur trois matériaux pour les besoins d'identification et de validation des modèles proposés. L'identification utilise un couplage entre le code ABAQUS et un programme MATLAB via un script en langage Python. Après l'implémentation numérique du modèle dans ABAQUS/Explicite et une étude paramétrique systématique, plusieurs procédés de mise en forme de structures minces sont simulés. Des comparaisons expériences-calculs montrent les performances prédictives de la modélisation proposée.

# Abstrakt

Das Ziel dieser Arbeit ist es, ein Materialmodell für die numerische Blechumformung zu entwickeln, welches eine "genaue" Vorhersage über das Werkstoffverhalten bei komplexen Belastungspfaden und bei hoher plastischer Umformung wiedergibt. Auf Basis irreversibler thermodynamischer Prozesse, werden vollständige gekoppelte Stoffgesetze vorgeschlagen, die die anfängliche und induzierte Anisotropien, die isotrope und kinematische Verfestigung sowie die isotrope duktile Schädigung berücksichtigt. Der Mikroriss-schließungsfaktor, die Spannungsmehrachsigkeit und der Effekte des Lodewinkels werden hierbei eingeführt, um den Einfluss der Schädigungsrate gegenüber verschiedener Bereiche der Triaxialität zu erhalten. Beschrieben wird die Verzerrung der Fließortfläche, indem der übliche Spannungstensor durch den „verzerrten Spannungstensor“ ersetzt wird und folglich die Verzerrung der Fließflächen geregelt werden kann. Für den Vergleich wurden FLD und FLSD Modelle auf Basis des MK-Ansatzes entwickelt.

Über eine Reihe von Versuchen wurden drei Werkstoffe für die Identifikation und Validierung des vorgeschlagenen Modells untersucht. Bei der vollständigen gekoppelten Parameteridentifikation des CDM-Modells wurde inverse Methodik verwendet. Für die Optimierung stand die MATLAB-basierte Software zur Verfügung, die in Verbindung mit dem Python-Skript in ABAQUS FE Code steht. Nach der Implementierung des Modells in ABAQUS / Explicit und einer systematische Parameterstudie wurden verschiedene Blechumformprozesse numerisch berechnet. Im Anschluss wurden die experimentellen und numerischen Ergebnisse hinsichtlich der Rissinitiierung und Ausbreitung von Schädigung verglichen, um die Gültigkeit des vollständigen gekoppelten CDM-Modells zu prüfen.

## Main notations

Operators	Significations
$X$	Scalar variable
$\vec{X}$	Vector variable
$\underline{X}, X_{ij}$	Second-rank tensor
$\underline{\underline{X}}, X_{ijkl}$	Fourth-rank tensor
$\underline{X} \cdot \underline{Y}, X_{ik} Y_{kj}$	Internal scalar product: contraction on one indice
$\underline{X} : \underline{Y}, X_{ij} Y_{ij}$	Internal scalar product: contraction on two indices
$tr \underline{X}, X_{ii}$	Trace of the tensor $\underline{X}$
$\underline{X}^{dev}$	Deviatoric part of the tensor $\underline{X}$
$\ \underline{X}\ _M$	von-Mises norm of the tensor $\underline{X}$ ; $\ \underline{X}\ _M = \sqrt{\frac{3}{2} \underline{X}^{dev} : \underline{X}^{dev}}$
$\ \underline{X}\ _H$	Hill norm of the tensor $\underline{X}$ ; $\ \underline{X}\ _H = \sqrt{\underline{X} : \underline{H} : \underline{X}}$
$\underline{X} \otimes \underline{Y}, X_{ij} Y_{kl}$	Tensor product
$\underline{X}^T$	Transposition of the tensor $\underline{X}$
$\underline{X}^{-1}$	Inverse of the tensor $\underline{X}$
$\underline{X}^{-T}$	Inverse of the tensor $\underline{X}^T$
$\det \underline{A}$	Determinant of the matrix $\underline{A}$
$\underline{X}^S$	Symmetric part of tensor $\underline{X} = \underline{X}^S = \frac{1}{2} [\underline{X}^T + \underline{X}]$

$\underline{\mathbf{X}}^A$	Skew-symmetric part of tensor $\underline{\mathbf{X}} = \underline{\mathbf{X}}^A = \frac{1}{2}[-\underline{\mathbf{X}}^T + \underline{\mathbf{X}}]$
$\langle \underline{\mathbf{X}} \rangle_+$	Positive part of tensor $\underline{\mathbf{X}}$
$\langle \underline{\mathbf{X}} \rangle_-$	Negative part of tensor $\underline{\mathbf{X}}$
$\langle \text{tr } \underline{\mathbf{X}} \rangle_+$	Positive part of the trace of tensor $\underline{\mathbf{X}}$
$\langle \text{tr } \underline{\mathbf{X}} \rangle_-$	Negative part of the trace of tensor $\underline{\mathbf{X}}$



# Introduction

Sheet metal forming is a very important technology in manufacturing of various mechanical components, especially in automotive industry. Many works have been performed to understand the sheet metal forming processes and to predict forming limits of sheets in metal forming. Since industry revolution, the problem of strength of materials, especially the metallic materials have been one of the most attractive scientific fields. In the current century, new demands for passengers' safety, vehicle performance and fuel economy enhance the requirements of high functions and high complexity of product geometries using lighter and higher strength materials. Fig. I-1 shows one example of high strength steel application in automotive industries. However, a higher strength is generally accompanied by the lower ductility with the understanding of the relationship between ductility, toughness and the energy absorbed in fracturing.

Due to the weak ductility of these high strength materials, accurate prediction of metal forming limits during deformation has become a big issue. Researchers have done never-ending efforts to build the relation between the occurrence of failure and the general engineering concepts. The accuracy of such prediction depends on many important factors such as the yield function, hardening law, initial and induced anisotropies, etc. Different terms related to the material forming behaviors such Bauschinger effect, hardening evolution especially after loading-path changes and initial or subsequent anisotropies due to texture evolution. In large-scaled structure, the failure is also caused by extreme loading conditions. All these are the active sources of understanding the failure in metal forming processes.

The term '*failure*' can be roughly classified as the onset of plastic instabilities such as buckling, the formation of localized necking or the final fracture. From the perspectives of sheet metal forming, failure can be defined by the formation of localized necking, wrinkles or macroscopic cracks. To accurately describe the deformation behavior of metal sheets, the corresponding constitutive equations should well represent the material behavior under complex loading conditions and also accurately predict the limit state conditions at the critical points during deformation process.

Experimental and theoretical determined Forming Limit Diagrams (FLDs) and Forming Limit Stress diagrams (FLSDs) are both the failure criteria formulated by principle strains or stresses, which define the failure when the specified criterion is satisfied. In the last three

decades, micromechanical modeling has been developed based on increasing understanding of macroscopic failure process. From the microscopic viewpoint, ductile damage resulting from the localization of large plastic strains of metallic materials develops in three main stages: (i) micro-voids nucleation around the pre-existing inclusions, precipitates or second phases, (ii) micro-voids growth and (iii) micro-voids coalescence leading to the initiation of macroscopically observed cracks. To reflect the gradual weakening sourced from the mentioned void and microcracks, the most largely used two coupled generic damage models are: the physically motivated porosity models (Gurson type models) and the phenomenologically motivated continuum damage mechanics based models (CDM).

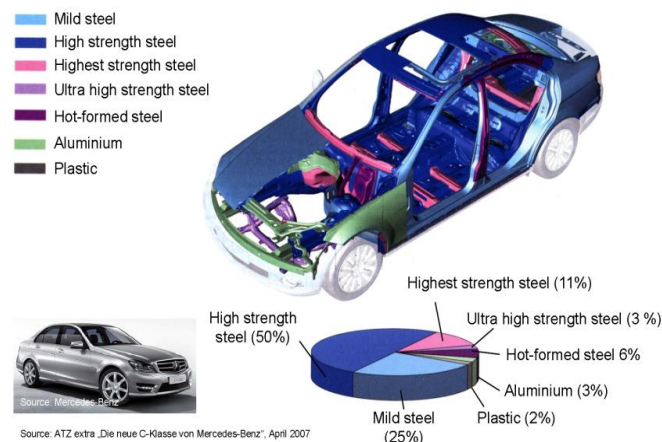


Fig. I - 1. Contour of the used materials in body structure of modern cars.

A robust behavior damage coupling model suitable for numerical implementation should be strong enough to predict not only the hardening behavior but also the onset of fracture and macroscopic crack propagation under a wide range of loading paths. In this study, a fully coupled ductile damage model is used, which takes into account the initial and induced anisotropies of yield surfaces, isotropic and kinematic hardening as well as isotropic ductile damage. Microcracks closure is introduced to affect the damage growth under various triaxiality ratios. Lode angle parameter takes three forms into the damage evolution equation to affect fracture strain under in high and negative triaxiality zones. This model is developed to fit many existing experimental results and will be further validated by a series of tests performed under various loading paths.

Numerical implementation has been performed in ABAQUS/Explicit and series of numerical studies are conducted to verify the predictive capability of the model. In addition, an M-K approach is developed to reproduce the FLDs and FLSDs of material Al7020 and the results are compared with the proposed ductile damage model.

A successful model depends on its ability to describe the underlying physical phenomena influencing the material deformation and fracture. On the other hand, the accuracy of numerical simulations is also affected by the parameters values assigned to the model. In this study, the contribution of the work includes three parts. Firstly, an advanced ductile damage model based on CDM framework is proposed, which takes into account the initial and induced anisotropies and the ductile damage evolution under various stress states. Secondly, the inverse methodology for model parameters determination is investigated, which includes the parametric study and calibration with experimental results. An optimization program based on MATLAB is used to determine the optimal material parameters values, including the elastoplasticity parameters, hardening and the ductile damage parameters. The initial anisotropic parameters and distortional parameters are determined with analytical approach. Thirdly, some complex loading paths like Nakazima tests, Cross-section deep drawing tests and rectangle drawing-redrawing tests are conducted with test materials for the validation purpose.

The thesis is organized as following:

Chapter I started by a review of the basic concepts of the continuum mechanics and thermodynamic framework as the kinematics of finite deformation, strain and stress measures as well as the main conservation laws. Before giving the fully coupled elastoplastic constitutive equations a literature survey about distortional hardening is given based on some published works. Following some published works, a new formulation of distortional hardening is introduced. On the other hand, the M-K approach structure is introduced, where the FLD and FLSD curves are plotted, including its yield criterion, hardening law and equilibrium equations, etc.

Chapter II is dedicated to the numerical aspects of two models, introducing the implementation of the proposed advanced CDM model and the M-K approach. In Section II.1 the time and space discretization's of the initial and boundary value problems (IBVP) are given, and then the local integration scheme for the fully coupled constitutive equations is presented in some details. In Section II.2, the Numerical aspects related to the plot of FLD and FLSD curves with the M-K approach are given.

In Chapter III, the experiments conducted in this work and the parametric studies of proposed models are given. Three commercial metallic materials are chosen as the test objectives: two high strength steels: DP1000, CP1200, and one aluminum alloy A17020. Series of monotonic (quasi-monotonic) loading tests and complex loading tests including: uniaxial tension tests, pre-notched tension tests, simple shear tests, cyclic torsion tests and combined loading tests

are given, which can help investigating the material behavior under different stress states. Then, several complex loading tests like: Nakazima tests and cross-section deep drawing tests are conducted which can help to assess the capabilities of the proposed models. At the same time, in order to facilitate the model parameters determination in the coming chapter, some parametric studies about microcracks closure, distortional parameters and Lode parameters' dependence are given.

In chapter IV, the parameters determinations and applications of fully coupled CDM model and M-K model are given. Based on different tests, these two models are calibrated. Finally, with the application of these two models on the simulations of Nakazima tests, Cross section deep drawing tests and rectangle deep-drawing tests, the comparisons of the capabilities of FLD and FLSD with CDM model are investigated.

Finally, the main conclusions and some perspectives of the present work are given.

# Chapter I

## Theoretical Aspects

### Content

---

I.1 Continuum mechanics and thermodynamics framework.....	7
I.1.1 Introduction .....	7
I.1.2 On kinematics of finite deformation: the strain measures and strain rates .....	7
I.1.3 Stress measures and stress rates .....	12
I.1.4 On the main conservation laws .....	14
I.1.4.1 Conservation of mass .....	14
I.1.4.2 Conservation of momentum or principle of virtual power .....	14
I.1.4.3 Conservation of energy or first principle of thermodynamics .....	15
I.1.4.4 Positivity of the entropy production or second principle of thermodynamics .....	15
I.1.4.5 Clausius-Duhem inequality.....	15
I.1.5 About the continuum damage mechanics (CDM) .....	16
I.1.5.1 Phenomenological aspects of the ductile damage .....	17
I.1.5.2 Mathematical representation of the ductile damage .....	18
I.1.5.3 Effect of ductile damage on the elastoplastic behavior of metals .....	18
I.1.5.4 State variables and effective state variables .....	19
I.2 Formulation of fully coupled elastoplastic-damage constitutive equations .....	20
I.2.1 Introduction .....	20
I.2.2 Overview of the distortional hardening without damage models .....	22

I.2.2.1 Barlat model.....	22
I.2.2.2 Feigenbaum and Dafalias model .....	23
I.2.2.3 Teodosiu model .....	23
I.2.2.4 Levkovitch and Svendsen model.....	24
I.2.2.5 François model.....	25
I.2.3 Formulation of the proposed fully coupled model .....	25
I.2.3.1 State variables and effective state variables .....	25
I.2.3.2 State potential and state equations.....	26
I.2.3.3 Yield function, dissipation potential and evolution equations.....	29
I.2.3.4 Thermodynamical admissibility .....	31
I.3 Forming limit curves for sheet metal forming (FLCs) .....	32
I.3.1 Introduction.....	32
I.3.2 About the construction of FLD curves .....	33
I.3.3 FLD curves from the M-K approach .....	35
I.3.3.1 A brief description of the M-K approach .....	35
I.3.3.2 Yield function and hardening law.....	37
I.3.3.3 Local necking definition .....	37
I.4 Conclusions .....	38

## I.1 Continuum mechanics and thermodynamics framework

### I.1.1 Introduction

In this section, some basic concepts of mechanics and thermodynamics of continuous media are reviewed. The objective is not to go with details, but to record the key points needed for the better reading of the subsequent chapters. Detailed discussions in this field can be found in [Cal60, Eri62, Fun65, Man74, Gur81, Hun83, Ger86, Bow89, Bou96], among many others.

### I.1.2 On kinematics of finite deformation: the strain measures and strain rates

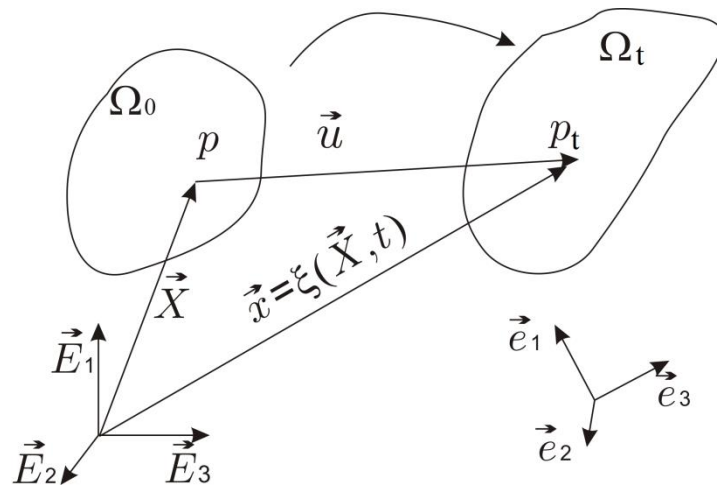


Fig. 1- 1. Configuration of the deformable body.

A fixed Cartesian coordinates system is assumed. An original (undeformed) body  $\Omega_0$  is defined in this frame with three Lagrange base vectors  $\vec{E}_1, \vec{E}_2$  and  $\vec{E}_3$ , in which each material point can be noted by  $p(\vec{X})$  of coordinates  $\vec{X}$ . After deformation  $\Omega_0$  is mapped to the new Eulerian configuration  $\Omega_t$  by the linear application  $\xi(\vec{X}, t)$ , where the current position of the particle  $p_t(\vec{x})$  of spatial (or Eulerian) coordinates  $\vec{x}$  is defined by:

$$\vec{x} = \xi(\vec{X}, t) \quad (1-1)$$

The corresponding displacement vector is defined by

$$\vec{u}(p) = \xi(\vec{X}, t) - \vec{X} \quad \text{or} \quad \vec{u}(p) = \vec{x} - \vec{X} \quad (1-2)$$

Based on this kinematics, the transformation gradient  $\underline{F}$  is introduced, which is noted as a

second-rank operator given by:

$$\underline{F} = \text{Grad}(\xi(\bar{X}, t)) = \frac{d\xi}{d\bar{X}} \quad (1-3)$$

Using Equation (1-2), the gradient  $\underline{F}$  can also be rewritten as:

$$\underline{F} = \frac{d(\bar{X} + \bar{u})}{d\bar{X}} = \underline{1} + \frac{d\bar{u}}{d\bar{X}} \quad (1-4)$$

The transport of a small volume element from  $\Omega_0$  to  $\Omega_t$  leads to the well-known relations:

$$\det(\underline{F}) = J = \frac{V}{V_0} = \frac{\rho_0}{\rho} > 0 \quad (1-5)$$

where  $V$  and  $\rho$  are the volume and density of the solid at  $\Omega_t$  while  $V_0$  and  $\rho_0$  are their respective values at the reference configuration.

Using the polar decomposition theorem, the gradient  $\underline{F}$  can be decomposed into Lagrangian and Eulerian stretches and rotation components schematized as in Fig. 1-2, giving:

$$\underline{F} = \underline{R} \cdot \underline{U} = \underline{V} \cdot \underline{R} \quad (1-6)$$

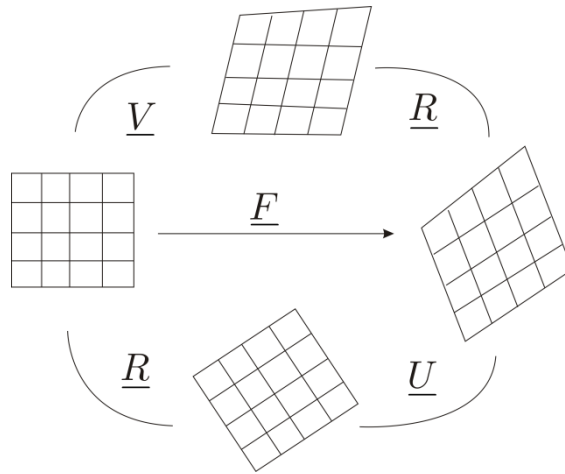


Fig. 1- 2. Schematic illustration of the polar decomposition theorem

$\underline{U}$  and  $\underline{V}$  are respectively the right (Lagrangian) and left (Eulerian) stretch tensors and  $\underline{R}$  is the orthogonal rotation tensor (rigid body rotation).

Considering the plane elementary surface transformation between original and deformed configurations, in order to define and quantify the change of distance between two particles, the right and left Cauchy-Green stretch tensors  $\underline{C}$  and  $\underline{B}$ , are respectively defined as:



$$\underline{C} = \underline{U}^2 = \underline{F}^T \cdot \underline{F} \quad \text{and} \quad \underline{B} = \underline{V}^2 = \underline{F} \cdot \underline{F}^T \quad (1-7)$$

Based on these two stretch tensors, two different strain measures are defined. Namely, the Green- Lagrange strain tensor  $\underline{E}$  (Lagrangian tensor):

$$\underline{E} = \frac{1}{2}(\underline{U}^2 - \underline{I}) = \frac{1}{2}(\underline{C} - \underline{I}) \quad (1-8)$$

and the Euler-Almansi strain tensor  $\underline{A}$  (Eulerian tensor):

$$\underline{A} = \frac{1}{2}(\underline{I} - \underline{V}^2) = \frac{1}{2}(\underline{I} - \underline{B}) \quad (1-9)$$

A number of other strain measures can be obtained with the Lagrangian and Eulerian stretch tensors. These definitions can be rationalized in the following forms ( $m$  being a given integer).

$$\underline{\varepsilon} = \begin{cases} \frac{1}{m}[\underline{U}^m - \underline{I}] & \text{if } m \neq 0 \\ \ln(\underline{U}) & \text{if } m = 0 \end{cases} \quad (1-10)$$

To define appropriate strain rates, the time derivative of Equation (1-3) gives:

$$d\dot{\underline{x}} = \dot{\underline{F}} \cdot d\bar{\underline{X}} = \dot{\underline{F}} \cdot \underline{F}^{-1} \cdot d\bar{\underline{x}} = \underline{L} \cdot d\bar{\underline{x}} \quad (1-11)$$

where  $\underline{L} = \dot{\underline{F}} \cdot \underline{F}^{-1}$  is called the Eulerian velocity gradient tensor. It can be decomposed into a symmetric tensor  $\underline{D}$  (strain rate tensor) and a skew-symmetric tensor  $\underline{W}$ , (spin or rotation tensor), defined as:

$$\underline{L} = \dot{\underline{F}} \cdot \underline{F}^{-1} = \underline{L}^S + \underline{L}^A = \underline{R} \cdot \dot{\underline{U}} \cdot \underline{U}^{-1} \cdot \underline{R}^T + \dot{\underline{R}} \cdot \underline{R}^T = \underline{D} + \underline{W} \quad (1-12)$$

$$\underline{D} = \underline{L}^S = (\dot{\underline{F}} \cdot \underline{F}^{-1})^S = \underline{R} \cdot (\dot{\underline{U}} \cdot \underline{U}^{-1})^S \cdot \underline{R}^T \quad (1-13)$$

$$\underline{W} = \underline{L}^A = (\dot{\underline{F}} \cdot \underline{F}^{-1})^A = \underline{R} \cdot (\dot{\underline{U}} \cdot \underline{U}^{-1})^A \cdot \underline{R}^T + \dot{\underline{R}} \cdot \underline{R}^T \quad (1-14)$$

Based on the concept of intermediate unloaded configuration, the total gradient  $\underline{F}$  can be multiplicatively decomposed into elastic  $\underline{F}^e$  and plastic  $\underline{F}^p$  parts, i.e.  $\underline{F} = \underline{F}^e \cdot \underline{F}^p$ . Several intermediate configurations can be used [Dogui89, Sidoroff01], among them,  $\bar{C}_i^p$  and  $\bar{C}_i$  which ensure the fulfillment of the objectivity requirement, as represented in Fig. 1-3. The configuration  $\bar{C}_i^p$  is named plastic 'isocline' configuration and its orientation is

defined by a rigid body rotation tensor  $\underline{Q}$  with respect to the actual configuration  $C_t$ .  $\bar{C}_t^p$  is obtained by the plastic transformation gradient  $\bar{F}^p$  from  $C^o$ , while the total ‘isocline’ configuration  $\bar{C}_t$  is obtained by the total transformation gradient  $\bar{F}$ . From Fig.1-3 we can obtain:

$$\underline{F} = \underline{F}^e \bar{F}^p = \underline{Q} \bar{V}^e \bar{F}^p = \underline{V}^e \underline{Q} \bar{V}^p \underline{Q}^T \underline{R}^{ep} = \underline{Q} \bar{F} \quad (1-15)$$

where  $\underline{F}^e$  is the elastic transformation gradient,  $\bar{F}^p$  the rotated plastic transformation gradient,  $\bar{V}^e$  the rotated right elastic stretch tensor,  $\bar{V}^p$  is the rotated plastic stretch tensor, With the rotating framework, any tensorial quantity.

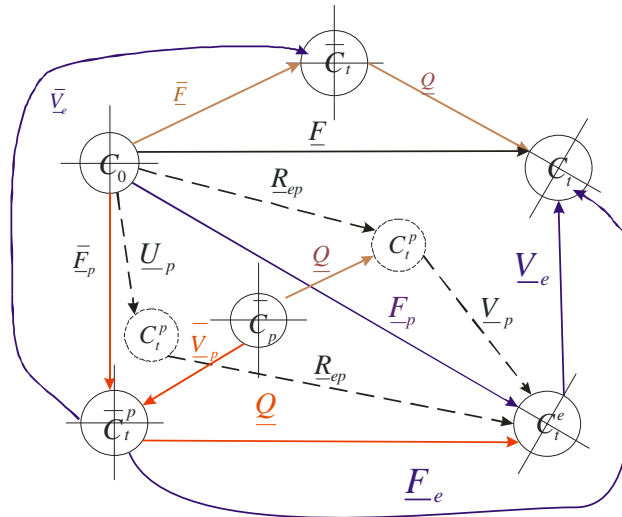


Fig. 1- 3. Transformation gradient: the rotating frame formulations [Badreddine10]

The rotated configuration  $\bar{C}_t$  and  $\bar{C}_t^p$  can be used in order to develop suitable constitutive equations accounting for various types of initial and induced anisotropies including mixed nonlinear hardening.

It is worth nothing that if the small elastic strain assumption is considered (i.e.  $\bar{V}^e = 1 + \bar{\underline{\varepsilon}}^e$  with  $\|\bar{\underline{\varepsilon}}^e\| \ll 1$ ), then the configurations  $\bar{C}_t^p$  and  $\bar{C}_t$  are approximately the same.

With Equation (1-15), the spatial velocity gradient  $\bar{\underline{L}} = \dot{\bar{F}} \bar{F}^{-1}$  can be decomposed into symmetric and antisymmetric parts [Badreddine10]:

$$\left[ \bar{V}^{e-1} \cdot \bar{\underline{L}} \cdot \bar{V}^e \right]^S = \left[ \bar{V}^{e-1} \cdot \dot{\bar{V}}^e \right]^S + \bar{\underline{D}}^p \quad (1-16)$$

$$\underline{W}_Q = \underline{\dot{Q}} \cdot \underline{Q}^T = \underline{W}^p - \underline{Q} \cdot \underline{\bar{W}}^p \cdot \underline{Q}^T \quad (1-17)$$

where  $\underline{\bar{D}}^p = [\underline{\bar{F}}^p \underline{\bar{F}}^{p-1}]^S$  and  $\underline{\bar{W}}^p = [\underline{\bar{F}}^p \underline{\bar{F}}^{p-1}]^A$  are respectively the plastic strain rate and the plastic spin. With the small elastic strain assumption, the equation 1-16 reduced to:

$$\underline{\bar{D}} = \underline{\bar{\varepsilon}}^e + 2 \left[ \underline{\bar{\varepsilon}}^e \underline{\bar{W}}^p \right]^S + \underline{\bar{D}}^p = \underline{\bar{\varepsilon}}^{eJ} + \underline{\bar{D}}^p \quad (1-18)$$

where  $\underline{\bar{D}}$  is the rotated total strain rate and  $\underline{\bar{\varepsilon}}^{eJ}$  is the rotated Jaumann rate of the small elastic strain tensor. Note that in equation 1-17,  $\underline{\bar{W}}^p$  can be defined in two different approaches. The first one deduces the plastic spin from an appropriate dissipation potential assuming the generalized normality rule [Dafalias85], this leads to:

$$\underline{\bar{W}}^p = \dot{\lambda} \left( \frac{\partial F_p}{\partial \underline{\bar{\Sigma}}} \right)^A = \dot{\lambda} \underline{\bar{N}}^A \quad (1-19)$$

where  $\underline{\bar{\Sigma}}$  is the generalized Mandel stress tensor to be defined later, and  $\underline{\bar{N}}^A$  is the non-symmetric part of the outward normal to the plastic potential  $F_p$  in the stress space.

The second way of defining  $\underline{\bar{W}}^p$ , consists in postulating, a priori, an appropriate kinematical relation of the type [Dogui89, Badreddine10, Saanouni12]:

$$\underline{\bar{W}}^p = \underline{\bar{K}}(\underline{\bar{V}}^p) : \underline{\bar{D}}^p \quad (1-20)$$

where  $\underline{\bar{K}}$  is a fourth-rank tensor, which is an isotropic function of the rotated plastic stretch tensor  $\underline{\bar{V}}^p$ . As shown in [Badreddine10] the shapes of the fourth-rank tensor  $\underline{\bar{K}}$  can be given as following:

- Corotational (or Jaumann) frame (J):  $\underline{\bar{W}}^p = \underline{0}$ , and  $\underline{\bar{K}}^J(\underline{\bar{V}}^p) = \underline{0}$
- Proper rotation (or Green-Naghdi) frame (R): Using  $\underline{Q} = \underline{R}^{ep}$  leading to the following relation:

$$\underline{\bar{W}}^{pR} = \underline{\bar{K}}^R(\underline{\bar{V}}^p) : \underline{\bar{D}}^p = \frac{2}{V_I V_{II} - V_{III}} \left[ V_I V_{III} \underline{\bar{D}}^p \cdot \underline{\bar{V}}^p + \underline{\bar{B}}^p \cdot \underline{\bar{D}}^p \underline{\bar{V}}^p \right]^A \quad (1-21)$$

where  $\underline{\bar{B}}^p = \underline{\bar{V}}^{p2}$  and  $V_I, V_{II}, V_{III}$  are the three elementary invariants of  $\underline{\bar{V}}^p$ .

- Plastic Eigen strain frame (V): This frame works together with the eigenvectors of the rotated plastic stretch tensor  $\underline{\underline{V}}^{-p}$ , and finally the frame can be given as:

$$\underline{\underline{W}}^{pR} = \underline{\underline{K}}^R(\underline{\underline{V}}):\underline{\underline{D}}^p = 2\zeta_1 \left[ \underline{\underline{B}}_p^{-D} \cdot \underline{\underline{D}}^p \right]^A + 2\zeta_2 \left[ \underline{\underline{B}}_p^{-D2} \cdot \underline{\underline{D}}^p \right]^A + 2\zeta_3 \left[ \underline{\underline{B}}_p^{-D} \underline{\underline{D}}^p \underline{\underline{B}}_p^{-D2} \right]^A \quad (1-22)$$

where  $\underline{\underline{B}}^{-pD}$  is the deviatoric part of the tensor  $\underline{\underline{B}}^{-p}$ ,  $\zeta_i$   $i = 1, 2, 3$  are the functions of the principal invariants of  $\underline{\underline{B}}^{-pD}$  (Dogui89).

- Logarithmic (or triaxial) frame (T): is defined as the frame in which the time derivatives of the Hencky plastic logarithmic strain ( $\underline{\underline{v}}^p = Ln(\underline{\underline{V}}^{-p})$ ) equals to the plastic strain rate  $\underline{\underline{D}}^p$ . The spin rotation of this frame is given by:

$$\underline{\underline{W}}^{pT} = \underline{\underline{K}}^T(\underline{\underline{V}}):\underline{\underline{D}}^p = \underline{\underline{W}}^{pV} - \underline{\underline{O}}^p \quad (1-23)$$

$$\underline{\underline{O}}^p = \underline{\underline{K}}^{ROS}(\underline{\underline{V}}_p):\underline{\underline{D}}^p = 2\zeta_{p1} \left[ \underline{\underline{v}}_p^D \underline{\underline{D}}^p \right]^A + 2\zeta_{p2} \left[ \underline{\underline{v}}_p^{D2} \underline{\underline{D}}^p \right]^A + 2\zeta_{p3} \left[ \underline{\underline{v}}_p^D \underline{\underline{D}}^p \underline{\underline{v}}_p^{D2} \right]^A \quad (1-24)$$

here,  $\zeta_{pi}$  are the principal invariants of  $\underline{\underline{v}}^p$  as shown in (Dogui89). This leads to:

$$\underline{\underline{K}}^T(\underline{\underline{V}}_p) = \underline{\underline{K}}^V(\underline{\underline{V}}_p) - \underline{\underline{K}}^{OS}(\underline{\underline{V}}_p) \quad (1-25)$$

### I.1.3 Stress measures and stress rates

Consider the elementary section  $d\bar{A}_0$  oriented by the normal  $\bar{n}_0$  in  $\Omega_0$ , so that  $d\bar{A}_0 = \bar{n}_0 dA_0$ . It can be transformed into elementary section  $d\bar{A}_t$  in  $\Omega_t$ , defined by  $d\bar{A}_t = \bar{n}_t dA_t$ . The elementary resultant force exerted at point  $p_t$  in  $\Omega_t$  on the section oriented by the normal  $\bar{n}_t$  is written as  $d\bar{F}_t = \bar{t}_t dA_t$  where  $\bar{t}_t$  denotes the elementary tension vector in this point.

The most widely used stress measure in a point of a continuum is the Cauchy stress tensor  $\underline{\underline{\sigma}}$ , which is defined using the measure of the elementary internal force in a point  $p_t$  of current configuration  $\Omega_t$  according to:

$$\bar{t}_t = \underline{\underline{\sigma}} \cdot \bar{n}_t \quad (1-26)$$

This resultant elementary force exerted in  $p_t$  is thus written in configuration  $\Omega_t$  as:

$$d\vec{F}_i = \vec{t}_i dA_i = \underline{\sigma} \cdot \vec{n}_i \cdot dA_i = \underline{\sigma} \cdot d\vec{A}_i \quad (1-27)$$

There are still many other common definitions for the stress tensors which can be found in the literature [Saanouni12] among others, like Kirchhoff stress tensor  $\underline{\tau}$ , the first and second Piola-Kirchhoff stress tensors  $\underline{\pi}$  and  $\underline{\underline{S}}$ , respectively defined as:

$$\underline{\tau} = J\underline{\sigma} \text{ leading to } \frac{\underline{\tau}}{\rho_0} = \frac{\underline{\sigma}}{\rho} \text{ (Eulerian)} \quad (1-28)$$

$$\underline{\pi} = J\underline{\sigma} \cdot (\underline{F})^{-T} \text{ (Mixed)} \quad (1-29)$$

$$\underline{\underline{S}} = J\underline{F}^{-1} \cdot \underline{\sigma} \cdot (\underline{F})^{-T} \text{ (Lagrangian)} \quad (1-30)$$

These various stress tensors can be easily expressed in terms of each other. Note that the first Piola-Kirchhoff stress tensor  $\underline{\pi}$  is clearly non-symmetric, and is neither purely Eulerian nor purely Lagrangian, while  $\underline{\underline{S}}$  is symmetric due to the symmetry of  $\underline{\sigma}$  and is purely Lagrangian.

In order to ensure the objectivity requirement, any Eulerian second-rank tensor  $\underline{T}$  and fourth-rank tensor  $\underline{\underline{T}}$  may be transported from the current configuration  $C_t$  to the rotated one  $\bar{C}_t$  thanks to  $\bar{\underline{T}} = \underline{Q}^T \underline{T} \underline{Q}$  and  $\bar{\underline{\underline{T}}} = (\underline{Q}^T \otimes \underline{Q}) : \underline{\underline{T}} : (\underline{Q} \otimes \underline{Q}^T)$ . The variable  $\underline{Q}$  is the rotation tensor which maps the current configuration  $C_t$  to the configuration  $\bar{C}_t$  as shown in Fig. 1-3. The rotation tensor is the solution of the ordinary differential equation Eq.1-17 with the initial condition  $\underline{Q}(t=t_0) = \underline{1}$ . These two configurations are Lagrangian by their orientation but Eulerian by the eigenvalues of the state variables.

In this work the simple total rotation configuration  $\bar{C}_t$  is used. The reader is referred to [Badreddine10] for the use of the rotated isocline configuration  $\bar{C}_t^p$  (see Saanouni12).

The objective rotational derivation of the second-rank tensor  $\underline{T}$  is given by:

$$\frac{d_{\underline{Q}} \underline{T}}{dt} = \underline{Q} \cdot \left( \frac{d\bar{\underline{T}}}{dt} \right) \cdot \underline{Q}^T = \underline{Q} \cdot \left( \frac{d}{dt} (\underline{Q}^T \cdot \bar{\underline{T}} \cdot \underline{Q}) \right) \cdot \underline{Q}^T = \dot{\underline{T}} + \underline{T} \cdot \underline{W}_{\underline{Q}} - \underline{W}_{\underline{Q}} \cdot \underline{T} \quad (1-31)$$

where  $\underline{W}_{\underline{Q}}$  is defined in Eq.1-17. The choice of  $\underline{W}_{\underline{Q}}$  through Eq.1-17 to Eq.1-25 gives rise to various objective rotational derivatives as can be found in [Badreddine10, Saanouni12]. These objective rotational derivatives performed in a locally rotated configuration give the simplest way to generalize the constitutive equations formulated under the small strain

assumption to the large strain framework.

## I.1.4 On the main conservation laws

In the following, we will provide, without detailed demonstrations, the main conservation laws of the physics of continuous media mainly in differential form for the case of materially simple continua.

### I.1.4.1 Conservation of mass

The first conservation law concerns the fact that the mass of the domain  $\Omega$  in its motion remains constant as time progresses during the motion.

$$\frac{d}{dt} \int \rho dV = 0 \quad (1-32)$$

This can be easily transformed into differential form:

$$\dot{\rho} + \rho \operatorname{div}_x \vec{u} = 0 \quad (1-33)$$

where  $\operatorname{div}_x [\vec{u}]$  denotes the spatial divergence of the velocity field.

### I.1.4.2 Conservation of momentum or principle of virtual power

The principle of virtual power states that in any area  $\Omega$  the momentum balance should be satisfied. The sum of the virtual power of internal force  $\delta P_{\text{int}}$  and the virtual power of external forces  $\delta P_{\text{ext}}$  is at any time equal to the total virtual power of inertia forces  $\delta P_a$ .

$$\delta P_{\text{int}} + \delta P_{\text{ext}} = \delta P_a \quad (1-34)$$

In its local form, this principle can be expressed by the following partial differential equation with associated Neumann boundary condition:

$$\begin{cases} \operatorname{div}(\underline{\sigma}) + \vec{f} - \rho \vec{u} = \vec{0} & \text{in } \Omega \\ \underline{\sigma} \vec{n} = \vec{F} & \text{on } \Gamma \end{cases} \quad (1-35)$$

$$\quad (1-36)$$

where  $\underline{\sigma}$  is the Cauchy stress tensor,  $\vec{f}$  is the body force vector,  $\vec{F}$  is the surface force vector acting on part  $\Gamma_F$  of boundary of  $\Omega$ ,  $\vec{u}$  is the acceleration vector, and  $\vec{n}$  denotes the outward vector normal to the boundary surface  $\Gamma$  of the solid.

### I.1.4.3 Conservation of energy or first principle of thermodynamics

The first principle of thermodynamic which also can be named energy conservation law, means the sum of internal energy rate per unit deformation volume of the isolated system is equal to the sum of the external stress power and the heat flux received by  $\Omega$ . By using the material time derivative of a volume integral as well as the divergence theorem in order to transform surface integrals into volume integrals, and by applying the spatial localization theorem for materially simple continua, we obtain the local form of the first principle of thermodynamics as below:

$$\underline{\sigma} : \underline{D} - \rho \dot{e} + \xi - \text{div}(\vec{q}) = 0 \quad (1-37)$$

where  $e$  is the specific internal energy (per unit of mass),  $\underline{D}$  is the total strain rate tensor,  $\xi$  is the internal heat source, and  $\vec{q}$  is the heat flux vector.

### I.1.4.4 Positivity of the entropy production or second principle of thermodynamics

The second principle of thermodynamics states that the energy systems have a tendency to increase their entropy rather than to decrease it. In another words, the rate of the entropy production is always greater than or equal to the amount of heat received divided by the absolute temperature:

$$\rho \dot{s} + \text{div}\left(\frac{\vec{q}}{T}\right) - \frac{\xi}{T} \geq 0 \quad (1-38)$$

where  $s$  is the specific entropy per unit mass and  $T$  defines the absolute temperature.

### I.1.4.5 Clausius-Duhem inequality

The Clausius-Duhem inequality expresses a statement concerning the irreversibility of natural processes, especially when energy dissipation is involved. The local forms of the first and second laws of the thermodynamics can be combined, eliminating the internal heat quantity, and a new inequality called Clausius-Duhem inequality is then obtained:

$$\underline{\sigma} : \underline{D} - \rho(\dot{\psi} + s\dot{T}) - \frac{q}{T} \text{grad}(T) \geq 0 \quad (1-39)$$

where the specific free energy or Helmholtz free energy per unit mass  $\psi$  is defined by:

$$\psi = e - Ts \quad (1-40)$$

This inequality plays an important role in the formulation of constitutive equations of

continua in the framework of the thermodynamics of irreversible processes.

### **I.1.5 About the continuum damage mechanics (CDM)**

In the few last decades, micromechanical modeling has been developed based on increasing understanding of the physical aspects of the material failure. An important modeling work has been done to describe these mechanisms using approximate models. They can be briefly classified into two groups, such as uncoupled and coupled damage approaches.

In the uncoupled approach, the effect of damage on elastic and plastic strains is neglected, and the so-called failure indicators which are based on maximum or equivalent stresses, maximum or equivalent strains, plastic work, or the equations of the strain rate, temperature and pressures, stress invariants [Freudenthal50, Rice69, Johnson85, Bai08, Ebnoether13] are introduced to represent the deterioration of the materials. Due to their uncoupled nature, these models do not consider stress and stiffness softening within the material caused by damage during deformation, thus they can't accurately predict the localization and failure under various stress states without additional criteria.

With the assumption of pre-existing microcracks and micro-voids, a theory based on the concept of growth and coalescence was introduced. Rice and Tracey [Rice69] theoretically presented a cavity growth model with a spherical cavity in the perfect plastic material. Later, a new model was introduced by [Gurson77]. The starting point of Gurson' theory is the microscopic idealization of porous metals as aggregates containing voids of simple geometric shapes embedded in a metallic matrix whose behavior is governed by a rigid plastic von Mises yield function. The damage variable is considered as the local fraction of volume occupied by voids. The interaction between micro-defects is also very complex during large deformation, thus a number of related studies have been performed [Ghosh82, Pilling85, Ridley89].

The other widely used fracture approach is the CDM (continuum damage mechanics theory). Since the pioneering work by Kachanov [Kachanov58], many works have been done for the formulation of constitutive models to describe the internal degradation of solids within the framework of continuum mechanics. A considerable work has been done in the field of CDM for many kinds of materials under various loading conditions, as can be found in the following books [Lemaitre85, Lemaitre92, Voyiadjis92, Lemaitre05, Lemaitre09, Besson10, Saanouni12, Murakami12]. For ductile damage dedicated to metal forming under large inelastic strain, the reader is referred to the recent book [Saanouni12].



### I.1.5.1 Phenomenological aspects of the ductile damage

Ductile damage in metallic materials can be regarded as a physical process of creation and growth of micro-voids or microcracks. During the material (microstructure) deformation process, the metal degradation is strongly dependent on the material, loading conditions, temperature and other environment factors to which the material is subjected. Therefore, it is important to enumerate the main damage mechanisms in the case of metallic materials. In Fig. 1-4, some types of damage under various conditions are shown. Depending on these conditions, damage can be briefly classified into two different types: brittle damage and ductile damage.

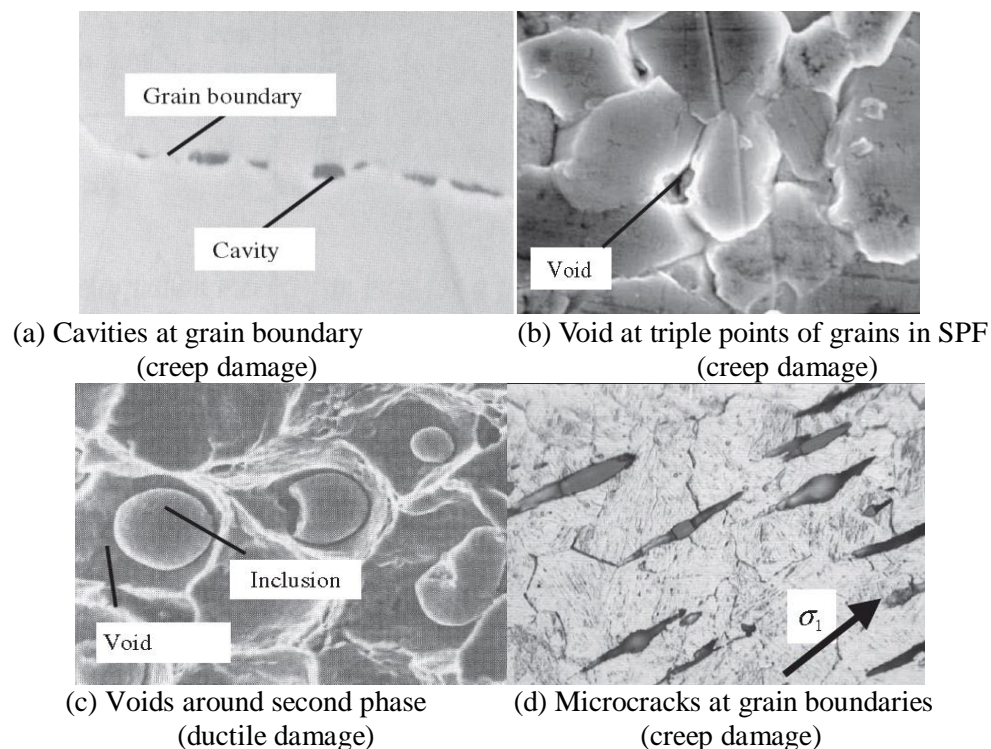


Fig. 1- 4. Damage in (a) high temperature creep; (b) superplastic forming; (c) cold forming; (d) hot forming [Lin05].

- Brittle damage normally occurs in the form of cleavage of crystallographic planes with cleavage forces not high enough to produce slip. This phenomenon always happens at low temperature, or under repeated loads at low level below the yield stress (high cycle fatigue) but it also appears for high temperature, associated with creep fracture.
- Ductile damage normally occurs with the nucleation and growth of cavities with large plastic deformations. When happened at an elevated temperature, it can be called creep damage.

### I.1.5.2 Mathematical representation of the ductile damage

For ductile damage, all kinds of defects in the material can be regarded as volume defects (micro-voids) together with surface defects (micro-cracks). Accordingly, a natural representation of these defects can be made using scalar variables as a simplest representation of isotropic damage:

$$\begin{cases} d_v = \frac{\delta V_{void}}{\delta V_{RVE}} & (a) \\ d_s = \frac{\delta S_s}{\delta S_{RVE}} & (b) \end{cases} \quad (1-41)$$

However, straightforwardly speaking ductile damage is of highly anisotropic nature at least at the microscopic scale. Many works have been dedicated to the modeling of anisotropic ductile damage for metallic material (e.g. [Murakami81, Murakami83, Ortiz85; Chow87, Chow88, Lubarda93, Seweryn98, Voyiadjis00, Menzel05] etc.). For the sake of simplicity, the ductile damage will be reduced to the isotropic damage in this work limiting ourselves to the plastic anisotropy. Recent works made by our team are dedicated to the anisotropy of the ductile damage [Rajhi14, Ngu12, Nasim14].

### I.1.5.3 Effect of ductile damage on the elastoplastic behavior of metals

For metallic materials, the fracture by ductile damage can be regarded as the irreversible phenomena that break the intermolecular bonds and destroy the continuity of the crystal planes. At the same time, the new breaking surfaces and volume discontinuities can be produced in the form of microcracks. These microcracks evolve through different mechanisms to form macroscopic cracks where plastic strain increases [Soyarslan10, Thuillier2011].

The presence of these microdefects inside deforming materials affects deeply the other phenomenon as strains, hardening, etc. This effect is schematized in Figure I-5, showing schematically a typical force-displacement curve with ductile damage effect at the origin of the final fracture. In the CDM framework, the ductile damage effect on the material behavior is called the damage – behavior coupling [Lemaitre85, Lemaitre05, Besson10, Saanouni12].

This coupling is performed thanks to the definition of effective state variables through four kinds of assumptions:

- The equivalent strain assumption leading to the definition of the sole effective stress tensors [lemaitre85].

- The equivalent stress assumption leading to the definition of the sole effective strain tensor.
- The elastic energy equivalence leading to the definition of both the effective stress and the strain tensors.
- The total energy equivalence leading to the definition of the overall effective state variables as pioneered by [Saanouni94, Saanouni12, Murakami12]. This is discussed in the next section.

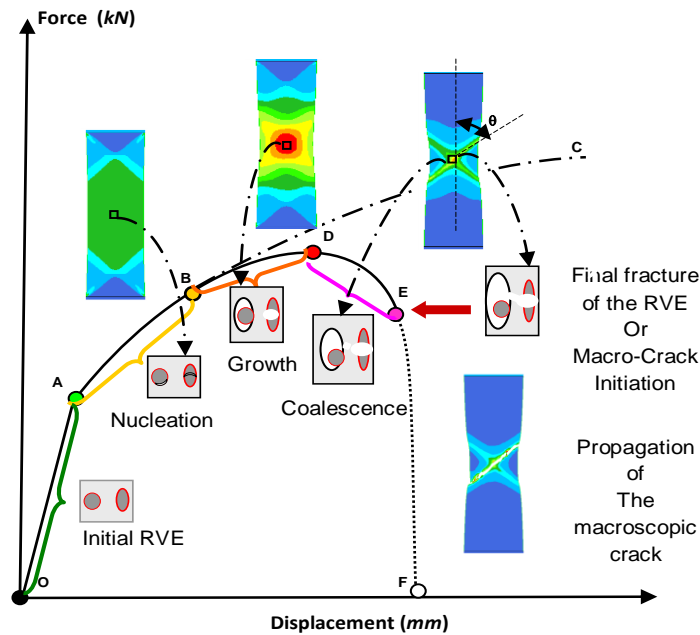


Fig. 1- 5. Schematic effect of the ductile damage on the force-displacement curve from the initial plastic yield to final fracture [Saanouni12].

#### I.1.5.4 State variables and effective state variables

The thermodynamics of irreversible processes requires the introduction of state variables. These state variables are divided into observable variables and internal variables. For the isothermal problems the observable variables are the total strain and stress tensors  $(\underline{\varepsilon}, \underline{\sigma})$ , and the internal variables represent different dissipative phenomena as the plastic flow  $(\underline{\varepsilon}^p, \underline{\sigma})$ , isotropic hardening  $(r, R)$ , kinematic hardening  $(\underline{\alpha}, \underline{X})$  and ductile damage  $(d, Y)$ . Observable and internal variables and their associated variables are summarized in Table 1-1.

Table 1-1. Internal variables and their associated or dual variables.

	Internal variables	Dual variables
Elasticity:	$\underline{\varepsilon}_e$	$\underline{\sigma}$
Kinematic hardening:	$\underline{\alpha}$	$\underline{X}$
Isotropic hardening:	$r$	$R$
Ductile damage	$d$	$Y$

The assumption of total energy equivalence is used to describe the effective state variables. This postulates the existence of a fictitious undamaged configuration (where  $d = Y = 0$ ), in which the state space is defined by the couples of effective variables  $(\underline{\varepsilon}_e, \underline{\sigma})$ ,  $(\underline{\alpha}, \underline{X})$ ,  $(\tilde{r}, R)$  associated with the actual configuration characterized by the pairs of state variables presented in Table 1-1. The total energy is assumed to be the sum of the elastic (reversible) energy  $W_e$ , the energy dissipated in the kinematic hardening  $W_\alpha$  and the energy stored in the isotropic hardening  $W_r$ . This total energy is assumed to be the same for both configurations. This leads to the following relations defining the effective variables:

$$W_e(\underline{\varepsilon}_e, d) = 1/2(\underline{\varepsilon}_e : \underline{\sigma}) = 1/2(\tilde{\underline{\varepsilon}}_e : \tilde{\underline{\sigma}}) \quad \Rightarrow \tilde{\underline{\varepsilon}}_e = \xi_e(d)\underline{\varepsilon}_e, \quad \tilde{\underline{\sigma}} = \frac{\underline{\sigma}}{\xi_e(d)} \quad (1-42)$$

$$W_\alpha(\underline{\alpha}, d) = 1/2(\underline{\alpha} : \underline{X}) = 1/2(\tilde{\underline{\alpha}} : \tilde{\underline{X}}) \quad \Rightarrow \tilde{\underline{\alpha}} = \xi_\alpha(d)\underline{\alpha}, \quad \tilde{\underline{X}} = \frac{\underline{X}}{\xi_\alpha(d)} \quad (1-43)$$

$$W_r(r, d) = 1/2(r \cdot R) = 1/2(\tilde{r} \cdot \tilde{R}) \quad \Rightarrow \tilde{r} = \xi_r(d)r, \quad \tilde{R} = \frac{R}{\xi_r(d)} \quad (1-44)$$

The damage effect functions  $\xi_e(d)$ ,  $\xi_\alpha(d)$  and  $\xi_r(d)$  are the positive and decreasing functions of the damage variables. These functions reduce to unity for an undamaged material and approach zero for a totally damaged material. These functions will be defined later.

## I.2 Formulation of fully coupled elastoplastic-damage constitutive equations

### I.2.1 Introduction

In sheet metal forming processes, it is well known that the deformation is accompanied by many anisotropic phenomena. In order to accurately describe the material behavior used for the numerical simulations, a comprehensive understanding of these initial and induced

anisotropies is required. Lots of researches have been done on the initial anisotropy of onset of the plasticity yield function ([Hill48, Barlat87, Barlat89, Barlat91], etc.), which is assumed to be result from the texture induced during the rolling process. For damage prediction, it is also a big issue to well understand the evolution of the subsequent yield surfaces or induced anisotropies under proportional and non-proportional loading paths. Since the failure is very sensitive to small changes in the yield surface, the evolution of the subsequent yield surfaces attracts great attentions.

Since several decades, lots of experiments have shown a significant distortion of the yield surface [Phillips72; Phillips76; Phillips77; Phillips79; Phillips84]. The same result have been obtained concerning the evolution of yield surfaces for the AISI 304 stainless steel under axial-torsional proportional loading [Wu91], and the common characteristics of yield surface was found in many experimental investigations [Ishikawa97, Brown03]. Most of experimental results were obtained in the combined axial-torsional or combined axial-internal pressure loading conditions using some thin-walled tubular specimens. Recently Khan and his group [Khan09, Khan10a, Khan10b] have done much effort on this research about two kinds of aluminum alloys (AL6061-T6511 and annealed 1100 AL) under tension-tension axial, hoop, combined hoop and axial proportional loading paths. The initial yield surface is very close to the von-Mises yield surface and subsequent surfaces undergo the translation, distortion, extension or shrinkage, shape with a sharp nose in the front and blunting in the opposite direction. Also different cross-effects were correlated to the different hardening properties.

From theoretical point of view, a wide number of publications proposed different approaches for modeling the distortion of the yield surfaces, see e.g. ([Ortiz83, Rees84, Helling86, Helling87, Yeh96, Yeh06, Cho96, Kowalsky99, François01, Wu02, Wu03, Feigenbaum07, Feigenbaum08]). On the whole, all these publications can be categorized into two types namely, the algebraic approaches and the geometric approaches. For the first kind, Ortiz and Popov [Ortiz83] proposed a general expression for the yield surface with distortional hardening in which the classical von Mises with mixed isotropic and kinematic hardening is found as a particular case. François [François01] extended the von Mises yield surfaces to include distortional hardening by modifying the expression of the deviatoric stress. Feigenbaum and Dafalias [Feigenbaum07, Feigenbaum08] introduced a thermodynamically-consistent framework of isotropic, kinematic and distortional hardening under small strains assumption.

In the geometric approach, the yield surface normally divided into forward and rear parts tried to fit the experimental responses from the geometric point of view [Yeh96, Yeh06]. However,

these geometrical approaches are subject to some problems:

- The physical signification of introduced model parameters: Even though many new material models can describe the distortion of the yield surfaces, but the less physical significance of the introduced parameters restrict their applicability.
- Lack description of the distortion ratio in experiment: The distortional ratio of the yield surfaces can be not accurately predicted compared to the experimental results.
- Test methods for sheet metal under changing loading paths. Commonly the distortions of subsequent yield surfaces are investigated using thin-wall tube specimen under axial torsion loading paths, which is not representative of sheet metal forming processes.

## I.2.2 Overview of the distortional hardening without damage models

### I.2.2.1 Barlat model

Barlat et al [Barlat11] proposed a distortional hardening model named HAH, which is based on the homogeneous yield surface defined by a stable component  $\phi$  and a fluctuating component  $\phi_h$ . This yield function  $f$  can be described by the following equation

$$\begin{aligned}
 f(\underline{s}, \varepsilon_{eq}^p) &= \left[ \phi^q + \phi_h^q \right]^{\frac{1}{q}} - \sigma_y(\varepsilon_{eq}^p) \leq 0 \\
 &= \left[ \phi^q + f_1^q \left[ \hat{h}^s : \underline{s} - \left| \underline{h}^s : \underline{s} \right| \right]^q + f_2^q \left[ \hat{h}^s : \underline{s} - \left| \underline{h}^s : \underline{s} \right| \right]^q \right]^{\frac{1}{q}} - \sigma_y(\varepsilon_{eq}^p) \leq 0
 \end{aligned} \tag{1-45}$$

where  $q$ ,  $f_1$  and  $f_2$  are three material parameters and  $\hat{h}_s$  is the microstructure controlled deviatoric stress tensor generated by the prior deformation history and can be viewed as a continuum representation of a given set of active slip systems, irrespective to the slip directions. This tensor is usually set equal to stress deviator initiating plastic strain but this is not always necessarily so. The  $f_1$  and  $f_2$  can be represented by two new parameters  $g_1$  and  $g_2$  [Barlat11], according to function below:

$$f_1 = \left[ \frac{1}{g_1^q} - 1 \right]^{\frac{1}{q}} \tag{1-46}$$

$$f_2 = \left[ \frac{1}{g_2^q} - 1 \right]^{\frac{1}{q}} \tag{1-47}$$

The yield surface depends on the sign of the scalar product  $\left(\hat{h}^s : \underline{s}\right)$  and can be divided into forward and negative parts, covering different shapes with a nearby mathematical way. With this model, the Bauschinger effect and more generally anisotropic hardening are captured without using specific state variables associated to kinematic hardening. If  $f_1 = f_2 = 0$ , the yield function (1-45) reduces to the traditional isotropic or anisotropic yield function  $f(\underline{s}) = \phi(\underline{s}) - \sigma_y(\varepsilon_{eq}^p) \leq 0$ .

### 1.2.2.2 Feigenbaum and Dafalias model

Based on Hill's quadratic yield criterion, a varying fourth-rank tensor is adopted to describe the distortion of the yield surface [Feigenbaum07]. The yield surface function is given as:

$$f = \sqrt{(\underline{S} - \underline{X}) : \underline{\underline{H}} : (\underline{S} - \underline{X})} - \sigma_y(\varepsilon_{eq}^p) \leq 0 \quad (1-48)$$

$\underline{\underline{H}}$  is a fourth-rank tensor describing the initial and induced anisotropies defined by:

$$\underline{\underline{H}} = \underline{\underline{H}}_0 + (\underline{n}_r : \underline{X}) \underline{\underline{A}} \quad (1-49)$$

where  $\underline{\underline{A}}$  is the fourth-rank evolving anisotropic tensor,  $\underline{\underline{H}}_0$  is a constant fourth-rank tensor representing the initial plastic anisotropy with Hill yield criterion. The orientation tensor  $\underline{n}_r$  is normal to the yield surface:

$$\underline{n}_r = \frac{\underline{S} - \underline{X}}{\|\underline{S} - \underline{X}\|} \quad (1-50)$$

$\underline{\underline{A}}$  is responsible for the distortional hardening, while  $\underline{n}_r : \underline{X}$  is responsible for the directionality of the distortion. This quantity varies from  $-\|\underline{X}\|$  to  $\|\underline{X}\|$  affecting directly the distortional tensor  $\underline{\underline{A}}$ . Note that the fourth-rank tensor  $\underline{\underline{A}}$  is governed by the following differential equations:

$$\underline{\underline{\dot{A}}} = -\lambda c_1 \|\underline{S} - \underline{X}\|^2 \left[ (\underline{n}_r : \underline{X}) \underline{n}_r \otimes \underline{n}_r + \frac{3}{2} c_2 \underline{\underline{A}} \right] \quad (1-51)$$

where  $c_1$  and  $c_2$  are material constants.

### 1.2.2.3 Teodosiu model

Based on the relationship between the flow-stress evolution and the micro-structural evolution, a physically-based constitutive model has been proposed by [Teodosiu95, Haddadi06]. The

yield function is based on a modified Hill-type yield function:

$$f = \|\underline{Z}\|_H - R - f(\underline{\zeta}) - \sigma_y \leq 0 \quad (1-52)$$

with the Hill equivalent stress:

$$\|\underline{Z}\| = \sqrt{\underline{Z} : \underline{H} : \underline{Z}} \quad (1-53)$$

where  $\underline{Z} = \underline{\sigma} - \underline{X}$  and  $\underline{\zeta}$  and  $\underline{H}$  are both fourth-rank tensors.  $f(\underline{\zeta})$  describes the directional strength of planar persistent dislocations related to the texture anisotropy. Isotropic and kinematic hardenings are governed by the classical Armstrong-Frederick evolution rule:

$$\dot{R} = C_R (R_{sat} - R) \dot{\underline{\epsilon}}^p \quad \text{and} \quad \dot{\underline{X}} = C_X (X_{sat} \underline{N} - \underline{X}) \dot{\lambda} \quad (1-54)$$

where  $C_R$  and  $C_X$  characterize the saturation rate of isotropic and kinematic hardening respectively, and  $R_{sat}$  and  $X_{sat}$  are both material parameters characterizing the saturation value of  $R$  and  $\underline{X}$ .  $\underline{N}$  denoting the current direction of the strain rate tensor, to the persistent dislocation structures whose effects are described by  $\underline{\zeta}$ .

Within the Teodosiu model, the strength due to the dislocation structures is decomposed into a part associated with current slip systems (denoted by  $\zeta_D = \underline{N} : \underline{\zeta} : \underline{N}$ ) and the one related to the latent slip systems (denoted by  $\zeta_L = \underline{\zeta} - \zeta_D \underline{N} \otimes \underline{N}$ ). From this letter we can get  $\underline{\zeta} = \zeta_D \underline{N} \otimes \underline{N} + \underline{\zeta}_L$ . For such quantities, Teodosiu postulated the evolution equations:

$$\dot{\underline{\zeta}}_L = -C_{SL} \left( \frac{\|\underline{\zeta}_L\|}{\zeta_{sat}} \right)^{nl} \underline{\zeta}_L \dot{\lambda} \quad \text{and} \quad \dot{\zeta}_D = -C_{SD} [g_1'(\zeta_{sat} - \zeta_D) - g_2' \zeta_D] \dot{\lambda} \quad (1-55)$$

$C_{SL}$  and  $C_{SD}$  are respectively the saturation rates of  $\underline{\zeta}_L$  and  $\zeta_D$ .  $\zeta_{sat}$  is the saturation value of  $\zeta_D$ .  $g_1'$  and  $g_2'$  are deformation-dependent parameters [Haddadi06, Shi13]. According to equations above, there is no evolution equation for the total tensor  $\underline{\zeta}$ .

#### 1.2.2.4 Levkovitch and Svendsen model

Although  $\underline{\zeta}$  is considered as internal variable by Teodosiu and Hu [Teodosiu95, Teodosiu98], but they did not give direct evolution relationship for it, since it is governed by (1-55). In the new constitutive equations, one possible evolution equation for  $\underline{\zeta}$  is defined by [Noman10]:



$$\underline{\underline{\zeta}} = c_{SD} h_p \zeta_{sat} \lambda \underline{N} \otimes \underline{N} - c_{SD} (g_1 + g_2) \lambda \zeta_D \underline{N} \otimes \underline{N} - c_{st} \left( \frac{\|\underline{\underline{\zeta}}\|}{\zeta_{sat}} \right)^{n1} \lambda \underline{\underline{\zeta}} \quad (1-56)$$

Neglecting initial flow anisotropy and texture effects, this model is similar to Teodosiu and Hu model [Teodosiu98]. More detailed comparisons can be found in [Teodosiu 98, Haddadi06, Baodong12].

### 1.2.2.5 François model

François [François01] proposed a simple model to describe the distortion of the yield surfaces within the classical thermodynamics framework. The idea of the model assumes that the distorted yield surface is nearby ‘egg-shaped’ controlled by the kinematic hardening variables. The yield surface has the following form:

$$f(\underline{\sigma}, \underline{X}, R) = \|\underline{S}_d - \underline{X}\| - R - \sigma_y \leq 0 \quad (1-57)$$

where  $\underline{S}_d$  is function of existing Cauchy stress and kinematic hardening stress:

$$\underline{S}_d = \underline{S} + \frac{\underline{S}_o : \underline{S}_o}{2X_{sat} (R + \sigma_y)} \underline{X} \quad (1-58)$$

where  $X_{sat}$  denotes the saturation value of the kinematic hardening,  $\underline{S}_o$  denotes the orthogonal part of  $\underline{S}_d$  to the kinematic hardening  $\underline{X}$ , and another collinear part to  $\underline{X}$  named  $\underline{S}_x$ . Their equations are:

$$\underline{S}_o = \underline{S} - \underline{S}_x \quad \text{and} \quad \underline{S}_x = \frac{\underline{S} : \underline{X}}{\|\underline{X}\|^2} \underline{X} \quad (1-59)$$

## 1.2.3 Formulation of the proposed fully coupled model

### 1.2.3.1 State variables and effective state variables

In this study, the elastoplastic constitutive equations fully coupled with the isotropic ductile damage using a thermodynamically-consistent framework [Saanouni94, Badreddine10, Saanouni12] are proposed. The detailed theoretical, numerical and applicative aspects of various versions of the fully coupled formulations can be found in [Saanouni12]. This general framework is used in this work in order to extend the fully coupled model presented in [Saanouni12] for the description of the yield surface distortion based on the François’ model described above.

The following couples of state variables are used: (i)  $(\underline{\varepsilon}^e, \underline{\sigma})$  for the elastoplastic flow; (ii)  $(\underline{\alpha}, \underline{X})$  for the kinematic hardening depicting the translation of the yield surface; (iii)  $(r, R)$  for the isotropic hardening depicting the change of yield surface radius, (v)  $(d, Y)$  represents the isotropic ductile damage in Lemaitre and Chaboche' sense [Lemaitre85, Saanouni12]. The distortion of the yield surface during the deformation is described by replacing the usual stress deviator  $\underline{S}$  by a 'distorted stress'  $\underline{S}_d$  [François01], which is not remarked as a new thermodynamic force, but only function of existing variables. It should be noted that the damage variable has a values between 0 and 1, the total fracture of the RVE (Representative Volume Element) is achieved when  $d = d_c = 1$ . The strong coupling between the plastic flow with hardening and the ductile damage is performed in the framework of the total energy equivalence assumption [Saanouni94, Saanouni12], leading to the definition of the effective state variables  $(\tilde{\underline{\varepsilon}}^e, \tilde{\underline{\sigma}})$   $(\tilde{\underline{\alpha}}, \tilde{\underline{X}})$  and  $(\tilde{r}, \tilde{R})$  through the use of two damage-effect functions given by:

$$(\tilde{\underline{\varepsilon}}^e = \sqrt{1-d} \underline{\varepsilon}^e, \tilde{\underline{\sigma}} = \frac{\underline{\sigma}}{\sqrt{1-d}}) \quad (1-60)$$

$$(\tilde{\underline{\alpha}} = \sqrt{1-d} \underline{\alpha}, \tilde{\underline{X}} = \frac{\underline{X}}{\sqrt{1-d}}) \quad (1-61)$$

$$(\tilde{r} = \sqrt{1-d^\gamma} r, \tilde{R} = \frac{R}{\sqrt{1-d^\gamma}}) \quad (1-62)$$

where  $\gamma$  is a parameter governing the effect of the ductile damage on the isotropic hardening [Saanouni12].

### 1.2.3.2 State potential and state equations

The effective variables chosen above are used in the state and dissipation potentials in order to describe the damaged elastoplastic behavior. The Helmholtz free energy  $\Psi = \Psi(\underline{\varepsilon}^e, \underline{\alpha}, r, d)$ , positive and convex function of all the state variables in the strain space is taken as a state potential. It is assumed here that the elastic strain is still very small compared to the plastic strain, so that (see equation 1-18)  $\overline{D} = \overline{\underline{\varepsilon}}^{el} + \overline{D}^p$ . Assuming that the plastic strain has no effect on the elastic behavior, the state potential is additively decomposed (isothermal case):

$$\rho\psi(\underline{\varepsilon}^e, \underline{\alpha}, r, d) = \rho\psi^e(\underline{\varepsilon}^e, d) + \rho\psi^p(\underline{\alpha}, r, d) \quad (1-63)$$

with

$$\begin{cases} \rho\psi^e(\underline{\varepsilon}^e, d) = \frac{1}{2}(1-d)\lambda_e(\underline{\varepsilon}^e : \underline{1})^2 + (1-d)\mu_e(\underline{\varepsilon}^e : \underline{\varepsilon}^e) \\ \rho\psi^p(\underline{\alpha}, r, d) = \frac{1}{3}(1-d)C\underline{\alpha} : \underline{\alpha} + \frac{1}{2}(1-d^\gamma)Qr^2 \end{cases} \quad (1-64)$$

The total differential of this free energy is:

$$\rho\dot{\Psi} = \rho \frac{\partial \Psi}{\partial \underline{\varepsilon}^e} : \dot{\underline{\varepsilon}}^e + \rho \frac{\partial \Psi}{\partial \underline{\alpha}} : \dot{\underline{\alpha}} + \rho \frac{\partial \Psi}{\partial r} : \dot{r} + \rho \frac{\partial \Psi}{\partial d} : \dot{d} \quad (1-65)$$

Accordingly, the Clausius-Duhem inequality can be written in the following way:

$$(\underline{\sigma} - \rho \frac{\partial \Psi}{\partial \underline{\varepsilon}^e}) : \dot{\underline{\varepsilon}}^e + \underline{\sigma} : \underline{D} - \rho \left( \frac{\partial \Psi}{\partial \underline{\alpha}} : \dot{\underline{\alpha}} + \frac{\partial \Psi}{\partial r} : \dot{r} - \frac{\partial \Psi}{\partial d} : \dot{d} \right) \geq 0 \quad (1-66)$$

According to the reversibility of elastic strain and no-dissipation hypothesis, assuming the Helmholtz free energy  $\Psi$  is an isotropic function of the arguments, and together with small elastic strain and incompressibility assumptions, the following state equations can be easily obtained:

$$\underline{\sigma}(\underline{\varepsilon}^e, d) = \underline{\tau}(\underline{\varepsilon}^e, d) = \rho \frac{\partial \Psi}{\partial \underline{\varepsilon}^e} = (1-d)\lambda_e \text{tr}(\underline{\varepsilon}^e) \underline{1} + 2\mu_e(1-d)\underline{\varepsilon}^e \quad (1-67)$$

$$\underline{X}(\underline{\alpha}, d) = \rho \frac{\partial \Psi}{\partial \underline{\alpha}} = \frac{2}{3}(1-d)C\underline{\alpha} \quad (1-68)$$

$$R(r, d) = \rho \frac{\partial \Psi}{\partial r} = (1-d^\gamma)Qr \quad (1-69)$$

$$Y(\underline{\varepsilon}^e, \underline{\alpha}, r, d) = -\rho \frac{\partial \Psi}{\partial d} = Y^e + Y^\alpha + Y^r \quad (1-70)$$

$$Y^e = \frac{1}{2} \left( \lambda_e (\underline{\varepsilon}^e : \underline{1})^2 + \mu_e \underline{\varepsilon}^e : \underline{\varepsilon}^e \right) \quad (1-70a)$$

$$Y^\alpha = \frac{1}{3} C \underline{\alpha} : \underline{\alpha} \quad (1-70b)$$

$$Y^r = \frac{1}{2} \gamma d^{\gamma-1} Q r^2 \quad (1-70c)$$

where  $\mu_e$  and  $\lambda_e$  are the classical Lamé's constants ( $\lambda_e = \nu E / ((1+\nu)(1-2\nu))$  ,  $\mu_e = E / (2(1+\nu))$ ), while the parameters  $C$  and  $Q$  are the kinematic and the isotropic hardening moduli respectively. Consequently, with the equations above, Equation (1-70) leads

to the well-known form of the intrinsic dissipation:

$$\Phi = \underline{\sigma} : \underline{D}^p - \underline{X} : \underline{\dot{\alpha}} - R\dot{r} + Y\dot{d} \quad (1-71)$$

where the rotational objective derivatives of the tensorial quantities are used.

It is widely admitted that when the stress (and strain) in a given point is compressive, the damage rate in that point is very slow, if not completely zero. The simplest way to account for this phenomenon while avoiding some drawbacks related to the loss of the convexity and continuity of the state and dissipation potentials is to decompose the elastic damage force  $Y^e$  to a compressive part and tension part as suggested by Lemaitre and Ladeveze [Lemaitre85].

This can be done using the straightforward spectral decomposition of the strain and stress tensors into positive and negative parts [Lemaitre05, Lemaitre09 and Saanouni12]. To do that, let's consider any symmetric second-rank tensor  $\underline{T}$  with  $\underline{T}^{dev} = \underline{T} - T^S \underline{1}$  its deviatoric part,  $T^S = 1/3 \text{tr}(\underline{T})$  is its mean value and  $\underline{1}$  is the second-rank unit tensor. The additive decomposition of this tensor into positive and negative parts  $\underline{T} = \langle \underline{T} \rangle_+ + \langle \underline{T} \rangle_-$  can be made with  $\langle \underline{T} \rangle_+ = \sum_{i=1}^3 \langle T_i \rangle \vec{e}_i \otimes \vec{e}_i$  and  $\langle \underline{T} \rangle_- = \underline{T} - \langle \underline{T} \rangle_+$  where  $\langle T_i \rangle$  is the  $i^{\text{th}}$  eigenvalue of the tensor  $\underline{T}$  and  $\vec{e}_i$  its associated eigenvector. The notation  $\langle x \rangle$  indicates the positive part of  $x$ , i.e.  $\langle x \rangle = x$  if  $x > 0$  and  $\langle x \rangle = 0$  if  $\langle x \rangle \leq 0$ . The elastic part of the state potential can be represented as:

$$\begin{aligned} \rho \psi^e(\underline{\varepsilon}^e, d) = & \frac{\nu E(1-d)}{2(1+\nu)(1-2\nu)} \langle \underline{\varepsilon}^e : \underline{1} \rangle_+^2 + \frac{E(1-d)}{2(1+\nu)} \langle \underline{\varepsilon}^e \rangle_+ : \langle \underline{\varepsilon}^e \rangle_+ + \\ & \frac{\nu E(1-hd)}{2(1+\nu)(1-2\nu)} \langle \underline{\varepsilon}^e : \underline{1} \rangle_-^2 + \frac{E(1-hd)}{2(1+\nu)} \langle \underline{\varepsilon}^e \rangle_- : \langle \underline{\varepsilon}^e \rangle_- \end{aligned} \quad (1-72)$$

Accordingly, the effect of the ductile damage on the elastic behavior described by the effective variables of Equation (1-60) is modified and decomposed into deviatoric and hydrostatic parts as following:

$$\left\{ \begin{aligned} \tilde{\underline{\varepsilon}}^e &= g_e(d) \langle \underline{\varepsilon}^e \rangle_+ + g_e(hd) \langle \underline{\varepsilon}^e \rangle_- \\ &= \sqrt{1-d} \left( \langle \underline{\varepsilon}^e \rangle_+ + \frac{1}{3} \langle \text{tr}(\underline{\varepsilon}^e) \rangle_+ \underline{1} \right) + \sqrt{1-hd} \left( \langle \underline{\varepsilon}^e \rangle_- - \frac{1}{3} \langle -\text{tr}(\underline{\varepsilon}^e) \rangle_- \underline{1} \right) \\ \tilde{\underline{\sigma}} &= \frac{\langle \underline{\sigma} \rangle_+}{g_e(d)} + \frac{\langle \underline{\sigma} \rangle_-}{g_e(hd)} \\ &= \frac{1}{\sqrt{1-d}} \left( \langle \underline{\sigma}^{dev} \rangle_+ + \frac{1}{3} \langle \text{tr}(\underline{\sigma}) \rangle_+ \underline{1} \right) + \frac{1}{\sqrt{1-hd}} \left( \langle \underline{\sigma}^{dev} \rangle_- - \frac{1}{3} \langle -\text{tr}(\underline{\sigma}) \rangle_- \underline{1} \right) \end{aligned} \right. \quad (1-73)$$

in which  $\underline{e}^e$  stands for the deviatoric part of the small elastic strain tensor  $\underline{\varepsilon}^e$  and the parameter  $h \in [0.0 \ 1.0]$  is the microcracks closure parameter. If  $h=1$ , the microcracks closure effect is skipped, while when  $h=0$  the microcracks close as soon as the stress tensor is negative (see discussion in [Saanouni12]).

By using the effective strain-like variables defined above in the Helmholtz free energy taken as a state potential, the following new expression of  $\underline{\sigma}$  and  $Y^e$  can be easily obtained [Saanouni12]:

$$\begin{cases} \underline{\sigma} = 2\mu_e \left[ (1-d) \langle \underline{e}^e \rangle_+ + (1-hd) \langle \underline{e}^e \rangle_- \right] + \lambda_e \left[ (1-d) \langle \text{tr}(\underline{\varepsilon}^e) \rangle - (1-hd) \langle -\text{tr}(\underline{\varepsilon}^e) \rangle \right] \underline{1} \\ Y^e = 2\mu_e \left[ \langle \underline{e}^e \rangle_+ : \langle \underline{e}^e \rangle_+ + h \langle \underline{e}^e \rangle_- : \langle \underline{e}^e \rangle_- \right] + \lambda_e \left[ \langle \text{tr}(\underline{\varepsilon}^e) \rangle^2 + h \langle -\text{tr}(\underline{\varepsilon}^e) \rangle^2 \right] \end{cases} \quad (1-74)$$

Clearly, Equation (1-74) shows that the microcracks closure parameter  $h$  serves to reduce the elastic damage force  $Y^e$  for compressive load if  $h < 1$ . If  $h=0$ , there is no more contribution of the compressive load on the damage force. This is the simplest way to differentiate the damage rate under tension and compression.

### 1.2.3.3 Yield function, dissipation potential and evolution equations

The framework of non-associative plasticity is used and a yield function  $f$  and a plastic potential  $F$ , both positive and convex functions of their main arguments in the stress space, are introduced from which the evolution relationships are obtained by the normality rule. In this study, a single surface model is used to describe the damaged elastoplastic behaviour using the same yield function and plastic potential chosen as:

$$\begin{cases} f = \frac{\|\underline{S}_d^c - \underline{X}\|_H}{\sqrt{1-d}} - \frac{R}{\sqrt{1-d'}} - \sigma_y & (a) \\ F = \frac{\|\underline{S}_d^p - \underline{X}\|_H}{\sqrt{1-d}} - \frac{R}{\sqrt{1-d'}} + \frac{3a}{4(1-d)C} \underline{X} : \underline{X} + \frac{b}{2(1-d')Q} R^2 + \frac{S}{s+1} \left\langle \frac{Y-Y_0}{S(\theta)} \right\rangle^{s+1} \frac{1}{(1-d)^\beta} & (b) \end{cases} \quad (1-75)$$

$$\|\underline{S}_d^i - \underline{X}\|_H = \sqrt{(\underline{S}_d^i - \underline{X}) : \underline{H} : (\underline{S}_d^i - \underline{X})} ; (i = \{c, p\}) \quad (1-76)$$

The stress norm  $\|\underline{S}_d^i - \underline{X}\|_H$  is the anisotropic Hill48 equivalent stress characterized by an anisotropic operator  $\underline{H}$  having six anisotropic parameters  $F, G, H, L, M$  and  $N$ , and  $\sigma_y$  is the initial yield stress. The parameters  $a$  and  $b$  represent the non-linearity of the kinematic and

isotropic hardening respectively, while  $s$ ,  $s$ ,  $\beta$  and  $Y_0$  govern the ductile damage evolution.

The parameter  $s$  governs directly the value of the equivalent plastic strain at fracture i.e. the material ductility. This parameter was always taken as constant under isothermal condition. However, it has been observed for many ductile materials that ductility is sensitive to the stress state which is represented by the stress invariants. In particular, the Lode angle  $\bar{\theta} = 1 - 6 \frac{\theta}{\pi}$  ( $\theta = \frac{1}{3} \cos^{-1}(\frac{27}{2} \frac{J_3}{\sigma_{eq}^3})$ ) has a great influence on the material ductility, as can be found in [Wierzbicki05, Cao13]  $J_3 = \det(\underline{\sigma})$  is the third stress invariant.

A simple way to account for this dependence is to suppose that  $s$  is function of  $\bar{\theta}$  according to (Equation 1-77).

$$s(\bar{\theta}) = \begin{cases} S_0 \left[ c_1 + \frac{\sqrt{3}}{2 - \sqrt{3}} c_2 \left( \sec(\frac{\bar{\theta}\pi}{6}) - 1 \right) \right]^{-1/s} & \text{Wierzbicki type} \\ S_0 \left[ c_1 + c_2 \bar{\theta}^2 \right]^{-1/s} & \text{Cao type} \end{cases}, \quad \bar{\theta} = 1 - 6 \frac{\theta}{\pi} \quad (1-77)$$

Note that the deviatoric tensor  $\underline{S}_d^i$  here is different from François's model. A new term is introduced to control the cross size (perpendicular to loading direction) of subsequent yield surface (see Part III.2.2.1), as shown below:

$$\begin{cases} \underline{S}_d^c = \underline{S} + \frac{\underline{S}_0 : \underline{S}_0}{2(1-d)X_{11}^c(R/\sqrt{1-d^\gamma} + \sigma_y)} \underline{X} - \frac{\underline{X} : \underline{X}}{2(1-d)X_{12}(R/\sqrt{1-d^\gamma} + \sigma_y)} \underline{S}_0 & (a) \\ \underline{S}_d^p = \underline{S} + \frac{\underline{S}_0 : \underline{S}_0}{2(1-d)X_{11}^p(R/\sqrt{1-d^\gamma} + \sigma_y)} \underline{X} & (b) \end{cases} \quad (1-78)$$

$$\text{where } \underline{S}_0 = \underline{S} - \underline{S}_x \quad \text{and} \quad \underline{S}_x = \frac{\underline{S} : \underline{X}}{\underline{X} : \underline{X}} \cdot \underline{X} \quad (1-79)$$

As in [François01], the egg-axis is parallel to kinematic hardening,  $\underline{X}$ , while  $\underline{S}$  is decomposed into its part  $\underline{S}_x$  collinear to  $\underline{X}$  and its orthogonal part  $\underline{S}_0$ .  $X_{11}^i$  is the same as in François model, used to help adjusting the distortion ratio of the subsequent yield surfaces. A new parameter  $X_{12}$  was introduced into  $\underline{S}_d^c$  to control the cross size of subsequent yield surfaces. Note that, from (1-78) it is possible to define the “damaged” parameters  $\tilde{X}_{11}^p = (1-d)X_{11}^p$ ,  $\tilde{X}_{11}^c = (1-d)X_{11}^c$  and  $\tilde{X}_{12} = (1-d)X_{12}$  which are decreasing with the damage increase. The influence of  $X_{11}^p$ ,  $X_{11}^c$  and  $X_{12}$  on subsequent yield surfaces will

be studied in next chapter.

Applying the generalized normality rule leads to the following flux variables which define the evolution of the dissipative phenomena:

$$\left\{ \begin{array}{l} \underline{D}^p = \lambda \frac{\partial F}{\partial \underline{\sigma}} = \lambda \underline{n}^p \\ \text{where} \\ \underline{n}^p = \frac{\underline{n}^d}{\sqrt{1-d}} : \left[ \underset{=}{1}^{dev} + \frac{\underline{X} \otimes \underline{S}_0}{\tilde{X}_{II}^p (R/\sqrt{1-d^\gamma} + \sigma_y)} \right] \text{ and } \underline{n}^d = \frac{\underline{H} : (\underline{S}_d^p - \underline{X})}{\|\underline{S}_d^p - \underline{X}\|_H} \end{array} \right. \quad (1-80)$$

$$\left\{ \begin{array}{l} \underline{\dot{\alpha}} = -\lambda \frac{\partial F}{\partial \underline{X}} = \lambda \left( -\frac{\underline{n}^x}{\sqrt{1-d}} - a\underline{\alpha} \right) \\ \text{where} \\ \underline{n}^x = \underline{n}^d - \frac{1}{(R/\sqrt{1-d^\gamma} + \sigma_y)} \left[ \frac{(\underline{S}_0 : \underline{S}_0)}{2\tilde{X}_{II}^p} \underline{n}^d - \frac{(\underline{S} : \underline{X})(\underline{X} : \underline{n}^d)}{\tilde{X}_{II}^p (\underline{X} : \underline{X})} \underline{S}_0 \right] \end{array} \right. \quad (1-81)$$

$$\left\{ \begin{array}{l} \dot{r} = -\lambda \frac{\partial F}{\partial R} = \lambda \left( \frac{n^i}{\sqrt{1-d^\gamma}} - br \right) \\ \text{where} \\ n^i = \frac{(\underline{S}_0 : \underline{S}_0)(\underline{n}_d^p : \underline{X})}{2\sqrt{1-d} \tilde{X}_{II}^p (R/\sqrt{1-d^\gamma} + \sigma_y)^2} + 1 \end{array} \right. \quad (1-82)$$

$$\dot{d} = \lambda \frac{\partial F}{\partial Y} = \frac{\dot{\lambda}}{(1-d)^\beta} \left( \frac{\langle Y - Y_0 \rangle}{S(\theta)} \right)^s \quad (1-84)$$

The plastic multiplier  $\lambda$  can be determined from the consistency condition  $\dot{f} = 0$  if  $f = 0$  [Saanouni94, Badreddine10, Saanouni12], however, it will be kept as the main unknown at each integration point of each finite element which will be determined from the FE calculation. The equivalent plastic strain rate is:

$$\dot{\underline{\epsilon}}_{eq}^p = \sqrt{\underline{D}^p : \underline{H}^{-1} : \underline{D}^p} = \dot{\lambda} \sqrt{\underline{n}^p : \underline{H}^{-1} : \underline{n}^p} \quad (1-85)$$

This model is implemented into ABAQUS/Explicit© finite element code through the VUMAT user defined subroutine (see the next chapter II).

### 1.2.3.4 Thermodynamical admissibility

After the formulation of all these equations of developed model, it is also necessary to verify the positivity of the dissipation in (1-71) by using (1-80) to (1-84), the dissipation equation can be written as below:

$$\dot{\lambda} \left( \underline{\sigma} : \underline{n}^p - \underline{X} : (\underline{n}^x - a\underline{\alpha}) - \frac{R}{(1-d^\gamma)} (n^r - br) + Y \right) \geq 0 \quad (1-86)$$

For  $\dot{\lambda} \geq 0$ , the equation becomes:

$$\underline{\sigma} : \underline{n}^p - \underline{X} : (\underline{n}^x - a\underline{\alpha}) - \frac{R}{(1-d^\gamma)} (n^r - b\tilde{r}) + \frac{1}{(1-d)^\beta} Y \left\langle \frac{Y - Y_0}{S(\theta)} \right\rangle^s \geq 0 \quad (1-87)$$

That is known  $\|\underline{S}_o\| \ll \|\underline{S}\|$ , especially when the loading path change is linear, so we can assumed  $\underline{n}^x \approx \underline{n}^p$  and  $n^i \approx 1$ . The equation above can be rewritten as:

$$\frac{(\underline{\sigma} - \underline{X}) : \tilde{n}^p}{\sqrt{1-d}} - \frac{R}{\sqrt{1-d^\gamma}} + a\underline{X} : \underline{\alpha} + \frac{b\tilde{r}R}{\sqrt{1-d^\gamma}} + \frac{1}{(1-d)^\beta} Y \left\langle \frac{Y - Y_0}{S(\theta)} \right\rangle^s \geq 0 \quad (1-88)$$

With the yield function (1-75a), we can simplify the equation to be:

$$\sigma_y + \frac{b}{Q} \frac{R^2}{(1-d^\gamma)} + \frac{3a}{2C} \frac{\underline{X} : \underline{X}}{(1-d)} + \frac{1}{(1-d)^\beta} Y \left\langle \frac{Y - Y_0}{S(\theta)} \right\rangle^s \geq 0 \quad (1-89)$$

As long as  $\sigma_y > 0$ ,  $\frac{b}{Q} > 0$ ,  $\frac{a}{C} > 0$  and  $Y > 0$ , the proposed model is thermodynamically admissible since the positivity of the intrinsic dissipation is warranted. This means that the constitutive equations defined by the state relations (1-67) to (1-70) and the evolution equations (1-80) to (1-84), fulfill the Clausius-Duhem inequality given by (1-39) which is the combination of the first and second principle of thermodynamics.

## I.3 Forming limit curves for sheet metal forming (FLCs)

### I.3.1 Introduction

Since 1950s, an extensive work has been done, which aims to find an effective way to find a relationship between the major principal strain  $\underline{\varepsilon}_1$  and the minor principal strain  $\underline{\varepsilon}_2$ . This has led to the construction of the so-called forming limit diagram (FLD), as pioneered by Keeler [Keeler63, Godwin68]. Since the FLDs are dependent on the stress paths, a Forming limit stress diagram has been proposed in the stress space and is shown to be insensitive to the strain paths [Arrieux82, Stoughton04]. From the theoretical point of view, various models have been proposed to calculate the forming limit curves. They can be classified in two



classes: (i) these assuming the homogenous sheet metal are necking theory (swift, Hill. etc), bifurcation theory [Stören75] and linearized perturbation theory [Dudzinski91]; (ii) those based on non-homogeneous sheet metal [Marciniak67].

### I.3.2 About the construction of FLD curves

In order to construct the FLD curves, many researchers have carried out experimental and theoretical analyses to achieve this. During this process, it is found that the maximum admissible limiting strains strongly depend on many physical factors, including the materials work-hardening, strain rate sensitivity, loading history, and the initial plastic anisotropy induced by the rolling process.

For experimental determination of the FLD, the Nakazima tests and Marciniak tests are the common used methods. Both two tests can be conducted on Erichsen sheet metal testing machine. Fig. 1-6 illustrates the schematic of these two tests setups. The Nakazima test is probably the most widely used since the Marciniak method is more complex to perform. The specimens for two tests are prepared with electro-etched using grid of circles or squares with a size of 2 mm on the surface (Fig. 1-7). with the help of digital system, we can accurately record the coordinates of each point on the captured pictures, and obtain the displacement and strain fields.

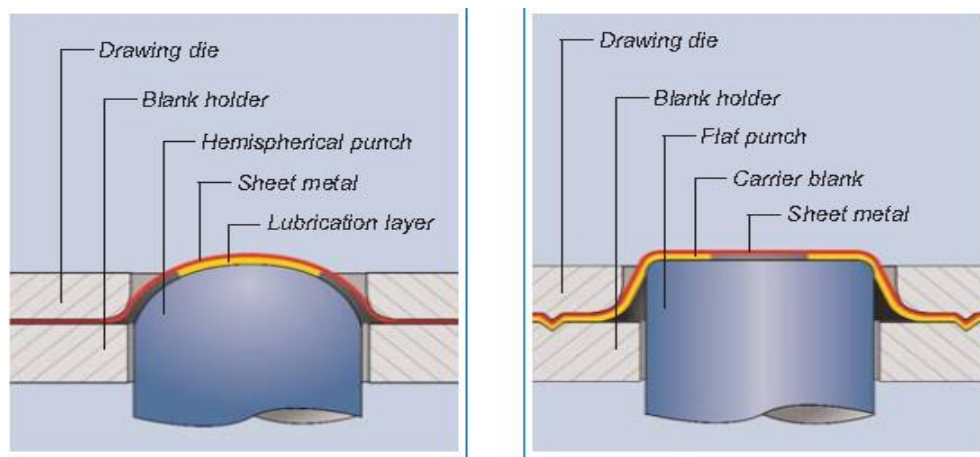
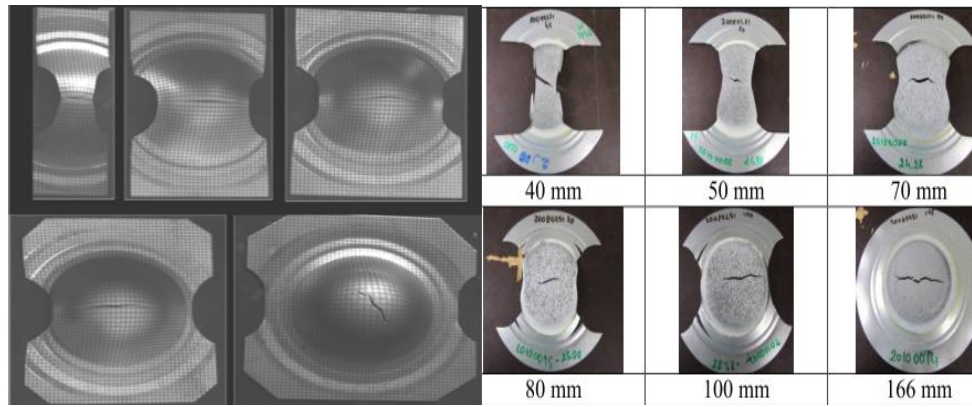


Fig. 1- 6. Experimental setups for the determination of FLD curves



(a) Nakazima [Uthaisangsuk08]

(b) Marciniak [Abspoel12]

Fig. 1- 7. Examples of test samples.

Parallel to the experimental approaches, many theoretical approaches can be used to get the FLDs, some more common known, such as: Bifurcation model, Marciniak–Kuczynski model (M-K). The first Bifurcation model was limited for left-hand side building of the forming limit curve, and there is no plane strain direction for materials with smooth yield loci and normal plastic flow. By adopting the deformation theory of plasticity into the approach and allowing for vertex-formation on the yield locus, the extension to the right-hand side of the FLD was made by [Stören75]. More recently, this bifurcation model has nevertheless been successfully used with the flow theory of plasticity, more commonly accepted in sheet metal forming. Flow theories in which non-normal plastic flow is allowed, are used in [Hashiguchi04] and [Ito08], while [Haddag07] added the damage model of Chaboche into plastic flow theory.

M-K model obtains its name from the highly cited paper [Marciniak67]. Here, the existence of an initial groove (initial perturbation) with diminished thickness, of infinite length and oriented along the minor strain direction, was assumed in order to predict the forming limit of monotonic strain paths in the right-hand side of the FLD. Sheet inhomogeneity is thus characterized by the initial thickness ratio of groove over surrounding matrix known as the imperfection parameter. The onset of localized necking instability is calculated by imposing geometric compatibility and force equilibrium between the groove in the model and the surrounding material. In this study, attention is paid to the Nakazima tests and M-K approach, to investigate FLDs of objective sheet metals. The Nakazima test will be introduced in Part III. In the coming chapter, we will briefly give the description of M-K approach.

### I.3.3 FLD curves from the M-K approach

#### I.3.3.1 A brief description of the M-K approach

Marciniak-Kuczynski model (M-K) is based on the growth of an initial defect as inhomogeneities in the form of a narrow band and oriented with an angle ( $\varphi^0$ ) with respect to the principal axis. Rigid plasticity, plane stress condition and isotropic work hardening of the material are assumed. Detailed description of the theoretical M-K analysis schematically is illustrated in Fig. 1-8, that can be found in many publications [Marciniak67, Barata89]. The geometry defect in the zone b is characterized by thickness ratio

$$f^0 = e_b^0 / e_a^0 \quad (1-90)$$

where  $e_b^0$  and  $e_a^0$  represents the initial thickness in zone b and zone a separately. The x, y, z axes correspond to the rolling, transverse and normal directions of the sheet, whereas 1, 2, and 3 are the principal stress and strain directions in the homogeneous region. In the imperfect groove zone,  $\vec{n}$  and  $\vec{t}$  represent the normal and longitudinal direction of the groove.

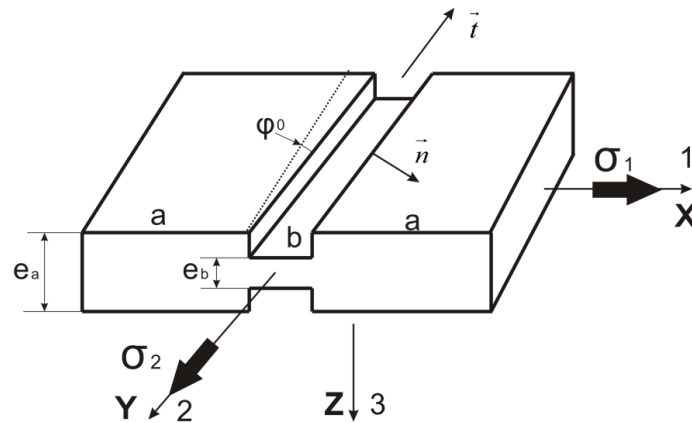


Fig. 1- 8. Initial conditions for the M-K approach.

This two-zone material is subjected to plastic deformation through applying a constant incremental stretching of the homogeneous part, but the plastic evolutions in these two zones are not the same. The flow localization occurs in the groove at a critical strain in the homogeneous region, at that time, the values of major and minor strains of homogeneous region can be reported for plotting of Forming limit diagrams, also values of major and minor stress of the same region can be reported for Forming limit stress diagrams, which is assumed to be independent on the pre-strain deformation.

In zone a, imposing the equivalent strain increment  $d\bar{\epsilon}^a$ , the hardening rule allows the

determination of equivalent flow stress  $\bar{\sigma}^a = f_{HR}(\bar{\varepsilon}^a)$ . The stress matrix  $[\sigma^a]_{xyz}$  is calculated using the yield function  $\bar{\sigma}_{YF} = f_{YF}(\sigma_{xx}, \sigma_{yy}, \sigma_{xy})$  coupled with the stress ratio  $\alpha = \sigma_2 / \sigma_1$ . The flow rule  $d\varepsilon_{ij} = d\bar{\varepsilon}(\partial\bar{\sigma}_{YF} / \partial\sigma_{ij})$  which describes the relationship among the strain increments permit the determination of  $[d\varepsilon^a]_{xyz}$ . The stress and strain states in the groove reference frame are also known by the axes change.

$$[\sigma]_{mz}^a = [T]^T \cdot [\sigma]_{xyz}^a \cdot [T] \quad [d\varepsilon]_{mz}^a = [T]^T \cdot [d\varepsilon]_{xyz}^a \cdot [T] \quad (1-91)$$

$$[T] = \begin{bmatrix} \cos \varphi & -\sin \varphi & 0 \\ \sin \varphi & \cos \varphi & 0 \\ 0 & 0 & 1 \end{bmatrix} \quad (1-92)$$

The defect band rotation during loading is described by:

$$\tan(\varphi) = \tan\varphi^0 (1 + d\varepsilon_x^a) / (1 + d\varepsilon_y^a) \quad (1-93)$$

In order to compute the equivalent increment strain  $d\bar{\varepsilon}_b$  and the stress value in the longitudinal direction of groove  $\sigma_{tt}^b$ , the force equilibrium condition and compatibility equations between two regions are proposed. The equilibrium condition which indicates the force balance leads the following equations:

$$\sigma_{mt}^a e_a = \sigma_{mb}^b e_b \quad \text{and} \quad \sigma_{mt}^a e_a = \sigma_{mt}^b e_b \quad (1-94)$$

The compatibility condition assumes that the elongation in the direction of the necking band is identical in two regions:

$$d\varepsilon_{tt}^a = d\varepsilon_{tt}^b \quad (1-95)$$

The equilibrium equations can be reduced to:

$$\begin{cases} f \sigma_{mt}^b = \sigma_{mt}^a \\ f \sigma_{mb}^b = \sigma_{mt}^a \end{cases} \quad (1-96)$$

where  $f = e_b / e_a$  is the non-homogeneity factor and can be described as:

$$f = f^0 \cdot \exp(\varepsilon_{zz}^b - \varepsilon_{zz}^a) \quad (1-97)$$

With the condition above, the flow stress value in the normal direction of the groove and the flow shear stress in the groove can be calculated. And then transposed to the stress matrix in

the principal referential frame  $[\sigma]_{xyz}$ , which through the yield function allows the evaluation of the equivalent flow stress  $\bar{\sigma}_{YF}^b$ . Through the hardening rule  $\bar{\sigma}^b = f_{HR}(\bar{\varepsilon}^b)$  and flow rule,  $[d\bar{\varepsilon}^b]_{xyz}$  can be determined.

Through the following two nonlinear equations with two invariable  $d\bar{\varepsilon}_b$  and  $\sigma_{II}^b$  can be written:

$$\begin{cases} F_1(d\bar{\varepsilon}_b, \sigma_{II}^b) = \bar{\sigma}^b - \bar{\sigma}_{YF}^b = 0 \\ F_2(d\bar{\varepsilon}_b, \sigma_{II}^b) = d\varepsilon_{II}^a - d\varepsilon_{II}^b = 0 \end{cases} \quad (1-98)$$

### I.3.3.2 Yield function and hardening law

The material is completely defined macroscopically by its yield function and its hardening law. In this study, the chosen yield criterion and hardening law are quadratic Hill'48 law [Hill48]:

$$\bar{\sigma} = \sigma_x^2 - 2H\sigma_x\sigma_y + (F+H)\sigma_y^2 + 2N\sigma_{xy}^2 \quad (1-99)$$

where  $F, H, N$  can be calculated using the anisotropy coefficients, and swift hardening law:

$$\bar{\sigma} = K(\bar{\varepsilon}_0 + \bar{\varepsilon})^n \quad (1-100)$$

Where  $\bar{\sigma}$  and  $\bar{\varepsilon}$  are the equivalent stress and strain, respectively,  $K, n, \bar{\varepsilon}_0$  are the material constants.

### I.3.3.3 Local necking definition

With the Newton-Raphson method the  $d\bar{\varepsilon}_b$  and  $\sigma_{II}^b$  can be determined, M-K necking criterion assumed that the plastic flow localization happened when the equivalent strain increment in defect band  $d\bar{\varepsilon}_b$  is 10 times larger than  $d\bar{\varepsilon}_a$  in the homogeneous zone. And at that time the corresponding strains ( $\varepsilon_{xx}^a, \varepsilon_{yy}^a$ ) accumulated at that moment in the homogeneous zone are the limit strains. The analysis is repeated for different values of  $\varphi^0$  (between  $0^\circ$  and  $90^\circ$ ) and the limit point on the FLD is obtained after minimization of the curve  $\varepsilon_{xx}^a$  versus  $\varphi^0$ .

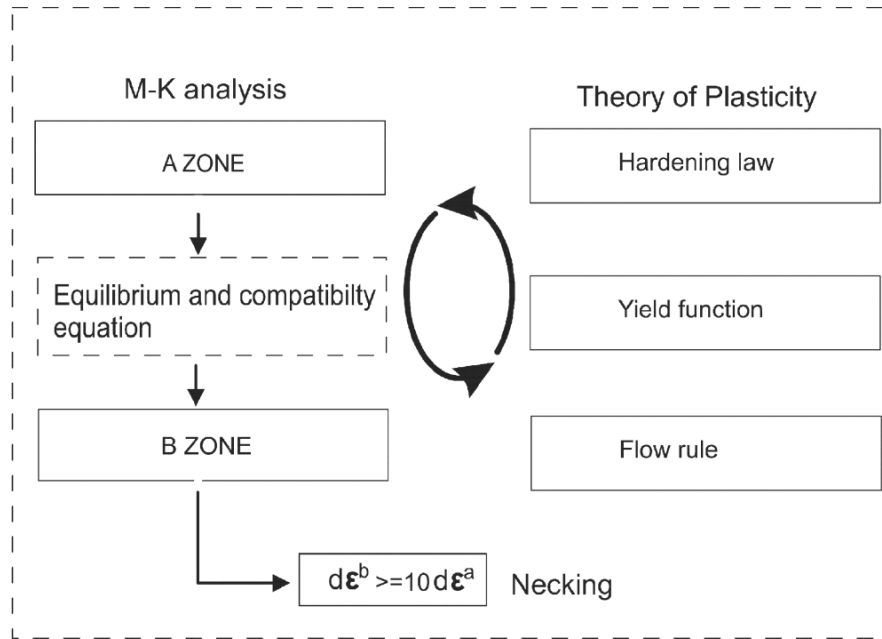


Fig. 1- 9 Structure of M-K code

## I.4 Conclusions

This chapter was dedicated to the modeling aspects. In the first section, the theoretical background of continuum mechanics and thermodynamics of irreversible processes with state variables are reviewed. Also the framework of continuum damage mechanism is shortly summarized. In the second section, fully coupled constitutive equations have been formulated in the framework of non-associative plasticity under large plastic strains. A new contribution has been introduced concerning the distortion of the yield surface based on the original work of François.

Finally, a short discussion of the forming limit curves is presented. The FLD based on the M-K approach is described in some detailed to be used later for the comparison with the fully coupled approach. The numerical aspect of both fully coupled approach and the M-K approach will be discussed in the next chapter.

# Chapter II

## Numerical Aspects

### Content

---

II.1 Introduction .....	40
II.2 Numerical implementation of the proposed model .....	40
II.2.1 Time and space discretizations of the IBVP .....	40
II.2.1.1 Strong and weak forms of the IBVP .....	40
II.2.1.2 Space discretizations of the IBVP .....	42
II.2.1.3 Time discretization of the IBVP .....	43
II.2.1.4 Global resolution scheme .....	44
II.2.2 Local integration scheme: state variables computation .....	46
II.2.3 Numerical treatment of contact with friction .....	56
II.3 Numerical Aspect of M-K approach .....	56
II.4 Conclusions .....	57

## II.1 Introduction

This chapter is dedicated to the numerical aspects related to:

- The initial and boundary value problems (IBVP) arising from equilibrium problem of an elastoplastic solid described by the fully coupled constitutive equations introduced in Section I.2.
- The M-K instability problem to compute the FLD for thin sheets, introduced in Section I.3.

## II.2 Numerical implementation of the proposed model

The highly nonlinear IBVP is defined in the space-time domain  $\Omega \times [t_0, t_f]$ , where  $\Omega$  is the space domain and  $[t_0, t_f]$  is the time domain with  $t_0$  is the initial time and  $t_f$  is the final time. The space domain will be discretized using the displacement based Galerkin finite element method; while the time domain will be discretized using central finite difference method. For all these aspects the reader is referred to the general books dedicated to the Finite Element Method for non-linear problems [Bathe81, Hughes87, Zienkiewicz84, Zienkiewicz89, Bonnet97, Belytschko01, Crisfield91, Simo98 among many others].

### II.2.1 Time and space discretization of the IBVP

#### II.2.1.1 Strong and weak forms of the IBVP

Let us consider a deformable and damageable solid occupying at any time  $t \in [t_0, t_f]$ , a space  $\Omega_t$  with boundary  $\Gamma_t$  schematized in Fig. 2-1.

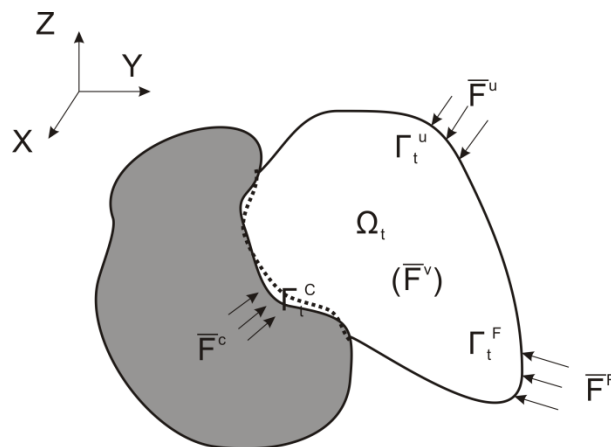




Fig. 2- 1. Deformable solid with boundary condition at time  $t \in [t_0, t_f]$ 

The following force fields are imposed:

- Force field  $\overline{\vec{F}}^F$  imposed on  $\Gamma_t^F$ ;
- Contact force  $\overline{\vec{F}}^C$  imposed in  $\Gamma_t^C$ ;
- Body force  $\overline{\vec{f}}^V$  on  $\Omega_t$ .

For this isothermal IBVP, the strong form is defined by the classical equilibrium equations together with mixed Dirichlet and Neumann Boundary conditions:

$$\begin{cases} \overline{\text{div}}(\overline{\underline{\sigma}}(\vec{x}, t)) + \overline{\vec{f}}^V(\vec{x}, t) = \rho_t \overline{\vec{u}}(\vec{x}, t) & \text{in } \Omega & (2-1) \\ \overline{\vec{u}}(\vec{x}, t) = \overline{\vec{u}}_t & \text{on } \Gamma_t^u & (2-2) \\ \overline{\underline{\sigma}}(\vec{x}, t) \cdot \overline{\vec{n}}_t = \overline{\vec{F}}^F & \text{on } \Gamma_t^F & (2-3) \end{cases}$$

The three subsurfaces  $\Gamma_t^u$ ,  $\Gamma_t^F$ , and  $\Gamma_t^C$  forming the boundary  $\Gamma_t$ , fulfill at each time  $t$  the following classical relationships:

$$\begin{cases} \Gamma_t^u \cup \Gamma_t^F \cup \Gamma_t^C = \Gamma_t \\ \Gamma_t^F \cap \Gamma_t^u = \Gamma_t^F \cap \Gamma_t^C = \Gamma_t^u \cap \Gamma_t^C = \emptyset \end{cases} \quad (2-4)$$

In Equation 2-1,  $\underline{\sigma}$  is the Cauchy stress tensor defined by the fully coupled constitutive equations,  $\overline{\vec{f}}^V$  is the body forces vector,  $\rho_t$  is the solid density and  $\overline{\vec{u}}$  is the acceleration vector. Appropriate initial conditions should be added. Note that for the sake of simplicity, the contact forces field is included in Equation 2-3.

The weak form of the IBVP is deduced from the strong form defined above by Eq. 2-1 to Eq. 2-3, thanks to the well-known weighted residual method together with Galerkin assumption. If the updated Lagrangian formulation is used, the weighted residual method applied to Equation 2-1 and after the integration by part and the use of the Neumann Boundary condition (Equation 2-3), the following weak form is obtained:

$$J(\dot{\vec{u}}, \dot{\vec{u}}) = \int_{\Omega} \underline{\sigma} : \underline{D} dV - \int_{\Omega} \rho_t \overline{\vec{u}} \cdot \overline{\dot{\vec{u}}} dV + \int_{\Omega} \overline{\vec{f}}^V \cdot \overline{\dot{\vec{u}}} dV - \int_{\Gamma^F} \left( \overline{\vec{F}}^F + \overline{\vec{F}}^C \right) \cdot \overline{\dot{\vec{u}}} ds = 0 \quad \forall \overline{\dot{\vec{u}}} \text{ K.A.} \quad (2-5)$$

where  $\overline{\dot{\vec{u}}}$  is the kinematically admissible (K.A.) virtual velocity field and  $\underline{D}$  is the associated virtual total strain rate tensor.

To Equation 2-5, the Dirichlet boundary conditions (Eq. 2-2) should be added after the

discretization of Equation 2-5 by the FEM.

### II.2.1.2 Space discretization of the IBVP

The total volume  $\Omega_t$  of the solid is discretized with  $N^e$  finite elements, each has an elementary volume  $\Omega^e$  so that:

$$\Omega_t = \bigcup_{e=1}^{N^e} \Omega^e \quad (2-6)$$

To each finite element  $\Omega^e$  with  $N^{nd}$  nodes defined in the working space  $(x_1, x_2, x_3)$  is associated a reference element  $\Omega_r$  defined in the reference space  $(\zeta_1, \zeta_2, \zeta_3)$ , so that:

$$\{x(\vec{\zeta})\} = [\bar{N}_i^e(\vec{\zeta})] \{x_i^e\} \quad (2-7)$$

where  $\{x(\vec{\zeta})\}$  is the coordinates vector of any material point of  $\Omega_r$ ,  $[\bar{N}_i^e(\vec{\zeta})]$  are the shape polynomial functions and  $\{x_i^e\}$  are the coordinates of the  $N^{nd}$  nodes of the element.

Now, following the Galerkin displacement based FEM, the displacement vector and the virtual displacement vector inside each reference FE ( $\Omega_r$ ) are approximated by:

$$\{u^e(\vec{\zeta}, t)\} = [N_i^e(\vec{\zeta})] \{u_i^e(t)\} \quad \text{and} \quad \{\hat{u}^e(\vec{\zeta}, t)\} = [N_i^e(\vec{\zeta})] \{\hat{u}_i^e(t)\} \quad (2-8)$$

where  $[N_i^e(\vec{\zeta})]$  are the interpolation functions of the displacement fields and  $\{u_i^e(t)\}$  (resp.  $\{\hat{u}_i^e(t)\}$ ) is the nodal displacement (resp. virtual displacement) vector.

The time derivatives of Equation 2-8 give the velocity fields:

$$\{\dot{u}^e(\vec{\zeta}, t)\} = [N_i^e(\vec{\zeta})] \{\dot{u}_i^e(t)\} \quad \text{and} \quad \{\dot{\hat{u}}^e(\vec{\zeta}, t)\} = [N_i^e(\vec{\zeta})] \{\dot{\hat{u}}_i^e(t)\} \quad (2-9)$$

Finally, the acceleration field is obtained from the time derivatives of (Equation 2-9a):

$$\{\ddot{u}^e(\vec{\zeta}, t)\} = [N_i^e(\vec{\zeta})] \{\ddot{u}_i^e(t)\} \quad (2-10)$$

where  $\{\ddot{u}_i^e\}$  is the accelerations vector of the element nodes.

By using the equations above, the weak form (2-5) written for a single isoparametric reference element can be easily expressed with the following matrix form:

$$J^e(\dot{u}^e, \dot{\hat{u}}^e) = \langle \dot{\hat{u}}^e \rangle ([M^e] \{\ddot{u}^e\} + \{F_{int}^e\} - \{F_{ext}^e\}) \quad (2-11)$$

where  $[M^e]$  is the consistent mass matrix given by:

$$[M^e] = \int_{\Omega_r} \rho [N_r^e]^T [N_r^e] J_r dV_r \quad (2-12)$$

the internal element force vector is given by:

$$\{F_{int}^e\} = \int_{V^e} [B^e]^T \{\sigma^e\} J_v dV_r \quad (2-13)$$

and the external forces vector is given by:

$$\{F_{ext}^e\} = \int_{V^e} [N^e]^T \{F_t^V\} J_v dV_r^e + \int_{\Gamma^e} [N^e]^T \{F_t^F\} J_s dA_r^e + \int_{\Gamma^c} [N^e]^T \{F_t^C\} J_s dA_r^e \quad (2-14)$$

$[B^e]$  is the deformation-displacement interpolation matrix, defined by:

$$[B^e] = \left[ \frac{\partial N^e}{\partial x^e} \right] = \left[ \frac{\partial N^e}{\partial \xi} \right] \left[ \frac{\partial \xi}{\partial x^e} \right] \quad (2-15)$$

If  $\Lambda$  indicates the finite element assembly operator, the discretized weak form (2-5) can be written as:

$$J = \sum_{e=1}^{N^e} J^e = \langle \dot{u} \rangle \left( \sum_{e=1}^{N^e} [M^e] \{ \ddot{u}^e \} + \sum_{e=1}^{N^e} \{ F_{int}^e \} - \sum_{e=1}^{N^e} \{ F_{ext}^e \} \right) = 0 \quad \forall \dot{u} \text{ K.A.} \quad (2-16)$$

Leading to:

$$R(u) = [M^L] \{ \ddot{u} \} + \{ F_{int} \} - \{ F_{ext} \} = 0 \quad (2-17)$$

where  $\{ \ddot{u} \}$  is the global (for all nodes of all elements) accelerations vector, and

$$[M^L] = \sum_{e=1}^{N^e} [M_L^e] \text{ is the global lumped mass matrix, } \{ F_{int} \} = \sum_{e=1}^{N^e} \{ F_{int}^e \} \text{ and } \{ F_{ext} \} = \sum_{e=1}^{N^e} \{ F_{ext}^e \}$$

are the global internal and external force vectors. These global operators are obtained by the assembly of the corresponding elementary operators defined by Equation (2-12), (2-13), (2-14).

Note that the lumped mass matrix is obtained from the consistent mass matrix (2-12), following the well-known mass concentration procedure which can be found in [Hughes87] among others.

### II.2.1.3 Time discretization of the IBVP

The total time interval is thus discretized into  $N^t$  subintervals with empty intersections, so

that the approximation  $[t_0, t_f] \approx \bigcup_{n=0}^{N^t} [t_n, t_{n+1} = t_n + \Delta t]$  is valid with sufficient precision. For each

time increment, the non-linear problem is solved to determine all the unknowns of the IBVP. In fact, the unknowns are supposed to be known at  $t_n$ , and their values are computed at the end of the time increment under concern ( $t_{n+1}$ ), with the load increment prescribed over that time increment.

#### II.2.1.4 Global resolution scheme

The algebraic system (Equation 2-17) constitutes a highly nonlinear algebraic system that should be solved numerically for each typical time increment of size  $\Delta t = t_{n+1} - t_n$ . Two widely used resolution schemes can be applied to solve the nonlinear algebraic system (2-17) over each time increment. The first one called the static implicit (SI) scheme, is applied when the inertia term (mass matrix) is neglected in (2-17) leading to (at  $t_{n+1}$ )

$$\mathbb{R}_{n+1} = \{F_{\text{int}}\}_{n+1} - \{F_{\text{ext}}\}_{n+1} = 0 \quad (2-18)$$

This system is generally solved thanks to a linearization process of Newton-Raphson type. In that case a consistent tangent stiffness matrix should be calculated [Saanouni12].

This second scheme, explicit in nature, is called the dynamic explicit (DE) scheme based on writing the system (2-17) at  $t_n$ :

$$[M^L] \{\ddot{u}\}_n + \mathbb{R}_{n+1} = 0 \quad (2-19)$$

It has been shown in [Saanouni03, Saanouni12] that for metal forming simulation the (DE) scheme is preferred if we want to perform any sheet or bulk metal forming process simulation. This is particularly true when damage-induced softening is accounted for and when the number of nodes concerned by the contact is very large.

In this work only the (DE) resolution scheme is used in the framework of ABAQUS/Explicit finite element code in which the numerical integration of our fully coupled constitutive equations have been precisely implemented. The main steps of this resolution scheme are:

1. Define the mass matrix  $[M^L]_n$  at time  $t_n$ .
2. Solve the equation 2-9, to calculate the displacement increment at the end of the step  $t_{n+1}$  by using the following explicit scheme:

$$\{\ddot{u}\}_n = [M^L]_n^{-1} (\{F_{\text{ext}}\}_n - \{F_{\text{int}}\}_n) \quad (2-20)$$

$$\{\dot{u}\}_{n+1/2} = \{\dot{u}\}_{n-1/2} + \frac{(\Delta t_{n-1} + \Delta t_n)}{2} \{\ddot{u}\}_n + \dots \quad (2-21)$$

$$\{u\}_{n+1} = \{u\}_n + \Delta t_{n+1} \{\dot{u}\}_{n+1/2} + \dots \quad (2-22)$$

3. Integrate all the constitutive equations for the state variables including  $(\underline{\sigma}_{n+1}, \underline{\varepsilon}_{n+1}^p)$  and hardening variables  $(\underline{\alpha}_{n+1}, \underline{X}_{n+1})$ ,  $(r_{n+1}, R_{n+1})$   $(d_{n+1}, Y_{n+1})$  at time  $t_{n+1}$ .
4. Calculate  $[M^L]$ ,  $\{F_{int}\}$ ,  $\{F_{ext}\}$  at  $t_{n+1}$ .
5. Predict the next time step  $\Delta t$ .
6. Update the time  $t_{n+1} = t_n + \Delta t$ . If  $t_{n+1} < t_f$  go back to step 1, if not, the simulation is terminated.

This explicit scheme does not require iterative or tangent stiffness matrix, but it is conditionally stable, as mentioned above. Consequently, the control of time step  $\Delta t$  is essential to ensure the stability and accuracy of the solution [Hughes87]. It has been shown that the stability limits are inversely proportional to the largest eigenvalue of the global system [Abaqus01]

$$\Delta t \leq \frac{2}{w_{\max}} (\sqrt{1 + g^2} - g) \quad (2-23)$$

where  $w_{\max}$  is the highest eigenvalue of the system, and  $g$  denotes the fraction of the critical damping in the highest frequency mode. In practice it is not necessary to solve the eigenvalue problem of the complete system. Indeed, an estimate of the largest eigenvalue of the system can be obtained by determining the highest value of volume expansion of all mesh elements, as the smallest transit time of a dilatational wave across any of the elements in the mesh. Accordingly the stable time increment is calculated using the expression:

$$\Delta t \leq \min\left(\frac{L^e}{C_d}\right) \quad (2-24)$$

where  $L^e$  is the smallest element dimension in the mesh (calculated as the smallest distance between adjacent nodes of element  $e$ ). and  $C_d$  is the dilatational wave speed travelling in the material, determined by:

$$C_d = \sqrt{\frac{\lambda_e + 2\mu_e}{\rho}} \quad (2-25)$$

or from Equation 2-24

$$\Delta t \leq \min\left(L^e \sqrt{\frac{\rho}{\lambda_e + 2\mu_e}}\right) \quad (2-26)$$

where  $\rho$  is the material density,  $\lambda_e$  and  $\mu_e$  are the Lamé's constants introduced in Chapter I. For IBVPs with time-independent behavior (non-viscous effect), it is benefit to increase artificially the material density in order to increase the time step (see Eq. 2-26) and hence save the CPU time. This procedure, called “mass scaling” in ABAQUS/Explicit (see ABAQUS theory manual [Abaqus01]), requires to check that higher value of the density does not give any induced viscous effect.

## II.2.2 Local integration scheme: state variables computation

Whatever the global resolution scheme used, we need to calculate the elementary operators as the matrices or vectors characterizing the IBVP, which are defined by the volume or surface integrals for each reference element, (see Equation 2-12, 2-13, 2-14).

To compute the internal forces vector defined by Equation 2-13 for any reference finite element, the Cauchy stress tensor is required at each  $t_{n+1}$ , the end of a typical time increment  $[t_n, t_{n+1} = t_n + \Delta t]$ . This requires the numerical integration of the complete set of the fully coupled constitutive equations defined in Chapter I by equations (1-67, 1-68, 1-69, 1-70, 1-73, 1-74).

Suppose that all the state variables are known at  $t_n$  and we have to compute their values  $((\underline{\sigma}_{n+1}, \underline{\varepsilon}_{n+1}^p), (\underline{X}_{n+1}, \underline{\alpha}_{n+1}), (R_{n+1}, r_{n+1}), (Y_{n+1}, d_{n+1}))$  at  $t_{n+1}$  resulting from an applied loading path in terms of an increment of total strain  $\Delta \underline{\varepsilon}$ , so that  $\underline{\varepsilon}_{n+1} = \underline{\varepsilon}_n + \Delta \underline{\varepsilon}$  is completely known.

Since we have assumed the small elastic strain, the total strain rate is additive:  $\underline{D} = \dot{\underline{\varepsilon}}^e + \underline{D}^p$ . In the incremental form, this is written  $\Delta \underline{\varepsilon} = \Delta \underline{\varepsilon}^e + \Delta \underline{\varepsilon}^p$  in which  $\underline{\varepsilon} = \int_t \underline{D} dt$  and  $\underline{\varepsilon}^p = \int_t \underline{D}^p dt$ . Besides, the numerical integration is performed in the locally rotated deformed configuration as discussed in Chapter I.1.2. However, the upper bar defining the rotated tensors are not used in order to simplify the rotations.

$$\begin{aligned}
 f &= \frac{\|\underline{S}_d^c - \underline{X}\|_H}{\sqrt{1-d}} - \frac{R}{\sqrt{1-d^\gamma}} - \sigma_y & (a) \\
 \underline{S}_d^c &= \underline{S} + \frac{\underline{S}_0 : \underline{S}_0}{2\tilde{X}_{11}^c(R/\sqrt{1-d^\gamma} + \sigma_y)} \underline{X} - \frac{\underline{X} : \underline{X}}{2\tilde{X}_{12}^c(R/\sqrt{1-d^\gamma} + \sigma_y)} \underline{S}_0 & (b) \\
 \underline{S}_d^p &= \underline{S} + \frac{\underline{S}_0 : \underline{S}_0}{2\tilde{X}_{11}^p(R/\sqrt{1-d^\gamma} + \sigma_y)} \underline{X} \quad \text{with} \quad \underline{S}_0 = \underline{S} - \frac{\underline{S} : \underline{X}}{\underline{X} : \underline{X}} \underline{X} & (c) \\
 \|\underline{S}_d^k - \underline{X}\|_H &= \sqrt{(\underline{S}_d^k - \underline{X}) : \underline{H} : (\underline{S}_d^k - \underline{X})} \quad k \in \{c, p\} & (d) \\
 \underline{S} &= \underline{\sigma} = \underline{\sigma}^{dev} - \frac{1}{3} tr(\underline{\sigma}) \underline{1} & (e) \\
 \underline{\sigma} &= 2\mu_e \left[ (1-d) \langle \underline{e}^e \rangle_+ + (1-hd) \langle \underline{e}^e \rangle_- \right] & (f) \\
 &+ \lambda_e \left[ (1-d) \langle tr(\underline{\varepsilon}^e) \rangle - (1-hd) \langle -tr(\underline{\varepsilon}^e) \rangle \right] \underline{1} & (g) \\
 \underline{X} &= \frac{2}{3} (1-d) C \underline{\alpha} & (h) \\
 R &= (1-d^\gamma) Q r & (i) \\
 Y &= 2\mu_e \left[ \langle \underline{e}^e \rangle_+ : \langle \underline{e}^e \rangle_+ + h \langle \underline{e}^e \rangle_- : \langle \underline{e}^e \rangle_- \right] & (j) \\
 &+ \lambda_e \left[ \langle tr(\underline{\varepsilon}^e) \rangle^2 + h \langle -tr(\underline{\varepsilon}^e) \rangle^2 \right] + \frac{1}{3} C \underline{\alpha} : \underline{\alpha} + \frac{1}{2} \gamma d^{\gamma-1} Q r^2 & (k) \\
 \underline{D}^p &= \dot{\lambda} \underline{n}^p \quad \text{with} \quad \underline{n}^p = \frac{\underline{n}^d}{\sqrt{1-d}} : \left[ \underline{1}^{dev} + \frac{\underline{X} \otimes \underline{S}_0}{\tilde{X}_{11}^p(R/\sqrt{1-d^\gamma} + \sigma_y)} \right] & (l) \quad (2-27) \\
 \underline{\dot{\alpha}} &= \dot{\lambda} \left( \frac{\underline{n}^x}{\sqrt{1-d}} - a \underline{\alpha} \right) \quad \text{with} \quad \underline{n}^x = \underline{n}^d - \frac{\left[ \frac{(\underline{S}_0 : \underline{S}_0) \underline{n}^d}{2} - \frac{(\underline{S} : \underline{X})(\underline{X} : \underline{n}^d)}{(\underline{X} : \underline{X})} \underline{S}_0 \right]}{\tilde{X}_{11}^p(R/\sqrt{1-d^\gamma} + \sigma_y)} & (m) \\
 r_{n+1} &= \dot{\lambda} \left( \frac{n^i}{\sqrt{1-d^\gamma}} - b r \right) \quad \text{with} \quad n^i = \frac{(\underline{S}_0 : \underline{S}_0)(\underline{n}^d : \underline{X})}{2\sqrt{1-d} \tilde{X}_{11}^p(R/\sqrt{1-d^\gamma} + \sigma_y)^2} + 1 & (n) \\
 \underline{n}^d &= \frac{\underline{H} : (\underline{S}_d^p - \underline{X})}{\|\underline{S}_d^p - \underline{X}\|_H} & (o) \\
 \dot{d} &= \frac{\dot{\lambda}}{(1-d)^\beta} \left( \frac{\langle Y - Y_0 \rangle}{S(\bar{\theta})} \right)^s & (p) \\
 S(\bar{\theta}) &= \begin{cases} S_0 \left[ c_1 + \frac{\sqrt{3}}{2-\sqrt{3}} c_2 \sec \left( (\bar{\theta} \frac{\pi}{6}) - 1 \right) \right]^{-1/s} & \text{Wierzbicki type} \\ S_0 \left[ c_1 + c_2 \bar{\theta}^2 \right]^{-1/s} & \text{Cao type} \end{cases}, \quad \bar{\theta} = 1 - 6 \frac{\theta}{\pi} & (q) \\
 \theta &= \frac{1}{3} \cos^{-1} \left( \frac{27}{2} \frac{J_3}{\sigma_{eq}^3} \right) \quad \text{where} \quad \sigma_{eq} = \|\underline{\sigma}\|_M = \sqrt{\frac{3}{2} \underline{S} : \underline{S}} \quad \text{and} \quad J_3 = \det(\underline{S}) & (r)
 \end{aligned}$$

Before going away, let us recall the fully coupled constitutive equations (see chapter I) to be numerically integrated by presenting them in the box above (Equations 2.27).

By using the fully explicit forward Euler scheme together with asymptotic scheme applied

only to the hardening equations, the discretized equations can be given by:

$$\begin{aligned}
 f_{n+1} &= \frac{\|\underline{S}_{d(n+1)}^c - \underline{X}_{n+1}\|_H}{\sqrt{1-d_{n+1}}} - \frac{R_{n+1}}{\sqrt{1-d_{n+1}^y}} - \sigma_y = 0 & (a) \\
 \|\underline{S}_{d(n+1)}^k - \underline{X}_{n+1}\|_H &= \sqrt{(\underline{S}_{d(n+1)}^k - \underline{X}_{n+1}) : \underline{H} : (\underline{S}_{d(n+1)}^k - \underline{X}_{n+1})} \quad k \in \{c, p\} & (b) \\
 \underline{S}_{d(n+1)}^c &= \underline{S}_{n+1} + \frac{\underline{S}_{0(n+1)} : \underline{S}_{0(n+1)}}{2(1-d_{n+1})X_{I1}^c(R_{n+1}/\sqrt{1-d_{n+1}^y} + \sigma_y)} \underline{X}_{n+1} \\
 &\quad - \frac{\underline{X}_{n+1} : \underline{X}_{n+1}}{2(1-d_{n+1})X_{I2}(R_{n+1}/\sqrt{1-d_{n+1}^y} + \sigma_y)} \underline{S}_{0(n+1)} & (c) \\
 \underline{S}_{d(n+1)}^p &= \underline{S}_{n+1} + \frac{\underline{S}_{0(n+1)} : \underline{S}_{0(n+1)}}{2(1-d_{n+1})X_{I1}^p(R_{n+1}/\sqrt{1-d_{n+1}^y} + \sigma_y)} \underline{X}_{n+1}, \quad \underline{S}_{0(n+1)} = \underline{S}_{n+1} - \frac{\underline{S}_{n+1} : \underline{X}_{n+1}}{\underline{X}_{n+1} : \underline{X}_{n+1}} \underline{X}_{n+1} & (d) \\
 \underline{S}_{n+1} &= \underline{\sigma}_{n+1} - \frac{1}{3} tr(\underline{\sigma}_{n+1}) \underline{1} & (e) \\
 \underline{\sigma}_{n+1} &= 2\mu_e \left[ (1-d_{n+1}) \langle \underline{e}_{n+1}^e \rangle_+ + (1-hd_{n+1}) \langle \underline{e}_{n+1}^e \rangle_- \right] & (f) \\
 &\quad + \lambda_e \left[ (1-d_{n+1}) \langle tr(\underline{\varepsilon}_{n+1}^e) \rangle - (1-hd_{n+1}) \langle -tr(\underline{\varepsilon}_{n+1}^e) \rangle \right] \underline{1} & (g) \\
 \underline{X}_{n+1} &= \frac{2}{3} (1-d_{n+1}) C \underline{\alpha}_{n+1} & (h) \\
 R_{n+1} &= (1-d_{n+1}^y) Q r_{n+1} & (i) \\
 \underline{\varepsilon}_{n+1}^p - \underline{\varepsilon}_n^p - \Delta \lambda \underline{n}_{n+1}^p &= 0 & (j) \\
 g_\alpha &= \begin{cases} \alpha_{n+1} - \frac{1}{(1+a\Delta\lambda)} \left( \Delta\lambda \frac{n_{n+1}^x}{\sqrt{1-d_{n+1}}} + \alpha_n \right) = 0 & \text{Forward Euler} \\ \alpha_{n+1} - \alpha_n e^{-a_n \Delta\lambda} - \frac{n_{n+1}^x}{a \sqrt{1-d_{n+1}}} (1 - e^{-a \Delta\lambda}) = 0 & \text{Asymptotic} \end{cases} & (k) \\
 g_r &= \begin{cases} r_{n+1} - \frac{1}{(1+b\Delta\lambda)} \left( \Delta\lambda \frac{n_{n+1}^i}{\sqrt{1-d_{n+1}^y}} + r_n \right) = 0 & \text{Forward Euler} \\ r_{n+1} - r_n e^{-b\Delta\lambda} - \frac{n_{n+1}^i}{b \sqrt{1-d_{n+1}^y}} (1 - e^{-b \Delta\lambda}) = 0 & \text{Asymptotic} \end{cases} & (l) \\
 \underline{n}_{n+1}^p &= \frac{n_{n+1}^d}{\sqrt{1-d_{n+1}}} : \left[ \underline{1}^{dev} + \frac{\underline{X}_{n+1} \otimes \underline{S}_{0(n+1)}}{(1-d_{n+1})X_{I1}^p(R_{n+1}/\sqrt{1-d_{n+1}^y} + \sigma_y)} \right] & (m) \\
 \underline{n}_{n+1}^x &= \underline{n}_{n+1}^d - \frac{\left[ \frac{(\underline{S}_{0(n+1)} : \underline{S}_{0(n+1)}) \underline{n}_{n+1}^d}{2} - \frac{(\underline{S}_{n+1} : \underline{X}_{n+1})(\underline{X}_{n+1} : \underline{n}_{n+1}^d)}{(\underline{X}_{n+1} : \underline{X}_{n+1})} \underline{S}_0 \right]}{(1-d_{n+1})X_{I1}^p(R_{n+1}/\sqrt{1-d_{n+1}^y} + \sigma_y)} & (n) \\
 n_{n+1}^i &= \frac{(\underline{S}_{0(n+1)} : \underline{S}_{0(n+1)}) (\underline{n}_{n+1}^d : \underline{X}_{n+1})}{2(1-d_{n+1})^{3/2} X_{I1}^p(R_{n+1}/\sqrt{1-d_{n+1}^y} + \sigma_y)^2} + 1 & (o) \\
 \underline{n}_{n+1}^d &= \frac{\underline{H} : (\underline{S}_{d(n+1)}^p - \underline{X}_{n+1})}{\|\underline{S}_{d(n+1)}^p - \underline{X}_{n+1}\|_H} & (p) \\
 d_{n+1} - d_n - \frac{\Delta\lambda}{(1-d_{n+1})^\beta} \left( \frac{\langle Y_{n+1} - Y_0 \rangle}{S(\bar{\theta}_{n+1})} \right)^s &= 0 & (q) \\
 S(\bar{\theta}_{n+1}) &= \begin{cases} S_0 \left[ c_1 + \frac{\sqrt{3}}{2-\sqrt{3}} c_2 \sec \left( (\bar{\theta}_{n+1} \frac{\pi}{6}) - 1 \right) \right]^{-1/s} & \text{Wierzbicki type} \\ S_0 \left[ c_1 + c_2 \bar{\theta}_{n+1}^2 \right]^{-1/s} & \text{Cao type} \end{cases}, \quad \bar{\theta}_{n+1} = 1 - 6 \frac{\theta_{n+1}}{\pi} & (r) \\
 \theta_{n+1} &= \frac{1}{3} \cos^{-1} \left( \frac{27}{2} \frac{J_{3(n+1)}}{\|\underline{\sigma}_{n+1}\|_M^3} \right) \quad \text{where } \|\underline{\sigma}_{n+1}\|_M = \sqrt{\frac{3}{2} \underline{S}_{n+1} : \underline{S}_{n+1}} \quad \text{and } J_{3(n+1)} = \det(\underline{S}_{n+1}) & (s)
 \end{aligned}
 \tag{2-28}$$

To solve these equations, the classical elastic prediction, plastic correction scheme is applied.



Note that before performing the numerical integration, the rotation tensors  $\underline{Q}_{n+1}$  required to rotate the actual deformed configuration should be calculated. This is made by solving the differential equations summarized in (2-28) after choosing the rotated frame  $\underline{W}_Q$  according to the discussion in Chapter I.1.2 (see Badreddine10, Saanouni12 for more details).

**Elastic prediction:** We first assume the total strain increment  $\Delta \underline{\varepsilon}$  is completely elastic, without any dissipation, i.e.

$$\begin{cases} \Delta \underline{\varepsilon}^p = 0 \\ \Delta \underline{\alpha} = 0 \\ \Delta r = 0 \\ \Delta d = 0 \end{cases} \Rightarrow \begin{cases} \underline{\varepsilon}_{n+1}^p = \underline{\varepsilon}_n^p \\ \underline{\alpha}_{n+1} = \underline{\alpha}_n \\ r_{n+1} = r_n \\ d_{n+1} = d_n \end{cases} \quad (2-29)$$

So the called trial stress  $\underline{\sigma}_{n+1}^*$  can be obtained with  $\underline{\varepsilon}^* = \underline{\varepsilon}_n + \Delta \underline{\varepsilon} - \underline{\varepsilon}_n^p = \underline{\varepsilon}^e + \Delta \underline{\varepsilon}$  is the assumed elastic strain:

$$\underline{\sigma}_{n+1}^* = 2\mu_e \left[ (1-d_n) \langle \underline{\varepsilon}_{n+1}^* \rangle_+ + (1-hd_n) \langle \underline{\varepsilon}_{n+1}^* \rangle_- \right] + \lambda_e \left[ (1-d_n) \langle tr(\underline{\varepsilon}_{n+1}^*) \rangle - (1-hd_n) \langle -tr(\underline{\varepsilon}_{n+1}^*) \rangle \right] \underline{1} \quad (2-30)$$

$$\underline{s}_{n+1}^* = \underline{\sigma}_{n+1}^* - tr(\underline{\sigma}_{n+1}^*) \underline{1} \quad (2-31)$$

$$\underline{e}_{n+1}^{e*} = \underline{\varepsilon}_{n+1}^{e*} - \frac{1}{3} tr(\underline{\varepsilon}_{n+1}^{e*}) \underline{1} \quad (2-32)$$

$$\underline{s}_{0(n+1)}^* = \underline{s}_{(n+1)}^* - \underline{s}_{x(n+1)}^* \quad \text{and} \quad \underline{s}_{x(n+1)}^* = \frac{\underline{s}_{(n+1)}^* : \underline{X}_n}{\underline{X}_n : \underline{X}_n} \cdot \underline{X}_n \quad (2-33)$$

$$\underline{s}_{d(n+1)}^{c*} = \underline{s}_{n+1}^* + \frac{\underline{s}_{0(n+1)}^* : \underline{s}_{0(n+1)}^*}{2(1-d_n)X_{l1}^c(R_{n+1}/\sqrt{1-d_n^\gamma} + \sigma_y)} \underline{X}_n - \frac{\underline{X}_n : \underline{X}_n}{2(1-d_n)X_{l2}(R_n/\sqrt{1-d_n^\gamma} + \sigma_y)} \underline{s}_{0(n+1)}^* \quad (2-34)$$

Then, the yield function at this trial state is:

$$f_{n+1}^*(\underline{\sigma}_{n+1}^*, \underline{X}_n, R_n, d_n) = \frac{\|\underline{s}_{d(n+1)}^{c*} - \underline{X}_n\|_H}{\sqrt{1-d_n}} - \frac{R_n}{\sqrt{1-d_n^\gamma}} - \sigma_y \quad (2-35)$$

If  $f_{n+1}^*(\underline{\sigma}_{n+1}^*, \underline{X}_n, R_n, d_n) < 0$ , then the assumption of elastic state is true, giving the following solution:

$$\begin{cases} \underline{\sigma}_{n+1} = \underline{\sigma}_{n+1}^*, & \underline{\varepsilon}_{n+1}^p = \underline{\varepsilon}_n^p & (a) \\ \underline{X}_{n+1} = \underline{X}_n, & \underline{\alpha}_{n+1} = \underline{\alpha}_n & (b) \\ R_{n+1} = R_n, & r_{n+1} = r_n & (c) \\ Y_{n+1} = Y_n, & d_{n+1} = d_n & (d) \end{cases} \quad (2-36)$$

**Plastic correction:** If  $f_{n+1}^*(\underline{\sigma}_{n+1}^*, \underline{X}_n, R_n, d_n) > 0$ , then the solution is plastic over  $[t_n, t_{n+1}]$  and the trial solution (i.e.  $\underline{\sigma}_{n+1}^*, \underline{X}_n, R_n, d_n$ ) should be corrected to determine  $(\underline{\varepsilon}_{n+1}^e, \underline{\sigma}_{n+1})$ ,  $(\underline{\alpha}_{n+1}, \underline{X}_{n+1})$ ,  $(r_{n+1}, R_{n+1})$   $(d_{n+1}, Y_{n+1})$ , so that the following plastic admissibility condition is fulfilled:

$$f_{n+1}(\underline{\sigma}_{n+1}, \underline{X}_{n+1}, R_{n+1}, d_{n+1}) = 0 \quad (2-37)$$

To proceed with this plastic correction, the discretized nonlinear equations summarized in 2-28 should be solved using the classical Newton-Raphson iterative scheme (see [Saanouni12] for more details). The stresses  $\underline{\sigma}_{n+1}(\Delta\lambda, \underline{n}_{n+1}^p, d_{n+1})$ ,  $\underline{X}_{n+1}(\Delta\lambda, \underline{n}_{n+1}^p, d_{n+1})$ ,  $R_{n+1}(\Delta\lambda, \underline{n}_{n+1}^p, d_{n+1})$  are given by:

$$\begin{aligned} \underline{\sigma}_{n+1}(\Delta\lambda, \underline{n}_{n+1}^p, d_{n+1}) &= \frac{(1-d_{n+1})}{1-d_n} \underline{\sigma}_{n+1}^* - \sqrt{1-d_{n+1}} 2\mu_e \Delta\lambda \underline{n}_{n+1}^p, \\ \text{with } \underline{n}_{n+1}^p(\Delta\lambda, \underline{n}_{n+1}^p, d_{n+1}) &= \frac{\underline{n}_{n+1}^d}{\sqrt{1-d_{n+1}}} : \left[ 1^{dev} + \frac{\underline{X}_{n+1} \otimes \underline{S}_{0(n+1)}}{(1-d_{n+1}) X_{I1}^p(R_{n+1} / \sqrt{1-d_{n+1}^y} + \sigma_y)} \right] \end{aligned} \quad (2-38)$$

$$\begin{aligned} \underline{X}_{n+1}(\Delta\lambda, \underline{n}_{n+1}^p, d_{n+1}) &= \frac{(1-d_{n+1})}{1-d_n} \underline{X}_n e^{-a\Delta\lambda} - \frac{2}{3} \frac{C}{a} \sqrt{1-d_{n+1}} (1-e^{-a\Delta\lambda}) \underline{n}_{n+1}^x \\ \text{with } \underline{n}_{n+1}^x &= \underline{n}_{n+1}^x = \underline{n}_{n+1}^d - \frac{\left[ \frac{(\underline{S}_{0(n+1)} : \underline{S}_{0(n+1)}) \underline{n}_{n+1}^d}{2} - \frac{(\underline{S}_{n+1} : \underline{X}_{n+1})(\underline{X}_{n+1} : \underline{n}_{n+1}^d)}{(\underline{X}_{n+1} : \underline{X}_{n+1})} \underline{S}_0 \right]}{(1-d_{n+1}) X_{I1}^p(R_{n+1} / \sqrt{1-d_{n+1}^y} + \sigma_y)} \end{aligned} \quad (2-39)$$

$$\begin{aligned} R_{n+1}(\Delta\lambda, \underline{n}_{n+1}^p, d_{n+1}) &= \frac{(1-d_{n+1}^y)}{1-d_n^y} R_n e^{-b\Delta\lambda} - \frac{Q}{b} \sqrt{1-d_{n+1}^y} (1-e^{-b\Delta\lambda}) \underline{n}_{n+1}^i \\ \text{with } \underline{n}_{n+1}^i &= \frac{(\underline{S}_{0(n+1)} : \underline{S}_{0(n+1)}) (\underline{n}_{n+1}^d : \underline{X}_{n+1})}{2(1-d_{n+1})^{3/2} X_{I1}^p(R_{n+1} / \sqrt{1-d_{n+1}^y} + \sigma_y)^2} + 1 \end{aligned} \quad (2-40)$$

They are function of the three unknowns namely:  $\Delta\lambda$ ,  $d_{n+1}$  and  $\underline{n}_{n+1}^p$ . With the help of 2-28a, 2-28m and 2-28q, the overall equations are reduced to the following three equations with  $\Delta\lambda$ ,  $d_{n+1}$  and  $\underline{n}_{n+1}^p$  as the main unknowns:

$$\left\{ \begin{aligned} f(\Delta\lambda, \underline{n}_{n+1}^p, d_{n+1}) &= \frac{\| \underline{S}_{d(n+1)}^c(\Delta\lambda, d_{n+1}, \underline{\sigma}_{n+1}, \underline{X}_{n+1}) - \underline{X}_{n+1} \|_H}{\sqrt{1-d_{n+1}}} - \frac{R_{n+1}(\Delta\lambda, d_{n+1})}{\sqrt{1-d_{n+1}^y}} - \sigma_y = 0 \quad (a) \\ g(\Delta\lambda, \underline{n}_{n+1}^p, d_{n+1}) &= d_{n+1} - d_n - \frac{\Delta\lambda}{(1-d_{n+1})^\beta} \left\langle \frac{Y_{n+1}^*(\Delta\lambda, d_{n+1}, \underline{\sigma}_{n+1}, \underline{X}_{n+1}) - Y_0}{S(\theta)_{n+1}} \right\rangle^s = 0 \quad (b) \\ \varphi(\Delta\lambda, \underline{n}_{n+1}^p, d_{n+1}) &= \underline{n}_{n+1}^p - \frac{\underline{n}_{d(n+1)}}{\sqrt{1-d_{n+1}}} : \left[ 1^{dev} + \frac{\underline{X}_{n+1} \otimes \underline{S}_{0(n+1)}}{(1-d_{n+1}) X_{I1}^p(R_{n+1} / \sqrt{1-d_{n+1}^y} + \sigma_y)} \right] = 0 \quad (c) \end{aligned} \right. \quad (2-41)$$

This system is solved thanks to the classical linearization by Newton-Raphson method according to:

$$\begin{cases} f_{n+1}^k + \left(\frac{\partial f}{\partial \Delta \lambda}\right)_{n+1}^k \cdot \delta \Delta \lambda + \left(\frac{\partial f}{\partial d_{n+1}}\right)_{n+1}^k : \delta d_{n+1} + \left(\frac{\partial f}{\partial \underline{n}_{n+1}^p}\right)_{n+1}^k \cdot \delta \underline{n}_{n+1}^p = 0 \\ g_{n+1}^k + \left(\frac{\partial g}{\partial \Delta \lambda}\right)_{n+1}^k \cdot \delta \Delta \lambda + \left(\frac{\partial g}{\partial d_{n+1}}\right)_{n+1}^k : \delta d_{n+1} + \left(\frac{\partial g}{\partial \underline{n}_{n+1}^p}\right)_{n+1}^k \cdot \delta \underline{n}_{n+1}^p = 0 \\ \varphi_{n+1}^k + \left(\frac{\partial \varphi}{\partial \Delta \lambda}\right)_{n+1}^k \cdot \delta \Delta \lambda + \left(\frac{\partial \varphi}{\partial d_{n+1}}\right)_{n+1}^k : \delta d_{n+1} + \left(\frac{\partial \varphi}{\partial \underline{n}_{n+1}^p}\right)_{n+1}^k \cdot \delta \underline{n}_{n+1}^p = 0 \end{cases} \quad (2-42)$$

or under the matrix form:

$$\begin{Bmatrix} f_{n+1}^k \\ g_{n+1}^k \\ \varphi_{n+1}^k \end{Bmatrix} + \begin{bmatrix} \left(\frac{\partial f}{\partial \Delta \lambda}\right)_{n+1}^k & \left(\frac{\partial f}{\partial d_{n+1}}\right)_{n+1}^k & \left(\frac{\partial f}{\partial \underline{n}_{n+1}^p}\right)_{n+1}^k \\ \left(\frac{\partial g}{\partial \Delta \lambda}\right)_{n+1}^k & \left(\frac{\partial g}{\partial d_{n+1}}\right)_{n+1}^k & \left(\frac{\partial g}{\partial \underline{n}_{n+1}^p}\right)_{n+1}^k \\ \left(\frac{\partial \varphi}{\partial \Delta \lambda}\right)_{n+1}^k & \left(\frac{\partial \varphi}{\partial d_{n+1}}\right)_{n+1}^k & \left(\frac{\partial \varphi}{\partial \underline{n}_{n+1}^p}\right)_{n+1}^k \end{bmatrix} \begin{Bmatrix} \delta \Delta \lambda \\ \delta D \\ \delta \underline{n}_{n+1}^p \end{Bmatrix} = \begin{Bmatrix} 0 \\ 0 \\ 0 \end{Bmatrix} \quad (2-43)$$

This system can be solved with respect to  $\delta \Delta \lambda$ ,  $\delta d_{n+1}$  and  $\delta \underline{n}_{n+1}^p$ :

$$\begin{Bmatrix} \delta \Delta \lambda \\ \delta d \\ \delta \underline{n}_{n+1}^p \end{Bmatrix} = \begin{bmatrix} \left(\frac{\partial f}{\partial \Delta \lambda}\right)_{n+1}^k & \left(\frac{\partial f}{\partial d_{n+1}}\right)_{n+1}^k & \left(\frac{\partial f}{\partial \underline{n}_{n+1}^p}\right)_{n+1}^k \\ \left(\frac{\partial g}{\partial \Delta \lambda}\right)_{n+1}^k & \left(\frac{\partial g}{\partial d_{n+1}}\right)_{n+1}^k & \left(\frac{\partial g}{\partial \underline{n}_{n+1}^p}\right)_{n+1}^k \\ \left(\frac{\partial \varphi}{\partial \Delta \lambda}\right)_{n+1}^k & \left(\frac{\partial \varphi}{\partial d_{n+1}}\right)_{n+1}^k & \left(\frac{\partial \varphi}{\partial \underline{n}_{n+1}^p}\right)_{n+1}^k \end{bmatrix}^{-1} \cdot \begin{Bmatrix} -f_{n+1}^k \\ -g_{n+1}^k \\ -\varphi_{n+1}^k \end{Bmatrix} \quad (2-44)$$

The components of the material Jacobian matrix in (2-44) are given here after. Once the correction variables  $\delta \Delta \lambda_{n+1}^k$ ,  $\delta d_{n+1}^k$ ,  $(\delta \underline{n}_{n+1}^p)^k$  obtained after the convergence at the iteration (k), the other state variables are calculated using (2-38) to (2-40).

Concerning the nine components of the material Jacobian matrix defined in (2-44) they are calculated as following:

$$\begin{aligned} \frac{\partial f}{\partial \Delta \lambda} &= \frac{1}{\sqrt{1-d_{n+1}}} \frac{\partial \left\| \underline{S}_{d(n+1)}^c(\Delta \lambda, d_{n+1}, \underline{\sigma}_{n+1}, \underline{X}_{n+1}) - \underline{X}_{n+1} \right\|_{Hill}}{\partial \Delta \lambda} - \frac{1}{\sqrt{1-d_{n+1}^{\gamma}}} \frac{\partial R_{n+1}}{\partial \Delta \lambda} \\ &= \frac{1}{\sqrt{1-d_{n+1}}} \underline{n}_{d(n+1)}^c \left( \frac{\partial \underline{S}_{d(n+1)}^c}{\partial \Delta \lambda} - \frac{\underline{X}_{n+1}}{\partial \Delta \lambda} \right) - \frac{1}{\sqrt{1-d_{n+1}^{\gamma}}} \frac{\partial R_{n+1}}{\partial \Delta \lambda} \end{aligned} \quad (2-45)$$

$$\frac{\partial f}{\partial \underline{n}_{n+1}^p} = \frac{1}{\sqrt{1-d_{n+1}}} \frac{\partial \left\| \underline{S}_{d(n+1)}^c(\Delta \lambda, d_{n+1}, \underline{\sigma}_{n+1}, \underline{X}_{n+1}) - \underline{X}_{n+1} \right\|_{Hill}}{\partial \underline{n}_{n+1}^p} = \frac{\underline{n}_{d(n+1)}^c}{\sqrt{1-d_{n+1}}} : \frac{\partial \underline{S}_{d(n+1)}^c}{\partial \underline{n}_{n+1}^p} \quad (2-46)$$

$$\frac{\partial f}{\partial d_{n+1}} = \frac{1}{2(1-d_{n+1})^{3/2}} \left\| \underline{S}_{d(n+1)}^c - \underline{X}_{n+1} \right\| + \frac{1}{\sqrt{1-d_{n+1}}} \frac{\partial \left\| \underline{S}_{d(n+1)}^c - \underline{X}_{n+1} \right\|}{\partial d_{n+1}} - \frac{\gamma d^{\gamma-1}}{2(1-d_{n+1}^\gamma)^{3/2}} R_{n+1} - \frac{1}{\sqrt{1-d_{n+1}^\gamma}} \frac{\partial R}{\partial d_{n+1}} \quad (2-47)$$

$$\frac{\partial g}{\partial \Delta \lambda} = -\frac{1}{(1-d_{n+1})^\beta} \left\langle \frac{Y_{n+1} - Y_0}{S(\theta)_{n+1}} \right\rangle^s - \frac{\Delta \lambda s}{S(\theta)_{n+1} (1-d_{n+1})^\beta} \left\langle \frac{Y_{n+1} - Y_0}{S(\theta)_{n+1}} \right\rangle^{s-1} \frac{\partial Y_{n+1}}{\partial \Delta \lambda} \quad (2-48)$$

$$\frac{\partial g}{\partial n_{n+1}^p} = -\frac{\Delta \lambda s}{S(\theta)_{n+1} (1-d_{n+1})^\beta} \left\langle \frac{Y_{n+1} - Y_0}{S(\theta)_{n+1}} \right\rangle^{s-1} \frac{\partial Y_{n+1}}{\partial n_{n+1}^p} \quad (2-49)$$

$$\frac{\partial \varphi}{\partial n_{n+1}^p} = I - \frac{1}{\sqrt{1-d_{n+1}}} \left[ \frac{\frac{\partial n_{d(n+1)}^p}{\partial n_{n+1}^p} + \frac{1}{AAI} \left( \frac{\partial n_{d(n+1)}^p}{\partial n_{n+1}^p} : \underline{X}_{n+1} \otimes \underline{S}_{0(n+1)} + n_{d(n+1)} : \underline{X}_{n+1} \cdot \frac{\partial \underline{S}_{0(n+1)}}{\partial n_{n+1}^p} \right)}{X_{I2} \frac{\partial n_{d(n+1)}^p}{\partial n_{n+1}^p} \left\| \underline{X}_{n+1} \right\|_M} \right] \quad (2-50)$$

$$\frac{\partial \varphi}{\partial \Delta \lambda} = -\frac{1}{\sqrt{1-d_{n+1}}} \left[ \frac{\frac{\partial n_{d(n+1)}^p}{\partial \Delta \lambda} + \frac{1}{AAI} \left( \frac{\partial n_{d(n+1)}^p}{\partial \Delta \lambda} : \underline{X}_{n+1} \cdot \underline{S}_{0(n+1)} + \frac{\partial \underline{X}_{n+1}}{\partial \Delta \lambda} : n_{d(n+1)}^p \cdot \underline{S}_{0(n+1)} + n_{d(n+1)}^p : \underline{X}_{n+1} \cdot \frac{\partial \underline{S}_{0(n+1)}}{\partial \Delta \lambda} \right)}{X_{I1} \frac{\partial R_{n+1}}{\partial \Delta \lambda} (n_{d(n+1)}^p : \underline{X}_{n+1} \cdot \underline{S}_{0(n+1)})} \right] \quad (2-51)$$

$$\frac{\partial \varphi}{\partial d_{n+1}} = \left[ \frac{n_{d(n+1)}^p}{2(1-d_{n+1})^{3/2}} : \left[ \frac{d^{ev}}{X_{I1} (R_{n+1} / \sqrt{1-d_{n+1}^\gamma} + \sigma_y)} + \frac{\underline{X}_{n+1} \otimes \underline{S}_{0(n+1)}}{X_{I1} (R_{n+1} / \sqrt{1-d_{n+1}^\gamma} + \sigma_y)} \right] - \frac{1}{\sqrt{1-d_{n+1}}} \left[ \frac{\frac{\partial n_{d(n+1)}^p}{\partial d_{n+1}} + \frac{1}{AAI} \left( \frac{\partial n_{d(n+1)}^p}{\partial d_{n+1}} : \underline{X}_{n+1} \cdot \underline{S}_{0(n+1)} + \frac{\partial \underline{X}_{n+1}}{\partial d_{n+1}} : n_{d(n+1)}^p \cdot \underline{S}_{0(n+1)} + n_{d(n+1)}^p : \underline{X}_{n+1} \cdot \frac{\partial \underline{S}_{0(n+1)}}{\partial d_{n+1}} \right)}{\left( \frac{X_{I1}}{AAI^2} \left( \frac{1}{\sqrt{1-d_{n+1}^\gamma}} \frac{\partial R_{n+1}}{\partial d_{n+1}} + \frac{\gamma d^{\gamma-1}}{2(1-d_{n+1}^\gamma)^{3/2}} \right) \right) (n_{d(n+1)}^p : \underline{X}_{n+1} \cdot \underline{S}_{0(n+1)})} \right] \right] \quad (2-52)$$

$$AAI = X_{I1}^p (R_{n+1} / \sqrt{1-d_{n+1}^\gamma} + \sigma_y) \quad \text{and} \quad BBI = X_{I2} (R_{n+1} / \sqrt{1-d_{n+1}^\gamma} + \sigma_y) \quad (2-53)$$

$$\frac{\partial n_{d(n+1)}^c}{\partial \Delta \lambda} = \frac{\partial}{\partial \Delta \lambda} \left( \frac{H : (\underline{S}_{d(n+1)}^c - \underline{X}_{n+1})}{\left\| \underline{S}_{d(n+1)}^c - \underline{X}_{n+1} \right\|_{Hill}} \right) = \frac{1}{\left\| \underline{S}_{d(n+1)}^c - \underline{X}_{n+1} \right\|_{Hill}} \left( \frac{H : \left( \frac{\partial \underline{S}_{d(n+1)}^c}{\partial \Delta \lambda} - \frac{\partial \underline{X}_{n+1}}{\partial \Delta \lambda} \right) + H : (\underline{S}_{d(n+1)}^c - \underline{X}_{n+1})}{\left( \frac{-n_{d(n+1)}^c}{\left\| \underline{S}_{d(n+1)}^c - \underline{X}_{n+1} \right\|_{Hill}^2} : \left( \frac{\partial \underline{S}_{d(n+1)}^c}{\partial \Delta \lambda} - \frac{\partial \underline{X}_{n+1}}{\partial \Delta \lambda} \right) \right)} \right) \quad (2-54)$$

$$\frac{\partial n_{d(n+1)}^p}{\partial \Delta \lambda} = \frac{\partial}{\partial \Delta \lambda} \left( \frac{H : (\underline{S}_{d(n+1)}^p - \underline{X}_{n+1})}{\left\| \underline{S}_{d(n+1)}^p - \underline{X}_{n+1} \right\|_{Hill}} \right) = \frac{1}{\left\| \underline{S}_{d(n+1)}^p - \underline{X}_{n+1} \right\|_{Hill}} \left( \frac{H : \left( \frac{\partial \underline{S}_{d(n+1)}^p}{\partial \Delta \lambda} - \frac{\partial \underline{X}_{n+1}}{\partial \Delta \lambda} \right) + H : (\underline{S}_{d(n+1)}^p - \underline{X}_{n+1})}{\left( \frac{-n_{d(n+1)}^p}{\left\| \underline{S}_{d(n+1)}^p - \underline{X}_{n+1} \right\|_{Hill}^2} : \left( \frac{\partial \underline{S}_{d(n+1)}^p}{\partial \Delta \lambda} - \frac{\partial \underline{X}_{n+1}}{\partial \Delta \lambda} \right) \right)} \right) \quad (2-55)$$

$$\begin{aligned} \frac{\partial \underline{S}_{d(n+1)}^c}{\partial \Delta \lambda} &= \frac{\partial \underline{S}_{n+1}}{\partial \Delta \lambda} + \frac{1}{2AA1} \left( 2\underline{S}_{o(n+1)} : \frac{\partial \underline{S}_{o(n+1)}}{\partial \Delta \lambda} \cdot \underline{X}_{n+1} + \underline{S}_{o(n+1)} : \underline{S}_{o(n+1)} \frac{\partial \underline{X}_{n+1}}{\partial \Delta \lambda} \right) - \frac{\underline{S}_{o(n+1)} : \underline{S}_{o(n+1)} \underline{X}_{n+1}}{2X_{11} \sqrt{1-d_{n+1}'}} \frac{\frac{\partial R_{n+1}}{\partial \Delta \lambda}}{\left( R_{n+1} \sqrt{1-d_{n+1}'} + \sigma_y \right)^2} + \\ &\quad \frac{1}{2BB1} \left( 2\underline{X}_{n+1} : \frac{\partial \underline{X}_{n+1}}{\partial \Delta \lambda} \cdot \underline{S}_{o(n+1)} + \underline{X}_{n+1} : \underline{X}_{n+1} \frac{\partial \underline{S}_{o(n+1)}}{\partial \Delta \lambda} \right) - \frac{\underline{X}_{n+1} : \underline{X}_{n+1} \underline{S}_{o(n+1)}}{2X_{11} \sqrt{1-d_{n+1}'}} \frac{\frac{\partial R_{n+1}}{\partial \Delta \lambda}}{\left( R_{n+1} \sqrt{1-d_{n+1}'} + \sigma_y \right)^2} \end{aligned} \quad (2-56)$$

$$\frac{\partial \underline{S}_{d(n+1)}^p}{\partial \Delta \lambda} = \frac{\partial \underline{S}_{n+1}}{\partial \Delta \lambda} + \frac{1}{2AA1} \left( 2\underline{S}_{o(n+1)} : \frac{\partial \underline{S}_{o(n+1)}}{\partial \Delta \lambda} \cdot \underline{X}_{n+1} + \underline{S}_{o(n+1)} : \underline{S}_{o(n+1)} \frac{\partial \underline{X}_{n+1}}{\partial \Delta \lambda} \right) - \frac{\underline{S}_{o(n+1)} : \underline{S}_{o(n+1)} \underline{X}_{n+1}}{2X_{11} \sqrt{1-d_{n+1}'}} \frac{\frac{\partial R_{n+1}}{\partial \Delta \lambda}}{\left( R_{n+1} \sqrt{1-d_{n+1}'} + \sigma_y \right)^2} +$$

$$\frac{\partial \|\underline{X}_{n+1}\|_M}{\partial \Delta \lambda} = \frac{3\underline{X}_{n+1}}{2\|\underline{X}_{n+1}\|_M} : \frac{\partial \underline{X}_{n+1}}{\partial \Delta \lambda} \quad (2-57)$$

$$\frac{\partial \underline{S}_{o(n+1)}}{\partial \Delta \lambda} = \frac{\partial \underline{S}_{n+1}}{\partial \Delta \lambda} - \frac{\partial \underline{S}_{s(n+1)}}{\partial \Delta \lambda} = \frac{\partial \underline{S}_{n+1}}{\partial \Delta \lambda} - \left( \frac{1}{\underline{X}_{n+1} : \underline{X}_{n+1}} \left( \frac{\partial \underline{S}_{n+1}}{\partial \Delta \lambda} : \underline{X}_{n+1} \cdot \underline{X}_{n+1} + \frac{\partial \underline{X}_{n+1}}{\partial \Delta \lambda} : \underline{S}_{n+1} \cdot \underline{X}_{n+1} + \underline{X}_{n+1} : \underline{S}_{n+1} \cdot \frac{\partial \underline{X}_{n+1}}{\partial \Delta \lambda} \right) - \left( \underline{S}_{n+1} : \underline{X}_{n+1} \cdot \underline{X}_{n+1} \right) \frac{2\underline{X}_{n+1} \cdot \frac{\partial \underline{X}_{n+1}}{\partial \Delta \lambda}}{(\underline{X}_{n+1} : \underline{X}_{n+1})^2} \right) \quad (2-58)$$

$$\left\{ \begin{aligned} \frac{\partial Y_{n+1}}{\partial \Delta \lambda} &= \frac{\partial \langle Y_{n+1} \rangle_+}{\partial \Delta \lambda} + \frac{\partial \langle Y_{n+1} \rangle_-}{\partial \Delta \lambda} + \frac{\partial Y_{n+1}^\alpha}{\partial \Delta \lambda} + \frac{\partial Y_{n+1}^r}{\partial \Delta \lambda} \\ \frac{\partial \langle Y_{n+1} \rangle_+}{\partial \Delta \lambda} &= \frac{1+\nu}{E(1-d_{n+1})^2} \left( \frac{\partial \langle \underline{\sigma}_{n+1} \rangle_+}{\partial \Delta \lambda} : \langle \underline{\sigma}_{n+1} \rangle_+ \right) - \frac{1+\nu}{E(1-d_{n+1})^2} \left( \frac{\partial \langle \text{tr}(\underline{\sigma}_{n+1}) \rangle_+}{\partial \Delta \lambda} : \langle \text{tr}(\underline{\sigma}_{n+1}) \rangle_+ \right) \\ \frac{\partial \langle Y_{n+1} \rangle_-}{\partial \Delta \lambda} &= \frac{1+\nu}{E(1-hd_{n+1})^2} \left( \frac{\partial \langle \underline{\sigma}_{n+1} \rangle_-}{\partial \Delta \lambda} : \langle \underline{\sigma}_{n+1} \rangle_- \right) - \frac{1+\nu}{E(1-hd_{n+1})^2} \left( \frac{\partial \langle \text{tr}(\underline{\sigma}_{n+1}) \rangle_-}{\partial \Delta \lambda} : \langle \text{tr}(\underline{\sigma}_{n+1}) \rangle_- \right) \\ \frac{\partial Y_{n+1}^\alpha}{\partial \Delta \lambda} &= \frac{3}{2C(1-d_{n+1})^2} \left( \frac{\partial \underline{X}_{n+1}}{\partial \Delta \lambda} : \underline{X}_{n+1} \right) \\ \frac{\partial Y_{n+1}^r}{\partial \Delta \lambda} &= \frac{md_{n+1}^m R}{Q(1-d_{n+1}^m)^2} \frac{\partial R_{n+1}}{\partial \Delta \lambda} \end{aligned} \right. \quad (2-59)$$

$$\frac{\partial \underline{S}_{n+1}}{\partial \Delta \lambda} = -(1-d_{n+1}) 2\mu_e \underline{n}_{n+1}^p \quad (2-60)$$

$$\frac{\partial \underline{X}_{n+1}}{\partial \Delta \lambda} = \frac{2}{3} C(1-d_{n+1}) \left( \underline{\alpha}_n e^{-a\Delta \lambda} (-a) + \frac{\underline{n}_{(n)}^x e^{-a\Delta \lambda}}{\sqrt{1-d_{n+1}}} \right) \quad (2-61)$$

$$\frac{\partial R_{n+1}}{\partial \Delta \lambda} = Q(1-d_{n+1}) \left( r_n e^{-b\Delta \lambda} (-b) + \frac{n_{(n)}^i e^{-b\Delta \lambda}}{\sqrt{1-d_{n+1}}} \right) \quad (2-62)$$

$$\frac{\partial \underline{S}_{d(n+1)}^c}{\partial \underline{n}_{n+1}^p} = \frac{\partial \underline{S}_{n+1}}{\partial \underline{n}_{n+1}^p} + \frac{1}{AA1} \left( \underline{S}_{o(n+1)} : \frac{\partial \underline{S}_{o(n+1)}}{\partial \underline{n}_{n+1}^p} \otimes \underline{X}_{n+1} \right) - \frac{\underline{X}_{n+1} : \underline{X}_{n+1}}{2BB1} \left( \frac{\partial \underline{S}_{o(n+1)}}{\partial \underline{n}_{n+1}^p} \right) \quad (2-63)$$

$$\frac{\partial \underline{S}_{d(n+1)}^p}{\partial \underline{n}_{n+1}^p} = \frac{\partial \underline{S}_{n+1}}{\partial \underline{n}_{n+1}^p} + \frac{1}{AAI} \left( \underline{S}_{o(n+1)} : \frac{\partial \underline{S}_{o(n+1)}}{\partial \underline{n}_{n+1}^p} \otimes \underline{X}_{n+1} \right) \quad (2-64)$$

$$\frac{\partial \underline{S}_{o(n+1)}}{\partial \underline{n}_{n+1}^p} = \frac{\partial \underline{S}_{n+1}}{\partial \underline{n}_{n+1}^p} - \frac{\partial \underline{S}_{x(n+1)}}{\partial \underline{n}_{n+1}^p} = \frac{\partial \underline{S}_{n+1}}{\partial \underline{n}_{n+1}^p} - \frac{\underline{X}_{n+1}}{\underline{X}_{n+1} : \underline{X}_{n+1}} : \frac{\partial \underline{S}_{n+1}}{\partial \underline{n}_{n+1}^p} \otimes \underline{X}_{n+1} \quad (2-65)$$

$$\begin{cases} \frac{\partial Y_{n+1}}{\partial \underline{n}_{n+1}^p} = \frac{\partial \langle Y_{n+1} \rangle_+}{\partial \underline{n}_{n+1}^p} + \frac{\partial \langle Y_{n+1} \rangle_-}{\partial \underline{n}_{n+1}^p} \\ \frac{\partial \langle Y_{n+1} \rangle_+}{\partial \underline{n}_{n+1}^p} = \frac{1+\nu}{E(1-d_{n+1})^2} \left( \frac{\partial \langle \underline{\sigma}_{n+1} \rangle_+}{\partial \underline{n}_{n+1}^p} : \langle \underline{\sigma}_{n+1} \rangle_+ \right) - \frac{1+\nu}{E(1-d_{n+1})^2} \left( \frac{\partial \langle \text{tr}(\underline{\sigma}_{n+1}) \rangle_+}{\partial \underline{n}_{n+1}^p} : \langle \text{tr}(\underline{\sigma}_{n+1}) \rangle_+ \right) \\ \frac{\partial \langle Y_{n+1} \rangle_-}{\partial \underline{n}_{n+1}^p} = \frac{1+\nu}{E(1-hd_{n+1})^2} \left( \frac{\partial \langle \underline{\sigma}_{n+1} \rangle_-}{\partial \underline{n}_{n+1}^p} : \langle \underline{\sigma}_{n+1} \rangle_- \right) - \frac{1+\nu}{E(1-hd_{n+1})^2} \left( \frac{\partial \langle \text{tr}(\underline{\sigma}_{n+1}) \rangle_-}{\partial \underline{n}_{n+1}^p} : \langle \text{tr}(\underline{\sigma}_{n+1}) \rangle_- \right) \end{cases} \quad (2-67)$$

$$\frac{\partial \underline{n}_{d(n+1)}^c}{\partial \underline{n}_{n+1}^p} = \frac{\underline{H} : \left( \frac{\partial \underline{S}_{d(n+1)}^c}{\partial \underline{n}_{n+1}^p} \right)}{\| \underline{S}_{d(n+1)}^c - \underline{X}_{n+1} \|_{Hill}} + \underline{H} : (\underline{S}_{d(n+1)}^c - \underline{X}_{n+1}) \left( \frac{-\underline{n}_{d(n)}^c}{\| \underline{S}_{d(n+1)}^c - \underline{X}_{n+1} \|_{Hill}^2} : \left( \frac{\partial \underline{S}_{d(n+1)}^c}{\partial \underline{n}_{n+1}^p} \right) \right) \quad (2-68)$$

$$\frac{\partial \underline{n}_{d(n+1)}^p}{\partial \underline{n}_{n+1}^p} = \frac{\underline{H} : \left( \frac{\partial \underline{S}_{d(n+1)}^p}{\partial \underline{n}_{n+1}^p} \right)}{\| \underline{S}_{d(n+1)}^p - \underline{X}_{n+1} \|_{Hill}} + \underline{H} : (\underline{S}_{d(n+1)}^p - \underline{X}_{n+1}) \left( \frac{-\underline{n}_{d(n)}^p}{\| \underline{S}_{d(n+1)}^p - \underline{X}_{n+1} \|_{Hill}^2} : \left( \frac{\partial \underline{S}_{d(n+1)}^p}{\partial \underline{n}_{n+1}^p} \right) \right) \quad (2-69)$$

$$\frac{\partial \underline{S}_{n+1}}{\partial \underline{n}_{n+1}^p} = -2(1-d_{n+1}) \Delta \lambda \mu_e \underline{I}^{dev} \quad (2-70)$$

$$\frac{\partial \underline{n}_{d(n+1)}^p}{\partial d_{n+1}} = \frac{\underline{H} : \left( \frac{\partial \underline{S}_{d(n+1)}^p}{\partial d_{n+1}} - \frac{\partial \underline{X}_{n+1}}{\partial d_{n+1}} \right)}{\| \underline{S}_{d(n+1)}^p - \underline{X}_{n+1} \|_{Hill}} + \underline{H} : (\underline{S}_{d(n+1)}^p - \underline{X}_{n+1}) \left( \frac{-\underline{n}_{d(n)}^p}{\| \underline{S}_{d(n+1)}^p - \underline{X}_{n+1} \|_{Hill}^2} : \left( \frac{\partial \underline{S}_{d(n+1)}^p}{\partial d_{n+1}} - \frac{\partial \underline{X}_{n+1}}{\partial d_{n+1}} \right) \right) \quad (2-71)$$

$$\frac{\partial \underline{S}_{n+1}^d}{\partial d_{n+1}} = \frac{\partial \underline{S}_{n+1}}{\partial d_{n+1}} + \left[ \begin{aligned} & \frac{1}{2AAI} \left( 2\underline{S}_{o(n+1)} : \frac{\partial \underline{S}_{o(n+1)}}{\partial d_{n+1}} \cdot \underline{X}_{n+1} + \underline{S}_{o(n+1)} : \underline{S}_{o(n+1)} \frac{\partial \underline{X}_{n+1}}{\partial d_{n+1}} \right) - \\ & \frac{\underline{S}_{o(n+1)} : \underline{S}_{o(n+1)} \underline{X}_{n+1}}{2X_{II}} \left( \frac{1}{\sqrt{1-d_{n+1}^{\gamma'}}} \frac{\partial R_{n+1}}{\partial d_{n+1}} + \frac{\gamma d^{\gamma-1}}{2(1-d_{n+1}^{\gamma'})^{3/2}} \right) - \frac{1}{2BBI} \left( 2\underline{X}_{n+1} : \frac{\partial \underline{X}_{n+1}}{\partial d_{n+1}} \cdot \underline{S}_{o(n+1)} + \underline{X}_{n+1} : \underline{X}_{n+1} \frac{\partial \underline{S}_{o(n+1)}}{\partial d_{n+1}} \right) + \\ & \frac{\underline{X}_{n+1} : \underline{X}_{n+1} \underline{S}_{o(n+1)}}{2X_{II} \sqrt{1-d_{n+1}^{\gamma'}}} \left( \frac{1}{\sqrt{1-d_{n+1}^{\gamma'}}} \frac{\partial R_{n+1}}{\partial d_{n+1}} + \frac{\gamma d^{\gamma-1}}{2(1-d_{n+1}^{\gamma'})^{3/2}} \right) \\ & \left( R_{n+1} \sqrt{1-d_{n+1}^{\gamma'}} + \sigma_y \right)^2 \end{aligned} \right] \quad (2-72)$$

$$\frac{\partial \underline{S}_{o(n+1)}}{\partial d_{n+1}} = \frac{\partial \underline{S}_{n+1}}{\partial d_{n+1}} - \left( \begin{array}{c} \frac{1}{\underline{X}_{n+1} : \underline{X}_{n+1}} \left( \frac{\partial \underline{S}_{n+1}}{\partial d_{n+1}} : \underline{X}_{n+1} \cdot \underline{X}_{n+1} + \frac{\partial \underline{X}_{n+1}}{\partial d_{n+1}} : \underline{S}_{n+1} \cdot \underline{X}_{n+1} + \right. \\ \left. \frac{\underline{X}_{n+1} : \underline{S}_{n+1}}{\underline{X}_{n+1} : \underline{S}_{n+1}} \cdot \frac{\partial \underline{X}_{n+1}}{\partial d_{n+1}} \right) \\ \left. - \left( \underline{S}_{n+1} : \underline{X}_{n+1} \cdot \underline{X}_{n+1} \right) \frac{2 \underline{X}_{n+1} \cdot \frac{\partial \underline{X}_{n+1}}{\partial d_{n+1}}}{(\underline{X}_{n+1} : \underline{X}_{n+1})^2} \right) \end{array} \right) \quad (2-73)$$

$$\left\{ \begin{array}{l} \frac{\partial Y_{n+1}}{\partial d_{n+1}} = \frac{\partial \langle Y_{n+1}^e \rangle_+}{\partial d_{n+1}} + \frac{\partial \langle Y_{n+1}^e \rangle_-}{\partial d_{n+1}} + \frac{\partial Y_{n+1}^\alpha}{\partial d_{n+1}} + \frac{\partial Y_{n+1}^r}{\partial d_{n+1}} \\ \frac{\partial \langle Y_{n+1}^e \rangle_+}{\partial d_{n+1}} = \frac{1+\nu}{E(1-d_{n+1})^2} \left( \frac{\partial \langle \underline{\sigma}_{n+1} \rangle_+}{\partial d_{n+1}} : \langle \underline{\sigma}_{n+1} \rangle_+ \right) - \frac{1+\nu}{E(1-d_{n+1})^2} \left( \frac{\partial \langle \text{tr}(\underline{\sigma}_{n+1}) \rangle_+}{\partial d_{n+1}} : \langle \text{tr}(\underline{\sigma}_{n+1}) \rangle_+ \right) \\ \frac{\partial \langle Y_{n+1}^e \rangle_-}{\partial d_{n+1}} = \frac{1+\nu}{E(1-hd_{n+1})^2} \left( \frac{\partial \langle \underline{\sigma}_{n+1} \rangle_-}{\partial d_{n+1}} : \langle \underline{\sigma}_{n+1} \rangle_- \right) - \frac{1+\nu}{E(1-hd_{n+1})^2} \left( \frac{\partial \langle \text{tr}(\underline{\sigma}_{n+1}) \rangle_-}{\partial d_{n+1}} : \langle \text{tr}(\underline{\sigma}_{n+1}) \rangle_- \right) \\ \frac{\partial Y_{n+1}^\alpha}{\partial d_{n+1}} = \frac{3}{2C(1-d_{n+1})^2} \left( \frac{\partial \underline{X}_{n+1} : \underline{X}_{n+1}}{\partial d_{n+1}} \right) \\ \frac{\partial Y_{n+1}^r}{\partial d_{n+1}} = \frac{\gamma d_{n+1}^\gamma R}{Q(1-d_{n+1}^\gamma)^2} \frac{\partial R_{n+1}}{\partial d_{n+1}} \end{array} \right. \quad (2-74)$$

$$\frac{\partial \underline{S}_{n+1}}{\partial d_{n+1}} = \underline{I}^{dev} : \left( \frac{-\underline{\sigma}_{n+1}^*}{1-d_{n+1}} + 2\mu_e \Delta \lambda \underline{n}_{n+1}^p \right) \quad (2-75)$$

$$\frac{\partial \underline{X}_{n+1}}{\partial d_{n+1}} = -\frac{2C}{3} \left( e^{-a\Delta\lambda} \cdot \underline{\alpha}_n + \frac{1-e^{-a\Delta\lambda}}{a\sqrt{1-d_{n+1}}} n_{x(n)} \right) - \frac{C}{3} (1-d_{n+1}) \left( \frac{1-e^{-a\Delta\lambda}}{a(1-d_{n+1})^{3/2}} n_{x(n)} \right) \quad (2-76)$$

$$\frac{\partial R_{n+1}}{\partial d_{n+1}} = -\gamma Q d_{n+1}^{\gamma-1} \left( e^{-b\Delta\lambda} \cdot \underline{r}_n + \frac{1-e^{-b\Delta\lambda}}{b\sqrt{1-d_{n+1}}} \right) - (1-d_{n+1}^\gamma) \left( \frac{1-e^{-b\Delta\lambda}}{2b(1-d_{n+1}^\gamma)^{3/2}} n_{(n+1)}^i \right) \quad (2-77)$$

Note that in the case of plane stress assumption, a new equation  $\mathfrak{S}(\Delta\lambda, d_{n+1}, \underline{\tilde{n}}_{n+1}^p, \underline{\epsilon}_{n+1}^{33})$  can be added to the equations 2-42, and the new system of four equations with four unknowns  $\Delta\lambda, d_{n+1}, \underline{\tilde{n}}_{n+1}^p, \underline{\epsilon}_{n+1}^{33}$  is:

$$\left\{ \begin{array}{l} f(\Delta\lambda, d_{n+1}, \underline{n}_{n+1}^p, \underline{\epsilon}_{n+1}^{33}) = \frac{\| \underline{S}_{d(n+1)}^c(\Delta\lambda, d_{n+1}, \underline{\sigma}_{n+1}, \underline{X}_{n+1}) - \underline{X}_{n+1} \|}{\sqrt{1-d_{n+1}}} - \frac{R_{n+1}(\Delta\lambda, d_{n+1})}{\sqrt{1-d_{n+1}^\gamma}} - \sigma_y = 0 \\ g(\Delta\lambda, d_{n+1}, \underline{n}_{n+1}^p, \underline{\epsilon}_{n+1}^{33}) = d_{n+1} - d_n - \frac{\Delta\lambda}{(1-d_{n+1})^\beta} \left\langle \frac{Y_{n+1}^*(\Delta\lambda, d_{n+1}, \underline{\sigma}_{n+1}, \underline{X}_{n+1}) - Y_0}{S(\theta)_{n+1}} \right\rangle^s = 0 \\ \wp(\Delta\lambda, d_{n+1}, \underline{n}_{n+1}^p, \underline{\epsilon}_{n+1}^{33}) = \underline{n}_{n+1}^p - \frac{n_{d(n+1)}}{\sqrt{1-d_{n+1}}} : \left[ \underline{1}^{dev} + \frac{\underline{X}_{n+1} \otimes \underline{S}_{0(n+1)}}{(1-d_{n+1})X_{II}(R_{n+1}/\sqrt{1-d_{n+1}^\gamma} + \sigma_y)} \right] = 0 \\ \mathfrak{S}(\Delta\lambda, d_{n+1}, \underline{n}_{n+1}^p, \underline{\epsilon}_{n+1}^{33}) = \underline{\epsilon}_{n+1}^{33} - \frac{V}{1-\nu} (\underline{\epsilon}_{n+1}^{11} + \underline{\epsilon}_{n+1}^{22}) \end{array} \right. \quad (2-78)$$

To solve this system a similar iterative scheme used to solve (2-41) is applied.

## II.2.3 Numerical treatment of contact with friction

The numerical treatment of contact with friction must be taken into account because the frictional behavior plays an important role in the solution of the metal forming problems. Here the well-known Coulomb model is used to describe the friction at the contact interfaces. This is an available standard way in ABAQUS/Explicit (Rep. ABAQUS theory Manuel). We note simply that the Coulomb friction parameter  $\mu$  is taken constant, and the numerical treatment of contacting nodes based on master/slave surfaces algorithm over the nodes is expected to come in contact.

## II.3 Numerical Aspect of M-K approach

In order to calculate the unknown variables in the groove zone, including the equivalent strain increment  $d\bar{\varepsilon}^b$  and the stress value  $\sigma_n^b$ , the Newton-Raphson method is applied, can be found [Assempour09, Butuc03]. The equations to be solved are:

$$\begin{cases} F_1(d\bar{\varepsilon}_b, \sigma_n^b) = \bar{\sigma}^b - \bar{\sigma}_{YF} = 0 \\ F_2(d\bar{\varepsilon}_b, \sigma_n^b) = d\varepsilon_n^a - d\varepsilon_n^b = 0 \end{cases} \quad (2-79)$$

With the hardening law, and yield function, the iterative formula for Newton-Raphson method is described as follows:

$$\begin{bmatrix} d\bar{\varepsilon}_{i+1}^b \\ \sigma_{n(i+1)}^b \end{bmatrix} = \begin{bmatrix} d\bar{\varepsilon}_i^b \\ \sigma_{n(i)}^b \end{bmatrix} - [J^{-1}] \begin{bmatrix} F_1(d\bar{\varepsilon}_i^b, \sigma_{n(i)}^b) \\ F_2(d\bar{\varepsilon}_i^b, \sigma_{n(i)}^b) \end{bmatrix} \quad (2-80)$$

Matrix  $[J]$  represents the derivatives of functions  $F_1$  and  $F_2$  as following shown:

$$J = \begin{bmatrix} \frac{\partial F_1}{\partial d\bar{\varepsilon}^b} & \frac{\partial F_1}{\partial \sigma_n^b} \\ \frac{\partial F_2}{\partial d\bar{\varepsilon}^b} & \frac{\partial F_2}{\partial \sigma_n^b} \end{bmatrix} \quad (2-81)$$

These derivatives can be obtained from the equations (2-61). In this study, Mises and Hill yield functions and Swift and Voce hardening function are used.

This has been implemented in Matlab and convergence is assumed when absolute value of



functions  $F_1$  and  $F_2$  becomes less than prescribed error  $[E]$ .

## **II.4 Conclusions**

In this chapter, the Numerical aspect of the proposed models is roughly discussed, which includes the time and space discretization of the initial and boundary value problems, local integration scheme of the proposed fully coupled CDM model. On the other hand, the numerical treatment of the proposed M-K approach is also given in the third part of this chapter. In the coming chapter, based on same typical tests of three materials, the developed models will be identified and validated.



# Chapter III

## Experimental aspects and parametric study

### Content

---

III.1 Introduction.....	60
III.2 Experimental procedure and results.....	60
III.2.1 Test materials.....	60
III.2.2 Experimental procedures.....	61
III.2.2.1 Uniaxial tensile tests (UT).....	61
III.2.2.2 In-Plane Torsion tests (IPT).....	67
III.2.2.3 Pre-Notched Tension tests (PNT).....	69
III.2.2.4 Simple shear tests (SS).....	73
III.2.2.5 Combined loading tests (CL).....	74
III.2.2.6 Nakazima tests (NAK).....	79
III.2.2.7 Cross section deep-drawing tests (CSD).....	82
III.3 Parametric study of the proposed fully coupled CDM models.....	85
III.3.1 Microcracks closure effects.....	85
III.3.2 Distortional parameters effects on the yield surfaces.....	86
III.3.3 Distortional parameters effect on damage evolution.....	97
III.3.4 Triaxiality ratio and Lode angle effect on damage evolution.....	98
III.4 Parametric study of M-K approach.....	101
III.4.1 Initial imperfection.....	101
III.4.2 Hardening laws.....	102
III.5 Conclusions.....	103

### **III.1 Introduction**

In the first part of this Chapter experimental tests performed on three selected materials are presented. The obtained experimental results will be used in Chapter III to identify the material parameters and to validate the proposed fully coupled model.

In the second part, a relatively extensive parametric study is conducted in order to examine the capabilities of the proposed model in describing some phenomena as the microcracks closure in compression, the distortion of the yield surface during plastic loading and the effect of the stress triaxiality and Lode angle on the ductile damage evolution.

The last section of this chapter is dedicated to a short parametric study of the M-K model and its sensitivity to the initial imperfection for a given hardening law.

### **III.2 Experimental procedure and results**

In this section, series of tests are carried out in order to calibrate and validate the proposed models. The forming capabilities of three materials under different deformation paths are investigated through various tests, including: the Uniaxial tensile tests (UT), In-plane torsion tests (IPT), Pre-notched tension tests (PNT), Simple shear tests (SS), Combined loading tests (CL), Nakazima tests (NAK) and Cross section deep-drawing tests (CSD).

#### **III.2.1 Test materials**

A general trend in steel product is the development towards higher strength grades in order to achieve higher structural strength while decreasing the metal weight. In the automotive industry, a large number of new high strength steels and aluminum alloys are used in the body structure components, as shown in Fig. 3-1, where the correlations between the total elongation and the tensile strength of the materials is given.

In this study, three 1.5 mm thickness commercial sheet metals are chosen as test materials. They are the dual phase steel DP1000, the complex phase steel CP1200 and the aluminum alloy Al7020, which are widely used in automotive industry. Their chemical compositions are shown in Table 3-1.

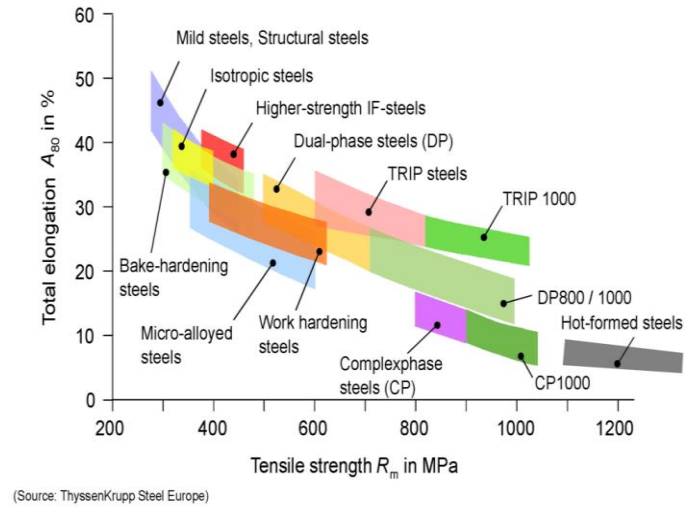


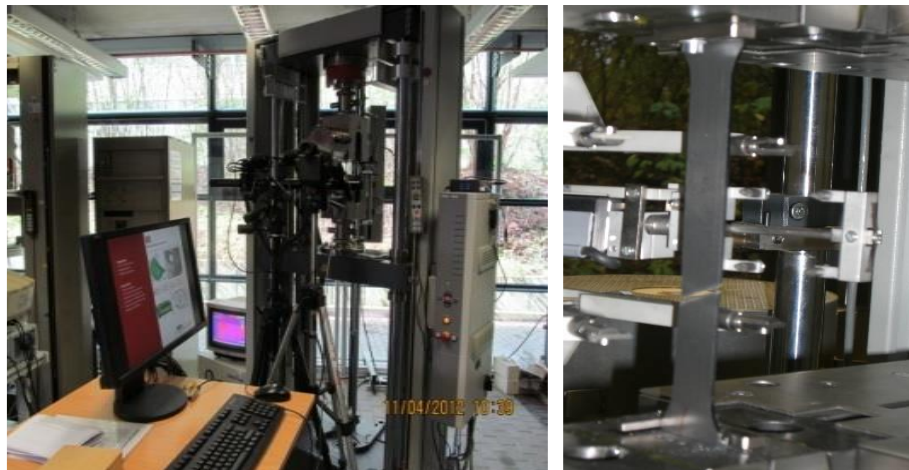
Fig. 3-1. Materials properties used in automotive body components.

Table 3-1. Chemical composition in wt. %

DP1000	Fe	C	Si	P	Mn	S	Cr	Ni	Al	Co
	Bal	0.16	0.49	1.5	0.011	0.002	0.44	0.035	0.043	0.016
CP1200	Fe	C	Si	P	Mn	S	Al	Ti+Nb	Cr+Mo	V
	Bal	0.23	0.8	0.08	2.2	0.015	2	0.15	1.2	0.2
Al7020	Al	Si	Fe	Cu	Mn	Cr	Mg	Zn	Zr+Ti	Other
	Bal	0.35	0.40	0.20	0.05-0.5	0.10-0.35	1.0-1.4	0.08-0.2	0.08-0.2	0.15

## III.2.2 Experimental procedures

### III.2.2.1 Uniaxial tensile tests (UT)

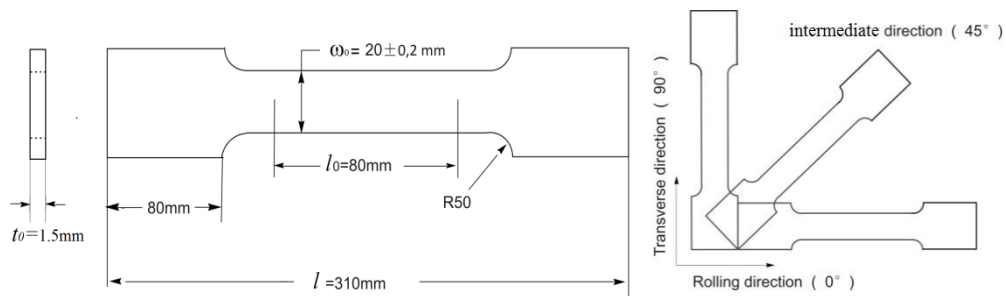


(a) Universal tensile machine

(b) Specimen position

Fig. 3-2. Experimental setup for UT test (IUL/TUD).

The uniaxial tensile test (or standard tensile test) is conducted on Zwick 250 machine with velocity of 0.1 mm/s (quasi-static loading conditions) available in IUL/TUD. UT tests are carried out on rectangular samples of dimension  $20 \times 80 \times 1.5 \text{ mm}^3$ . The experimental setup and specimen geometry are separately shown in Fig. 3-2 and Fig. 3-3. In order to determine the initial anisotropy, the test pieces are cut in three material directions: rolling direction ( $0^\circ$ ), transverse direction ( $90^\circ$ ) and intermediate direction ( $45^\circ$ ).

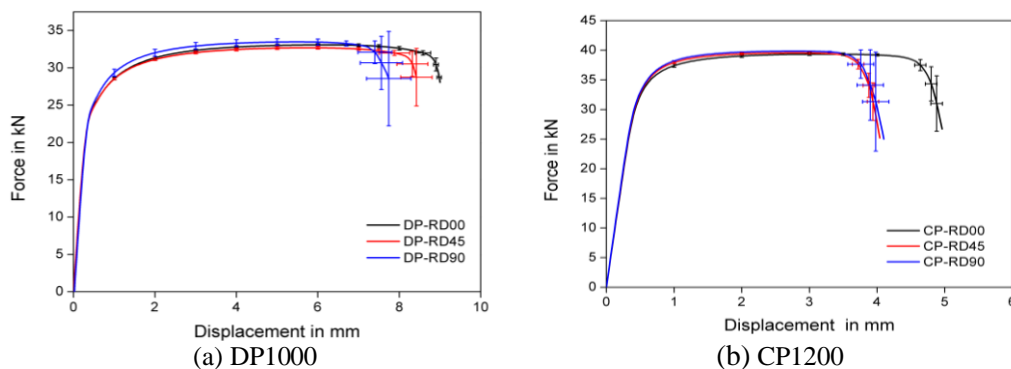


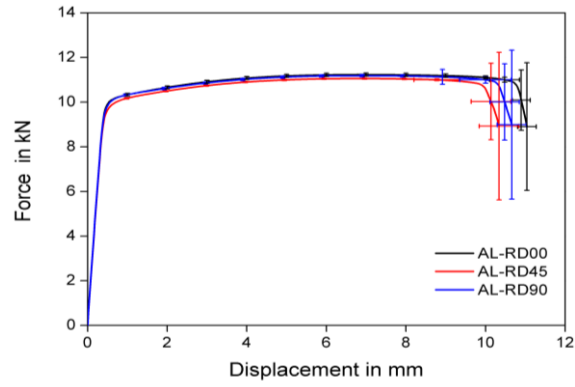
(a) Geometry of the test specimen      (b) Cutting directions

Fig. 3-3. Geometry of UT specimen.

With the help of the Zwick software, the force-displacement curves can be directly obtained during test. In order to well describe the material property, and also keep the reproduction of the test, each test is conducted five times, and the mean value of the test response is used for the analysis in each direction. The standard deviations are also calculated to well express the confidence area of the tests.

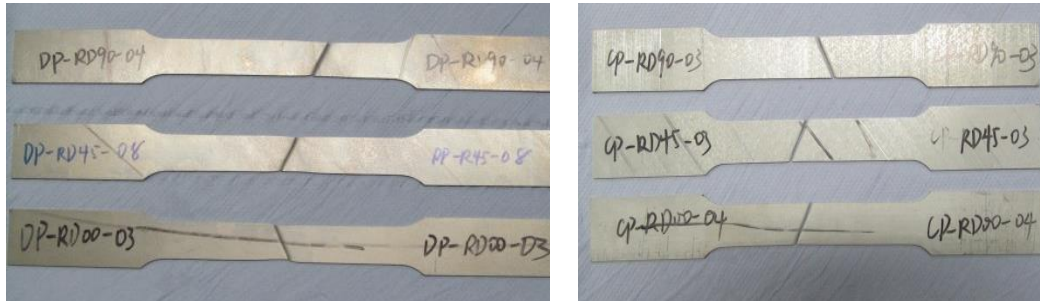
**Force-Displacement responses:** Some information like force-displacement curves can be directly obtained. The first part of the curve is the elastic strain, followed by plastic strain, and then necking and force decrease till the final fracture. The averaged force-displacement curves for three materials are shown in Fig. 3-4, which also give us the deviation of the tests. The post mortem specimens are shown in Fig. 3-5.





(c) Al7020

Fig. 3-4. Force-displacement curves for UT tests.



(a) DP1000

(b) CP1200



(c) Al7020

Fig. 3-5. Post mortem of UT specimens after the final fracture.

**Engineering strain-stress curves:** The engineering strain and engineering stress (Piola Kirchhoff stress) are defined by:

$$\sigma_{eng} = \frac{F}{S_0} = \frac{F}{t_0 w_0} \quad (3-1)$$

$$\varepsilon_{eng} = \frac{\Delta l}{l_0} = \frac{l - l_0}{l_0} = \frac{l}{l_0} - 1 \quad (3-2)$$

where  $F$  is the applied load;  $l_0$ ,  $t_0$ ,  $\omega_0$  are the initial length, thickness, width and the initial area of the test zone respectively (Fig. 3-3a). The engineering stress-strain curves for three materials in three loading directions are shown in Fig. 3-6.

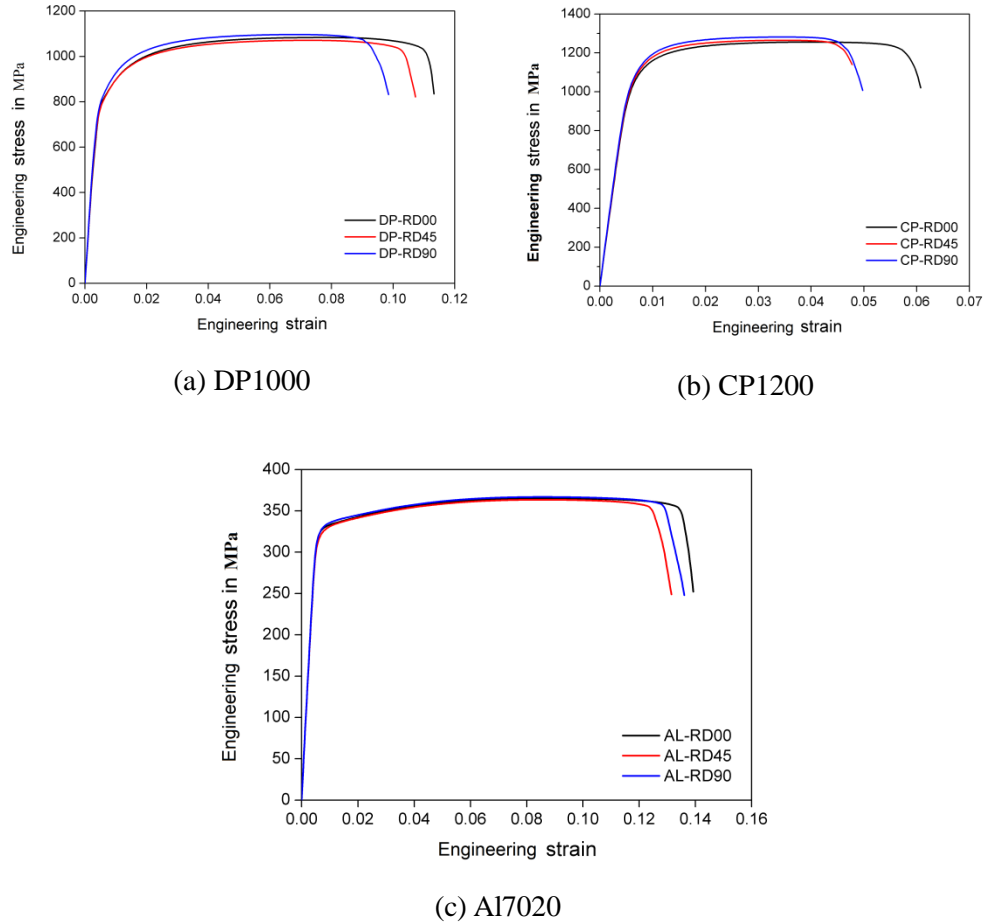


Fig. 3-6. Engineering stress-strain curves for three materials

**True stress-strain curves:** The true (or Cauchy) stress is obtained from the engineering quantities defined by (3-1) and (3-2) with the help of the volume conservation to get:

$$\sigma_{true} = \frac{F}{S} = \frac{F}{t\omega} \sigma_{eng} \left(\frac{l}{l_0}\right) = \sigma_{eng} (1 + \varepsilon_{eng}) \quad (3-3)$$

where  $S$  is the current cross-sectional area. The true strain is given by the integral of the strain increment, i.e.

$$\varepsilon = \int_{\varepsilon} d\varepsilon = \int_{l_0}^l \frac{dl}{l} = \ln \frac{l}{l_0} = \ln(1 + \varepsilon_{eng}) \quad 3-4$$

The true stress-strain curves for the three materials under concern are given Fig. 3-7.



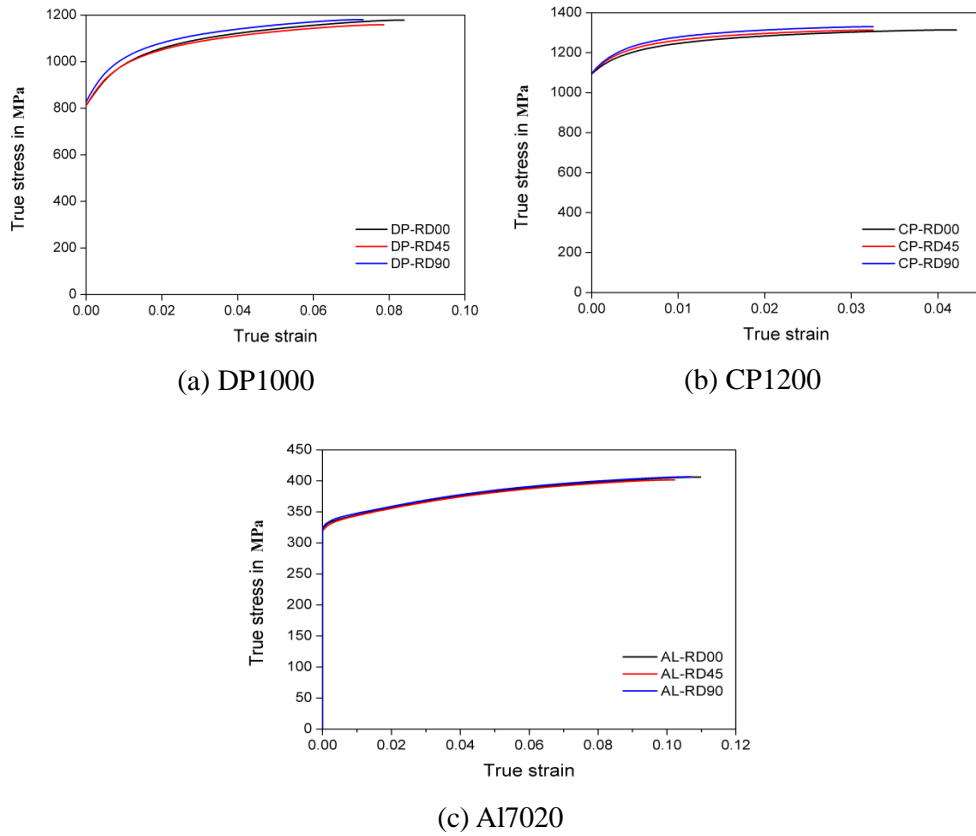


Fig. 3-7. True strain-stress response

#### Anisotropic parameters determination:

The  $r_{\theta}^L$ -value (Lankford ratio) equation can be constructed as the form below. According to the volume conservation principle:

$$\Delta\varepsilon_1 + \Delta\varepsilon_2 + \Delta\varepsilon_3 = 0 \quad (3-5)$$

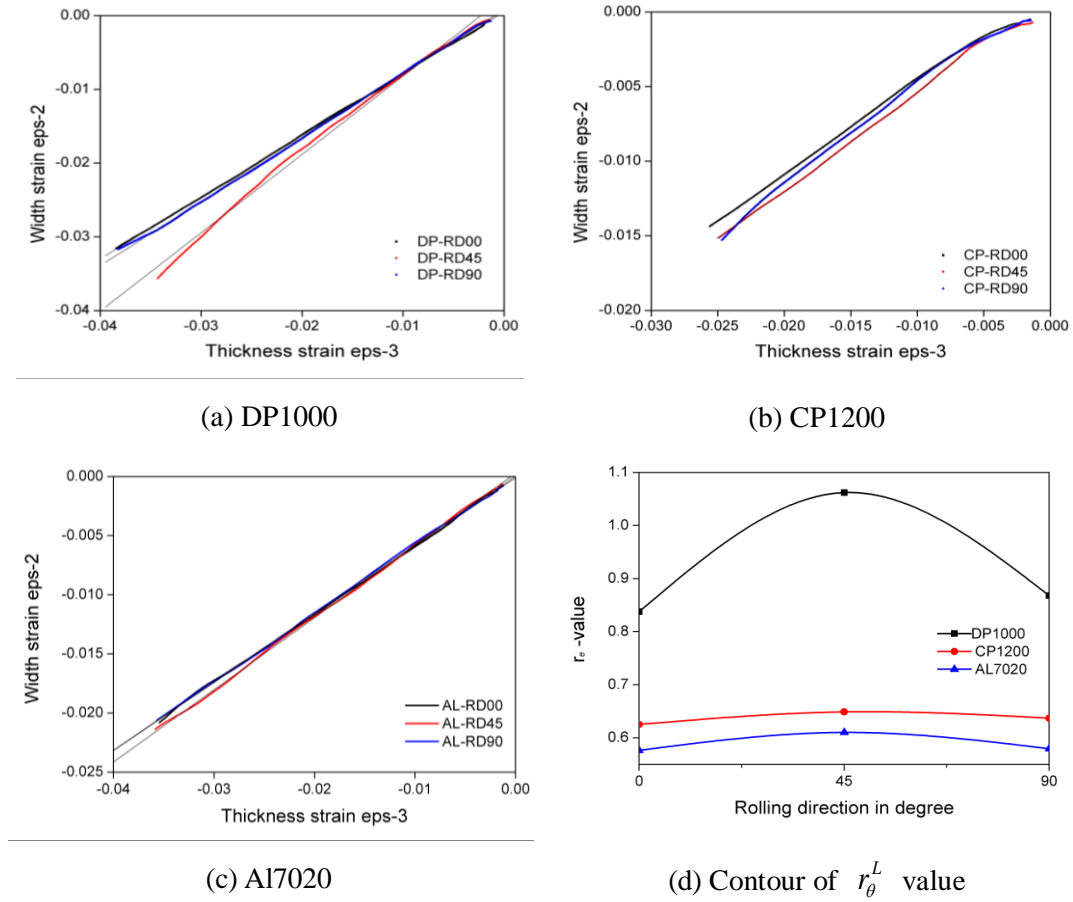
The through thickness strain is given by:

$$\Delta\varepsilon_3 = -(\Delta\varepsilon_1 + \Delta\varepsilon_2) \quad (3-6)$$

$$r_{\theta}^L = \frac{\Delta\varepsilon_2}{\Delta\varepsilon_3} = -\frac{\Delta\varepsilon_2}{\Delta\varepsilon_1 + \Delta\varepsilon_2} \quad (3-7)$$

Then, based on the equations above, the slop of the  $\varepsilon_2 - \varepsilon_3$  curve gives the  $r_{\theta}^L$ -values.

These  $r_{\theta}^L$  values for each material on each direction are shown in Fig. 3-8.


 Fig. 3-8. Ratio of the width and thickness strain and Contour of  $r_{\theta}^L$  -value

For the  $r_{\theta}^L$  -values, the hand calculated results (Eq. 3-7) are a bit different from the measured results, and the error rate can be calculated according to:

$$\text{Error(\%)} = \frac{(\text{measured result}) - (\text{calculated result})}{(\text{measured result})} \times 100\% \quad (3-8)$$

The  $r_{\theta}^L$  -values for given orientation ( $\theta$ ) can be expressed function of the Hill anisotropy parameters [Banabic00]:

$$r_{\theta}^L = \frac{H + (2N - F - G - 4H) \times \sin^2 \theta \times \cos^2 \theta}{F \times \sin^2 \theta + G \times \cos^2 \theta} \quad (3-9)$$

With the assumption of  $G+H=1$ , we can get the anisotropic parameters as shown in Table 3-3:

 Table 3-2.  $r_{\theta}^L$  -value for three directions of each material.

Rolling	DP1000	CP1200	Al7020
---------	--------	--------	--------

direction	calculated result $R_{0,002-0,07}$	measured result	Error %	calculated result $R_{0,002-0,04}$	measured result	Error %	Calculated result $R_{0,002-0,06}$	Measured result	Error %
0°	0.8376	0.8728	4.04	0.6375	-	-	0.5766	0.5907	2.4
45°	1.062	0.9776	-8.63	0.6697	-	-	0.6103	0.6230	2.04
90°	0.8679	0.9021	3.79	0.6861	-	-	0.5796	0.5917	2.04

Table 3-3. Plastic anisotropy parameters for three materials.

Anisotropic parameters	F	G	H	L	M	N
DP1000	0.525	0.544	0.455	1.5	1.5	1.67
CP1200	0.567	0.610	0.389	1.5	1.5	1.37
Al7020	0.631	0.634	0.366	1.5	1.5	1.40

### III.2.2.2 In-Plane Torsion tests (IPT)

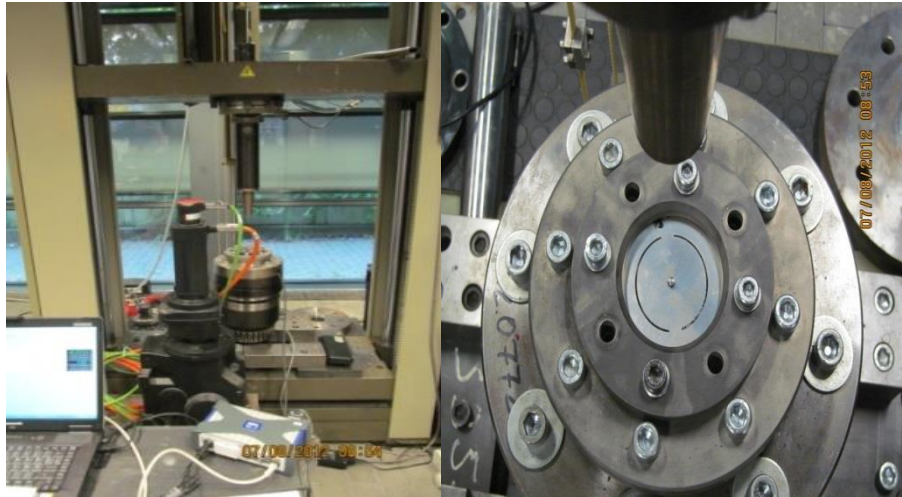


Fig. 3-9. Experimental setup for IPT tests (IUL/TUD).

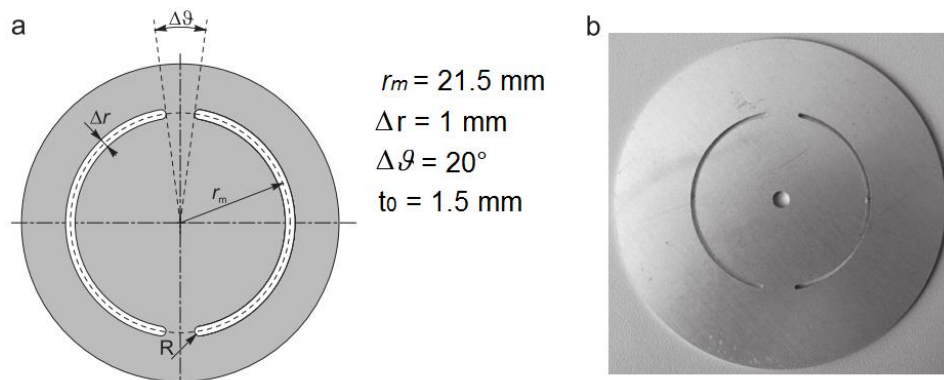


Fig. 3-10. Specimen geometry for IPT tests.

The IPT test is proposed to apply the cyclic loading in order to test the Bauschinger effects for

this sheets. Its experimental setup is shown in Fig. 3-9. The geometry of the used specimen is shown in Fig. 3-10 [Yin12, Yin14]. Two round slits are cut out of the specimen, thus the shear strain is localized in the two bridges when the outer grip is twisted in-plane against the inner grip. The clamping forces  $F_i$  and  $F_o$  are applied on the inner and outer clamps separately. Compared to the full specimens of other torsion tests, an averaging of the anisotropic behavior over the whole circumference can be avoided. By arranging two identical shear zones on opposite positions, the specimen can be twisted stably while the shear direction is the same relative to the rolling direction. The dimensions of IPT specimen is are given in Fig.3-10:

Also for each material, the test is conducted repetitively five times. The results in terms of moment versus torsion angle are shown in Fig.3-11.

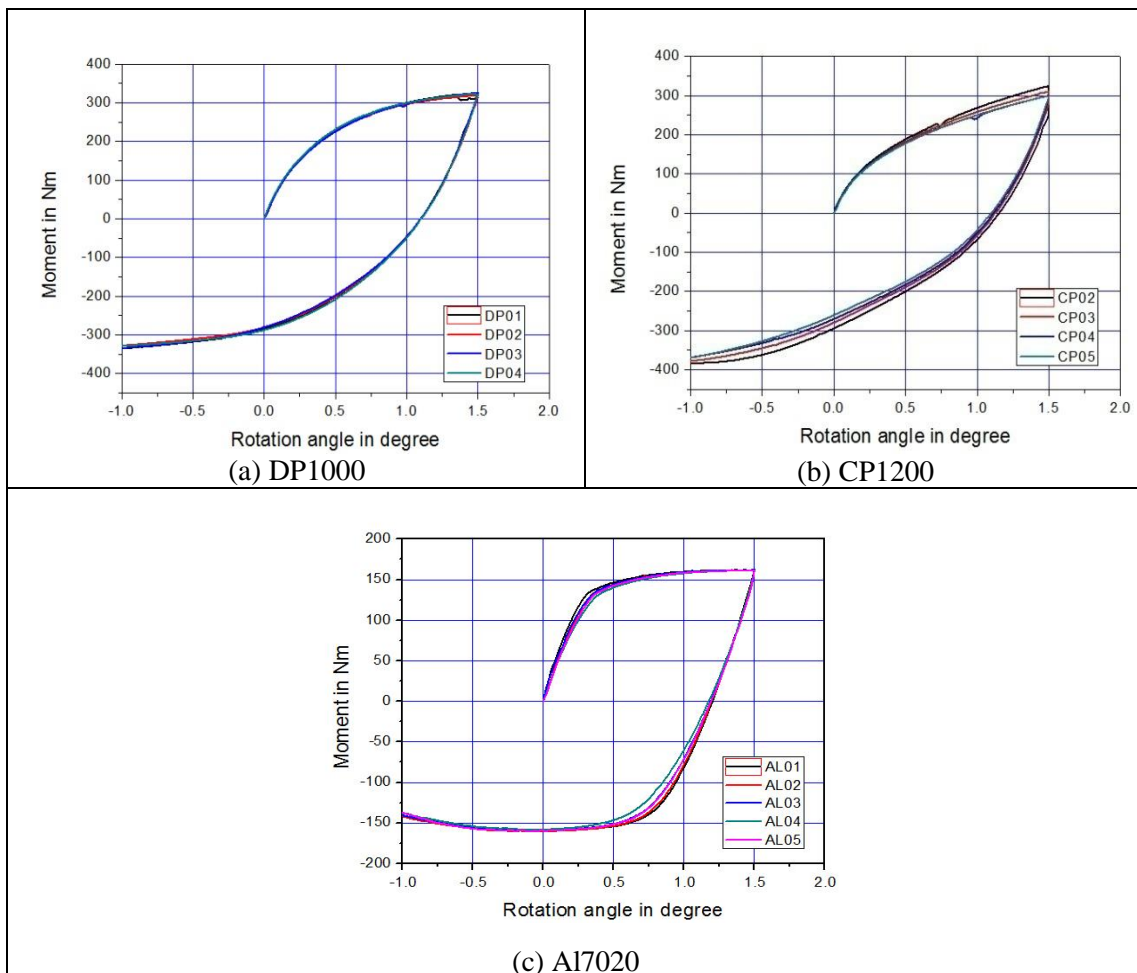


Fig. 3-11. IPT tests results for the three materials.

III.2.2.3 Pre-Notched Tension tests (PNT)

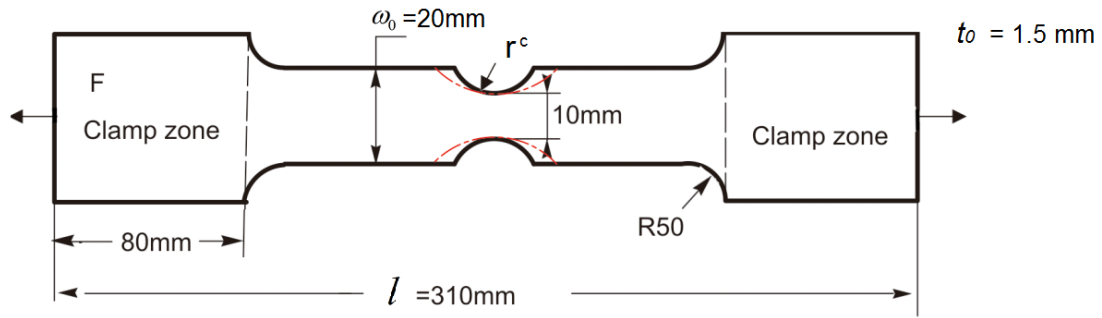


Fig. 3-12. Geometry of the notched specimen.

The PNT test is conducted on the universal Zwick 250 machine available in IUL/TUD. Test specimen geometry is shown in Fig. 3-12. Except the notched part, the whole geometry is similar to the UT tests specimens (Fig. 3-3). The notched radii of the specimen are 5.0 mm, 10.0 mm and 20.0 mm, which can help to create different tension loading conditions. The specimen is elongated until the final rupture at the constant velocity of 0.1 mm/s.

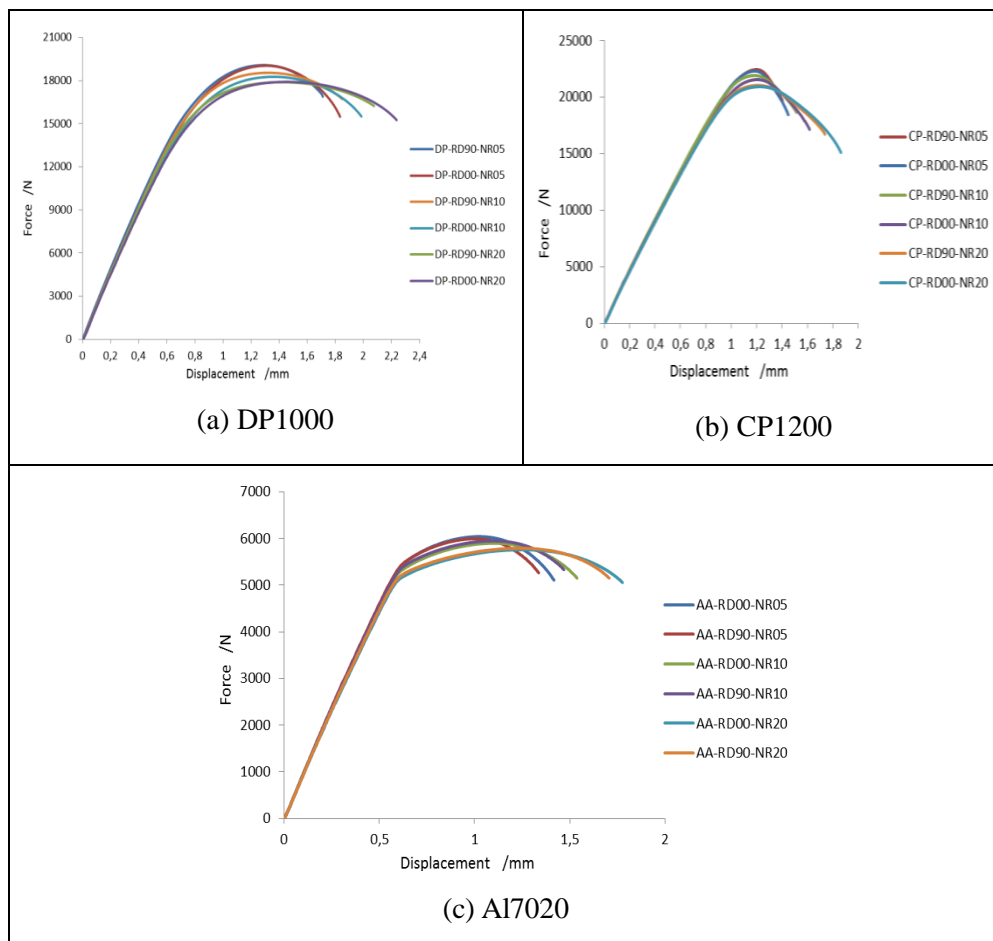


Fig. 3-13. Force-Displacement responses for PNT tests for the three materials.

The force-displacement curves obtained directly from Zwick machine are shown in Fig. 3-13 and the post-mortem of specimens is shown in Fig. 3-14. We remark that the displacements at the final fracture of the PNT specimens are smaller for the small notch radii. The fracture displacement for specimen with  $r^c = 20.0$  mm is higher than the one with  $r^c = 5.0$  mm. This is the well-known behavior of ductile fracture, called notch sensitivity of ductile materials. The trend is due to the different stress triaxiality ratios in the critical notched zone.

The post-mortem specimens are shown in Fig. 3-14, where the final shapes of the fracture surfaces are shown. For DP1000, the shear slip first appears at the center and extends to the notch edge by the different sides. Meanwhile, for CP1200 and Al7020, the shear slip keeps on the same sides of the crack.

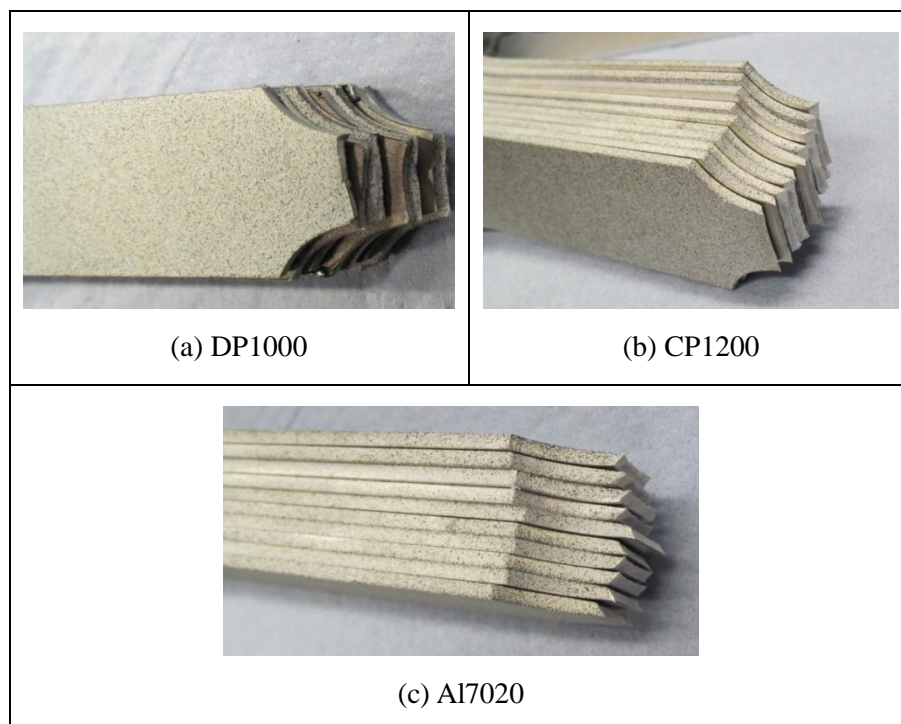


Fig. 3-14. Post-mortem of PNT tests after loading.

**Global force - local displacement response:** In order to avoid the testing machine stiffness effect, the digital image analysis system ARAMIS is used. It is one among very efficient tools to capture the displacement and strain distribution on the specimen surface by tracking the gray value patterns in small neighborhood during deformation. Fig. 3-15 shows an example of data dealing process in the tests. The digital system can accurately record the coordinates of each point on the captured pictures. The frequency of the picture acquisition is set to be 5.0 Hz, and pixel size is set to be 0.2 mm. Due to the loss of speckle pattern of the paint on the specimen boundaries, it is not possible to accurately keep track of evolution of the curvature

at the edges with deformation. The pixel points on the central line following loading direction, 1.0 mm and 4.0 mm ( $X_1 = 2.0$  mm and 8.0 mm, as shown in Fig. 3-15) away from the central line of cutting section are chosen as the reference coordinates.

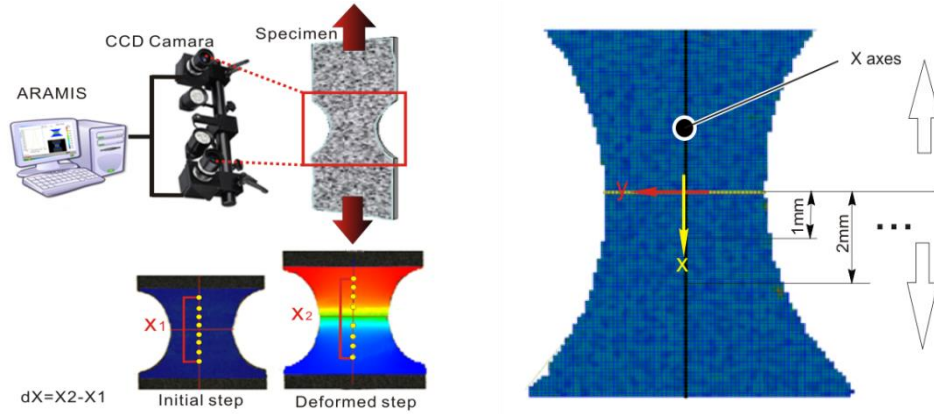
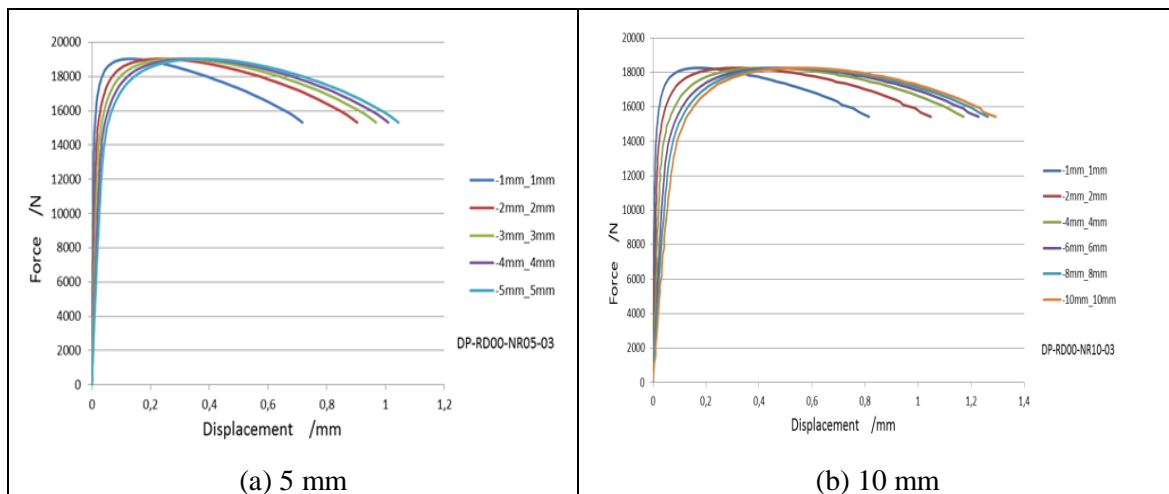


Fig. 3-15. Local gray chosen method by Aramis.

Table 3-4. Chosen local gray arrangement for different radius

Notched radius (mm)	Node position on the X axis (mm)								
5.0	1	2	3	4	5	6	-	-	-
10.0	1	2	-	4	-	6	-	8	10
20.0	1	2	-	4	-	6	-	8	10

The gray points are symmetric distributed on the  $x$  axes, and the position is determined according to the distance to the horizontal symmetric line of the notched area. The arrangement of the values is listed in Table 3-4. The curves of global force versus local gray point displacement are shown in Fig. 3-16, 3-17, 3-18, respectively for DP1000, CP1200 and AI7020.





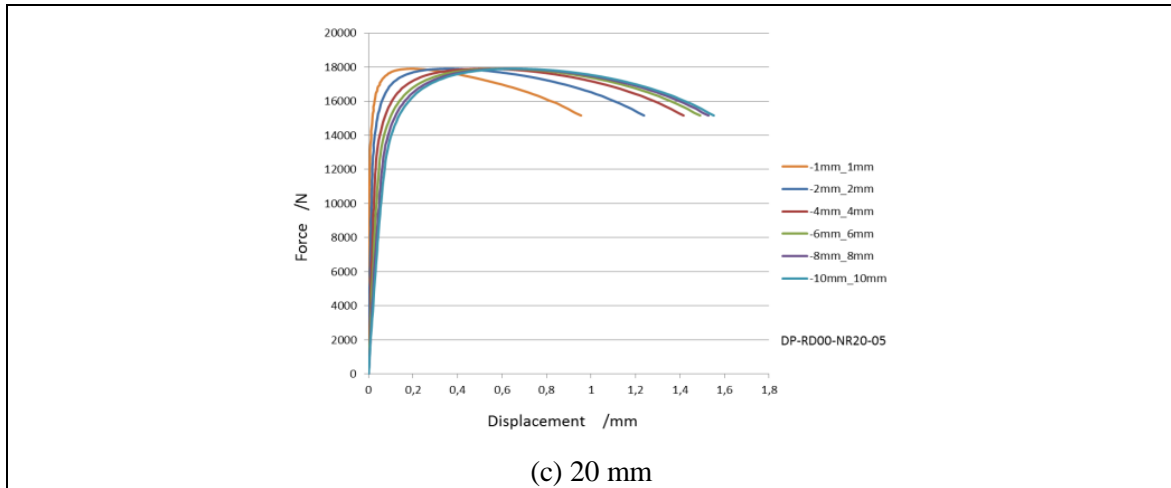


Fig. 3-16. Global force versus local displacement for DP1000.

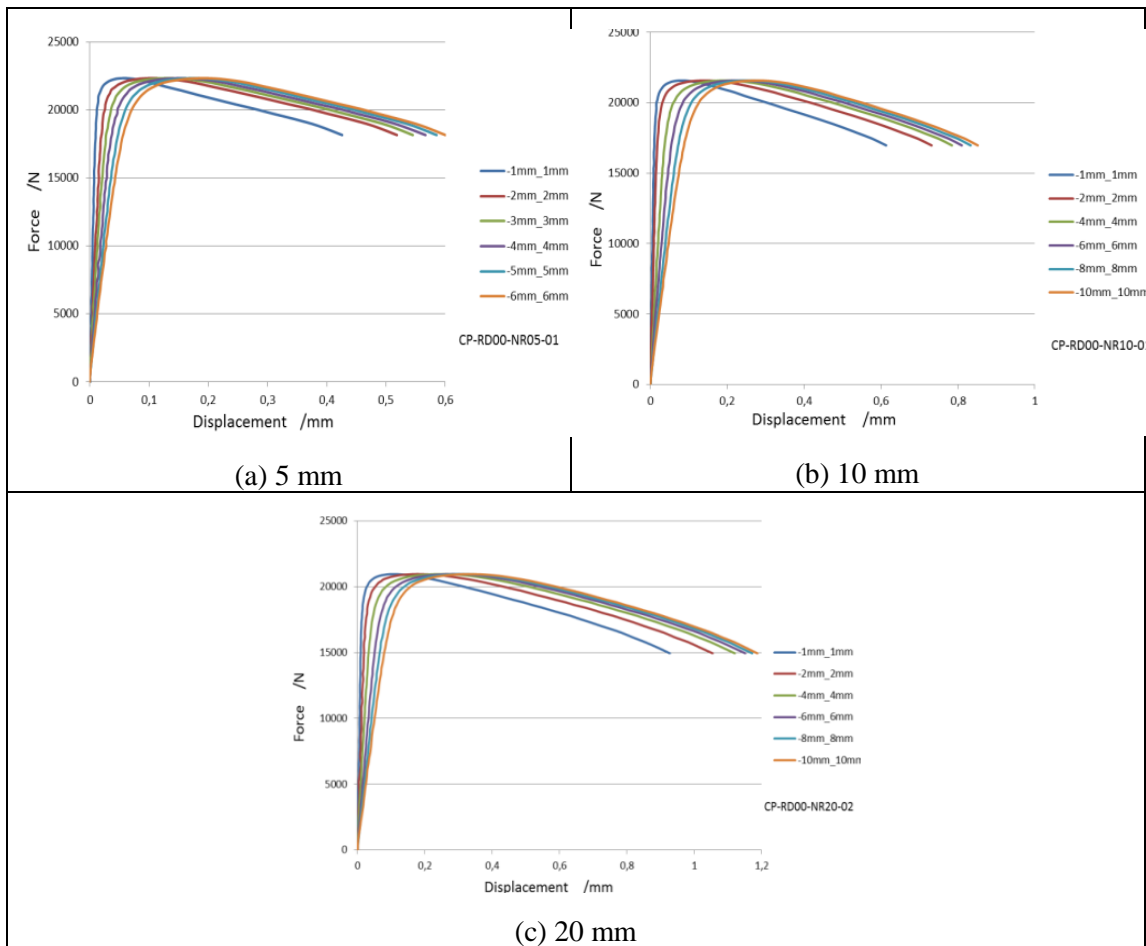


Fig. 3-17. Global force versus local displacement for CP1200.



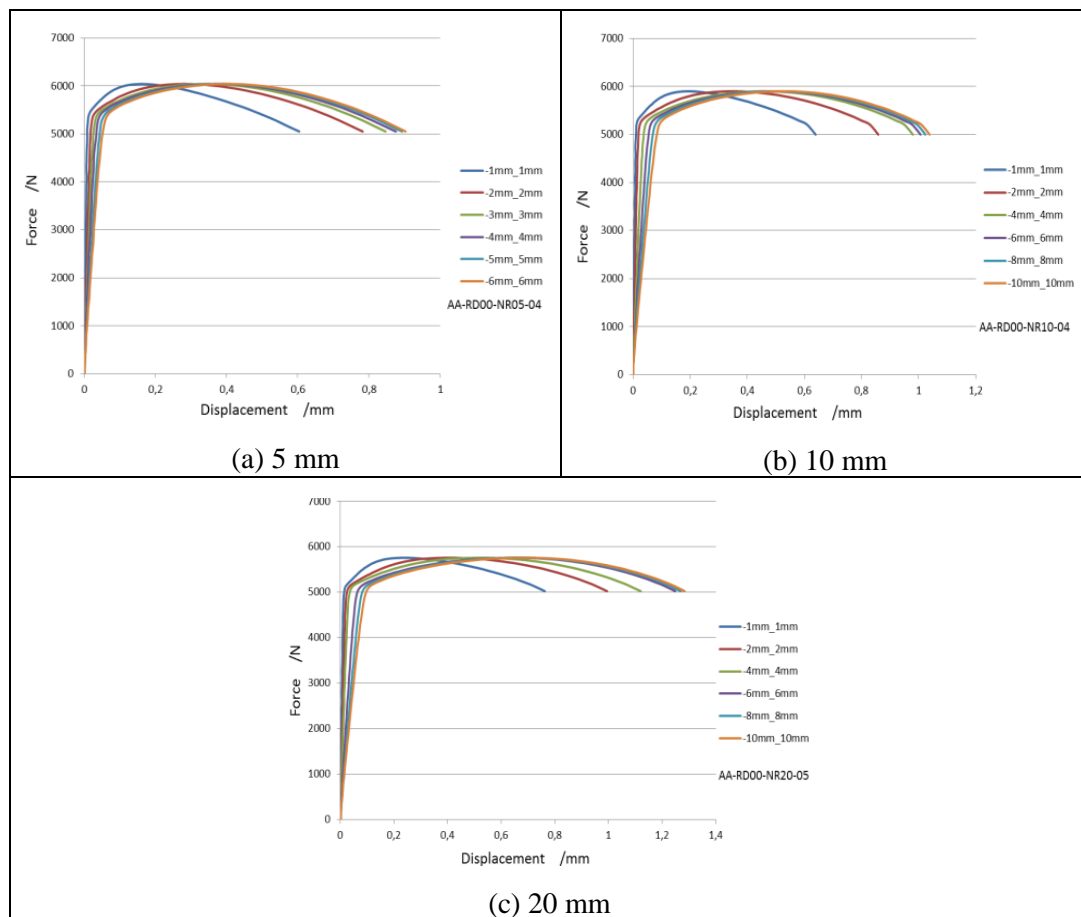


Fig. 3-18. Global force versus local displacement curves for A17020.

### III.2.2.4 Simple shear tests (SS)

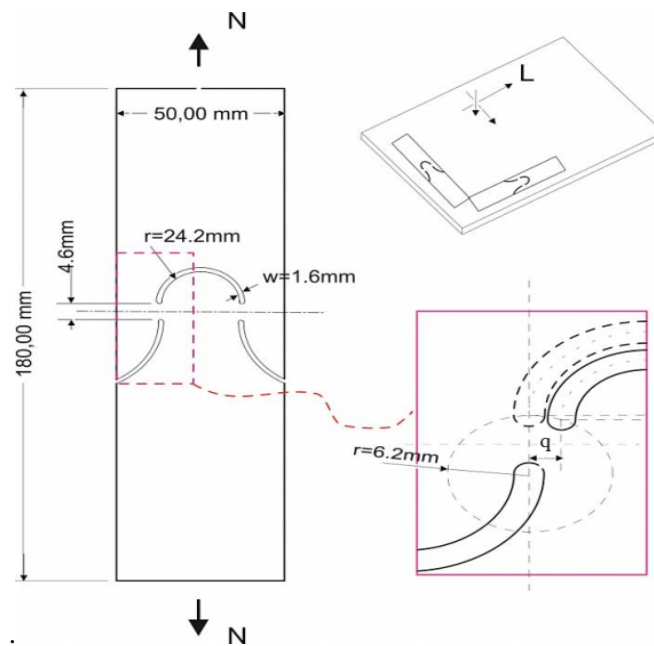


Fig. 3-19. Specimen geometry for simple shear (SS) tests.

The SS test is recently proposed by Shouler and Allwood [Shouler10]. There are double test zones which can efficiently avoid the torque caused by the load imbalance on each test zone (see Fig. 3-19). When  $q = 0.0$  mm, simple shear stress state is obtained in the critical zone. When  $q = 1.25$  mm and  $q = 2.5$  mm, and keeping the distance of the connection band constant, a combined tension and shear stress state is created. This test is also conducted on universal Zwick 250 machine available in IUL/TUD. The constant loading velocity is 0.1 mm/s. Each test is conducted five times to check the accuracy, and the average value is chosen as the experimental responses of each material. The results of the SS tests are presented in terms of force versus displacement, as shown in Fig. 3-20.

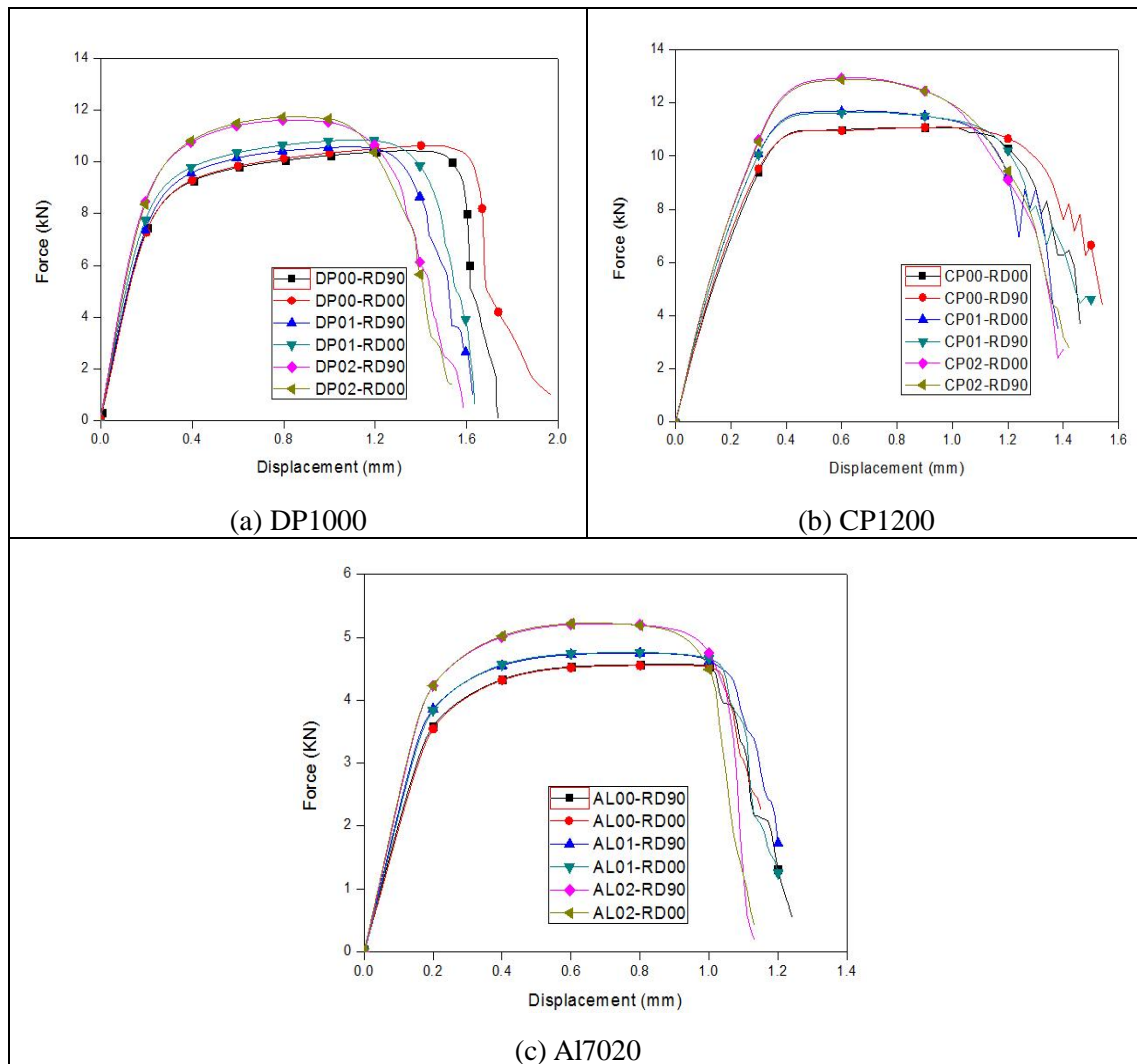


Fig. 3-20. Experimental results for SS tests for the three materials.

### III.2.2.5 Combined loading tests (CL)

To investigate the macroscopic behavior under complex loading paths, a most simple change of the deformation mode can be chosen, passing from a constant strain rate test (e.g. uniaxial

tensile test), to a different constant strain rate tensor (e.g. simple shear). Because the cross product of the two strain rates describing the imposed strain path changes is equal to zero, we can name the strain-path change as the Combined loading tests (CL). Here, the CL tests are conducted on one biaxial test equipment developed at the faculty of Engineering Technology at the University of Twente, named TWENTE BIAXIAL TESTER [Riel08]. Based on a Uniaxial testing device, a subframe is mounted on the device in order to accommodate the actuator for shear deformation. The geometry and scheme of the loading method were shown in Fig. 3-21. This developed device can be used to investigate the effects of strain path change on the mechanical response.

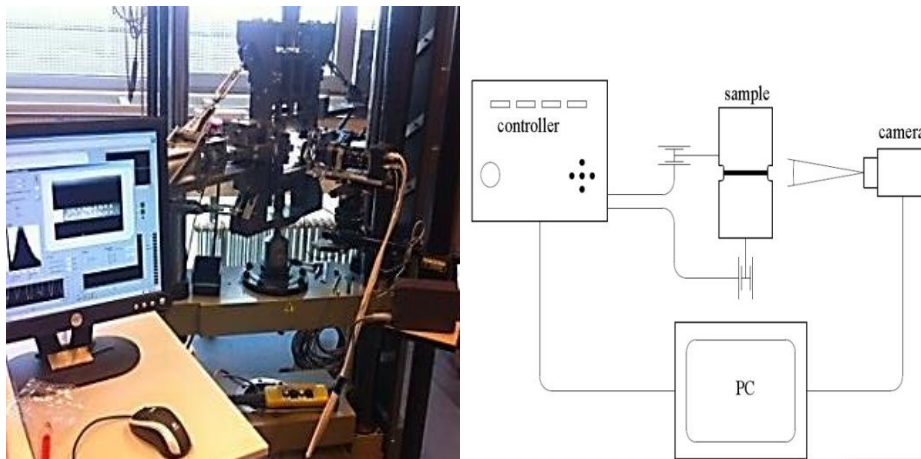


Fig. 3-21. Experimental setup for CL tests (AM/TWENTE)

There are two actuators respectively in vertical and horizontal directions which can be used to apply the tensile and shear loading on objective specimens. When tension loading is applied, a tensile stress state between the plane-strain tension and uniaxial tension stress state can be produced in the critical test zone.

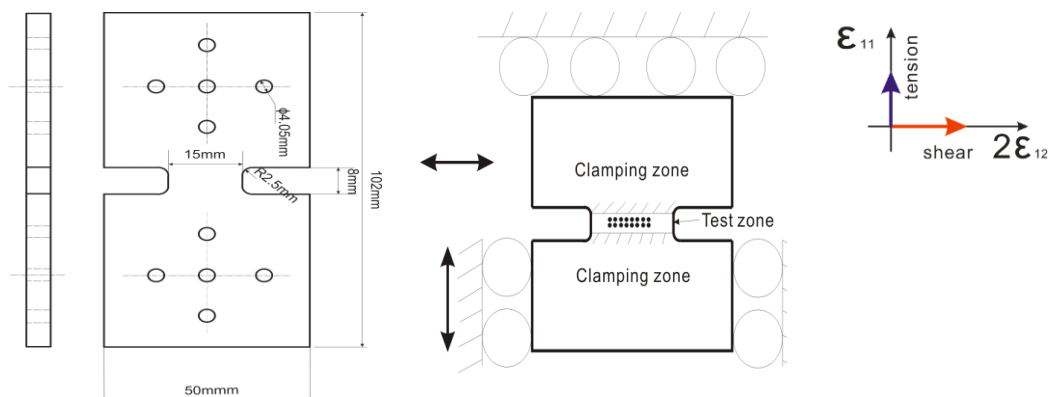


Fig. 3-22. Drawing of the specimen geometry and loading method for CL tests.

In the critical zone, in order to capture the small strain and enhance the accuracy of the

observation, the optical strain measurement is used. On the specimen, the tested critical zone is a rectangular zone of  $15 \times 3 \text{ mm}^2$ , and two rows of 8 dots are sprayed on the center of testing zone. The camera can capture the trace of the dot to be used for the strain calculation with average value of dots position information. The specimens are first loaded in monotonic tension and shear directions, the stress-strain curves are obtained according to the equations below, which is only suitable for small deformation and can cause some error when the strain reaches some big values. During test, loading velocity is kept constant around  $1.0 \text{ mm/min}$  to ensure the quasi-static deformation and avoid the strain rate effect on stress.

$$\varepsilon_{33} = -(\varepsilon_{11} + \varepsilon_{22}) \quad (3-10)$$

$$\varepsilon_{equ} = \sqrt{2/3(\underline{\varepsilon} : \underline{\varepsilon})} \quad (3-11)$$

$$\varepsilon_{equ}^{pl} = \varepsilon_{equ} - \frac{\sigma}{E} \quad \text{or} \quad \varepsilon_{equ}^{pl} = \varepsilon_{equ} - \frac{\tau}{G} \quad (3-12)$$

The deformation of the sample is reflected in the change of the coordinates of the dots (shown in Fig. 3-22). With the referred study, the error of the strain measurement is less than  $5 \cdot 10^{-4}$  [Riel08], so with this optical system, we can capture the elastic domain during tests. The stresses are calculated by:

$$\sigma_y = \frac{F_{yy}}{t \cdot \omega \cdot \exp(\varepsilon_{33})} \quad (3-13)$$

$$\tau = \frac{F_{xx}}{t \cdot \omega \cdot \exp(\varepsilon_{33})} \quad (3-14)$$

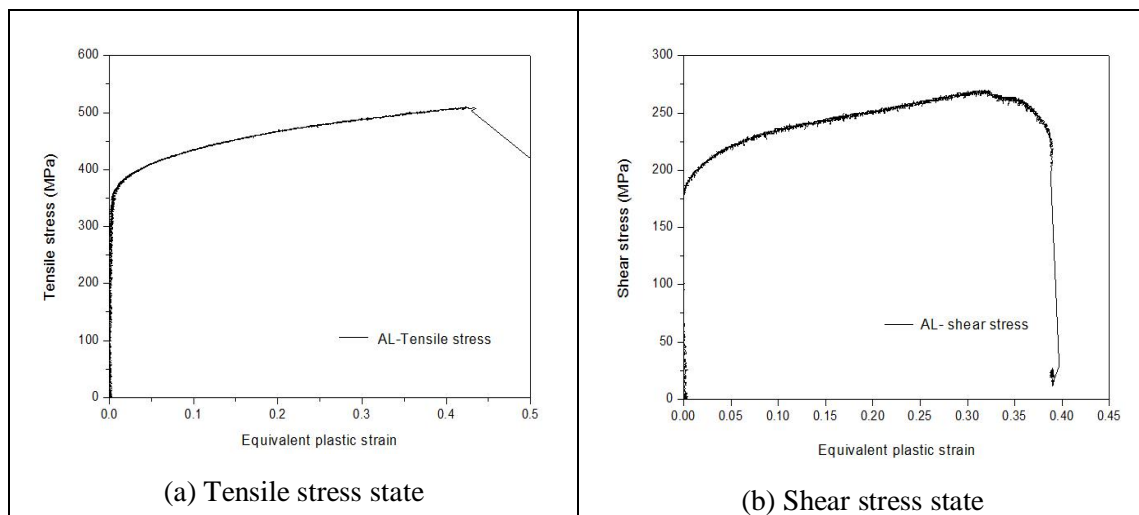


Fig.3-23. Stress-strain curves for monotonic loading paths for Al7020.

In order to test the deformation capability of the material under single loading direction, the monotonic loading test is conducted first. The stress-strain responses under tension and shear loading paths for Al7020 and DP1000 are given in (Fig.3-23 and Fig.3-24. Considering the less capability of deformation of CP1000, it will not be considered in this test (shown in Fig.3-25).

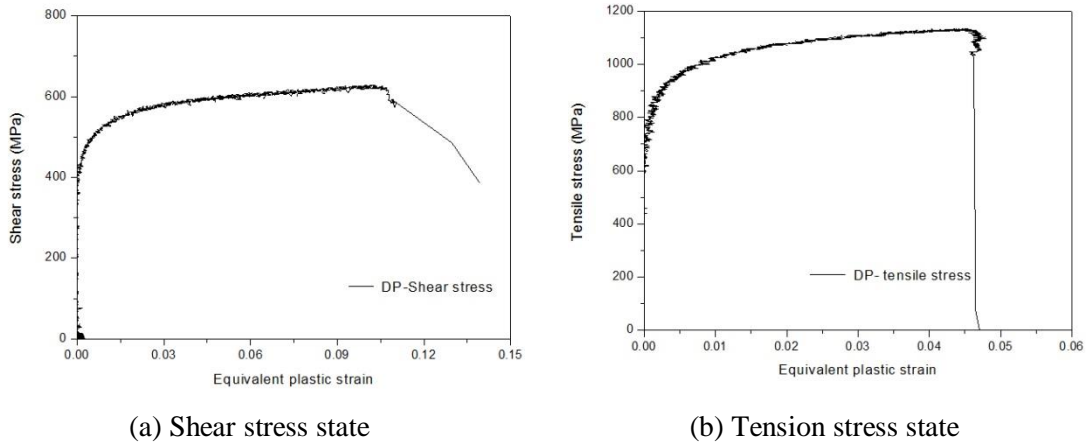


Fig.3-24. Monotonic stress-strain curves for DP1000

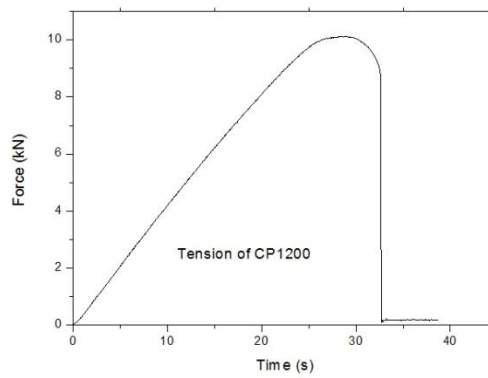


Fig.3-25. Monotonic force-time curve for CP1200.

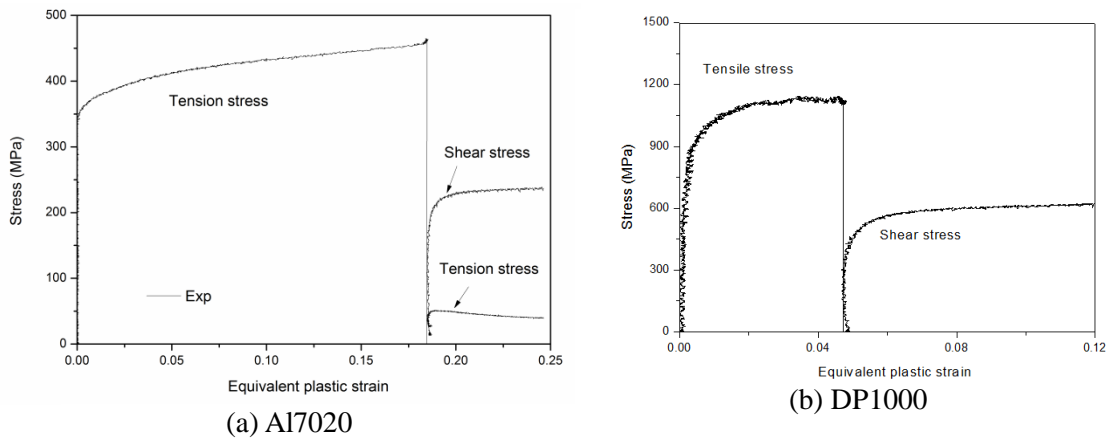


Fig. 3-26. Stress-strain curves for combined tension-shear for Al7020 and DP1000

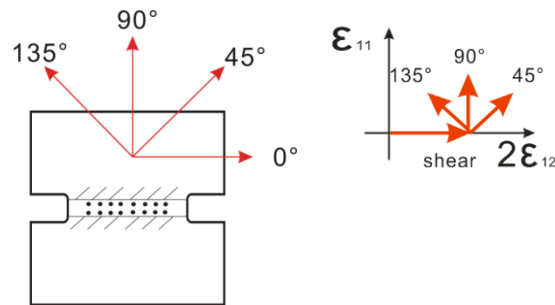


Fig. 3-27. Scheme of the loading directions

From the microstructure viewpoint, for monotonic loading test the material deforms from an initial microstructure free of organized patterns, and dislocations gradually arrange themselves into planar polarized dense dislocations boundaries, which are more or less parallel to the main slip system. This also can be called dislocation walls. The active slip systems will give great influence on the following deformation behavior, and explains the observed induced anisotropy. If a combined loading path is given after the pre-strain, like shear after tension or tension after shear. The effect of current slip system on the latent slip system is observed. As shown in Fig. 3-26, for Al7020, the subsequent shear hardening behavior after 18% pre-tension is given. For DP1000, the subsequent shear hardening behavior is observed after 4.8% pre-tension.

At the same time, the shear-tension loading tests are also conducted to investigate another kind of combined loading condition. After shear loading, three tension directions are given, 45°, 90° and 135° (shown in Fig.3-27). The subsequent tensile stress and shear stress components after pre-shear are shown in Fig.3-28 and Fig.3-29 for Al7020 and DP1000 separately. The materials exhibit more or less a relatively large and parabolic work hardening in the forward strain for tension load, while the shear load exhibit more linear transient work-hardening.

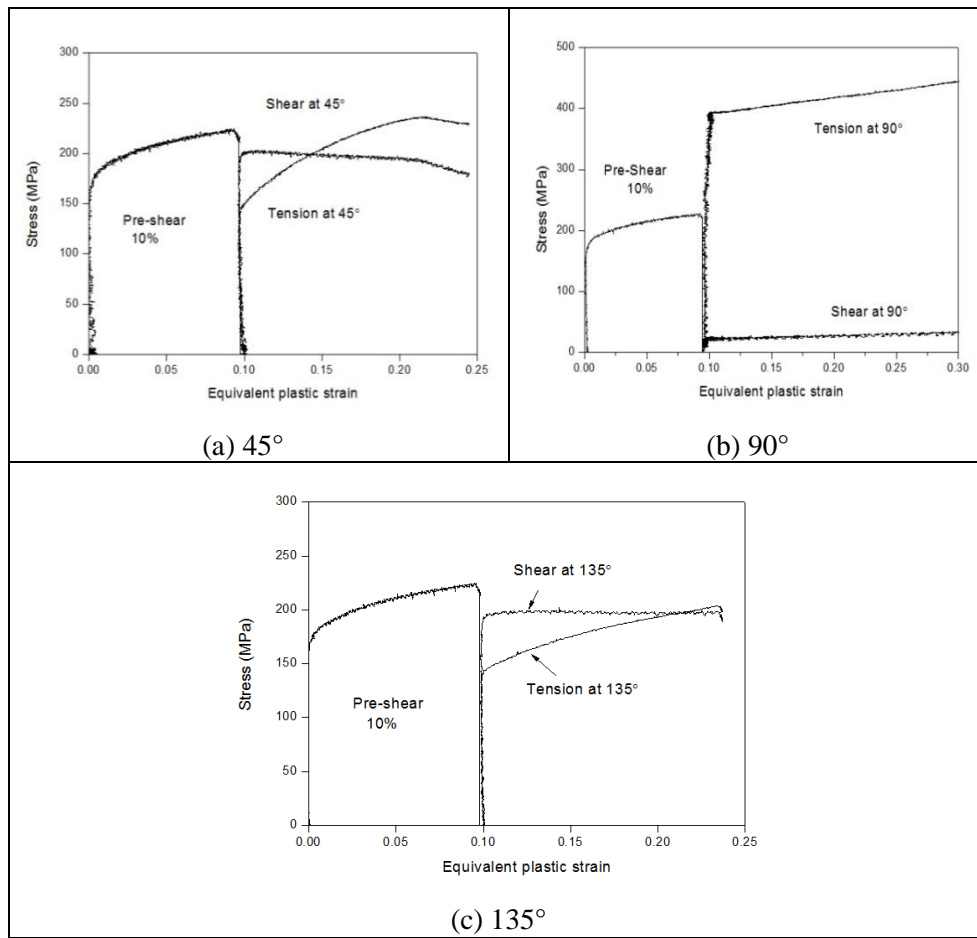


Fig. 3-28. Stress versus plastic strain curve after 10% pre-shear with respect to the different directions for Al7020.

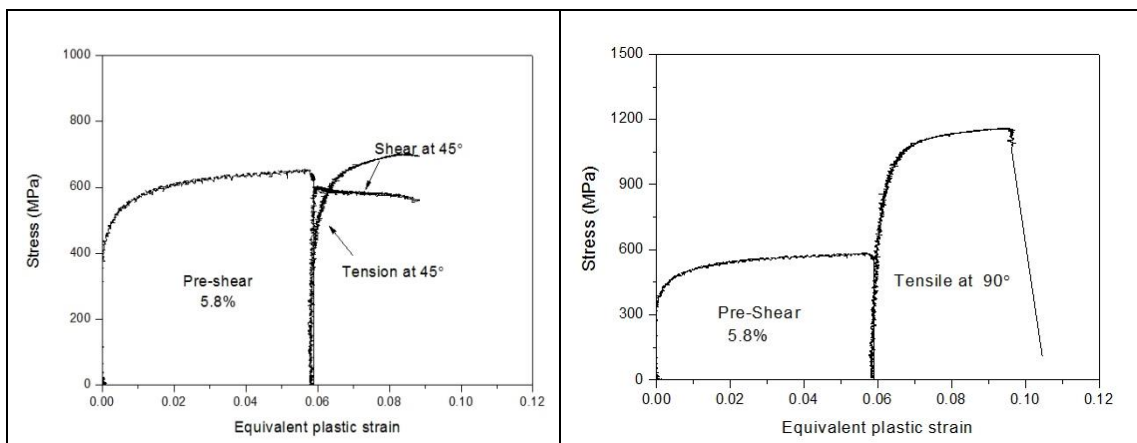


Fig. 3-29. Shear versus plastic strain after 10% pre-shear in form of equivalent stress and strain of DP1000.

### III.2.2.6 Nakazima tests (NAK)

Nakazima tests (NAK) are the most widely used tests to apply biaxial loading paths to sheet



metals. The load is applied by a hemisphere punch on metal blanks of different shapes till the final fracture. The forming limit diagram is obtained by conducting the hemispherical dome test based on the GB/T 15825.8-2008 standard (shown in Fig. 3-30). During the test, the optical measurement system ARAMIS is also used to measure the strain on the critical zone. Then the specimens should be placed between the die and blank holder and be pressed by blank holding force at room temperature. The middle part of the test piece will appear bulging deformation and form a convex hull under the action of the punch force. The punch velocity is set to be 1.5 mm/s and 0.3 mm thickness plastic layer is used as the test lubricant with assumed friction ratio of 0.05.



Fig. 3-30. Experimental setups for NAK tests (IUL/TUD).

The test specimens are prepared by varying the width of blanks (the radii of cutting circle are respectively 0.0 mm, 40.0 mm, 50.0 mm, 57.5 mm, 65.0 mm, 72.5 mm and 80.0 mm). The thickness of the sample is 1.5 mm. In order to obtain enough test data under different strain states, each geometry sample is conducted at least three times.

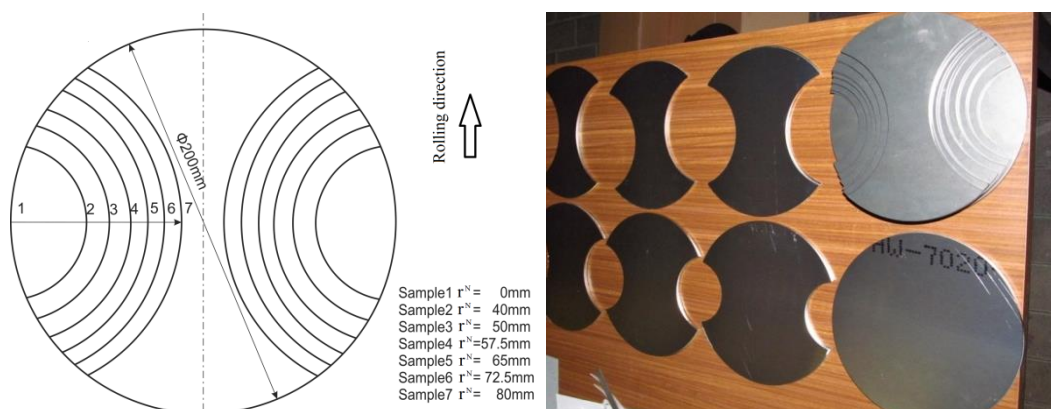


Fig. 3-31. Specimen geometry for NAK tests (IUL/TUD).





Fig. 3-32. Post-mortem of NAK after loading (IUL/TUD).

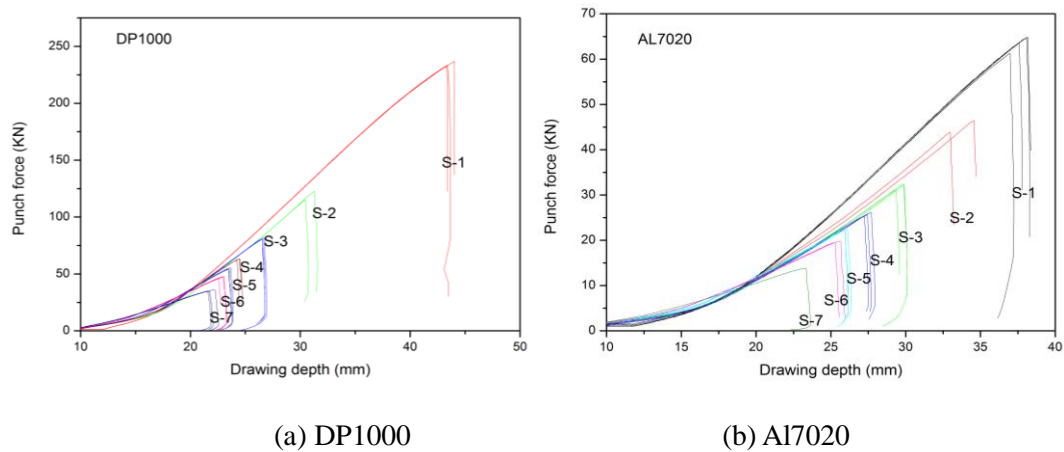


Fig. 3-33. Force-displacement curves obtained from Nakazima tests (IUL/TUD).

The force-displacement curves obtained from tests are shown in Fig.3-33. For a fast calculation of the points on the Forming Limit Curve, sometimes only the reference image pairs before applying the load and the last image pairs directly before the fracture occurs is evaluated. This guarantees that heavily loaded areas are captured and included into the FLC determination. With the ARAMIS software, some defined sections perpendicular to the break line should be given. From this section data (normally five parallel sections), a FLC point with its measuring deviation is calculated automatically according to the currently valid guidelines. For customized FLC calculations, this section data can be exported and processed using proprietary evaluation algorithms.

The characteristic values (theoretical maximum of major and minor strains) can be obtained with ARAMIS system by the computation of an ideal shape of the curve from the captured measuring values. The measuring points (major and minor strains) averaged from the different specimen geometries are now connected and thus allow for designing the Forming Limit Diagram of the currently tested material. The FLD curves and FFLD (critical strain plot for crack) are given, shown in Fig. 3-34. From the comparison of these two curves, we can

found the FFLD curves is higher than the FLD curves, which means the fracture points happen later than the necking points.

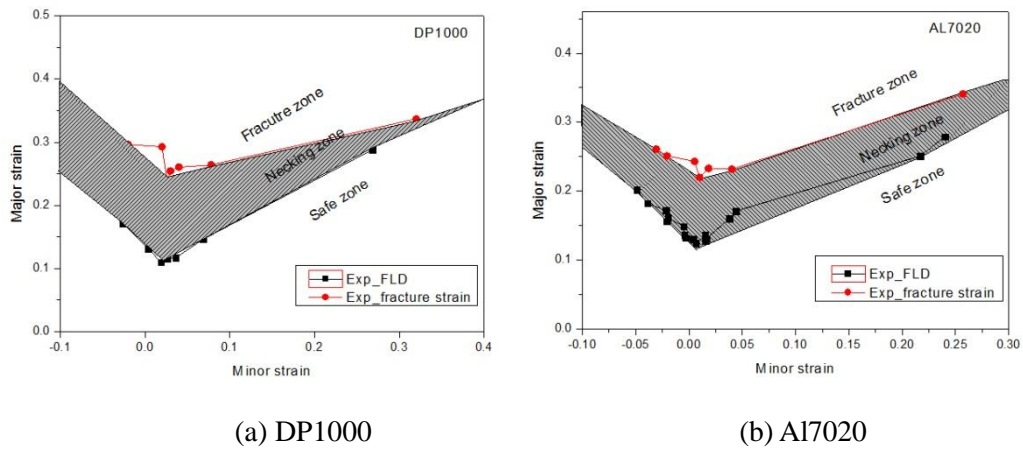


Fig. 3-34. FLD and FFLD curves obtained from Nakazima tests(IUL/TUD).

### III.2.2.7 Cross section deep-drawing tests (CSD)



Fig. 3-35. Experimental setup for cross-section deep drawing tests (IUL/TUD).

The cross section deep-drawing tests (CSD) are conducted in order to valid the deformation behavior of three test materials under complex loading paths. The experimental setup is shown in Fig. 3-35. Test velocity is 0.5 mm/s. A 0.1 mm thickness CHF oil layer is used as the lubricant. Blank holder force is 120 KN for Al7020, and 400 KN is chosen for DP1000 and CP1200 for their higher strength.

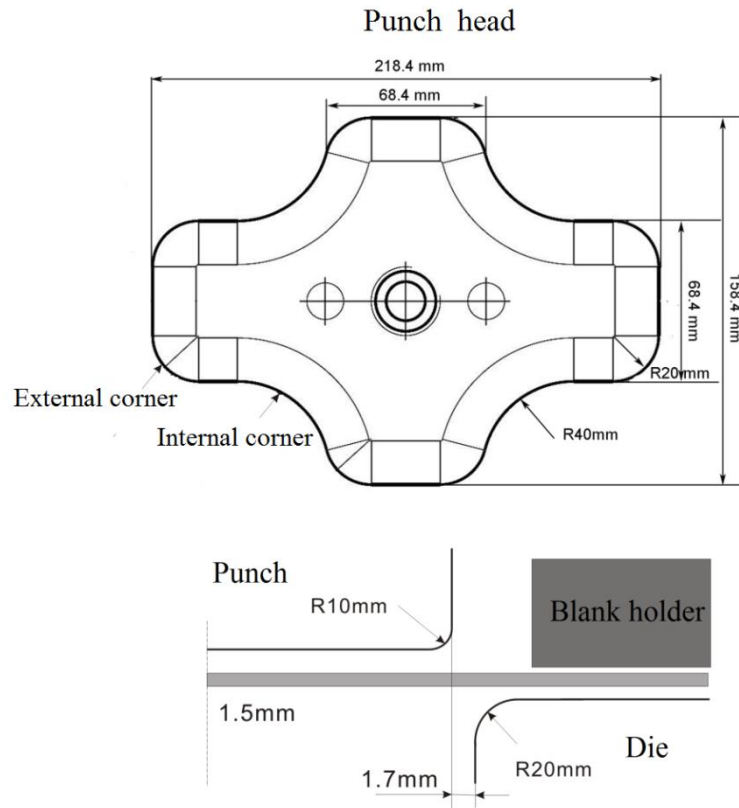


Fig. 3-36. Schematic diagram of the deep-drawing process.

In the CSD testing device, the specimen is clamped between the die and the blank-holder (shown in Fig. 3-36). A cross-section punch with different widths in horizontal and vertical directions is centrally moved downwards with prescribed low velocity. Thereby the vertical displacement of the punch and the acting force are measured.

These tests are conducted at least five times, in order to capture the initial fracture points and investigate the crack propagation. As shown in fig. 3-37, the profiles of the specimens with initial and developed cracks are observed. In fig. 3-38, the force-displacement curves for the tests which are conducted until fracture are given.



(a) DP1000



(b) Al7020



(c) CP1200

Fig. 3-37. Experimental failure examples for CSD specimens after testing (IUL/TUD).

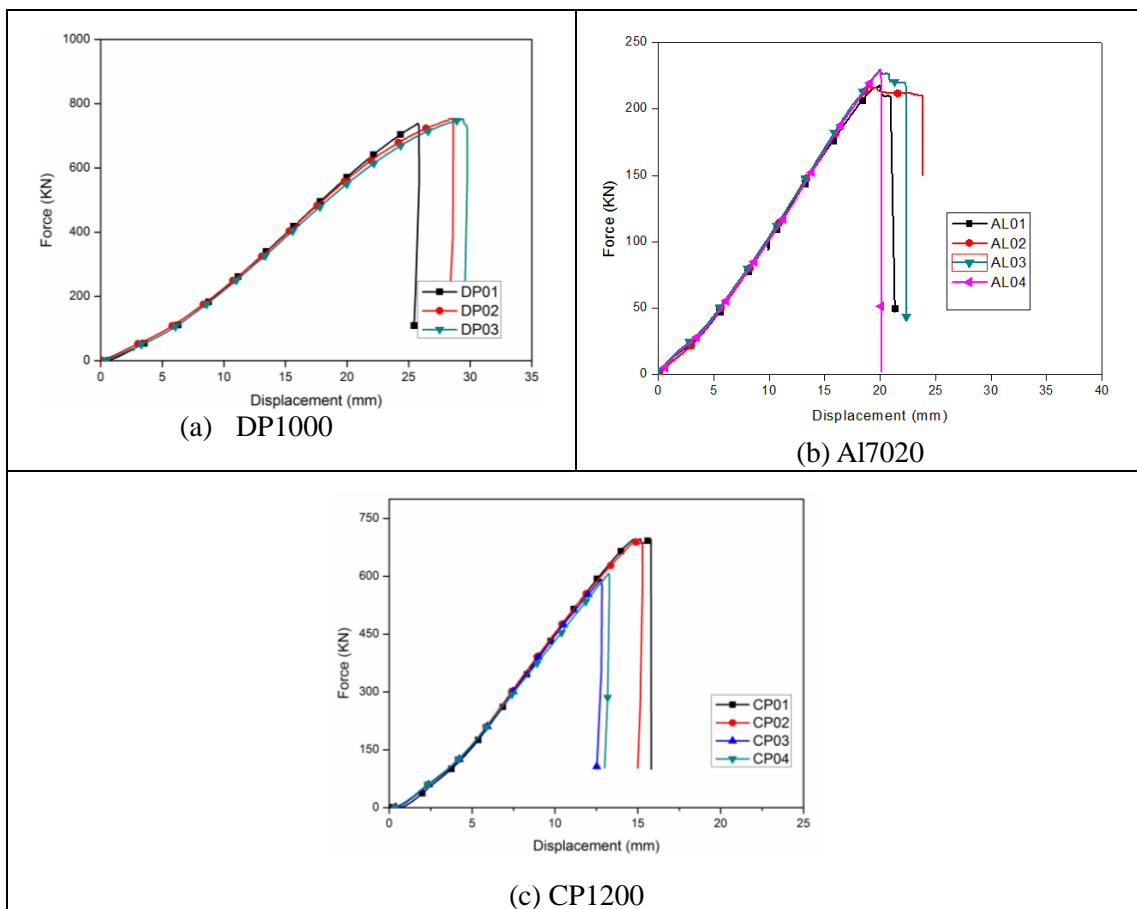


Fig. 3-38. Force-Displacement curves of Deep-drawing tests for three materials.

All these experimental results will be used in the next chapter (Chapter IV) for the identification and validation purposes.

### **III.3 Parametric study of the proposed fully coupled CDM models**

As shown in Chapter I, The proposed constitutive equations are characterized by a given number of material parameters which need to be determined for each material based on appropriate experimental data. Evaluating accurately and efficiently these material parameters which govern the mechanical constitutive equations are essential for the design of structural components. The determination of the values of these parameters for a given material is not an easy task. Before determining the parameters entering the constitutive equations, a study about the sensitivity of the parameters effect on the macroscopic behavior should be carried out, which can help users to well understand the model. The detailed study of the effect of the material parameters entering the fully coupled constitutive equations is given in [Saanouni12]. Moreover, here we will focus on the effect of the parameters related to (i) the microcracks closure  $h$  under the compressive stage of the loading path; (ii) to the distortional hardening; and (iii) to the effect of Lode angle on the predicted material ductility.

#### **III.3.1 Microcracks closure effects**

Note that the use of the total energy release rate given by equations Equation (1-70, 1-74) in the damage evolution equation (see Equation (1-84)) leads to a contribution of the elastic as well as the hardening parts in the damage energy release rate. It is important to highlight that the microcracks closure effect is only applied to the elastic part of the damage energy release rate.

In Fig. 3-39 the microcracks closure effect on the ductility, here given as the equivalent plastic strain at fracture, comparing both elastic and total energy in the damage evolution, is depicted. This Figure describes the evolution of the ductility (i.e. equivalent plastic strain before final failure  $d=0.9$ ) with respect to the triaxiality ratio obtained with the material parameters given in Table 4-2 and Table 4-4 in chapter IV. From this Figure, the ductility increases for negative triaxiality when  $h < 1.0$  i.e. when the microcracks closure effect is accounted for. This increase is more important when considering only the elastic part of the damage energy release rate, for which it is observed that the ductility tends to infinity for the

triaxiality values below  $-1/3$ , i.e. uniaxial compression, for the case  $h=0.0$ . This strong increase of the material ductility seems meaningless. However, when the contribution of the hardening in the damage energy release rate is taken into account, this increase is much less lower i.e. around  $\varepsilon_{eq}^p \cong 50\%$  for  $h=0.0$  and  $\varepsilon_{eq}^p \cong 42\%$  for  $h=0.5$  at the point of fracture. Note that in the original Lemaitre's damage model, which uses only the elastic part  $Y^e$  of the energy release rate as the damage driving force,  $h=0.2$  is suggested for metallic materials leading to a ductility higher than 100%.

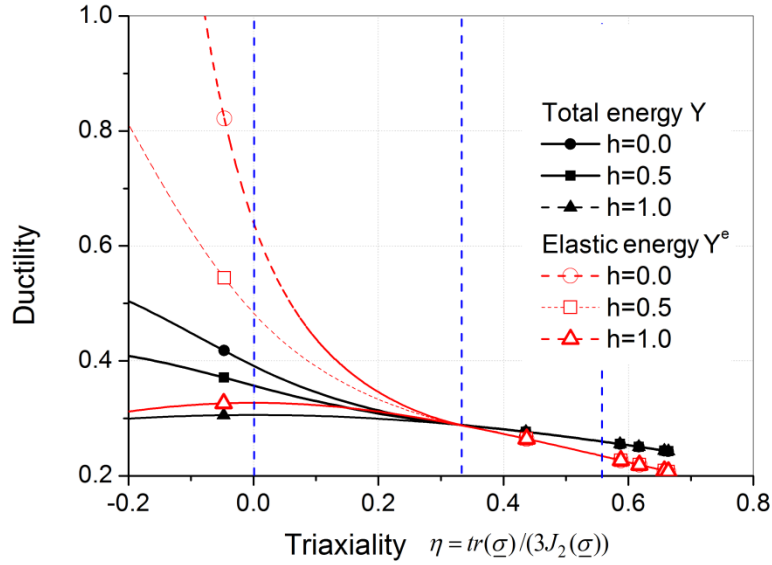


Fig. 3-39. Effect of the microcracks closure parameter  $h$  on the variation of plastic equivalent strain for DP1000 at final rupture ( $d=0.9$ ) versus the triaxiality ratio.

### III.3.2 Distortional parameters effects on the yield surfaces

To examine the effect of the distortion parameters ( $X_{11}^c$ ,  $X_{11}^p$  and  $X_{12}$ ) on the response of the proposed fully coupled model, we consider an initially isotropic material defined by the parameters shown in Table 3-5. Different proportional and non-proportional loading paths are considered with 5.0% total strain amplitude: cyclic tension, cyclic shear, combined cyclic tension and shear, sequential non-proportional square form of tension-shear and non-proportional elliptic form of tension-shear. For the cases of proportional loadings we will consider associative normality with  $X_{11}^c = X_{11}^p = X_{11}$ . However, for non-proportional loadings we will consider some non-associative cases for which  $X_{11}^c \neq X_{11}^p$ . Note that when  $X_{11}^c = X_{11}^p = X_{12} = \infty$  (larger than  $10^4$ ), the influence of the distortion of the yield surface is ignored and the current fully coupled CDM model proposed in this study will become the

classical fully coupled ductile damage model proposed in [Badreddine10].

Table 3-5 Assumed Model parameters

E (GPa)	$\nu$	$\sigma_y$ (MPa)	$F$	$G$	$H$	$L$	$M$
72.	0.3	70.	1.5	1.5	1.5	0.5	0.5
$N$	$C$ (MPa)	$a$	$Q$ (MPa)	$b$			
0.5	3080.0	56.2	158.0	7.0			

The Fig. 3-40 compares the initial yield surface without distortion to the yield surfaces after 5% of  $\varepsilon_{eq}^p$  in different stress spaces, respectively the deviatoric plane ( $\pi$ -plane), the principal stresses plane ( $\sigma_1, \sigma_2$ ) and the tension – shear plane ( $\frac{3}{2}\underline{e}_1 : \underline{\sigma}, \sqrt{3}\underline{e}_4 : \underline{\sigma}$ ). Note that every symmetric stress tensor can be expressed as a six-dimensional unit tensor in the following cases:

$$\underline{e}_1 = \frac{1}{\sqrt{6}} \begin{bmatrix} 2 & 0 & 0 \\ 0 & -1 & 0 \\ 0 & 0 & -1 \end{bmatrix}, \underline{e}_2 = \frac{1}{\sqrt{6}} \begin{bmatrix} -1 & 0 & 0 \\ 0 & 2 & 0 \\ 0 & 0 & -1 \end{bmatrix}, \underline{e}_3 = \frac{1}{\sqrt{6}} \begin{bmatrix} -1 & 0 & 0 \\ 0 & -1 & 0 \\ 0 & 0 & 2 \end{bmatrix}, \underline{e}_4 = \frac{1}{\sqrt{2}} \begin{bmatrix} 0 & 1 & 0 \\ -1 & 0 & 0 \\ 0 & 0 & 0 \end{bmatrix}, \underline{e}_4^\perp = \frac{1}{\sqrt{2}} \begin{bmatrix} 0 & 0 & 0 \\ 0 & -1 & 0 \\ 0 & 0 & 1 \end{bmatrix} \quad (3-15)$$

In the deviatoric plane ( $\pi$ -plane) the influences of the parameters  $X_{11}^c$  and  $X_{12}$  are investigated separately shown in Fig.3-40a and Fig.3-40b. Through the variation of the distortion parameter  $X_{11}^c$ , with maximum value 400 and minimum value 30, it is found that the parameter  $X_{11}^c$  controls the distortional ratio of the yield surface, but does not change the size of the yield surface. The distortional ratio is increased by decreasing the value of  $X_{11}^c$  (shown in Fig.3-40a). It is worth remarking that when  $X_{11}^c$  reaches the value less than the saturation value of the kinematic hardening that will cause losing of the yield surfaces convexity.

Fig.3-40b gives the demonstration of the effect of the parameter. Through the variation of parameter  $X_{12}$ , with maximum value 1000 and minimum value 200 (all are positive values), and it shows that  $X_{12}$  controls the cross size of the yield surfaces orthogonal to the loading direction, and the decreasing value of  $X_{12}$  gives increasing extend of the yield surfaces. It is should be remarked that the introduce of  $X_{12}$  affects the influence of  $X_{11}^c$ , which means the distortion ratio of the yield surface increases and also can cause losing of the yield surfaces convexity when absolute value of  $X_{12}$  is too small.

Fig.3-40c and Fig.3-40d show the effects of  $X_{11}^c$  and  $X_{12}$  in the principal stresses plane ( $\sigma_1, \sigma_2$ ), whose initial shape of the yield surface is not a circle but an ellipse. The similar features about the contribution of  $X_{11}^c$  and  $X_{12}$  are found. It should be remarked that when



the value of  $X_{12}$  is negative, the yield surface is compressed in the direction orthogonal to the loading direction. In Fig.3-40e and Fig.3-40f, the effects of  $X_{11}^c$  and  $X_{12}$  in the tension – shear plane ( $\frac{3}{2}\underline{e}_1 : \underline{\sigma}, \sqrt{3}\underline{e}_4 : \underline{\sigma}$ ) are given, which shows exactly the same results with in the deviatoric plane.

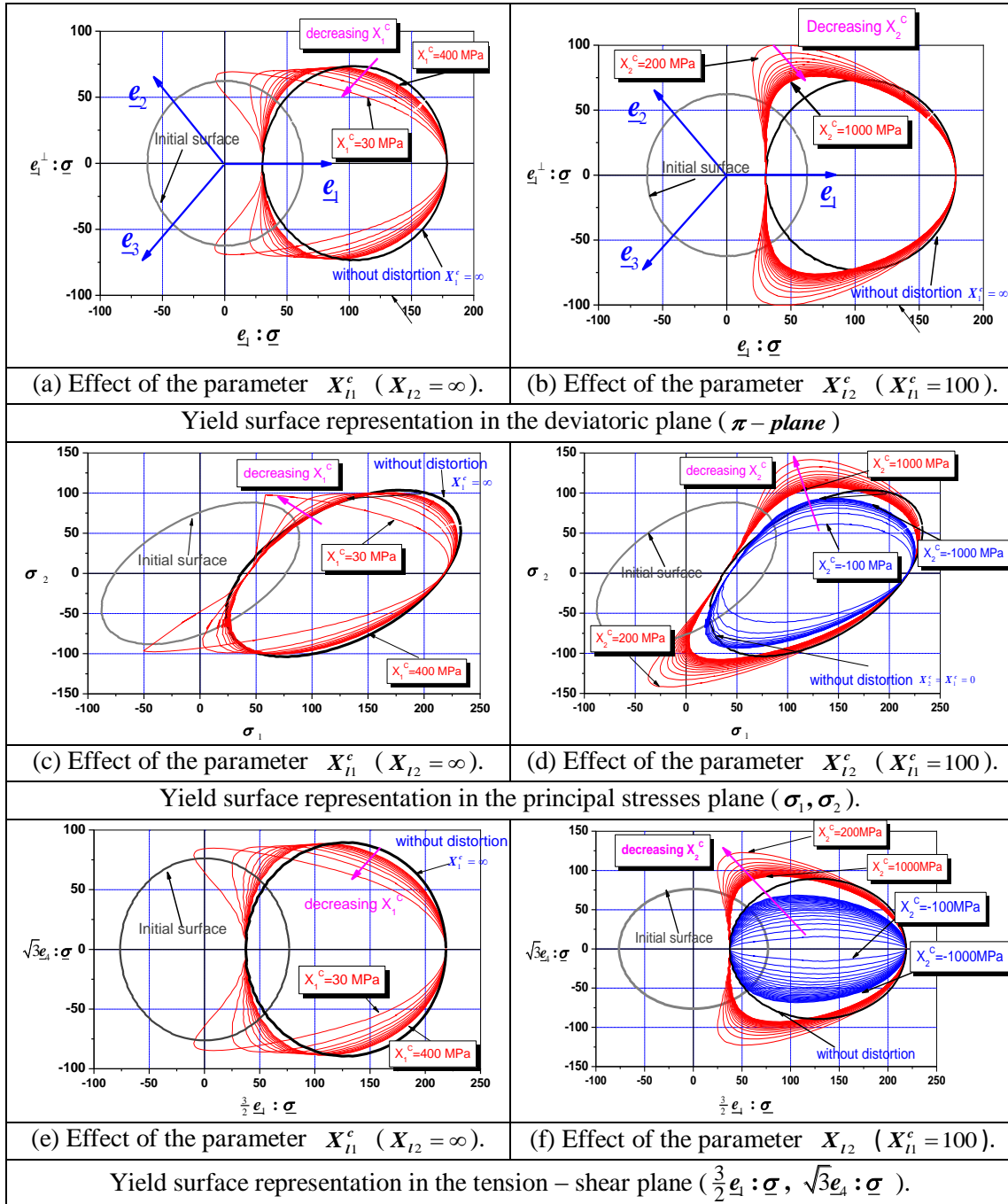
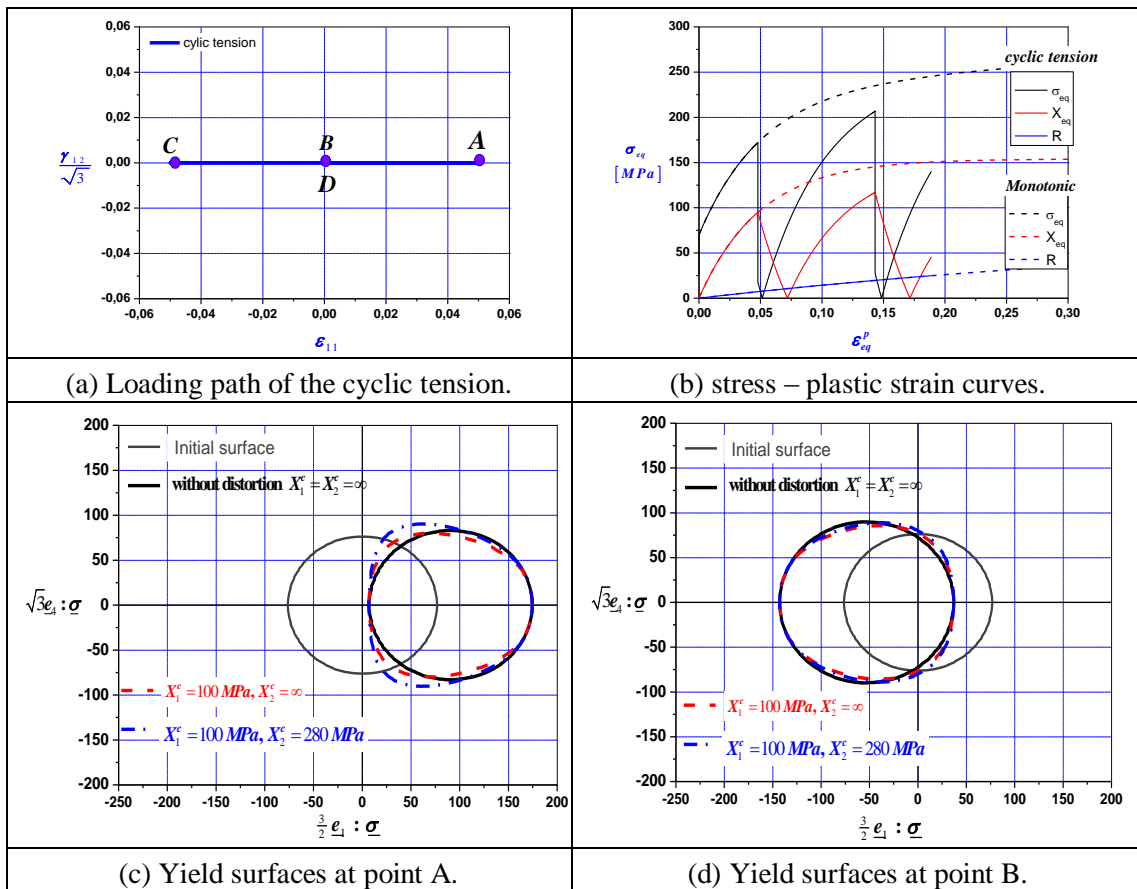


Fig. 3-40. Yield surface representation in different stress spaces: effect of the distortion parameters  $X_{11}^c$  and  $X_{12}$ .

Fig. 3-41 gives the simulation responses under cyclic tension loading condition. Fig.3-41a



gives the scheme of the loading path. Through the strain step control, a tension loading is applied until  $\varepsilon_{11}$  reaches 5.0%, and then an opposite compression is applied until  $\varepsilon_{11}$  reaches -5.0%, at last  $\varepsilon_{11}$  returns back to 0.0. During these processes, different distortional values are assigned to  $X_{11}^c$ ,  $X_{11}^p$  and  $X_{12}$  to see their different influences of the simulation results through the stress-strain curves and yield surface evolutions. In Fig.4-41b the stress-strain curves about Cauchy stress  $\sigma_{eq}$ , equivalent kinematic hardening  $X_{eq}$  and isotropic hardening  $R$  are given, in which their responses under monotonic and cyclic tension loading paths are compared. Fig. 4-41c gives the yield surfaces evolution at point A (first tension stage). The yield surfaces with different distortion parameters values are compared with initial yield surface. The conditions with  $X_{11}^c = 100$  and  $X_{12} = 280$ ,  $X_{11}^c = 100$  and  $X_{12} = \infty$  and  $X_{11}^c = X_{12} = \infty$  are discussed. As we can see that the centers and the front points following the loading direction of the yield surfaces under the conditions above are the same regardless of the values of  $X_{11}^c$  and  $X_{12}$ . These same results have been found in other stages, separately shown in Fig. 4-41d, Fig. 4-41e and Fig. 4-41f. So we can remark that the distortion of the yield surfaces does not affect the stress responses under cyclic tension loading paths.



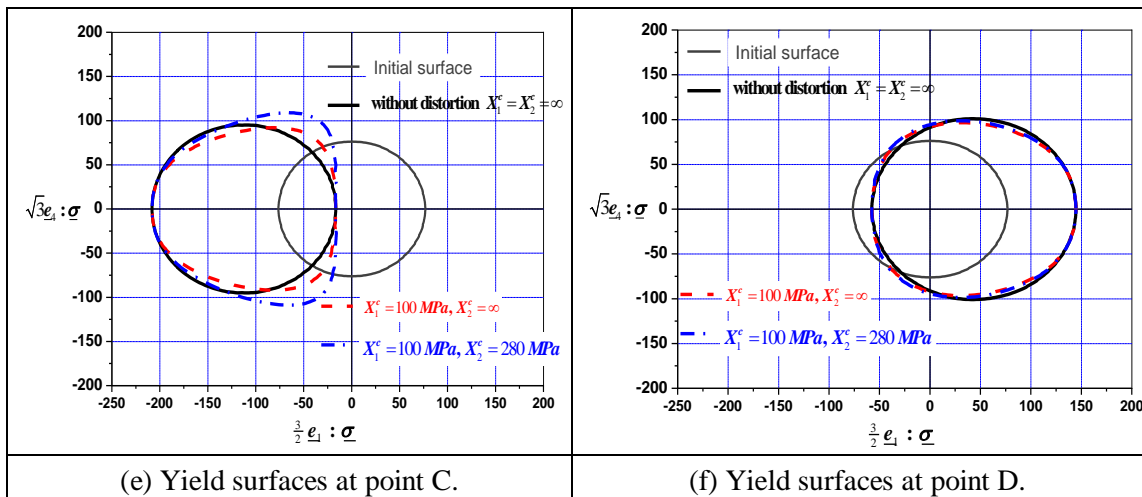
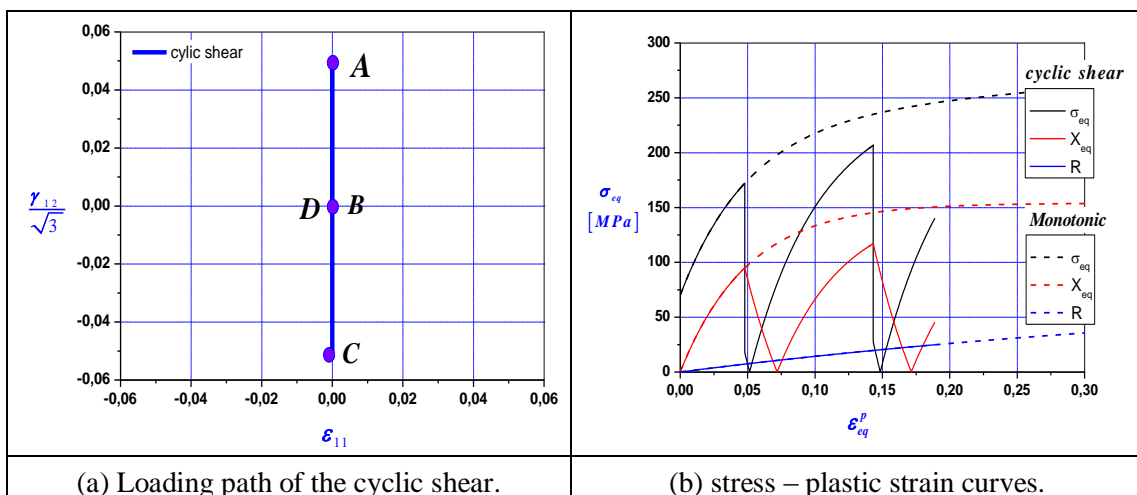


Fig. 3-41. Results of cyclic tension

The numerically predicted responses for the cyclic shear loading tests are shown in Fig. 3-42. Fig.3-32a gives the scheme of the loading paths of the cyclic shear loading. In Fig. 3-42b the Cauchy stress  $\sigma_{eq}$ , equivalent kinematic hardening  $X_{eq}$  and isotropic hardening  $R$  under monotonic and cyclic shear loading paths are compared. In other figures (Fig.3-42c for Point A, Fig.3-42d for Point B, Fig.3-42e for Point C and Fig.3-42f for Point D) the distorted yield surfaces are compared with the initial yield surface. Similar to the cyclic tension loading, the center and the front point following the loading direction of the yield surfaces are the same regardless of the values of  $X_{11}^c$  and  $X_{12}^c$ . So we can remark that the distortion of the yield surfaces does not affect the stress responses under cyclic shear loading paths.



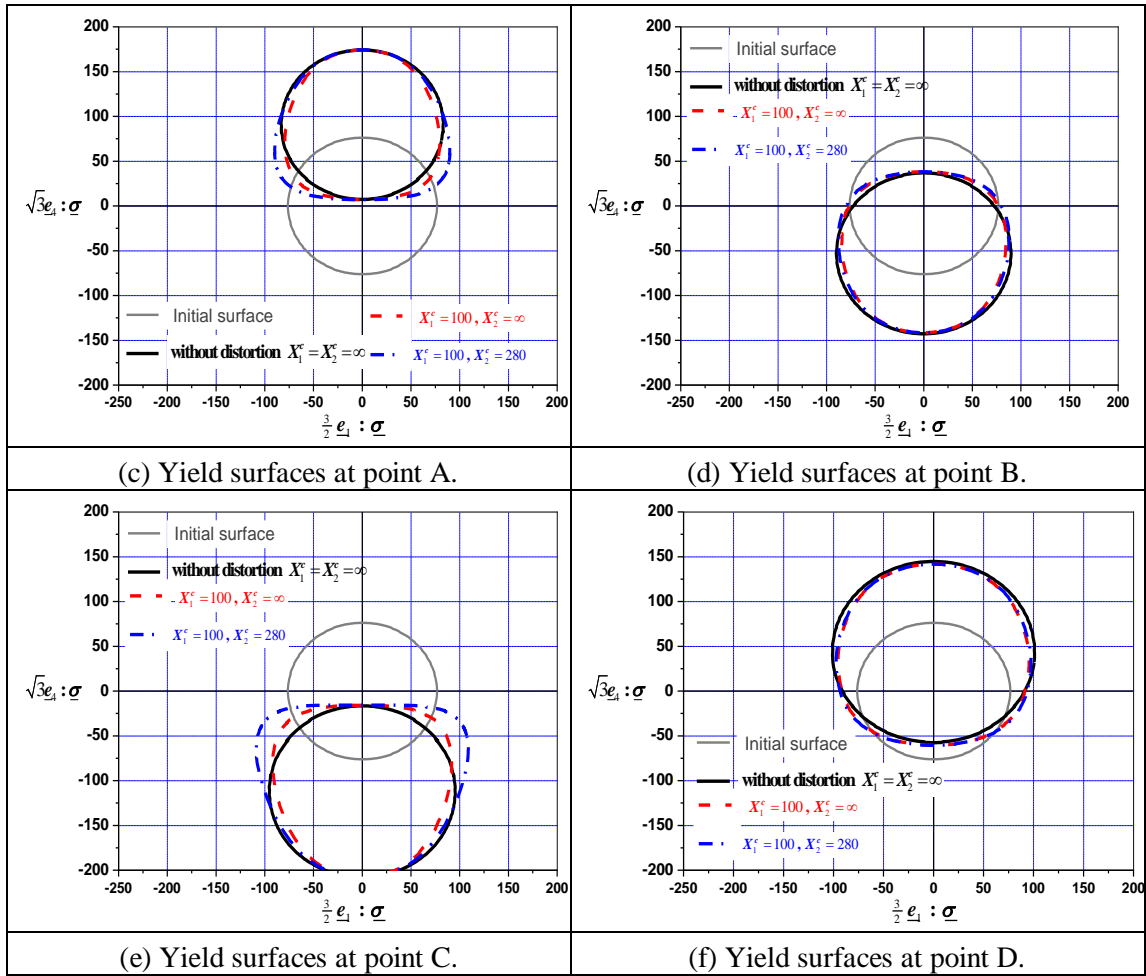


Fig. 3-42. Results of cyclic shear

For the cyclic combined tension-shear loading the numerically predicted results are shown in Fig. 3-43. The scheme of the loading paths for the test is shown in Fig. 3-43a, in which the shear strain component  $\gamma_{12}/\sqrt{3}$  is equal to tension strain component  $\varepsilon_{11}$ . Similar to the cyclic tension loading and cyclic tension loading, the center and the front point following the loading direction of the yield surfaces are the same regardless of the values of  $X_{11}^c$  and  $X_{12}$ , so the effect of the yield surface distortion can be ignored during the combined cyclic tension-shear loading paths. Based on the simulation results of the cyclic tension, cyclic shear and combined tension-shear loading paths, it can be remarked that the contribution of the yield surface distortion on hardening can be ignored if the loading paths is proportional. In order to better present the performance of the proposed fully coupled model on changing

loading paths tests, some non-proportional loading paths tests are conducted to see the influences of the yield surface distortion.

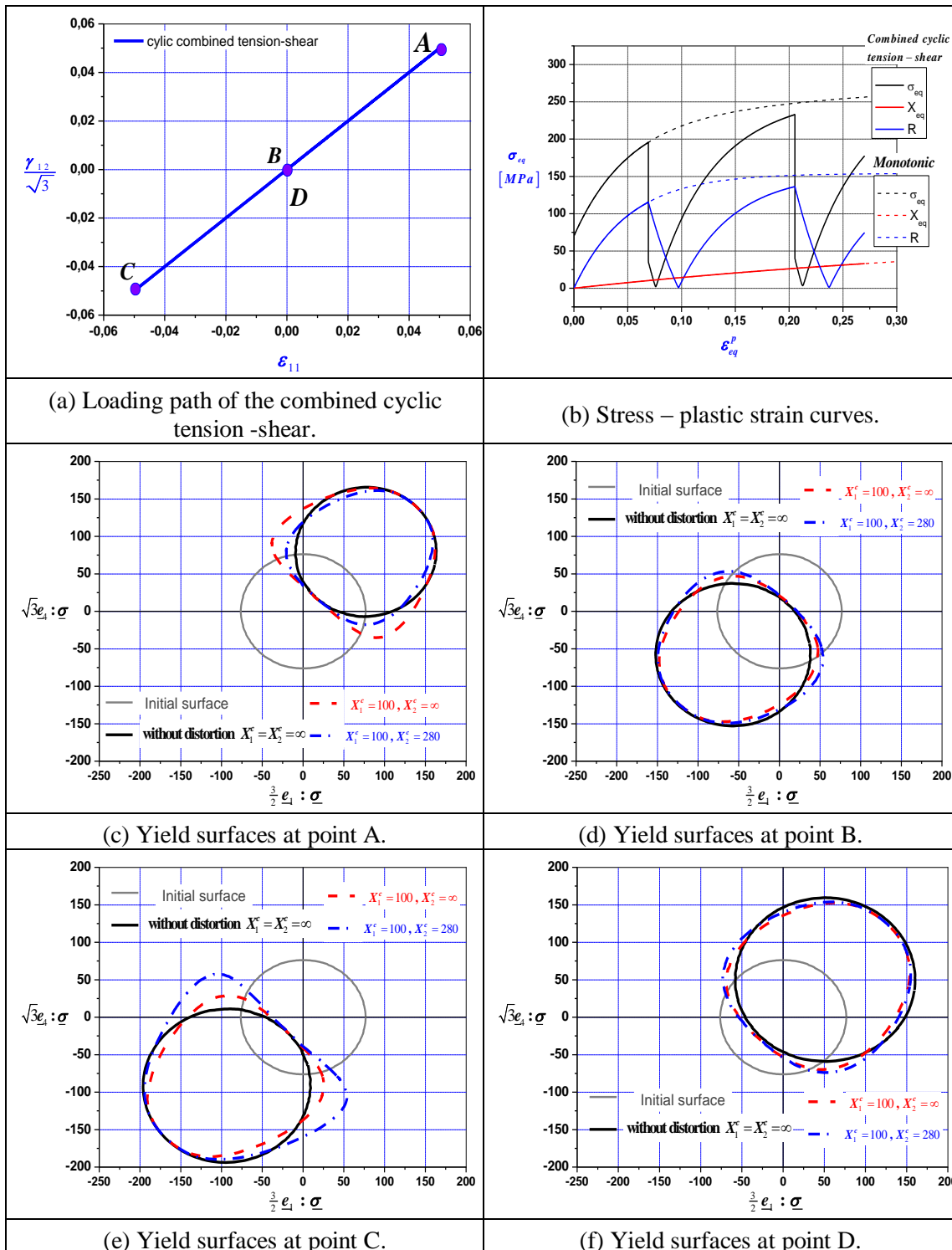


Fig. 3-43. Results of combined cyclic tension-shear.

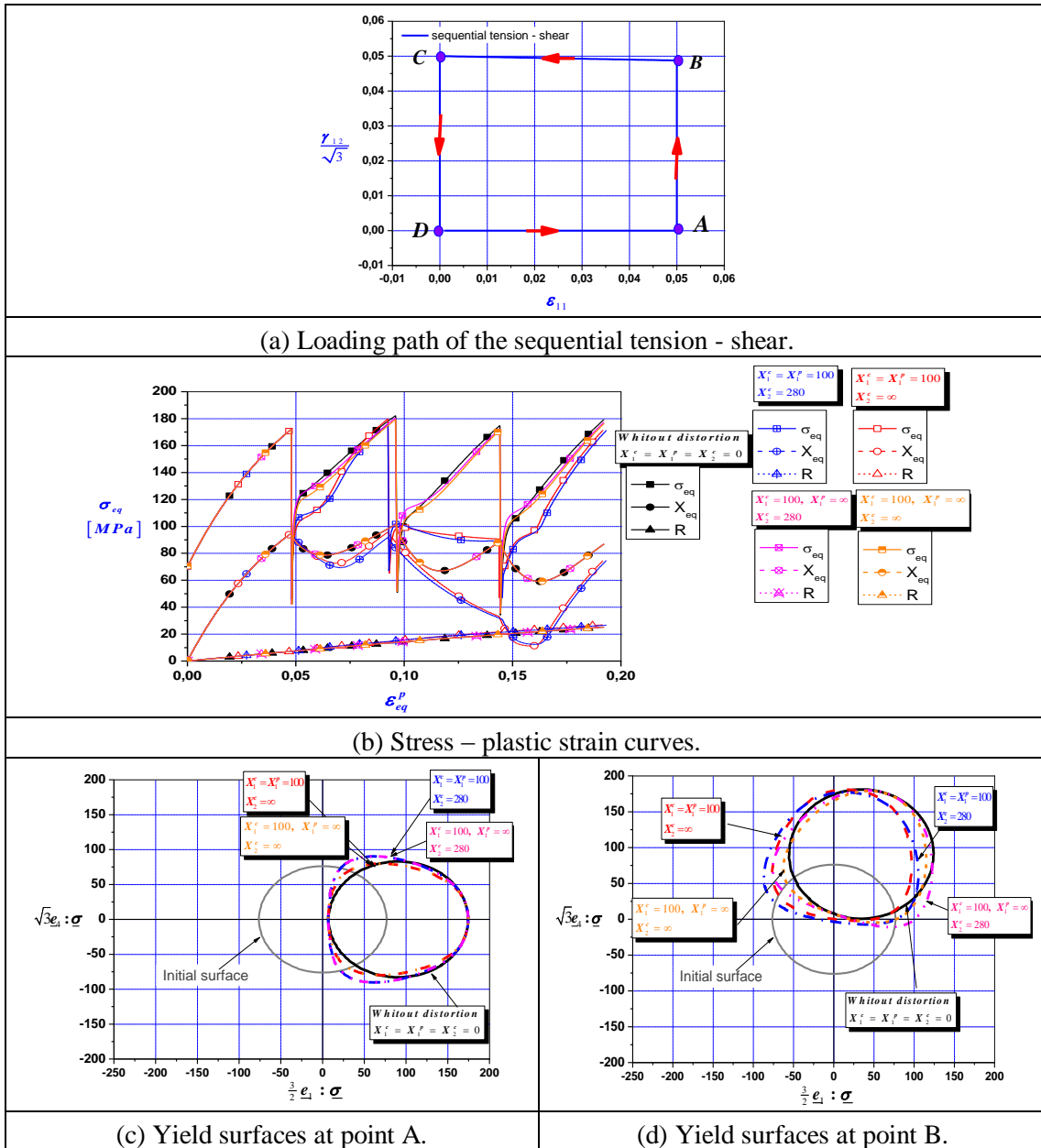
The sequential tension-shear loading tests and elliptic shape tension-shear tests simulation are chosen as the non-proportional loading paths tests and conducted respectively. Their results are separately shown in Fig. 3-44 and Fig. 3-45.

For the sequential non-proportional tension-shear loading path, its scheme of the loading path is shown in Fig. 3-44a, which can be described as a rectangle. In Fig. 3-44b the Cauchy stress  $\sigma_{eq}$ , equivalent kinematic hardening  $X_{eq}$  and isotropic hardening  $R$  under five different conditions are compared. The parameters  $X_{11}^c$ ,  $X_{11}^p$  and  $X_{12}$  are assigned with different values. In the tension step ( $O-A$ ) the yield surface evolutions under different conditions are shown in Fig.4-44c. As we can found that the center and the front point following the loading direction of the yield surfaces are the same in this stage regardless of the values of  $X_{11}^c$ ,  $X_{11}^p$  and  $X_{12}$ . Their responses on the stress-strain curves are the same ( $\varepsilon_{eq}^p \leq 0.05$  in Fig.4-44b).

When the loading path is changed to shear ( $A-B$ ), the center and the front point following the loading direction of the yield surfaces are not all fit (Fig.4-44d). This difference happens when  $X_{11}^p \neq \infty$ , that can be explained by its contributions on the hardening normality (Eq.1-80, Eq.1-81 and Eq.1-82). The stress-strain curves give the different responses ( $0.05 < \varepsilon_{eq}^p < 0.1$ ). Through the comparisons of the stress-strain curves, we can found that when  $X_{11}^c = 100$ ,  $X_{11}^p = \infty$  and  $X_{12} = \infty$ , the yield point in the subsequent stage decreases and very small decrease happens on the hardening evolution. When  $X_{11}^c = 100$ ,  $X_{11}^p = \infty$  and  $X_{12} = 280$ , the yield point in the subsequent stage increases comparing with the condition  $X_{11}^c = 100$ ,  $X_{11}^p = \infty$  and  $X_{12} = \infty$ , and there is also very small decrease on the hardening evolution. On the other hand, when the contribution of  $X_{11}^p$  is introduced, like the condition  $X_{11}^c = X_{11}^p = 100$  and  $X_{12} = \infty$  the hardening evolution is highly decreased, and the total equivalent plastic strain value is decreased. The similar influence is found for kinematic hardening. It can be remarked that the  $X_{11}^c$  and  $X_{12}$  affect the subsequent yield points, but  $X_{11}^p$  gives more effect on hardening evolution.

In the following stages ( $B-C$ ,  $C-D$ ) the influence of the three parameters become more important. But for the isotropic hardening the contributions of three distortion parameters are

very limited, so the change of the isotropic hardening evolution and the size of the yield surface parallel the loading during these whole stages are very small.



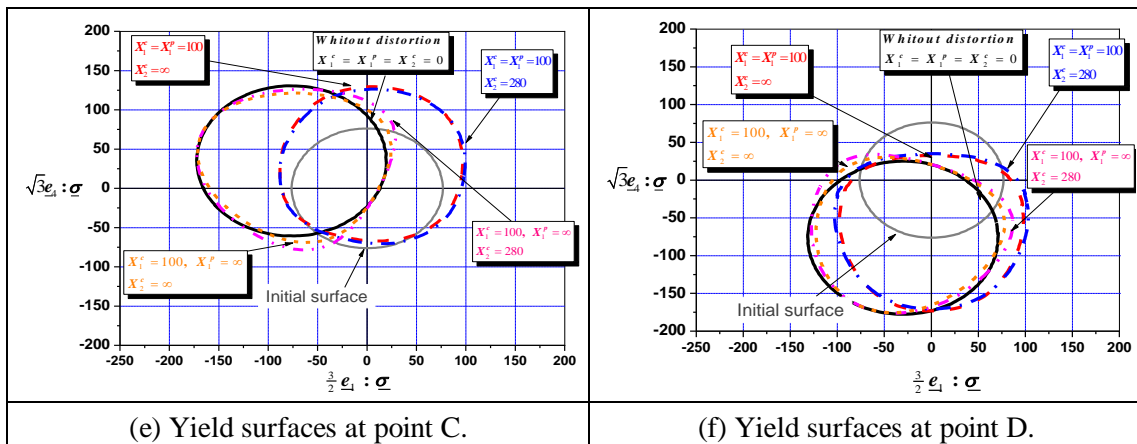
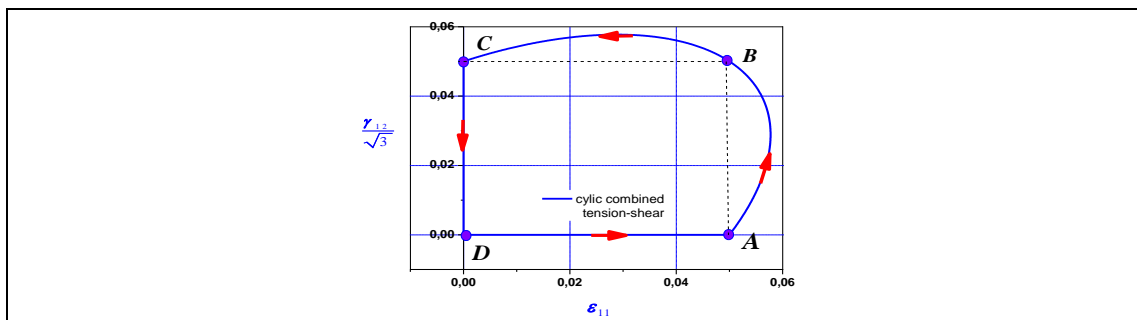
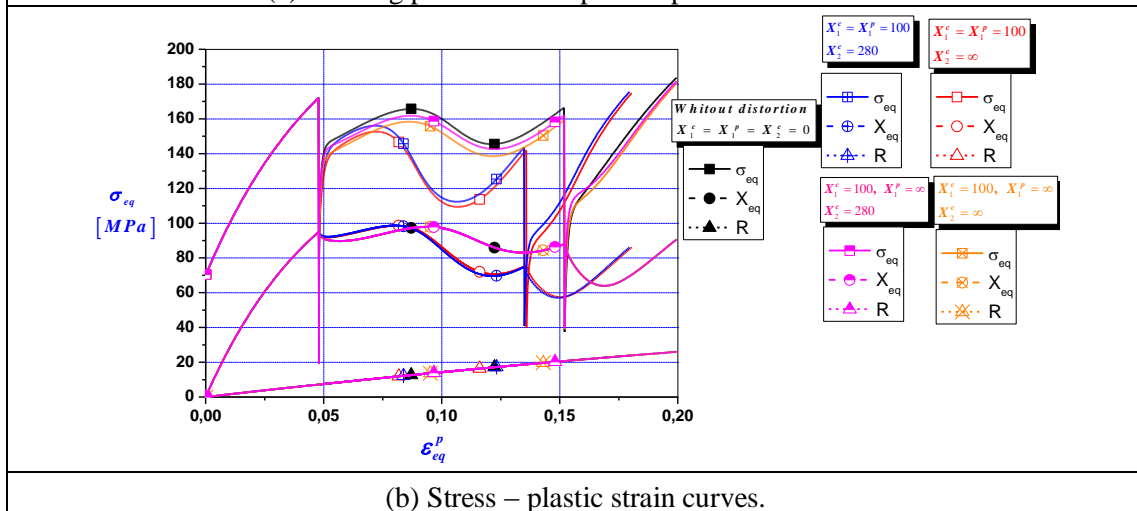


Fig. 3-44. Results of sequential non-proportional tension-shear.



(a) Loading path of the elliptic shape tension - shear.



(b) Stress – plastic strain curves.

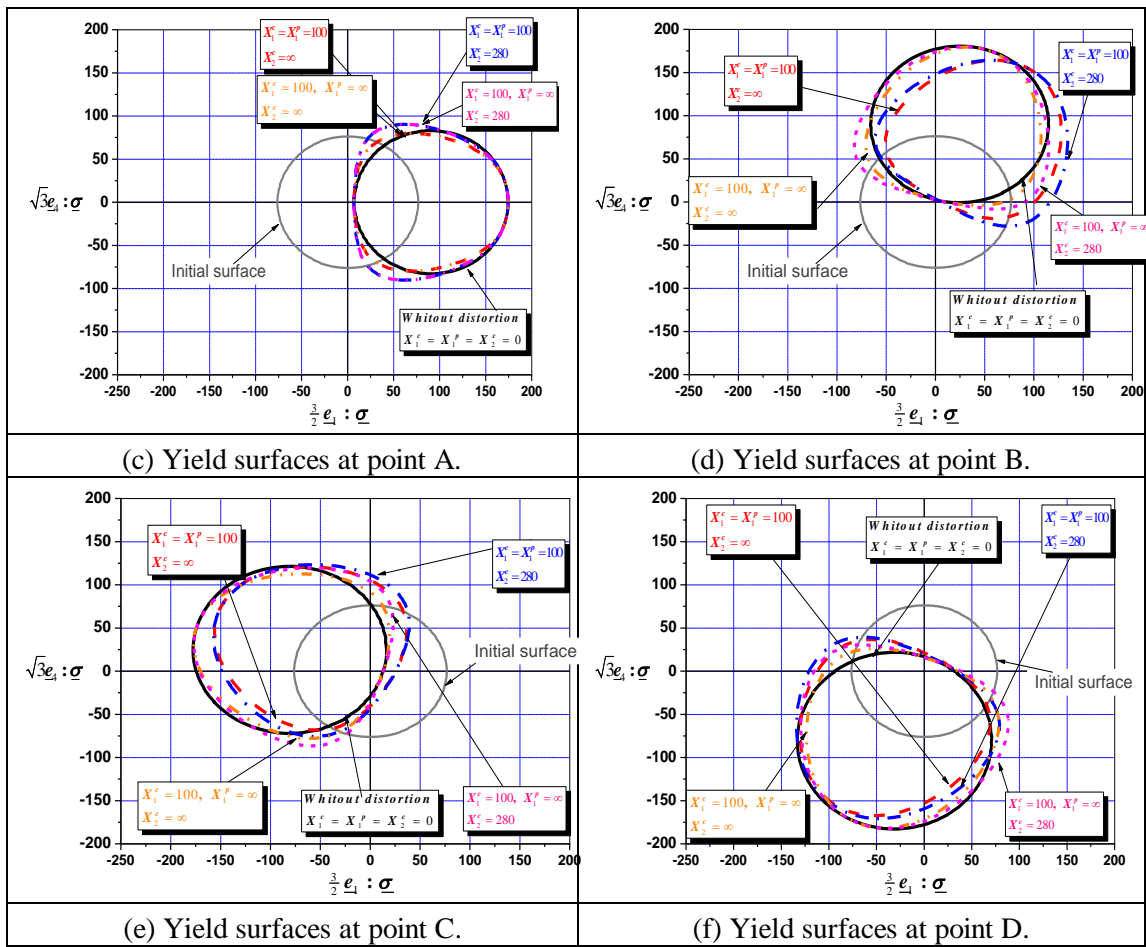


Fig. 3-45. Results of elliptic shape of the non-proportional tension-shear loading path.

For the elliptic shape of the non-proportional tension-shear loading path, its simulation results are shown in Fig. 3-45. The scheme of the loading path is shown in Fig. 3-45a. In Fig. 3-45b the evolutions curves for Cauchy stress  $\sigma_{eq}$ , equivalent kinematic hardening  $X_{eq}$  and isotropic hardening  $R$  in four stages are given, and at the same time the simulation results about the yield surface evolution in four stages with and without distortion effect are compared. These differences on the stress-strain curves can be explained by the evolutions of the yield surface during different stages.

Through the comparison, more proofs can be found about the effect of  $X_{11}^c$  and  $X_{12}$  on the subsequent yield point and the effect of  $X_{11}^p$  on hardening evolutions. When  $X_{11}^c = X_{11}^p = 100$ ,  $X_{12} = \infty$  and  $X_{11}^c = X_{11}^p = 100, X_{12} = 280$ , the decreases of the hardening



evolutions and total equivalent plastic strain due to  $X_{II}^p$  are more important compared with other conditions (Fig.4-45b).

After the first tension stage, it is also found that the center and the front point following the loading direction of the yield surfaces are not all fit due to the non-proportional loading paths. Together with the simulation results of sequential non-proportional tension-shear, we can conclude that, when the loading paths are non-proportional, the influence of the yield surface distortion on hardening evolution becomes important.

### III.3.3 Distortional parameters effect on damage evolution

In order to test the distortional hardening effect on the subsequent hardening and damage evolution, a pre-tension (16%) is applied on RVE, and then a followed shear process is conducted. Caused by the loss of the investigation on damage during tests, an assumed material is chosen as the test objective, whose material parameters are shown in Table 3-6. The pre-deformed state variables (hardening and ductile damage) are recorded as the initial conditions before tension loading applied with elastic unloading. Due to the distortion of the yield surfaces, both the hardening evolution and the ductile damage evolution in the subsequent step are affected.

Table 3-6 Assumed material parameters.

E (GPa)	$\nu$	$\sigma_y$ (MPa)	$F$	$G$	$H$	$L$	$M$
69.8	0.3	322.0	1.5	1.5	1.5	0.5	0.5
$N$	$C$ (MPa)	$a$	$Q$ (MPa)	$b$	$X_{II}^p$	$X_{II}^c$	$X_{I2}$
0.5	2260.0	75.0	675.0	7.0	100.0	100.0	150.0
$S$	$s$	$\beta$	$Y0$	$Dc$	$h$		
2.5	1.5	3.0	0.0	0.99	0.2		

In Fig. 3-46, the evolution of the equivalent stress is plotted with different distortion value ( $X_{II}^c, X_{II}^p, X_{I2}$ ). By comparing the subsequent stress curves between the results with and without distortional hardening effect, it has been found that with the decrease of the  $X_{II}^c$ , the distortional ratio increases and the failure occurs later and clear work-hardening stagnation stage is found. The parameter  $X_{II}^p$  does not affect the yield stress, but will give influence on the hardening evolution. When  $X_{I2}$  is positive, the subsequent yield surface expands, but when hardening increases, the stress-strain curve coincides again with the original curves. On

the other hand, when  $X_{12}$  is negative, the yield surface will decrease permanently.

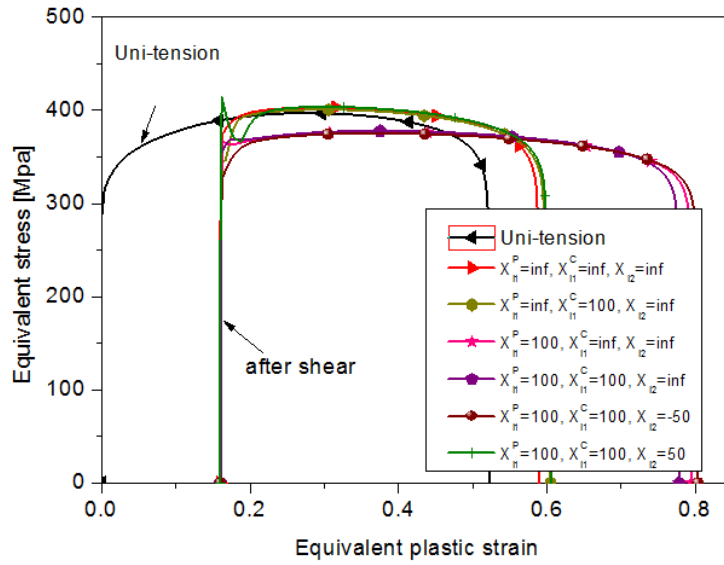


Fig. 3-46. Distortional parameters effect on subsequent equivalent stress-equivalent plastic strain curves after 16% pre-strain.

### III.3.4 Triaxiality ratio and Lode angle effect on damage evolution

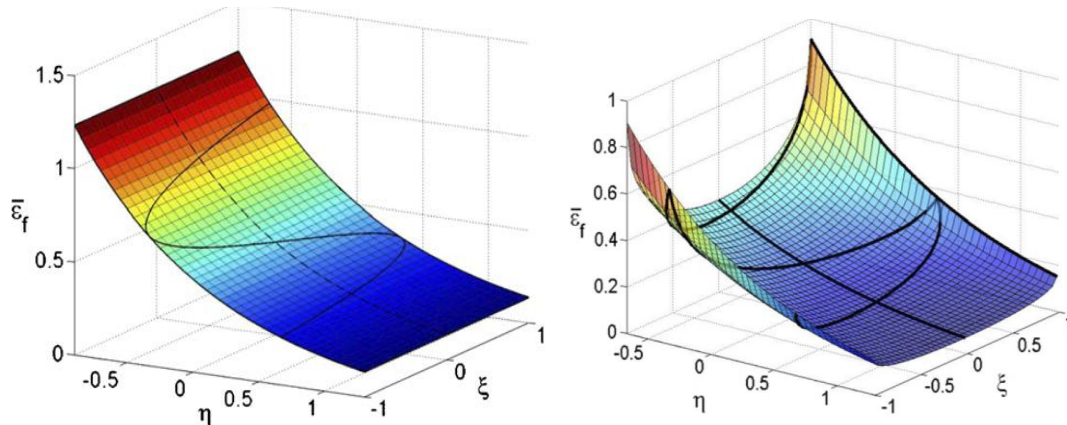


Fig. 3-47. Behavior of the ductile material in three dimensional fracture loci (a) postulated by [Johnson85], (b) postulated by [Wierzbicki05].

Experimental evidence of the difference of ductile fracture under high, low or even negative triaxiality ratios has been observed by several authors [McClintock71, Johnson85]. Nevertheless, Bao and Wierzbicki have conducted numbers of tests with the specimens with different geometries to determine the fracture location under a wide range of triaxiality [Bao04]. Fig. 3-47 shows the behavior of two ductile materials on the three dimensional

fracture loci for a range of stress triaxiality ratio between [-1, 1]. The extension of Wilkin's model and Johnson-Cook's model, Wierzbicki and Xue postulated a non-separable but symmetric 3D fracture locus in the space of stress triaxiality and normalized third stress invariant (Lode angle parameter) [Wierzbicki05, Xue05], as shown in Fig. 3-47.

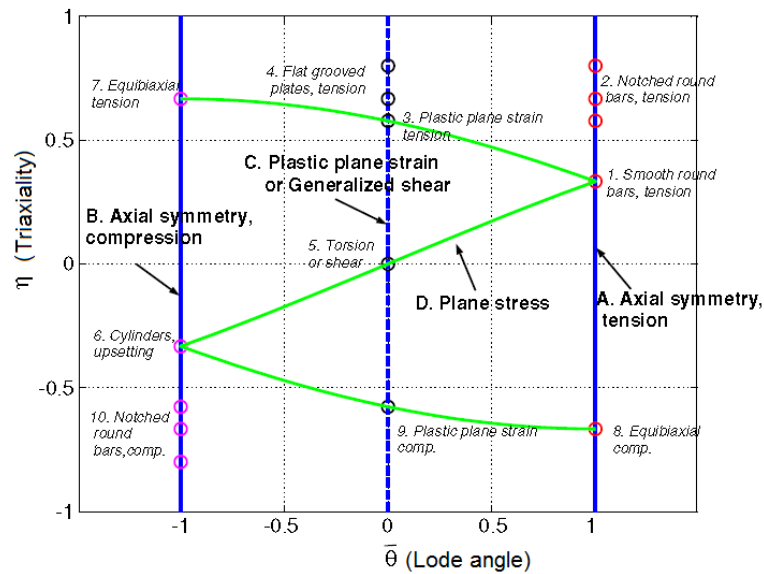


Fig. 3-48. Representation on the space of stress triaxiality versus Lode angle parameter.

Adapted from [Bai08].

The representation of the initial stress state on the plane of stress triaxiality versus Lode angle is shown in Fig. 3-48. In this study, the effect of triaxiality ratio and Lode angle on damage evolution will be conducted in the plane stress condition (2D fracture) with the assumed material parameters:  $E = 69.85 \text{ MPa}$ ,  $\nu = 0.3$ ,  $\sigma_y = 322.0 \text{ MPa}$ ,  $F = 0.5$ ,  $G = 0.5$ ,  $H = 0.5$ ,  $L = 1.5$ ,  $M = 1.5$ ,  $N = 1.5$ ,  $Q = 1000.0 \text{ MPa}$ ,  $b = 50.0$ ,  $\gamma = 1.0$ ,  $C = 10000.0 \text{ MPa}$ ,  $a = 100.0$ ,  $S = 1.0$ ,  $s = 1.0$ ,  $\beta = 1.0$ ,  $Y_0 = 0.2$ ,  $m = 1$ ,  $h = 0.2$ ,  $D_c = 0.99$ .

In Fig. 3-49 the contributions of the Lode parameter to  $S(\bar{\theta})$  for Wierzbicki and new proposed form of the damage evolutions are compared using ( $c_1 = 1$  and  $c_2 = 0$ ). It is found that these two forms give nearby the same values with changing Lode parameters, so these two forms can be regarded as the same. In Fig.3-50 the equivalent plastic strains at fracture are plotted versus the triaxiality ratio using ( $c_1 + c_2 = 1$ ). These results have shown that the fracture strain is not a monotonically decreasing function of stress triaxiality when the Lode parameter is introduced. For a high level of stress triaxiality ratio, where the spherical void growth mechanism plays a major role in the damage evolution process, the equivalent plastic strain decreases with the increase of the stress triaxiality ratio. However, within the range of

$0 \leq \eta \leq 0.33$  and  $0.57 \leq \eta \leq 0.66$  the equivalent plastic strain at fracture increases with the increase of the stress triaxiality ratio, which is in good agreement with the test results [Bao04]. The dependence on pressure and Lode angle of the damage can be adjusted by the parameters  $c_1$  and  $c_2$ .

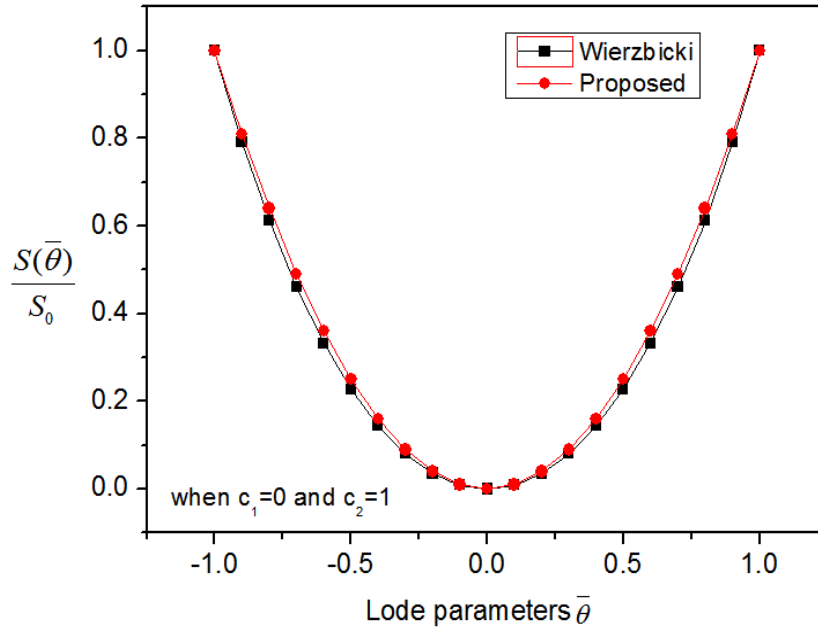


Fig. 3-49. Influence of Lode parameter on  $S(\bar{\theta})$ .

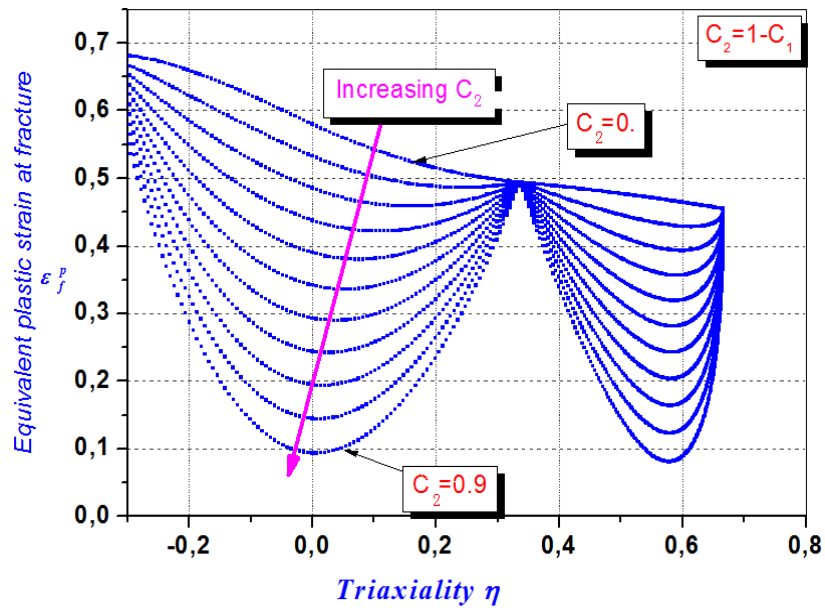


Fig. 3-50. Fracture locus in plane stress state for proposed type damage evolution.

### III.4 Parametric study of M-K approach

Besides the proposed fully coupled CDM model, FLD and FLSD will be used as another failure criterion. For the comparison with CDM model, the material Al7020 will also be chosen as the test objective of M-K approach. The FLD and FLSD curves for Al7020 will be constructed for the simulation. In order to well present the influence of the subframes like yield criteria and hardening on the FLD and FLSD curves, Al7020 is chosen as the test objective material to input the program. With the help of uniaxial tension along different directions, the directionalities and anisotropic ratio r-value can be determined (Chapter IV.3). The true stress-true plastic strain data measure in uniaxial tensile test can help to fit the swift hardening law and Voce hardening law:

$$\sigma_{eq} = 502 (0.012 + \varepsilon_{eq}^p)^{0.0983} \quad (3-16)$$

$$\sigma_{eq} = 417.7 - 88.7 \exp(-18.8 \varepsilon_{eq}^p) \quad (3-17)$$

As shown in Fig. 3-51, it gives the comparison between the experimental and modeled true stress-true strain curves and it shows a good agreement before necking. The modeled true stress-true strain curves are related to Swift and Voce hardening law, respectively shown in Eq.3-16(Swift) and Eq.3-17 (Voce).

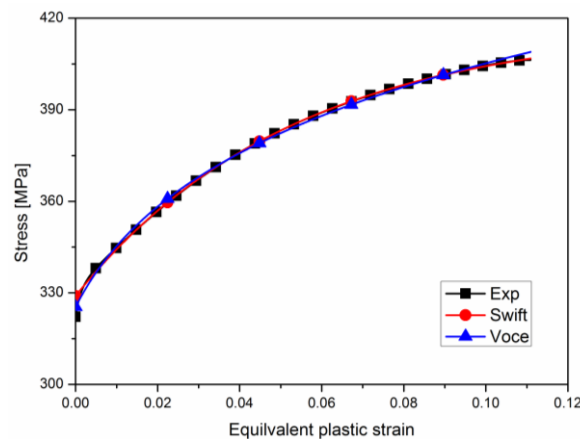


Fig. 3-51. True stress-true plastic strain curve for Al7020

#### III.4.1 Initial imperfection

Here, we chose the same Hill48 as the yield function, swift hardening as the hardening law, so

in the case, just the initial imperfection is investigated variable.

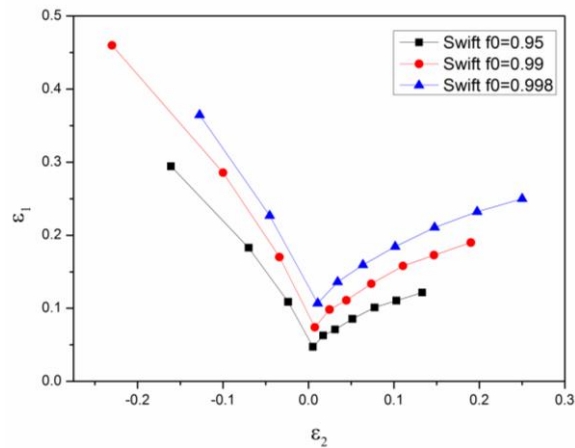


Fig. 3-52. FLD curves related to different initial imperfect value.

In Fig. 3-52, we can see with the decrease of initial imperfect value (0.998, 0.99 and 0.95), the FLD curve moves down, which means the failure of the material come earlier. These results are in a good agreement with the conventional understanding of the imperfect factor.

### III.4.2 Hardening laws

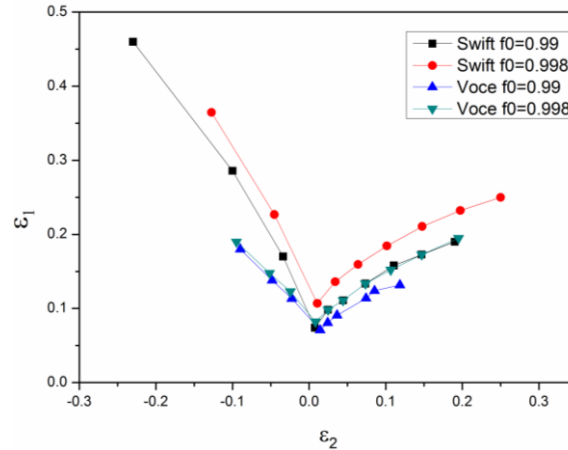


Fig. 3-53. Forming limit diagram using swift or voce hardening law.

The influences of hardening laws (Swift and Voce hardening laws) are pointed out in Fig. 3-53 by using related to changing initial imperfection values, whereas the yield surface is described by the same Hill48 yield function. These results show that the forming limit diagrams obtained using swift equation is always higher than those obtained using Voce equation whatever the same yield function is used.

### III.5 Conclusions

In this chapter, we first gave the test materials: two kinds of high strength steels DP1000 and CP1200 and one aluminum alloy Al7020. Through series of tests: tensile tests, shear tests, in-plane torsion tests and combined loading tests, the material formability were investigated under different loading paths. On the other hand, we have also done some validation tests, Nakazima tests and Cross section deep-drawing tests, which can create complex loading paths.

In the third part of this chapter, before the identification of the models parameters, some parametric studies of fully coupled CDM model were performed first: (i) the microcracks closure  $h$  under the compressive stage of the loading path; (ii) to the distortional hardening; and (iii) to the effect of lode angle on the predicted material ductility. All these studies will help us well understand the novelty of the proposed fully coupled CDM model.

In the fourth part of this chapter, similar parametric studies for M-K approach have been done: including the initial imperfection and the hardening laws study. Two kinds of hardening laws were introduced in this approach: Swift and Voce, but in the coming chapter, we will just take the Swift hardening law for the FLD and FLSD prediction.





## Chapter IV

# Identification and validation of the proposed fully coupled CDM model and comparisons with FLCs approach

### Content

---

IV.1 Introduction.....	106
IV.2 The identification methodology of fully coupled CDM model.....	106
IV.2.1 Elastoplasticity parameters identification .....	108
IV.2.2 Distortion parameters identification .....	110
IV.2.3 Ductile damage parameters identification.....	116
IV.3 Determination of FLD and FLSD for Al7020.....	124
IV.4 Nakazima tests simulation with fully coupled CDM model .....	125
IV.5 Cross section deep drawing tests (CSD).....	133
IV.6 Rectangular drawing tests (RD) .....	152
IV.7 Conclusions.....	157

## IV.1 Introduction

After the experimental investigations of three metallic materials under different loading conditions and parametric study of the proposed models (fully coupled CDM and M-K), the parameters of two models suited to three materials should be determined and validated. Different series of tests will be chosen for the parameter identification of two models, separately shown in section IV.2 and section IV.3. After the parameters determination, the Nakazima tests (NAK), Cross Section Deep drawing tests (CSD) and Rectangular Drawing tests (RD) are used to validate the parameters input for the fully coupled CDM model. By comparing the force-displacement curves, limit major strain distributions and final cracks occurrence with experimental responses, the capability of the fully coupled CDM model is assessed. CSD tests are simulated with proposed fully coupled CDM model for three given materials Al7020, DP1000, CP1200, and two additional simulations are conducted with FLC and FLSD curves of Al7020. Comparisons are made to show the different capabilities of fully coupled CDM, FLD and FLSD models. On the other hand, the CSD and RD tests are simulated with and without yield surface distortion effect for fully coupled CDM model in order to assess the effect of yield surface distortion on forming processes. Through the comparison of the draw-in amount the edges of the specimens and also the stress, strain distribution.

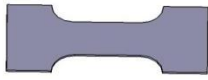

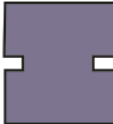


## IV.2 The identification methodology of fully coupled CDM model

An inverse methodology is used for the material parameters identification. Various identification methodologies based on inverse approach have been proposed to identify different kinds of constitutive equations [Khoddam96, Yoshida98, Bonora99, Yoshida03, Thuillier09, Eggertsen10, Bouchard11, Yoshida11, Cao13a, Cao13b]. These methods enable the usage of unusual tests set-ups or even the forming process themselves as long as the assumption of homogeneous stress field is not needed anymore [Unger08, Gelin94].

In this study, concerning the kinematic hardening parameters ( $C$ ,  $a$ ), the measured moments versus rotation angles obtained from TBT tests (see Chapter III) are used under loading-unloading conditions. In order to form the objective function to be minimized, the experimental and numerical curves having different discretization will be linearly interpolated at the same rotation angle values. Fifty integration intervals are used for forward and backward steps, adding up to 100 data points for one loading cycle. There are the same

weighting between the forward and backward curves. The similar scheme is used to determine  $S, s, \gamma, Y_0$  with local node distance versus global force from PNT tests, and also to determine the microcracks closure parameter  $h$  with the global distance versus the global force from SS tests.

Table 4-1. Experimental specimens and their association to material parameters

		Test Design	Parameters	Number of parameters	Methodology
Elastoplasticity	UT		$E, \nu, \sigma_s, F, G, H, L, M, N$	9	Analytical
	IPT		$C, a, Q, b$	4	Inverse
Distortion	CL		$X_{l1}^C, X_{l1}^P, X_{l2}$	3	Analytical
Damage	PNT		$S, s, \beta, Y_0$	4	Inverse
	SS		$h$	1	Inverse

The identification methodology combines the Python script, the ABAQUS FE software with the MATLAB-based minimization code. The scheme of the optimization program is shown in Fig. 4-1, which compares the output results with the experimental measurements, builds and minimizes the objective function and delivers the best set of the material parameters which minimizes the difference between the numerically predicted and the experimental results. More details about the inverse methodology are shown in Appendix A.

According to the characteristics of the used fully coupled CDM model, the parameters including Elastoplasticity parameters, distortion parameters and ductile damage parameters are determined separately according to different procedures, as shown in Table 4-1. More details description can be found in [YUE13].

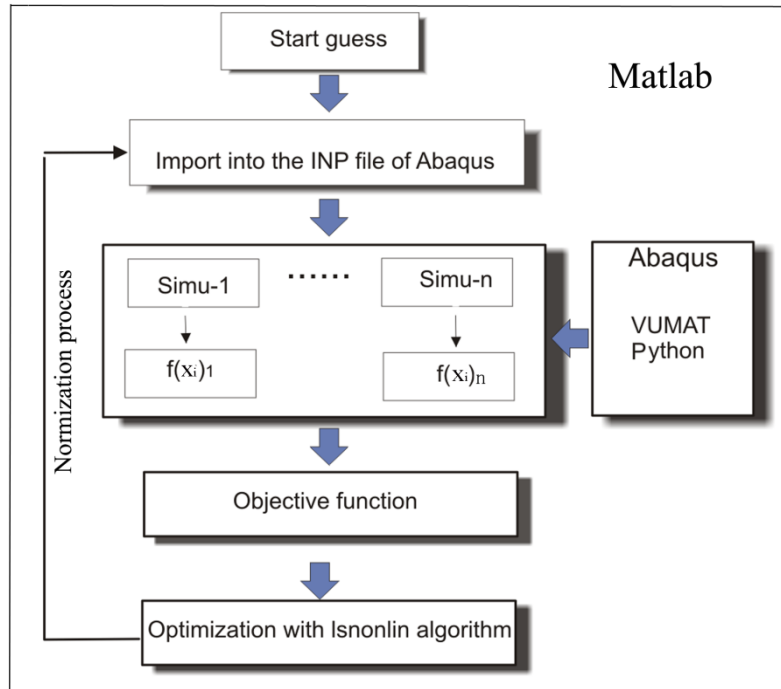


Fig. 4-1. The optimization program flowchart.

### IV.2.1 Elastoplasticity parameters identification

From UT tests, the isotropic elasticity parameters ( $E, \nu$ ) and the initial yield stress  $\sigma_y$  can be obtained directly. From the Lankford parameters  $r_\theta^L$  in three directions (Fig. 3-8) and the Equation 3-9, the Hill48 anisotropic parameters can be determined with the analytical approach (see chapter 4 of [Saanouni12]). The mixed hardening parameters are determined with the IPT and UT experimental responses with the inverse approach.

Concerning the experimental responses used by the inverse methodology, the tensile load versus global displacement curves obtained from the uniaxial tensile tests (UT, Fig. 3-3) as well as the torsion angle versus the torsion torque curves in the two bridge torsion tests (IPT, Fig. 3-10) are used. Without the ductile damage effect, the simulations are conducted with ABAQUS/Explicit using user's subroutine VUMAT, and compared with experimental responses before the maximum values of loads. It is assumed that the damage affects the material response before the experimental maximum load point. For the explicit simulation of the quasi-static deformation process, kinetic energy should be controlled less than 10% of the internal energy, in order to minimize the inertia effects [Abaqus01]. The displacement rate is 10.0 mm/s, and the initial time increment is fixed to be 2.0E-6 with mass scaling method.

After dozens of optimization cycles, the determined best values of the material parameters of the proposed model are summarized in Table 4-2.

Table 4-2 Elastoplastic parameters obtained from UT and IPT specimens for the materials under concern

	$E$ (GPa)	$\nu$	$\sigma_y$ (MPa)	$Q$ (MPa)	$b$	$C$ (MPa)	$a$	$F$	$G$	$H$	$L$	$M$	$N$
DP 1000	208.0	0.3	809.0	4000.0	13. 0	32000.0	150. 0	0.52 5	0.546	0.455	1.5	1.5	1.6 7
CP 1200	207.0	0.3	980.0	5848.0	37. 0	37000.0	507. 0	0.56 7	0.610	0.389	1.5	1.5	1.3 7
AL 7020	69.8	0.3	322.0	675.0	8.0	2260.0	75.0	0.63 1	0.634	0.366	1.5	1.5	1.4

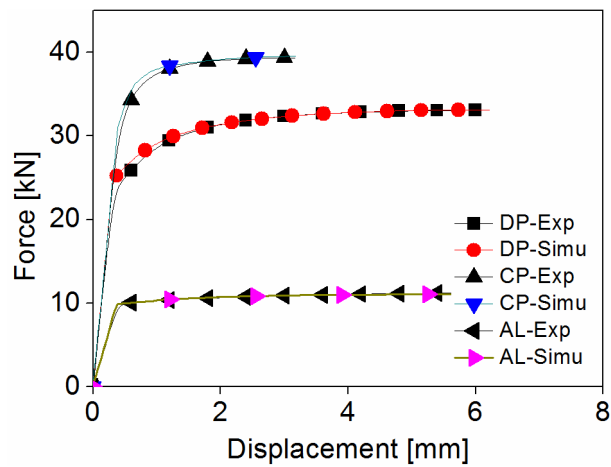


Fig.4-2. Comparison of force-displacement curves for uniaxial tensions (plot before  $F_{max}$  ).

Fig. 4-2 shows the comparison of Experimental-numerical responses in monotonic tension loading path in terms of force-displacement curves before the maximum force is reached. Fig. 4-3 summarized the results obtained for the three materials when subject to one loading cycle in torsion (loading-unloading). With the same pre-strain 0.6 degree of torsion for DP1000 (Fig.4-3a) and CP1200 (Fig.4-3b), the CP1200 presents less Bauschinger effect and its saturation value is  $0.07\sigma_y$  for kinematic hardening, compared to  $0.26\sigma_y$  for DP1000. With pre-strain 1.5 degrees of torsion for Al7020 (Fig. 3-53c) the saturation value is  $0.1\sigma_y$ , the Bauschinger effect can be obtained using the determined hardening parameters.

Note that all the numerically predicted curves in Fig. 4-2 and Fig. 4-3 are obtained using the best values of the material parameters given in Table 4-2.

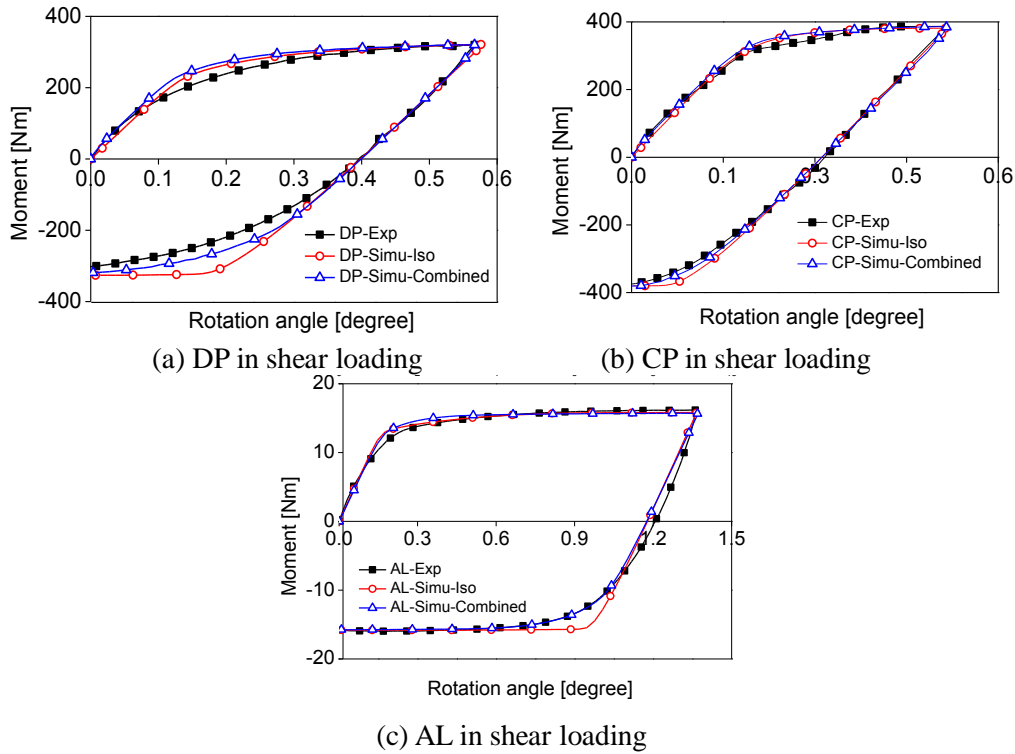


Fig. 4-3. Numerical and experimental moment-Angle curves using the IPT tests loaded in rolling direction.

## IV.2.2 Distortion parameters identification

**Based on CL tests:** The strategy of the CL tests is to calibrate the distortional parameters  $X_{11}^C$  and  $X_{11}^P$  through one tension-shear test with a fixed equivalent plastic strain, and then other tension-shear and shear-tension tests following different tension directions will be used for the validation. The determination of  $X_{12}$  depends on the need for each material.

For Al7020, the pre-tension equivalent plastic strain value is 18.0%. After 18.0% pre-tension, the subsequent shear yield stresses are 197.0 MPa, while simulated result (without the effect of yield surface distortion) is 220.0 MPa, and at that time, the kinematic hardening values are ( $X_{11} = 36.0$ ,  $X_{22} = -18.0$ ,  $X_{33} = -18.0$ ,  $X_{12} = 0.0$ ,  $X_{13} = 0.0$ ,  $X_{23} = 0.0$ ) MPa and isotropic hardening value is  $R = 49.0$  MPa.

The  $X_{11}^C$  value can be determined in the tension-shear stress space with the decrease of the yield stress (as shown in Fig 4-4). When  $X_{11}^C$  equals to 30.0, the yield surface can cover the experimental observed yield point  $\sqrt{3} \times 197$  MPa, The optimal value of  $X_{11}^P$  which controls

the flowing trend after yield is chosen to be 100.0. The parameter  $X_{l2}$  is set to be infinite (value higher than  $10^4$ ), and will not affect the subsequent hardening.

In Fig. 4-5, the results for DP1000 are given for a pre-strain 5% in tension, and the determined distortion parameters are ( $X_{l1}^C = 200$ ,  $X_{l1}^P = \text{inf}$ ,  $X_{l2} = \text{inf}$ ).

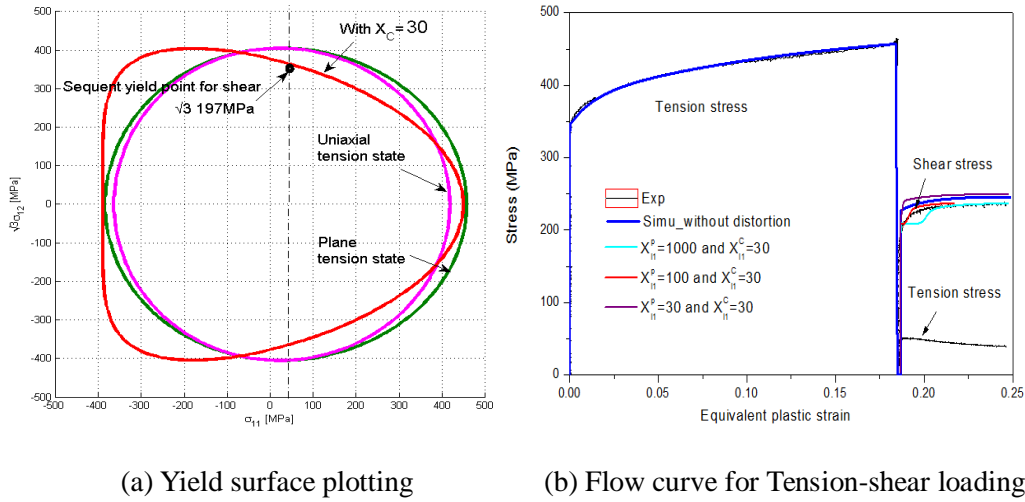


Fig. 4-4. Subsequent behavior after 18% pre-tension for Al7020.

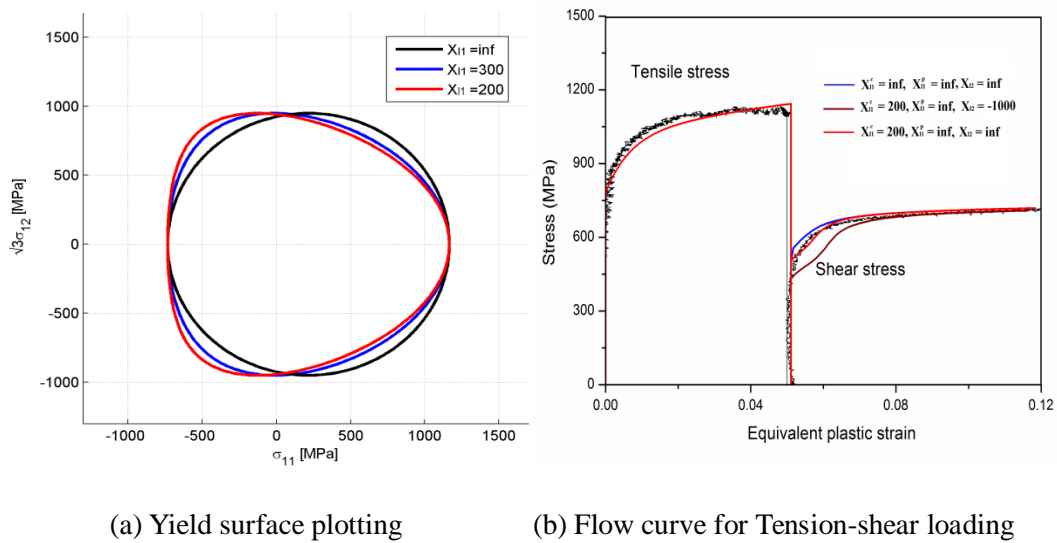


Fig. 4-5. Subsequent behavior after 5% pre-tension for DP1000.

In order to verify the accuracy of the model under shear-tension loading path for Al7020 and DP1000, similar simulations have been performed. With the determined parameters above, the subsequent work hardening behaviors in different loading directions are shown in Fig. 4-6 and Fig. 4-7, respectively for Al7020 and DP1000. As we can see, a consistent of transient work-hardening at the beginning of the second loading-stage is observed. But with the

increment of the plastic strain, a clear difference between the simulation and experimental results is observed. This can be caused by the complex dislocation and slip texture system when changing the loading path, or partially caused by the lack of accuracy in the large strain measurement during the test.

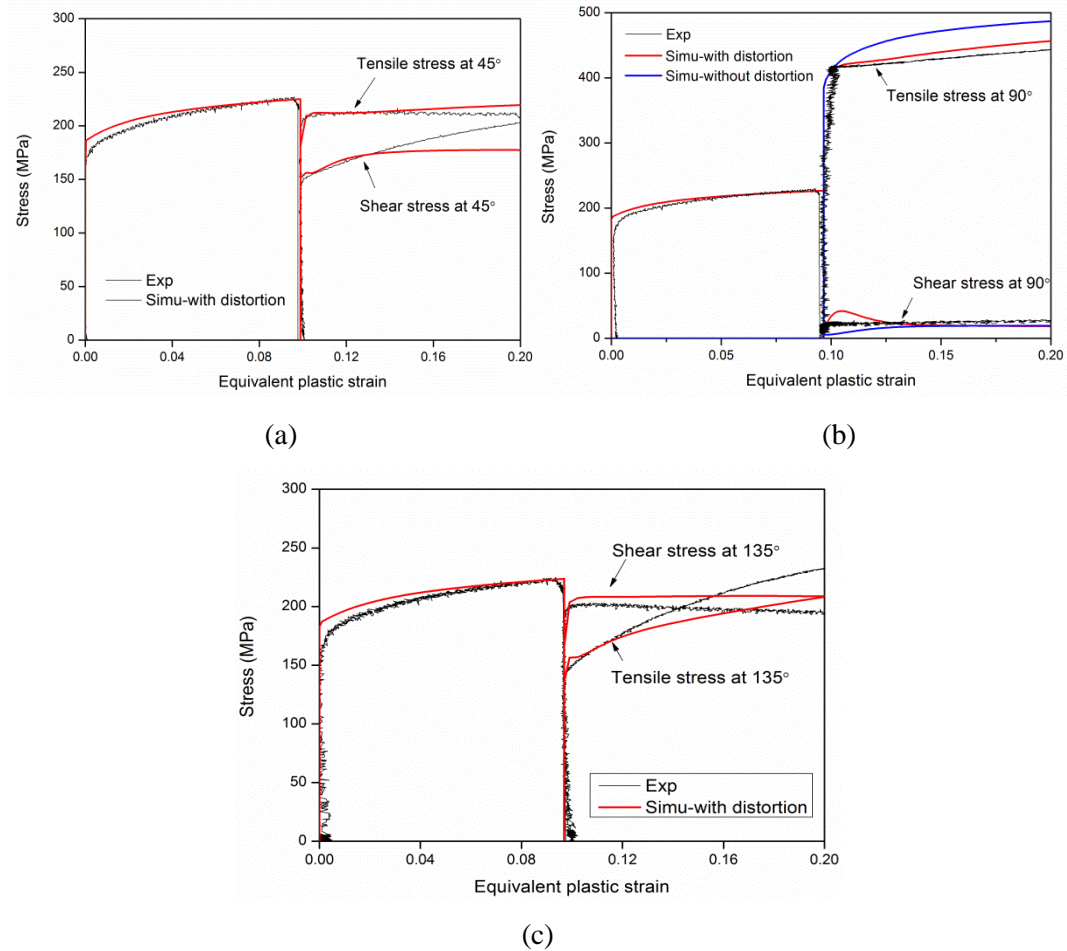


Fig. 4-6. Comparison between the experimental and numerical results (a) 45°, (b) 90°, (c) 135° for Al7020.

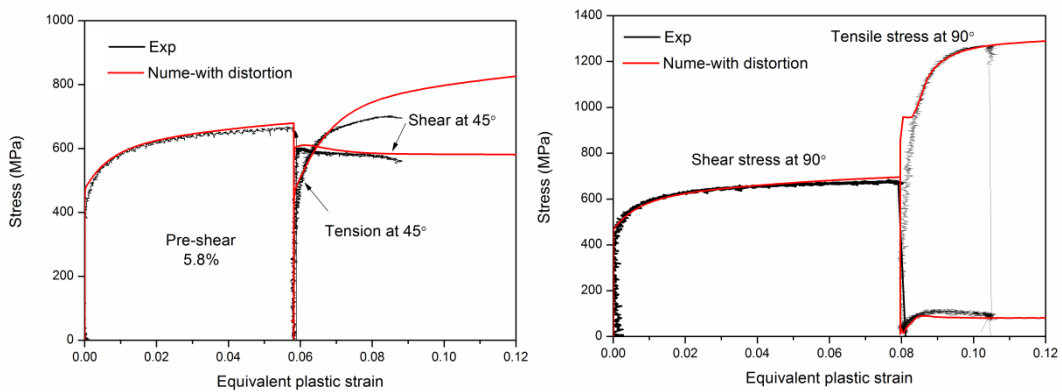




Fig. 4-7. Comparison between the experimental and numerical results (a) 45°, (b) 90° for DP1000.

**For AL1100:** In Fig 4-8(a) are summarized the experimental results of Khan et al [Khan10a] showing the evolution of the yield surface for AL1100 when subject to three different loading paths: (i) tension, (ii) torsion and (iii) combined tension-torsion. Besides the initial yield surface, the subsequent ones are measured after 2.0%, 8.0% and 16.0% of equivalent plastic strain for the tension and tension-torsion paths and after 4.0%, 10.0% and 20.0% of the equivalent plastic strain for torsion paths. One yield surface is determined with one specimen in each loading direction at several levels of strain. After pre-strain, the specimen needs to be relaxed for 1 h to remove the strain-rate effect from the previous measurement and performed using less than  $10\mu\epsilon$  definition of yield surface.

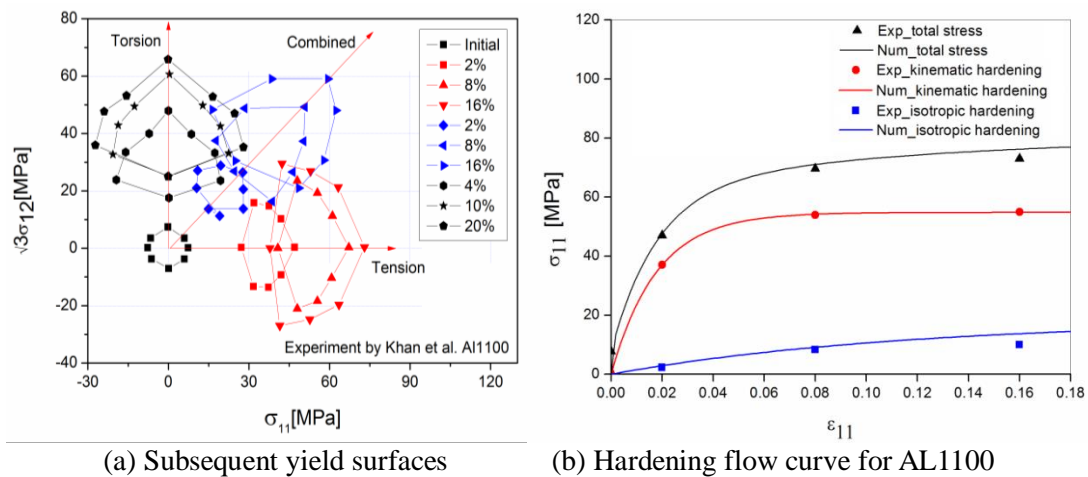


Fig. 4-8. Experimental observations for AL1100.

From Fig. 4-8a the shape of subsequent yield surfaces reveals a well-defined ‘nose’ in the loading direction and flat in the opposite direction. Considering the character of our model, the parameters can be first identified with the data in pure tensile path. The pure shear and combined situation can be chosen to validate the model.

Focus on the tensile loading data, the material is assumed to be plastically isotropic and the initial yield stress and plastic hardening evolution can be observed directly from the tensile path with a step-wise fashion, as shown in Fig. 4-8(b). As expected, the transition of the yield surfaces centers is regarded as the equivalent kinematic hardening value. Considering the shrink of the yield surfaces, the minimum radius value following the loading direction is regarded as isotropic hardening value. The parameter identification process is performed in a step-wise method. First, with the observed three steps evolution points of the kinematic hardening and isotropic hardening, the kinematic hardening parameters  $C$  and  $a$ , isotropic

hardening parameters  $Q$  and  $b$  are determined. The determined elastoplastic parameters for AL1100 are shown in Table 4-3.

Table 4-3 Determined Model parameters without damage for AL1100

E (GPa)	$\nu$	$\sigma_y$ (MPa)	$F$	$G$	$H$	$L$	$M$	
72	0.3	7.0	1.5	1.5	1.5	0.5	0.5	
$N$	$C$ (MPa)	$a$	$Q$ (MPa)	$b$				
0.5	3080.0	56.2	158.0	7.0				

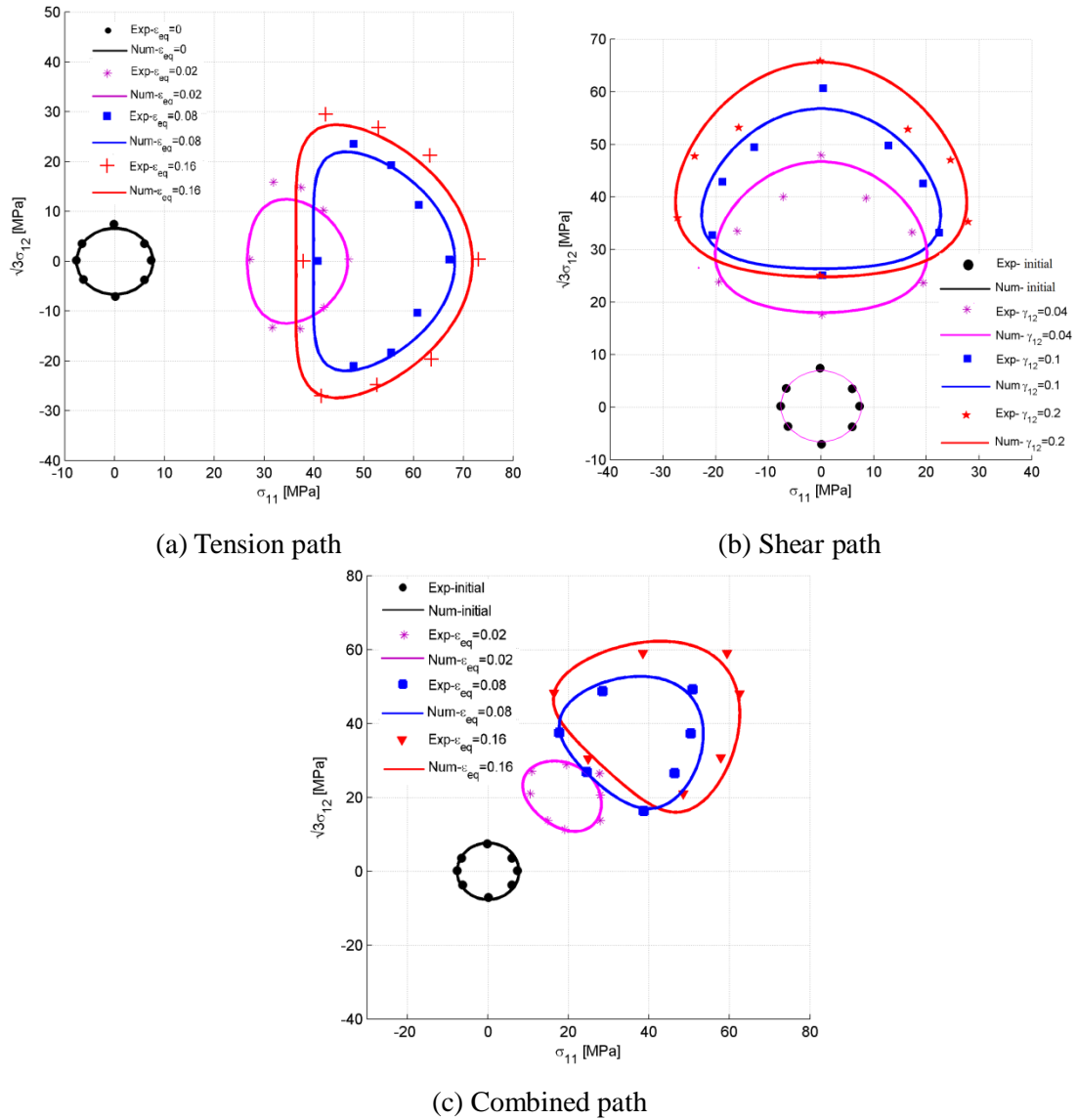


Fig. 4-9. Comparison between numerically predicted and experimentally measured yield surfaces for AL1100.

From the Fig. 4-8(b), it can be found that the kinematic hardening increases very fast, and saturates at about 8% strain value, while the isotropic hardening increases nearly linearly with the strain increase. Secondly, the increase of yield stress in the direction perpendicular to the

loading direction can be satisfied by changing  $X_{I1}^C$  and  $X_{I2}$ :  $X_{I1}^C$  controls the shape distortion of the yield surfaces, but does not change the width of the surface on the direction perpendicular to the loading direction. By varying the values of the material parameters, a good fit between experimentally measured and numerically predicted yield surfaces can be found, and the final determined values are  $X_{I1}^C = X_{I1}^P = 100.0$  and  $X_{I2} = 150.0$ .

The comparisons between experimental and numerical results under three different loading paths are shown in Fig. 4-9. Clearly, the proposed model describes well the yield surfaces evolutions including the distortion of the yield surfaces. From Fig. 4-9a, the numerically predicted kinematic hardening (center of the yield surfaces) is in good agreement with experimental results, while the predicted shear stress (i.e; in the orthogonal direction) is a little bit underestimated. From Fig. 4-9b it is found that the predicted kinematic hardening and isotropic hardening are both slightly underestimated, and the distortional ratio seems also poorly predicted.

The subsequent yield surfaces after combined tension-torsion are shown in Fig. 4-9c. The position and size of subsequent yield surfaces are close to the experimental results.

**Subsequent yield surface evolution under complex loading paths:** The same material parameters of Table 4-3 are used, to investigate the evolution of the subsequent yield surfaces under complex loading paths. The pre-tension path consists on applying a tension loading until 16% of equivalent plastic strain is obtained, and the loading path is translated to shear direction increasingly.

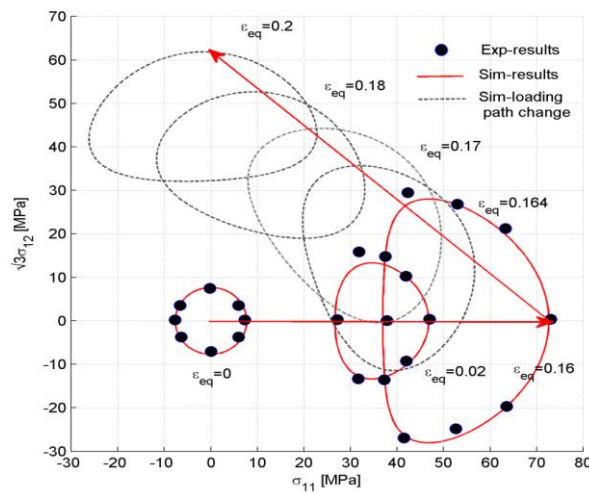


Fig. 4-10. Evolution of subsequent yield surfaces under tension-shear loading path for Al1100.

From Fig. 4-10, the yield surface clearly rotates, when the loading path moves from tension to shear. With the strain increasing, a clear nearby “egg” shaped subsequent yield surfaces appear, with a “nose” on the front, and a flat on the opposite direction. The observed distortional surfaces well fit the experimental observation when  $\varepsilon_{eq} = 2.0\%$  and  $\varepsilon_{eq} = 16.0\%$ , which also proves the good capability of the proposed model. During the loading path change, the subsequent yield surface rotates in such a manner that the “nose” keeps on the front of yield surface following the kinematic hardening direction.

### IV.2.3 Ductile damage parameters identification

For the determination of the damage parameters ( $S, s, \beta, Y_0, h$ ), PNT tests and SS tests are performed until the final fracture to investigate the ductile damage development under these different loading paths characterized by various triaxiality ratios. With ARAMIS system, 1.0 mm and 4.0 mm away to the horizontal central line of notched part on PNT specimens are chosen as the reference coordinates for local displacement output. Local displacement versus global force for PNT tests is chosen as experimental output, and global displacement versus global force for SS tests can test the damage evolution in shear stress state for microcracks closure  $h$  determination. A constant displacement rate of 0.1 mm/s is controlled to insure the quasi-static deformation state.

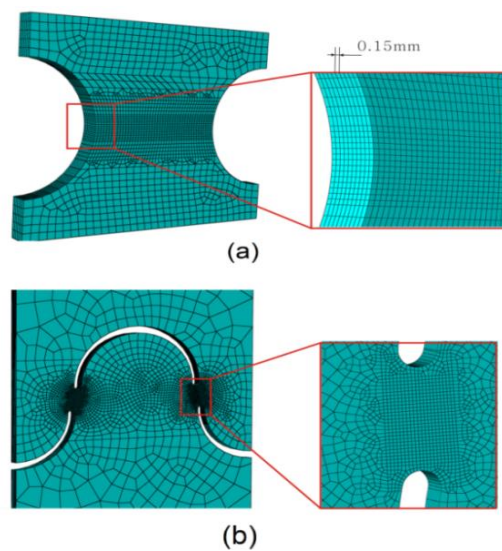


Fig. 4-11. Design and FEM Mesh for (a) the notched specimen (13240 brick elements C3D8R with the minimum mesh size of 0.15mm) (b) the shear specimen (12410 brick elements C3D8R with the minimum mesh size of 0.15mm).

With the elastoplasticity parameters and distortional parameters determined above, The PNT and SS tests are simulated with the same setting conditions in ABAQUS as used above. Since the present model is fully local and accounts for damage-induced softening, the influence of mesh size on damage evolution is handled via accounting the smallest mesh size as a process parameter as well [Saanouni12]. A finer mesh will lead to a faster damage evolution meaning that the numerical solution depends on the mesh size. In fact, the straightforward way to ensure the mesh independency is to use appropriate nonlocal formulations as deeply discussed in the literature (see [Saanouni12]). Accordingly, a constant minimum mesh size of 0.15 mm on the plate surface and in thickness direction is used in the critical deformation zone where the fracture is expected to occur. Fig. 4-11 shows the examples of the mesh conditions for PNT and SS specimens.

The numerical responses of PNT tests (global forces over local info-node displacements) are used into the optimization program to be compared with the experimental responses. For the inverse optimization methodology, the initial values of input damage parameters and normalization method have big influence on the convergence of the objective function (more details in Appendix A). In order to minimize the objective function, the Trust Region reflective method is used. The experimental responses related to the average linearly interpolated displacements of the local nodes with equal weighting. The optimization process involves the approximate solution of a large linear system based on the method of preconditioned conjugate gradients. For the time consuming, the first guessed input damage parameters can be determined firstly with local method, and then taken into the optimization program as the initial parameters values. The critical damage value at fracture is fixed to be constant of 0.99 in order to capture the full process of material fracture, and  $\gamma$  here is fixed to be  $\gamma=4.0$ .  $Y_0$  is the threshold damage force value for which the damage influences clearly the stress-strain curve.

The contributions of any other damage parameters ( $S, s, \beta$ ) to damage evolution and their influences on the damage evolution have been well described in [Saanouni12]. With the help of the inverse approach, by minimizing the error of the objective functions of each test simulations with the nonlinear least squares method, after dozens of optimization cycles the optimal damage parameters ( $S, s, \beta, h$ ) obtained with PNT and SS tests are shown in Table 4-4, which also includes the parameters ( $\gamma, Y_0$ ) obtained with analytical approach for the three materials.

As an example, the evolutions of damage parameters ( $S, s, \beta$ ) for DP1000 are plotted in Fig.4-11 during the iterative process with PNT tests.

Table 4-4 Damage parameters obtained from PNT and SS tests

	$S$ (MPa)	$s$	$\beta$	$\gamma$	$Y_0$ (MPa)	$h$
DP1000	12.5	1.15	2.5	4	2.0	0.25
CP1200	10.2	1.31	1.98	4	2.0	0.21
Al7020	4.50	1.48	3.4	4	0.0	0.3

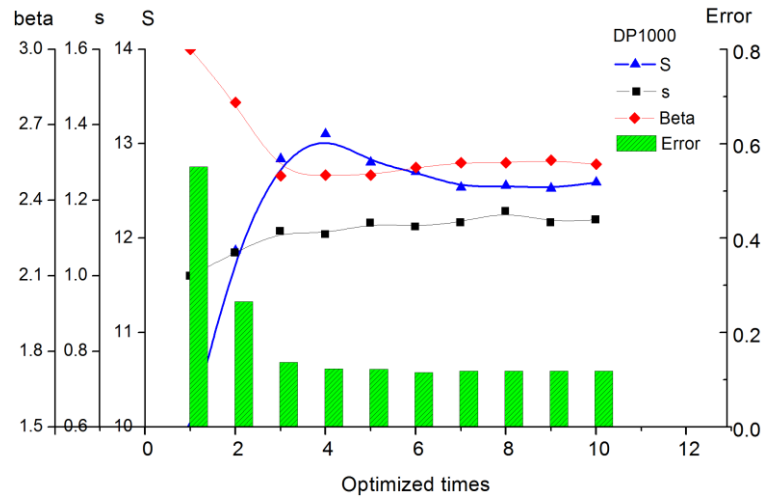
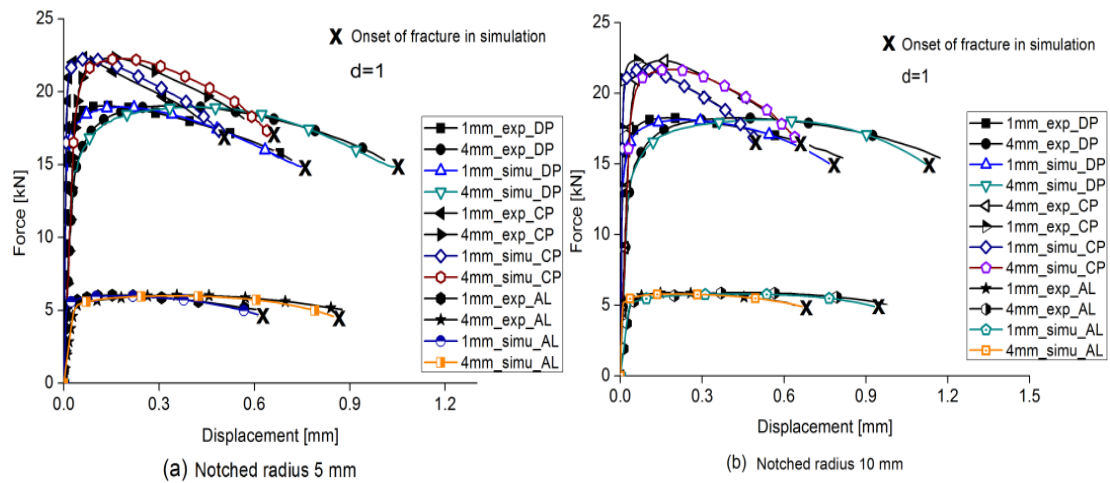


Fig. 4-11. Convergence of damage parameters of DP1000 during the iterative process.



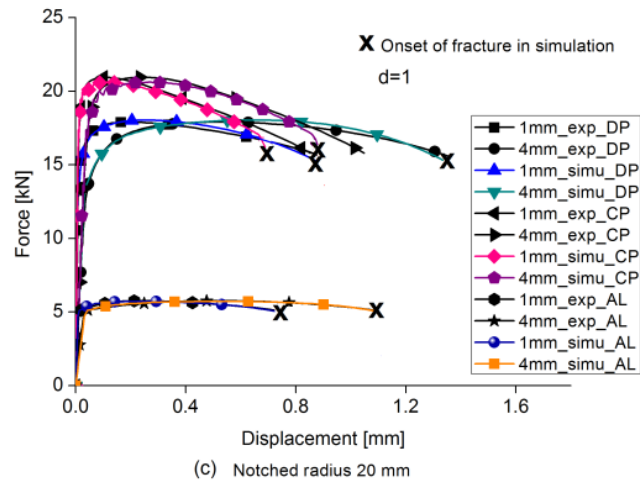


Fig. 4-12. Numerical and experimental responses comparison of PNT tests (The symbol X indicates the first fully damaged integration point in the specimen) (a) Radius 5.0 mm, (b) Radius 10.0 mm, (c) Radius 20.0 mm.

In Fig. 4-12, the results of PNT tests in terms of force-displacement curves for each measurement point using ARAMIS are given for the different notched radii: Fig. 4-12(a) for 5.0 mm, Fig. 4-12(b) for 10.0 mm and Fig. 4-12(c) for 20.0 mm. These curves are plotted for the nodes 1.0 mm and 4.0 mm away from the central axis in the notch section. A good fitting is observed between the experimental and numerically predicted results. However, some discrepancy of the maximum deformation loading is observed in Fig. 4-12(a, b) compared with Fig. 4-12(c), which can be explained by the change of the stress states. The crack initiation points of the simulation results well cover the experimental points as shown in Fig. 4-12 for the three materials.

From Fig. 4-13 to Fig. 4-15, the simulation responses with crack initiation and propagation for three radii 5.0 mm, 10.0 mm and 20.0 mm of Al7020 are given. For these simulation results, the contours of their von-Mises stress, ductile damage (SDV14) and equivalent plastic strain (SDV15) are given for comparison.

From these contours, we can find the stress, strain and ductile damage localize at the notched parts of the specimens during the loading paths, and the final crack initiates in the center of the notched part, and propagates horizontally to the both notched edges. As expected due to the strong coupling, with the increase of the ductile damage in the center the equivalent von Mises stress decreases and reaches zero. The macroscopic crack initiation seems to happen at  $1.0 < U < 1.05$  mm for  $r^c = 5.0$  mm (Fig.4-13), at  $1.1 < U < 1.2$  mm for

$r^c = 10.0\text{mm}$  (Fig.4-14) and at  $1.3 < U < 1.4\text{mm}$  for  $r^c = 20.0\text{mm}$  (Fig.4-15). As expected the crack initiation is delayed as the notched radius increases. This is conforming to the experimental results.

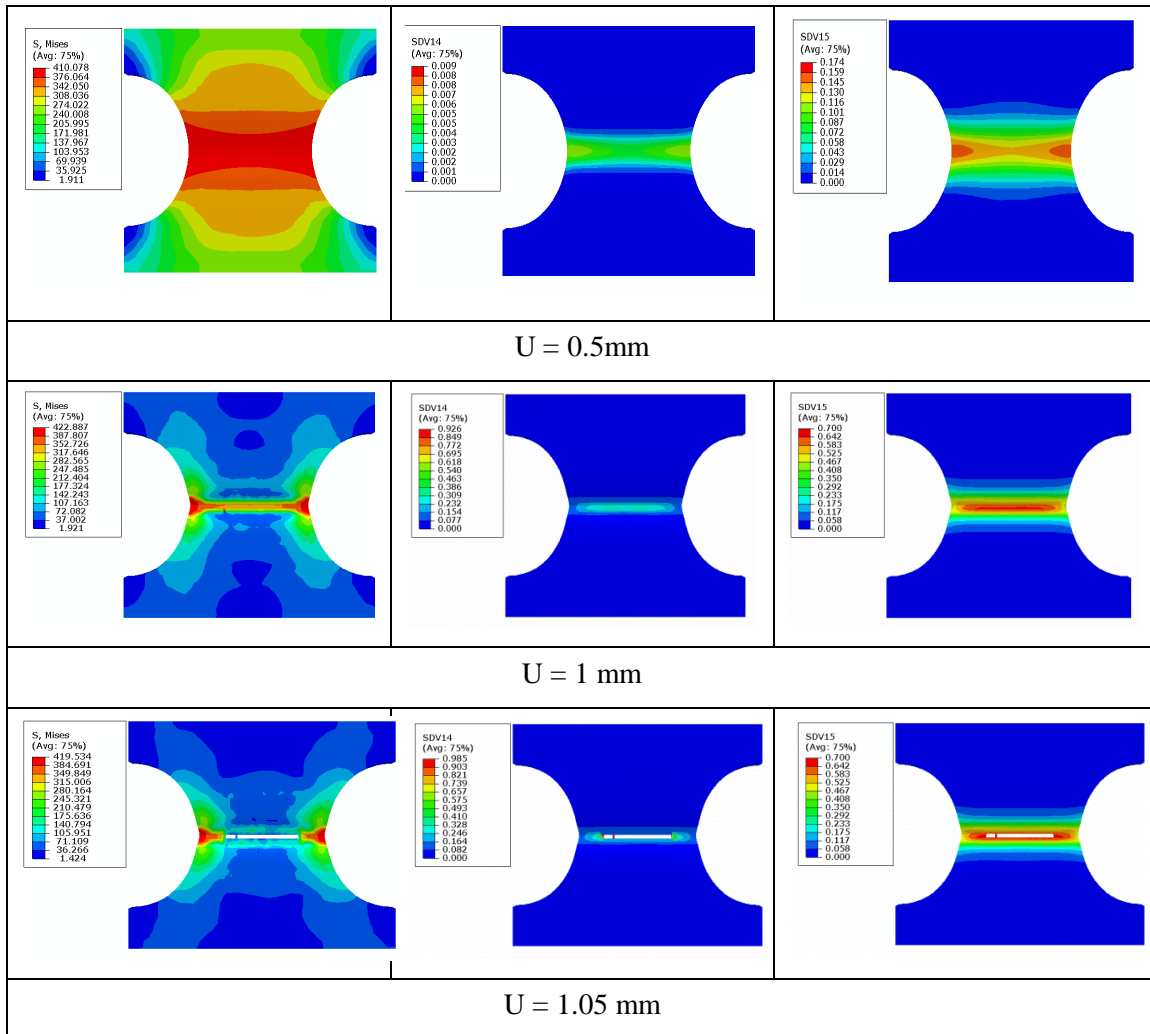
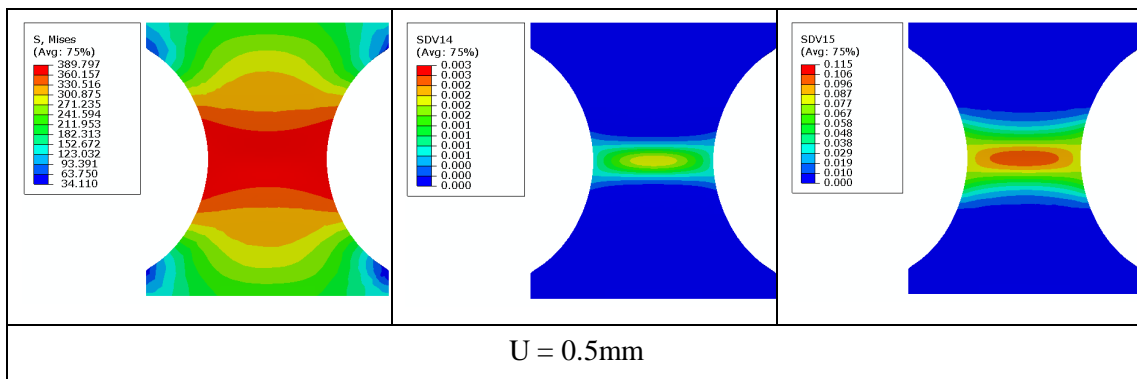


Fig. 4-13. Contour of the equivalent von Mises stress, damage (SDV14) and plastic strain (SDV15) for PNT test of Al7020 with  $r^c = 5.0\text{mm}$ .





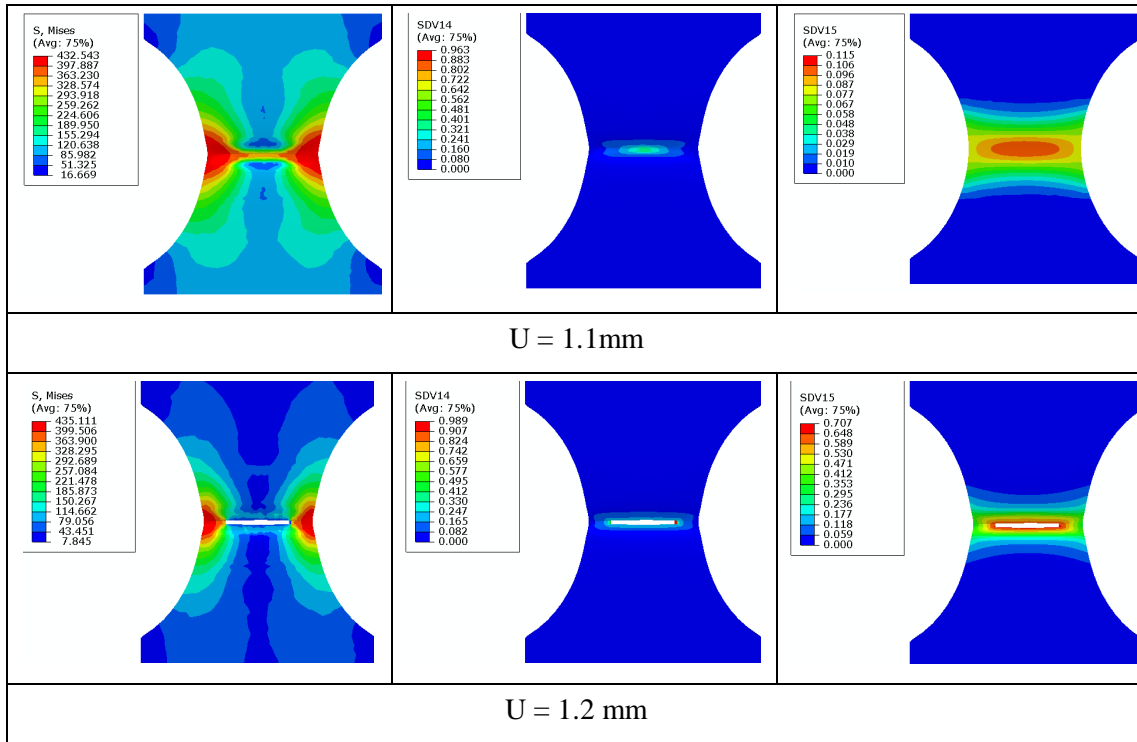
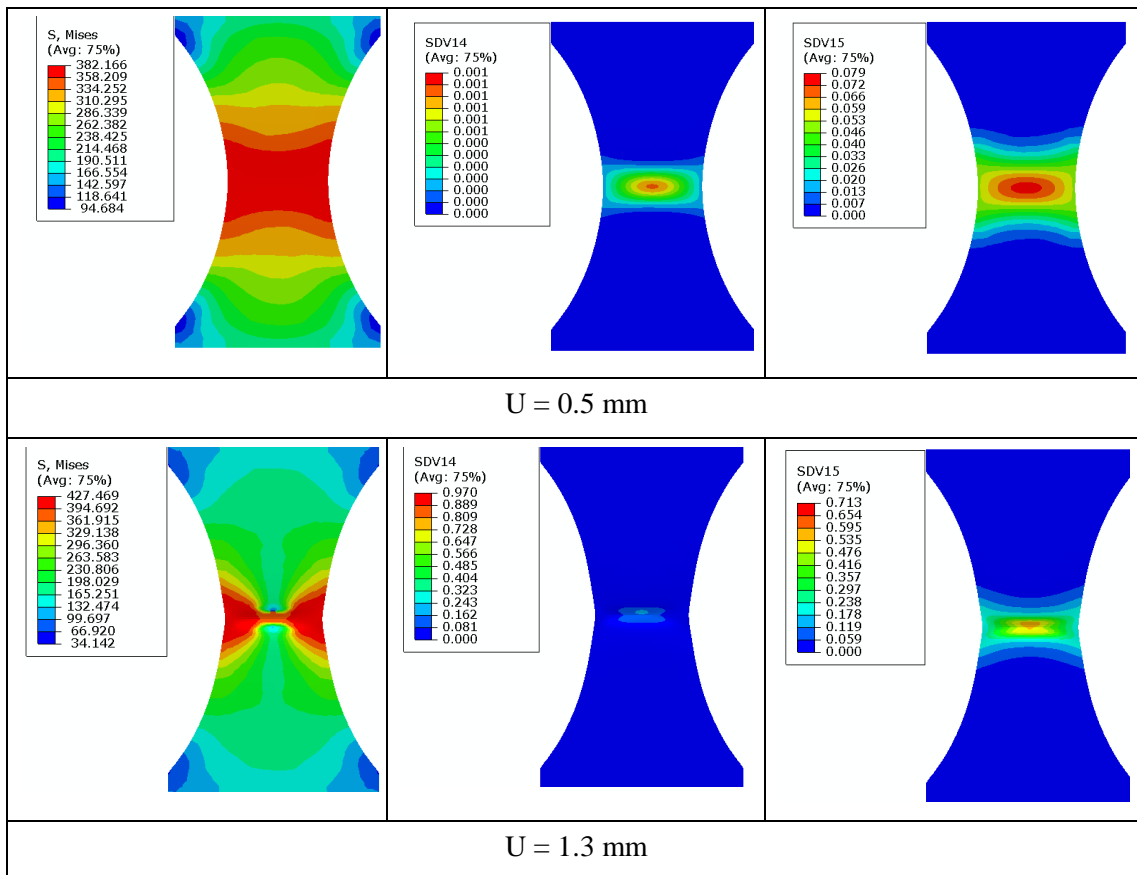


Fig. 4-14. Contour of the equivalent von Mises stress, damage (SDV14) and plastic strain (SDV15) for PNT test of Al7020 with  $r^c = 10.0$  mm.



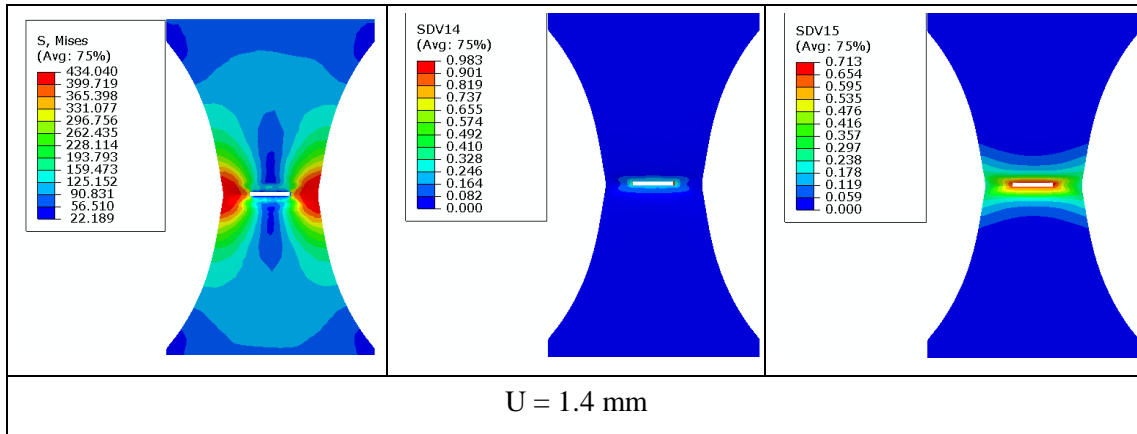


Fig. 4-15. Contour of the equivalent von Mises stress, damage (SDV14) and plastic strain (SDV15) for PNT test of Al7020 with  $r^c = 20.0$  mm.

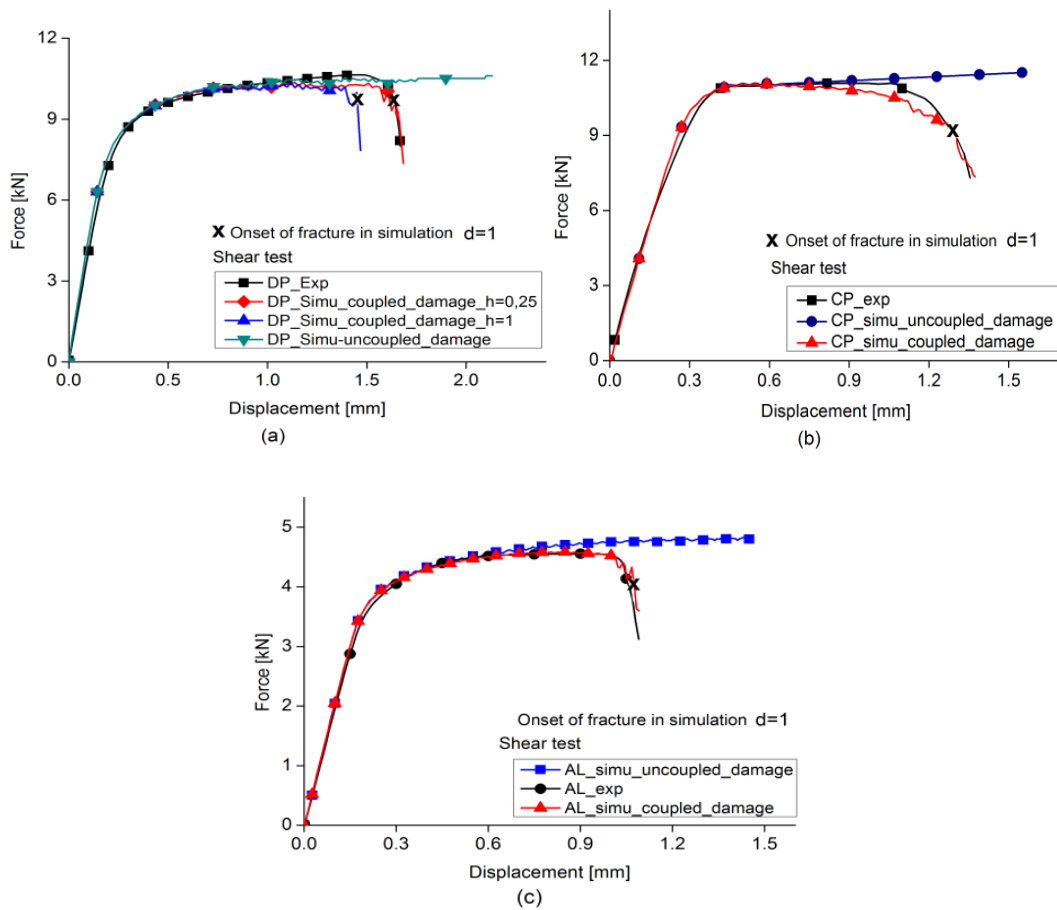


Fig. 4-16. Comparison of numerical and experimental force-displacement responses for SS tests (a) DP1000 (b) CP1200 (c) Al7020.

Fig. 4-16 shows the comparisons of experimental responses and numerical responses for SS tests in two cases: fully coupled and uncoupled models with the same model parameters, which can clearly show the ductile damage influence (induced softening). In Fig.4-16a, the

simulation results with  $h = 1$  (without microcracks closure) and  $h = 0.25$  are given (with microcracks closure), which can clearly indicates the contribution of microcracks closure effect on the limit plastic strain in simple shear conditions.

**Analysis of the damage effect:** With the optimized parameters, the contour of the crack surface of PNT specimen for Al7020 is shown in Fig.4-17. The notched radius of the specimen is 5.0 mm. A constant minimum mesh size of 0.15 mm on the plate surface and in thickness direction is used in the critical deformation zone where the fracture is expected to occur.

During the whole deformation history, when  $d = 1.0$ , the element is failed and deleted from the mesh (kill-element technique). The initial failure element locates in the center of notched zone, and finally extends to the edge of the specimen, that can be explained by the relationship of triaxiality ratio  $\eta$  and equivalent limit plastic strain. For the material in tension states, the equivalent limit plastic strain will decrease with the increase of triaxiality ratio  $\eta$ . In the notched tension tests, the  $\eta$  value in the center point is higher than the value on the edge of the specimen. When the notched radius is changed (three radii used in our tests:  $r^c = 5.0\text{ mm}$ ,  $r^c = 10.0\text{ mm}$ ,  $r^c = 20.0\text{ mm}$ ), the  $\eta$  value in the critical zones is changed at the same time ( $\eta_5 > \eta_{10} > \eta_{20}$ ), and further the limit equivalent strains should be  $\bar{\epsilon}_5^{eq} < \bar{\epsilon}_{10}^{eq} < \bar{\epsilon}_{20}^{eq}$ , which explains why the onset of fracture of the specimen with  $r^c = 5.0\text{ mm}$  is earlier than the one with  $r^c = 20.0\text{ mm}$ .

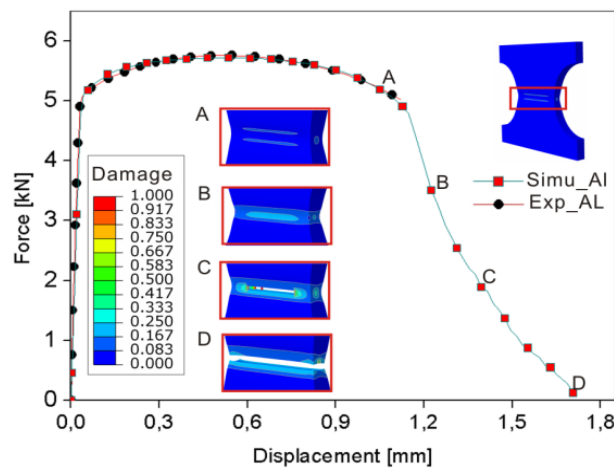


Fig. 4-17. Crack initiation and propagation at the notch region regarding its location on the Force-displacement curve ( $r^c = 5.0\text{ mm}$ ).

The relationship between equivalent plastic strain and stress triaxiality ratio at the critical

point is shown in Fig. 4-18. During the whole process, the flow tendencies of triaxiality ratios development at the critical and central points of the specimens show to be different. For the central point of SS specimen, it shows constant waving near the 0.1 value, while the value of critical point increases with the strain.

For PNT specimen, it is found that with the increase of notched radius, the triaxiality ratio decreases, and the equivalent plastic strain increases. The triaxiality ratio actually affects the deformation capability of the sheet.

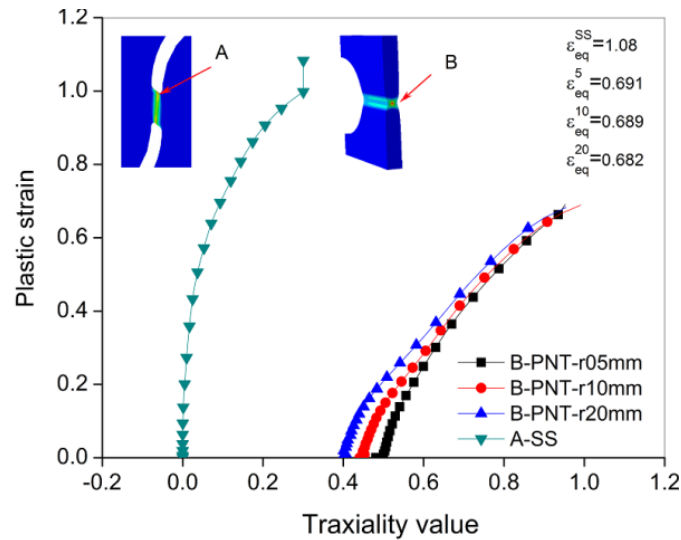


Fig. 4-18. Evolution of the equivalent plastic strain as a function of triaxiality ratio until the final fracture for SS and PNT tests.

### IV.3 Determination of FLD and FLSD for Al7020

For FLD and FLSD determination, only the Swift isotropic hardening rule is considered. The determined parameters are shown in Equation 3-16. Fig 3-51 shows the comparison between the experimental and numerical true stress-true strain curves with a good agreement between them before necking.

After the material parameters for Al7020 are determined, we set the strain increment  $\varepsilon_i = 0.002$  and the stress states between simple shear and biaxial tension are divided into 10 parts. The FLD and FLSD curves can be easily obtained with hundreds of calculations with M-K model. As shown in Fig. 4-19, with two initial imperfection factors  $f_0 = 0.99$  and  $f_0 = 0.998$ . The FLD and FLSD give different responses. The greater value of  $f_0$  postpones the coming of

failure of the material. From the Fig. 4-19a, we can find that when  $f_0=0.998$ , the simulated failure points cover with the experimental responses, which mean giving good results, so  $f_0 = 0.998$  is chosen as the defined imperfection factor for Al7020. In the coming works, the calculated FLD and FLSD curves of Al7020 will be input into ABAQUS as the failure criterion in order to estimate the capability of the CDM model.

Table 4-5 Elasto-plastic parameters for Al7020

E (GPa)	$\nu$	$\sigma_y$ (MPa)	F	G	H	L	M	N
69.8	0.3	322	0.631	0.634	0.366	1.5	1.5	1.4

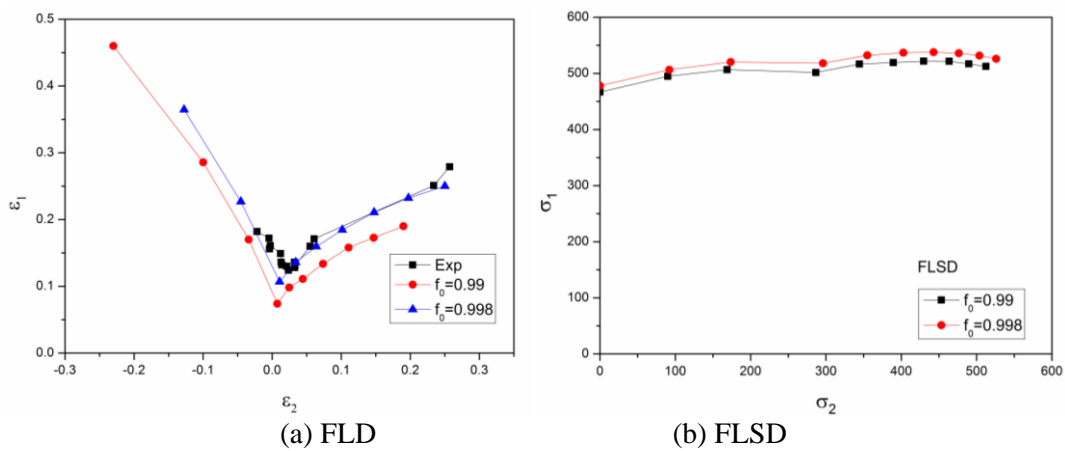


Fig. 4-19. Experimental and theoretical FLDs and FLSDs with M-K model for Al7020

#### IV.4 Nakazima tests simulation with fully coupled CDM model

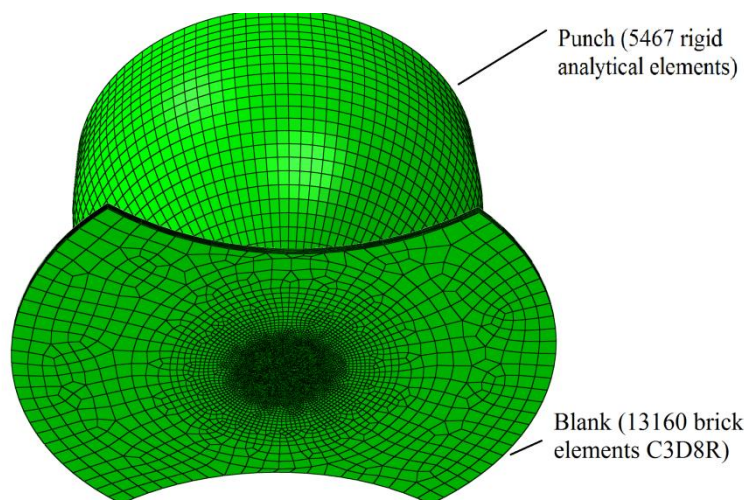


Fig. 4-20. Mesh condition for Sample 4 of Nakazima tests.

The calculations are also carried out using the ABAQUS/Explicit. The material parameters input for three materials are listed in Table 4-2 and Table 4-4 neglecting the yield surface distortion. The geometrical model is shown in Fig. 4-20. There gives the example for the specimen with  $r^N = 65.0$  mm. The C3D8R brick element is used to mesh the sheet. In the critical zone, the minimum mesh size of 0.15 mm is used, giving 10 elements throughout the thickness and a total of 13160 elements. The punch moves vertically with a constant speed of 10.0 mm/s. When the punch comes in contact with the blank, the Coulomb friction model with friction coefficients  $\mu = 0.05$  is used. The simulation will stop when the final fracture happens on the blank.

The comparisons of the experimental and numerical force-displacement responses of A17020 and DP1000 are shown Fig. 4-21. As we can see, with the decreasing of the width (i.e., increasing of notched radius) of specimens, the maximum limit force and displacement decrease at the same time. The simulation results well capture this effect. In Fig. 4-21(a) are shown the comparisons of Force-displacement curves for A17020. Except sample 3 and 6, a good agreement between experiment and simulation is observed. The maximal difference is less than 5%. But for sample 3 and 6, the maximum differences between limit displacements seem more than 10%. In Fig. 4-21(b), there gives the comparisons for DP1000. The maximum differences of the limit displacement are for sample 1 and 2. In Fig. 4-22 we give the more intuitive comparisons for these two simulations of NAK for A17020 and DP1000, including the maximum values of drawing depths and equivalent strains.

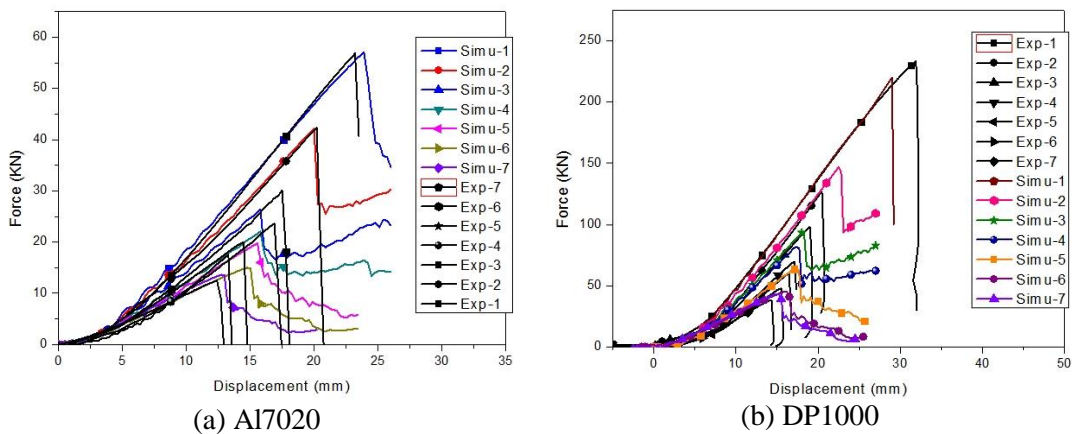
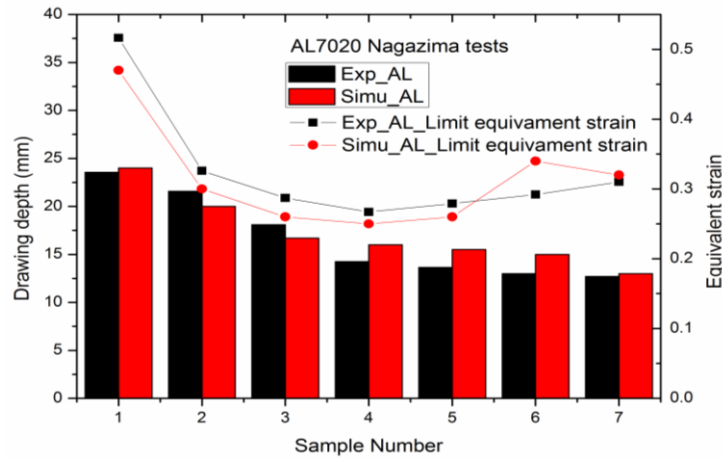
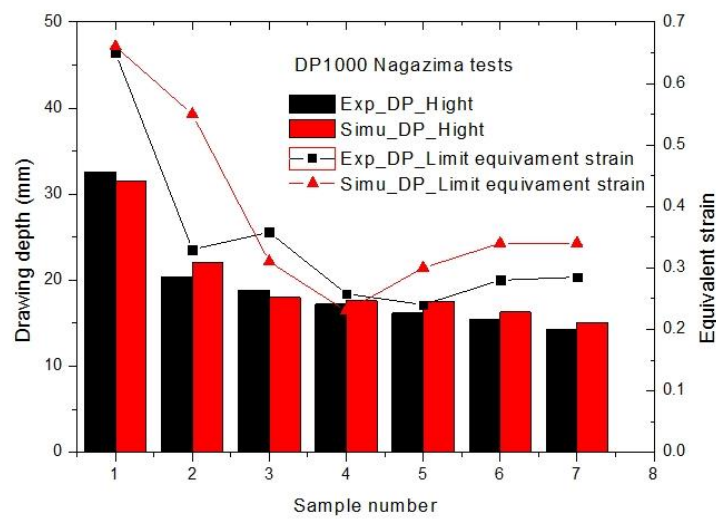


Fig. 4-21. Comparison of the Force-Displacement between experimental and simulation responses.



(a) Al7020



(b) DP1000

Fig. 4-22. Comparison of the limit displacement and equivalent plastic strain for (a) Al7020, (b) DP1000.

In order to better present the stress, plastic strain and damage development during the deformation history, the example of sample 4 of Al7020 and DP1000 is chosen. Fig. 4-23 gives the spatial distribution of the von Mises equivalent stress, the accumulated plastic strain and damage at different displacement values namely:  $u = 5.0$  mm,  $u = 10.0$  mm and  $u = 16.0$  mm corresponding to the crack occurrence for Al7020. As expected, the localizations of all the mechanical fields including the ductile damage, takes place at the central areas of the specimens.

Clearly, the ductile damage localization follows the accumulated plastic strain, and its localization becomes stronger than the accumulated plastic strain localization (Fig. 4-24). The similar distributions of these fields are observed in Fig. 4-26, 4-27, 4-28 for DP1000. Note

that, for this local formulation the thickness of the macroscopic crack is clearly correlated to the smallest mesh size (i.e. 0.15 mm).

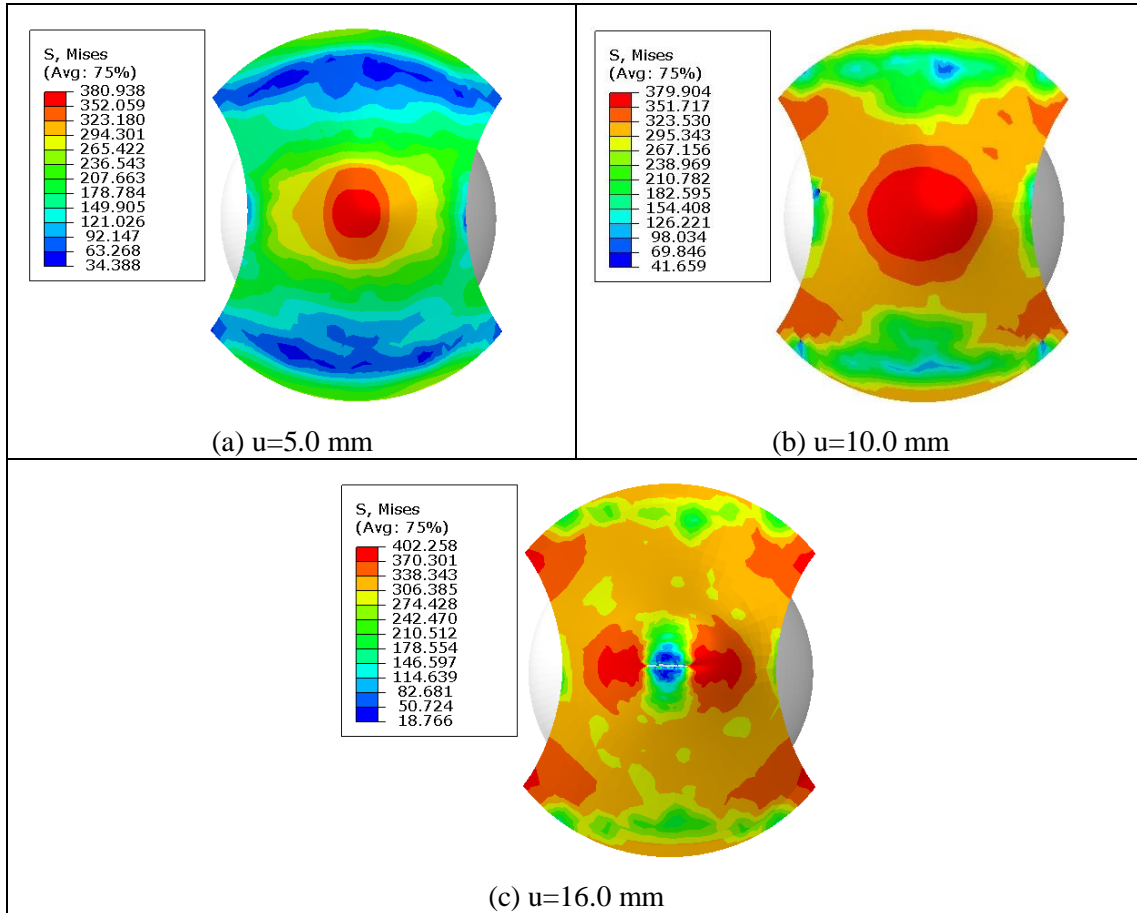
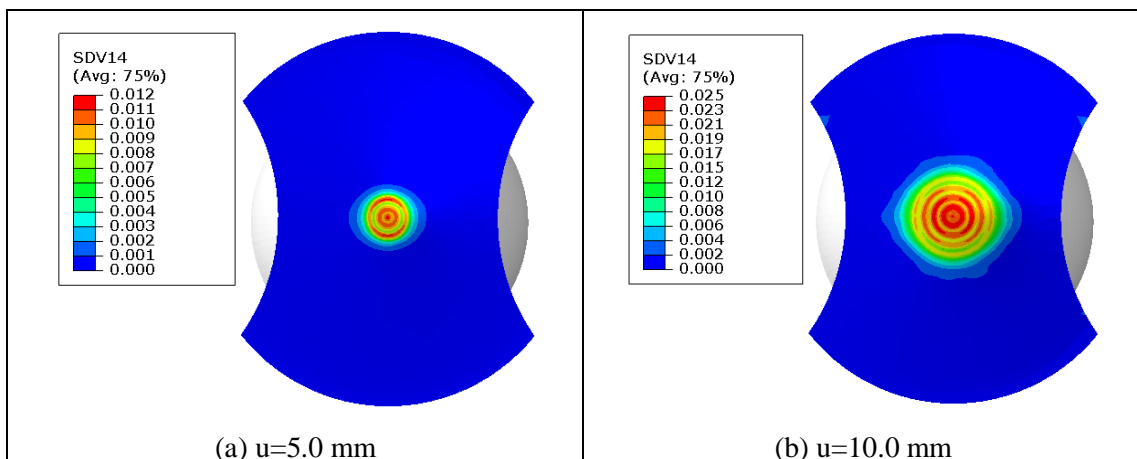


Fig. 4-23. Equivalent von Mises stress distribution for Al7020.





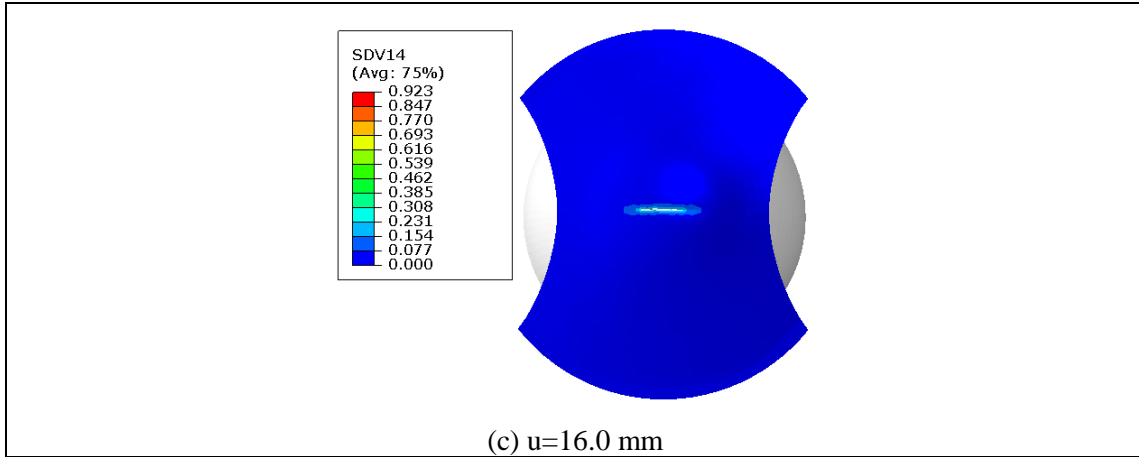


Fig. 4-24. Equivalent plastic strain distribution for Al7020.

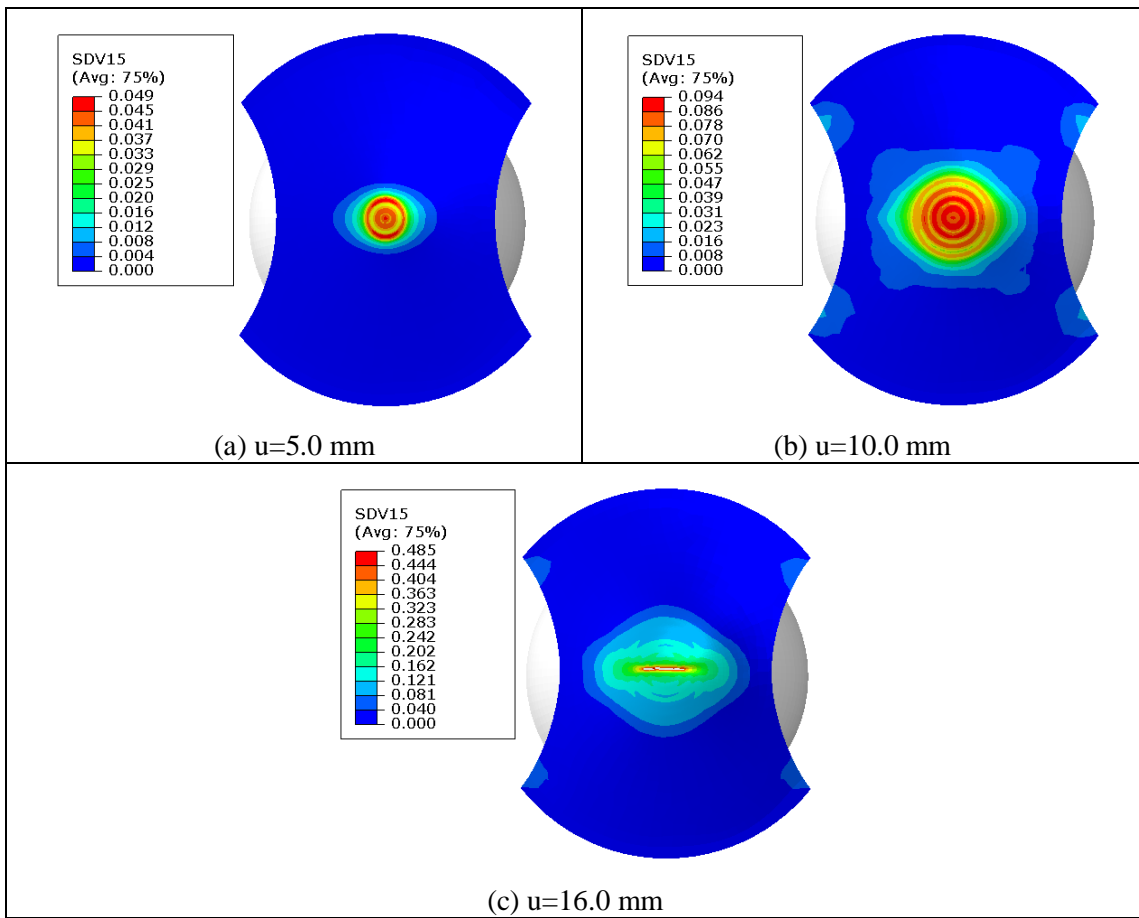


Fig. 4-25. Damage distribution for Al7020.

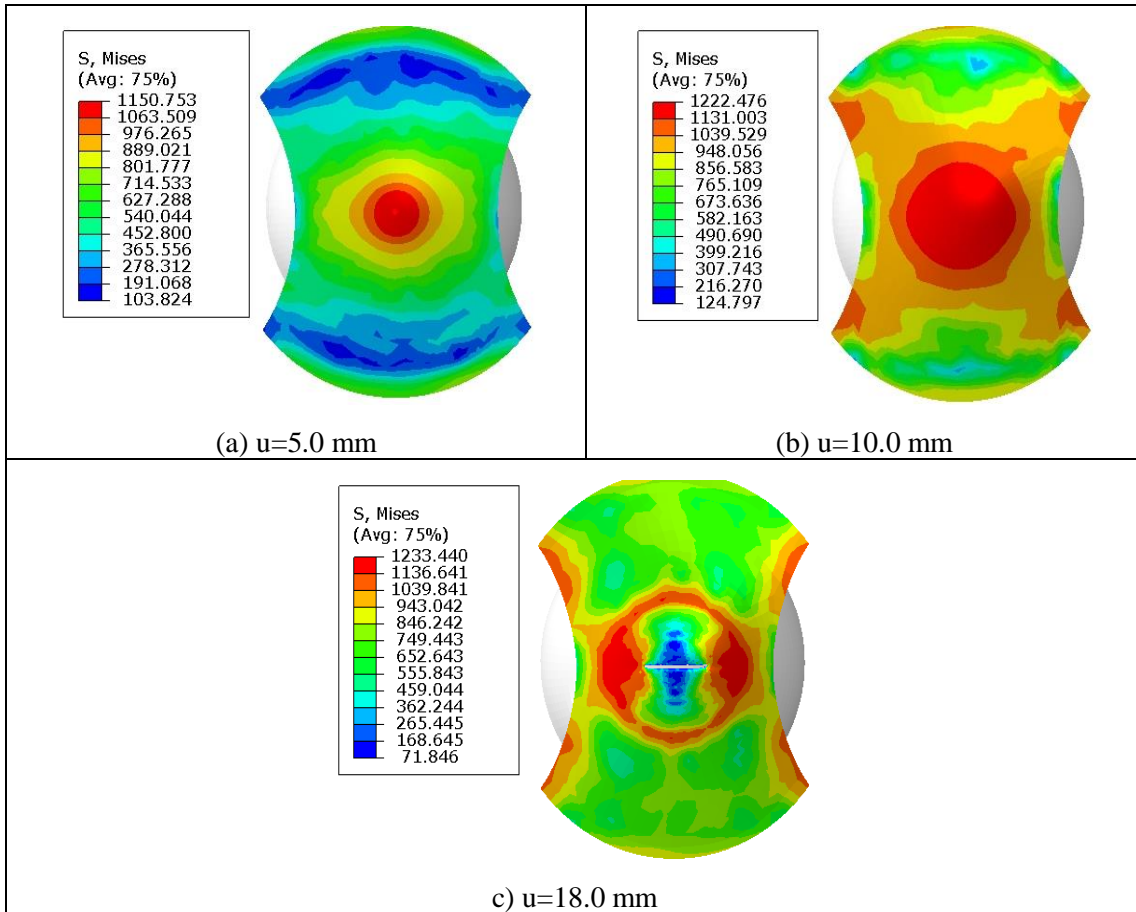
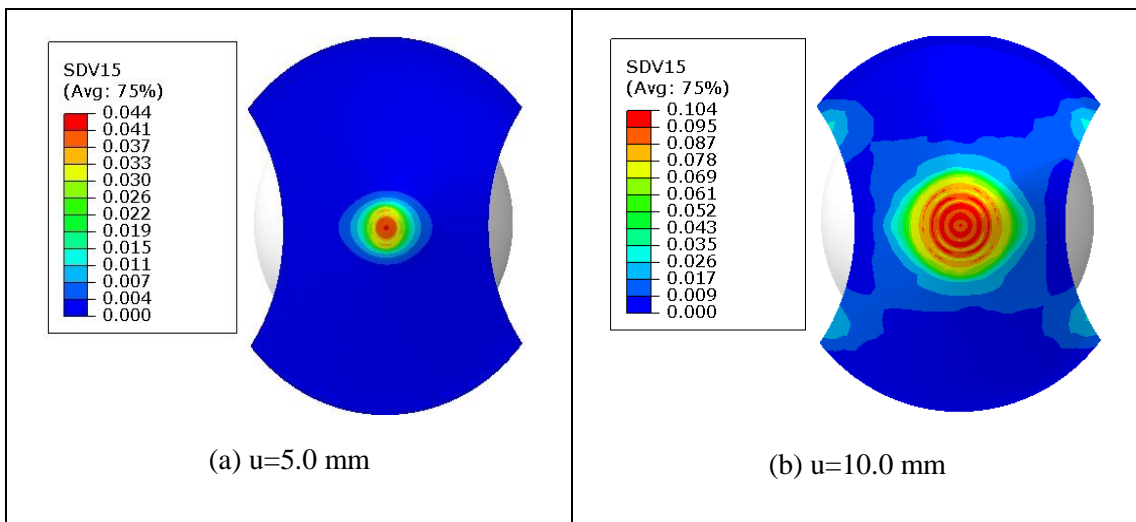


Fig. 4-26. Equivalent von Mises stress distribution for DP1000.



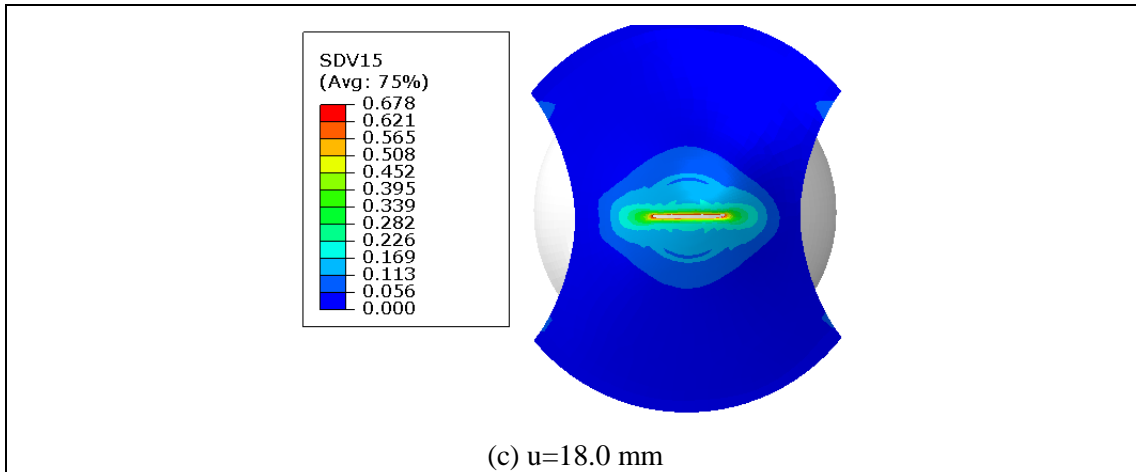


Fig. 4-27. Equivalent plastic strain distribution for DP1000.

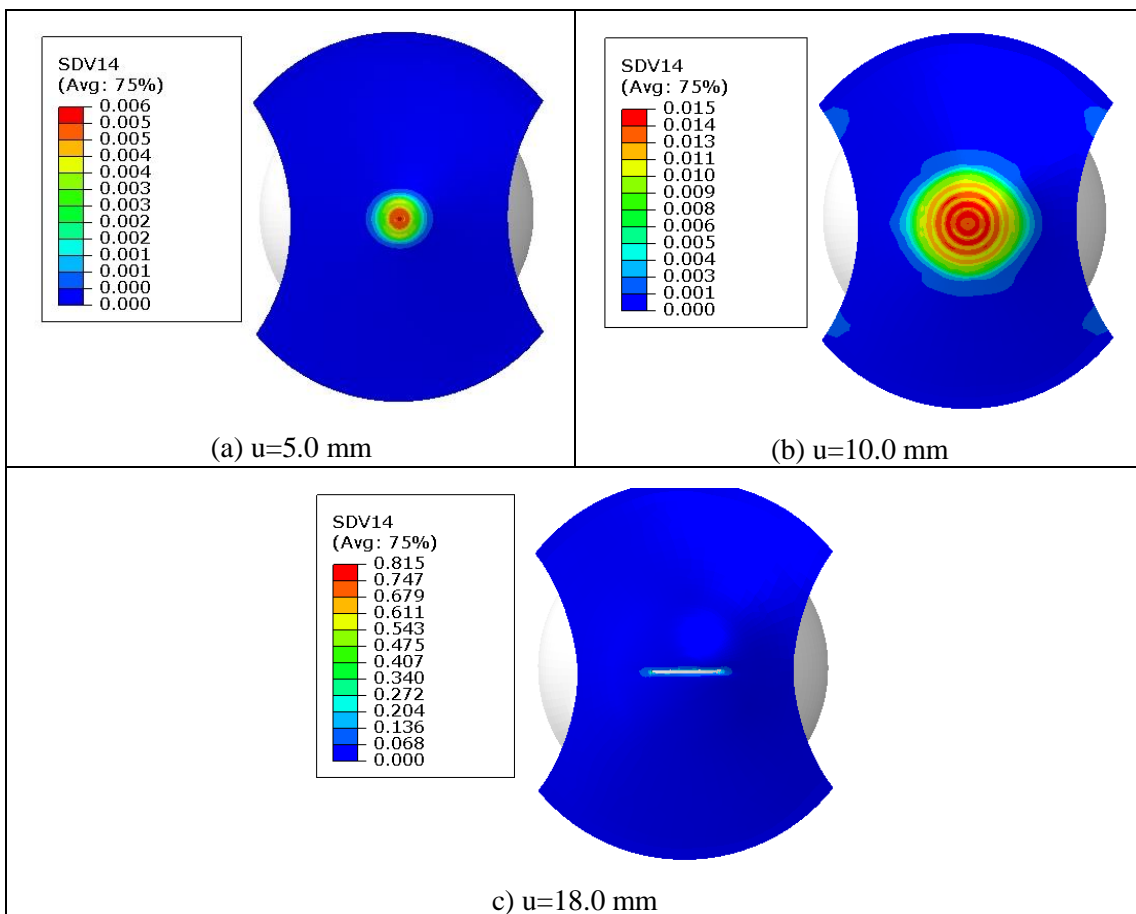
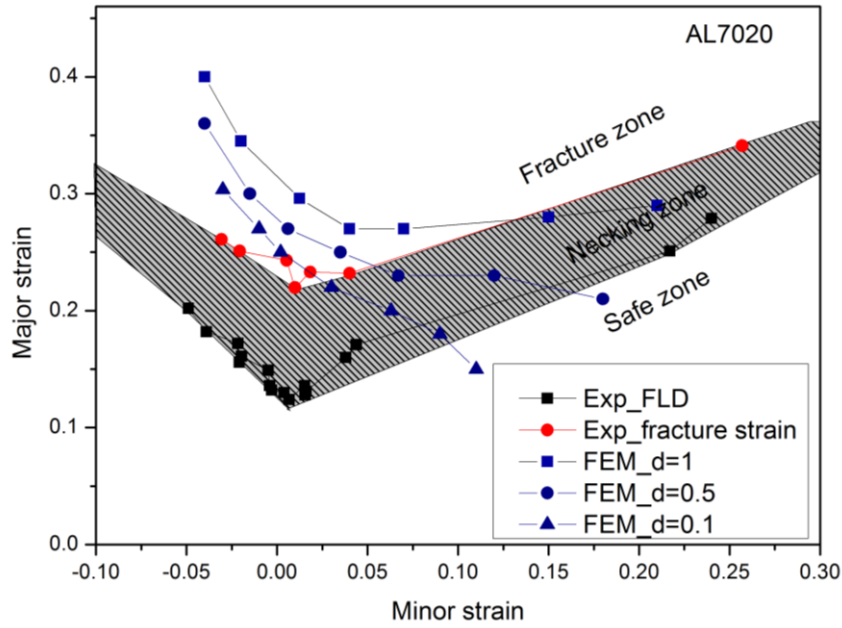


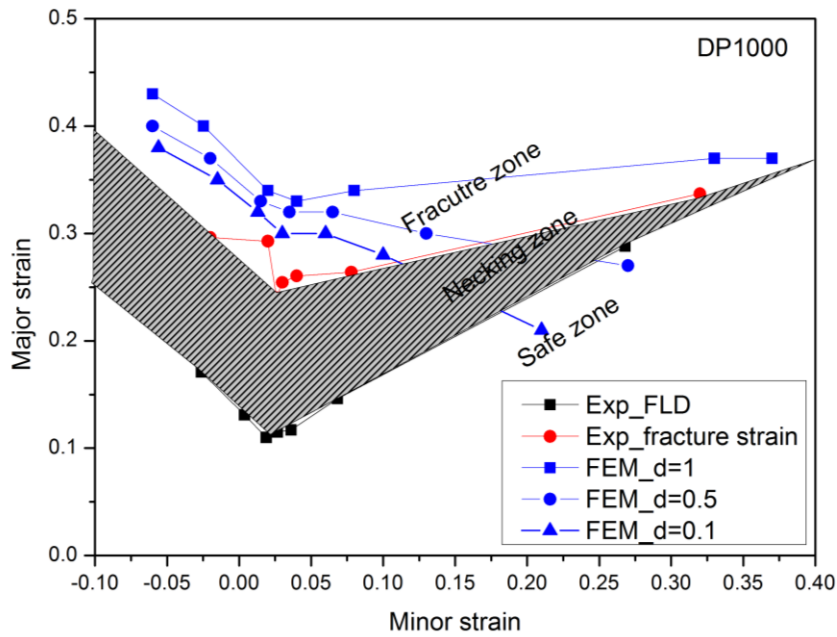
Fig. 4-28. Damage distribution for DP1000.

After the simulations of the whole NAK tests, we also can plot the forming limit curves corresponding to the damage value in order to compare the difference with FLD curves as shown in Fig. 4-29, separately for Al7020 and DP1000. The critical damage value  $d_f$  is defined as 0.1, 0.5 and 1.0 separately. With the decreasing  $d_f$ , the FLCs predicted by the

CDM model get close to the experimental FLC, but there still some big differences between them. In the low triaxiality ratio region (left hand of FLD), the CDM predicted FLCs is higher than the FLC and FFLD (fracture forming limit diagram) obtained from experiments, and the opposite is observed in the high triaxiality ratio region (right hand of FLD). The CDM predicted FLC is more close to FFLD when  $d_f = 0.1$ , but still underestimate the limit strains in high triaxiality ratio region.



(a) AL7020



(b) DP1000

Fig. 4-29. Comparison of the numerical predicted FLCs and experimental FLCs.

The difference between the FLD curves obtained from the simulation results with fully coupled CDM model and experiments seems due to the experimental strain measurements, which underestimate the values of the plastic strain inside the highly localized zones. It is clear from Fig.4-29 that our model predicts higher values of the major strains compared to the experimentally measured ones. This point need to be deeply examined in the future by using complementary accurate measurement technologies as ESPI (Electronic speckle pattern interferometry).

## IV.5 Cross section deep drawing tests (CSD)

The cross section deep drawing tests (CSD) of the three studied materials are also simulated using ABAQUS/Explicit with fully coupled CDM model to predict their forming limits. In addition for Al7020, the FLD and FLSD got with M-K approach are also used to compare with the proposed fully coupled CDM method. The modeled geometry (in order to well present the model structure, only half of the geometry is given) and the adopted finite element mesh are shown respectively in Fig. 4-30 and Fig. 4-31. In order to avoid the boundary condition effect, the full specimen is modeled in the simulation. The C3D8R brick element is used to construct the blank. With the 0.15 mm mesh size in the critical deformation (shown in Fig. 4-31). There are totally 675615 eight-nodes solid elements used for the discretization of the sheet metal specimen.

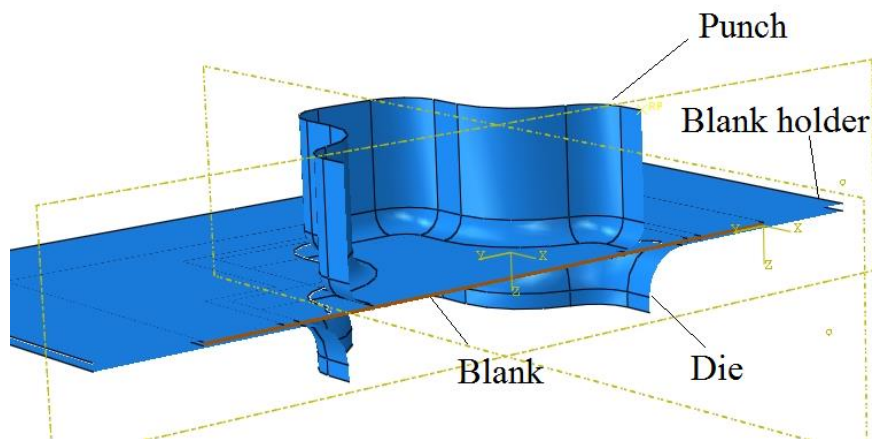


Fig. 4-30. Half part of the FEM model for CSD test.

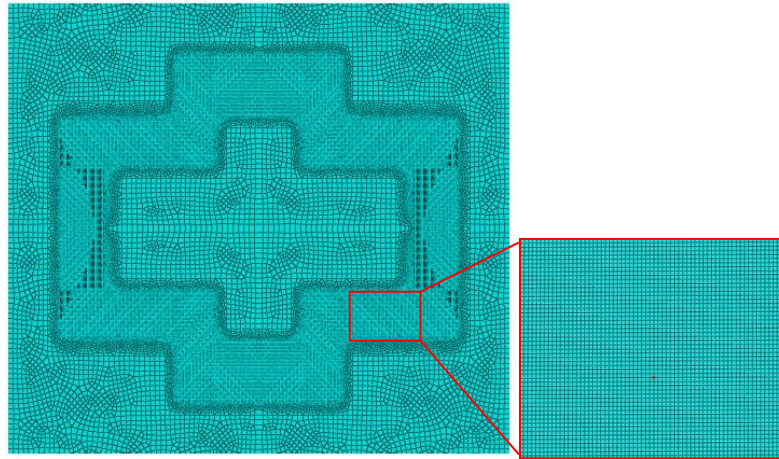


Fig. 4-31. Mesh condition of blank for CSD tests (157860 brick elements C3D8R with  $0.15 \times 0.15 \text{ mm}^2$  in the critical zone).

**CSD simulation for Al7020:** For Al7020, the blank holder force is set to be 120.0 kN. The comparison between experimental and numerical force-displacement curves is shown in Fig. 4-32. A good agreement is shown between these two responses.

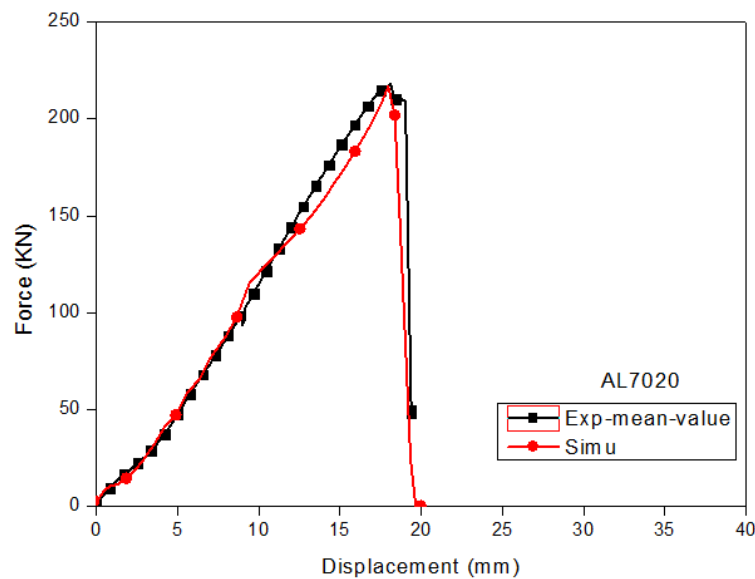


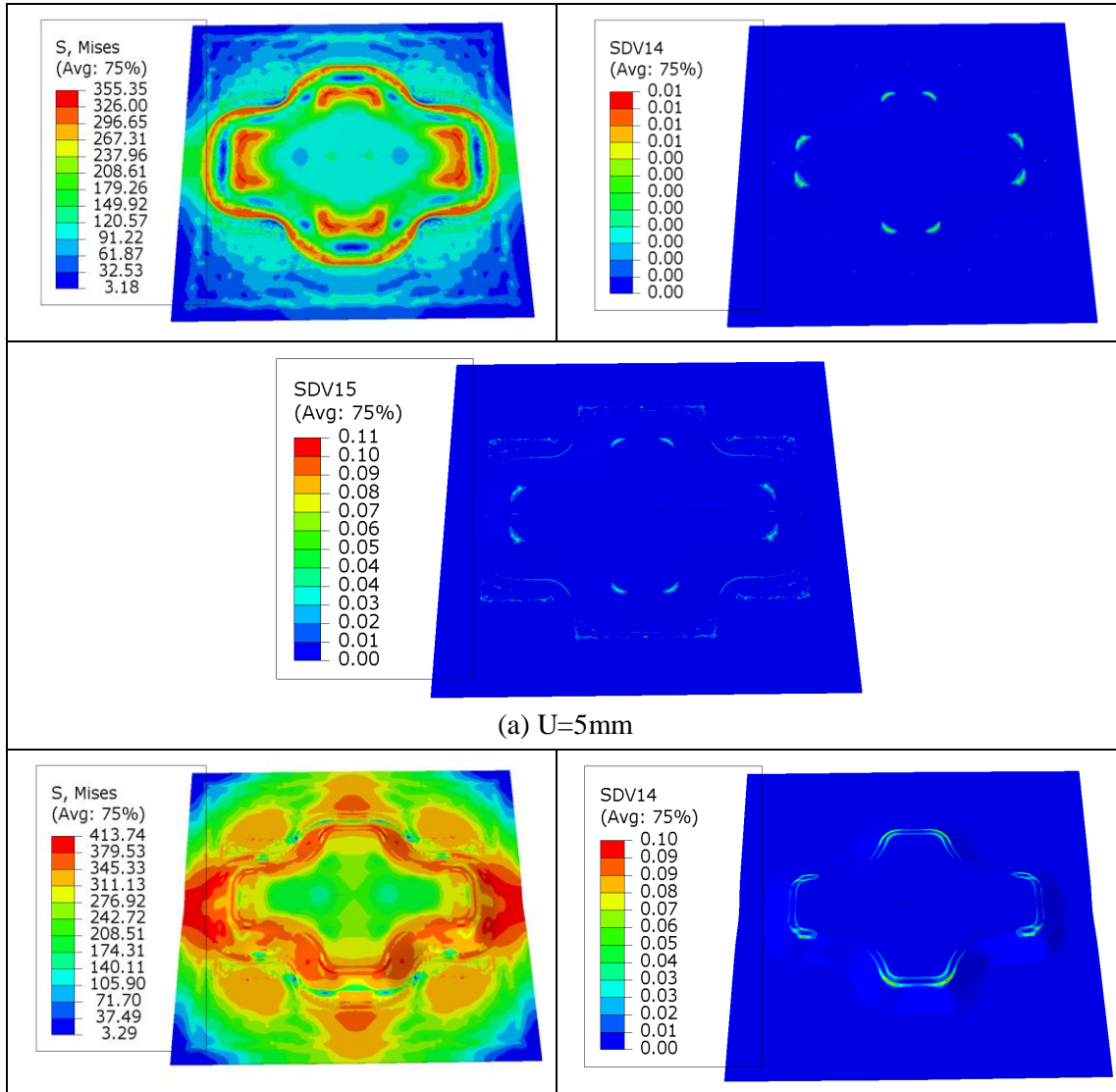
Fig. 4-32. Comparison of the force-displacement curves of numerical and experimental responses for CSD tests for Al7020.

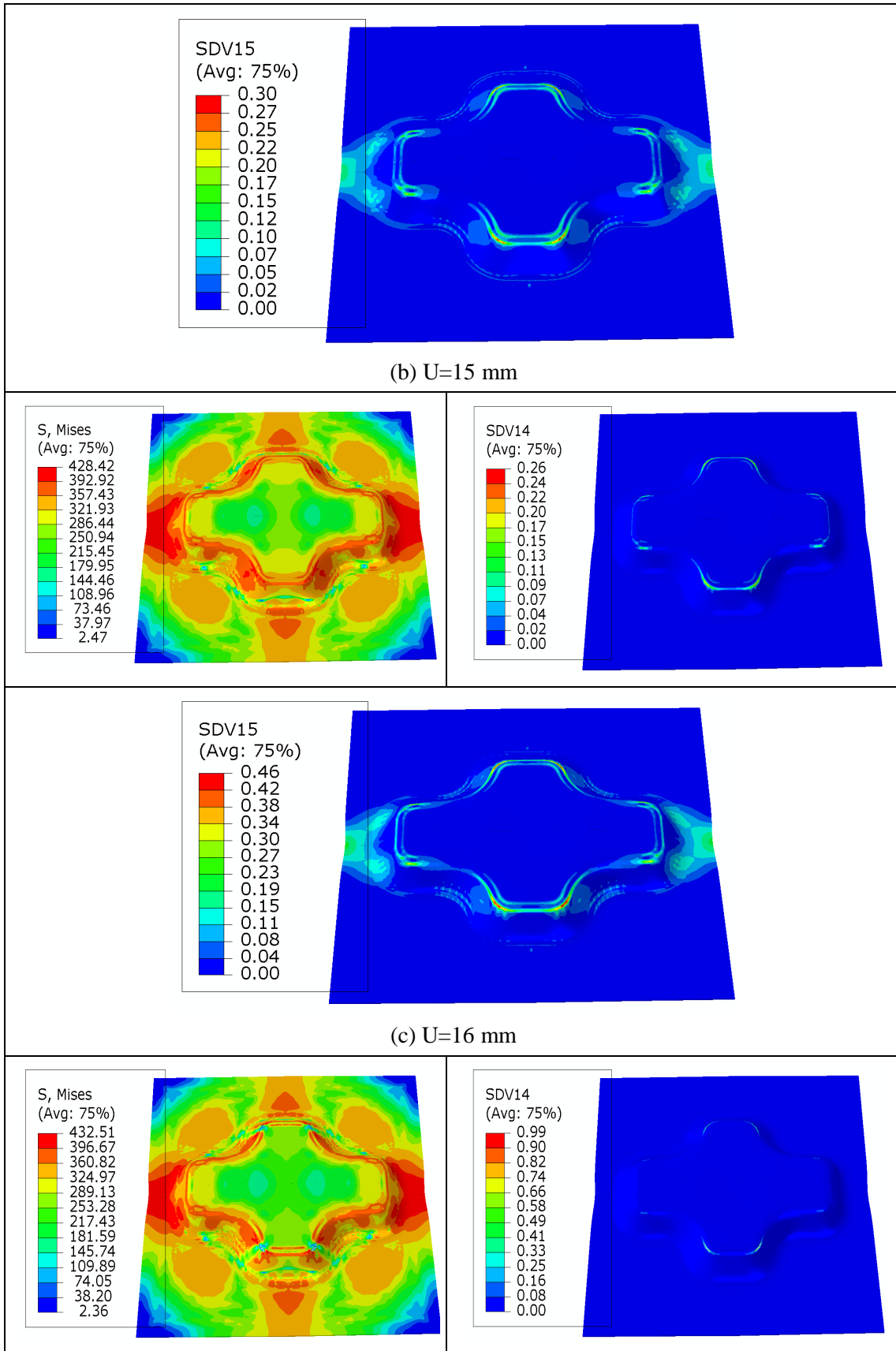
In Fig. 4-33, the von Mises stress ductile damage (SDV14) and accumulated plastic strain (SDV15) distribution during the forming process of Al7020 are given for  $U = 5.0 \text{ mm}$ ,  $U = 15.0 \text{ mm}$ ,  $U = 16.0 \text{ mm}$ ,  $U = 17.0 \text{ mm}$  and  $U = 18.0 \text{ mm}$ . These fields localized at the eight corners of the cross-shaped punch (Fig. 4-33a) and the extend along the edges of the punch as



shown in Fig.4-33b, c, d, e.

At  $U = 16.0$  mm the higher values of the ductile damage is located along the same edges with a maximum value of 0.26 (Fig. 4-33c). The first macroscopic cracks (4 cracks) appear for  $U = 17.0$  mm as shown in Fig.4-33d. These four cracks propagate along the edges of the punch as indicated in Fig. 4-33e. From these figures we can clearly observe that the equivalent stress decreases inside the zone where ductile damage increases. At the final fracture the stress is clearly zero inside the fully damaged zone as shown in Fig. 4-33e.







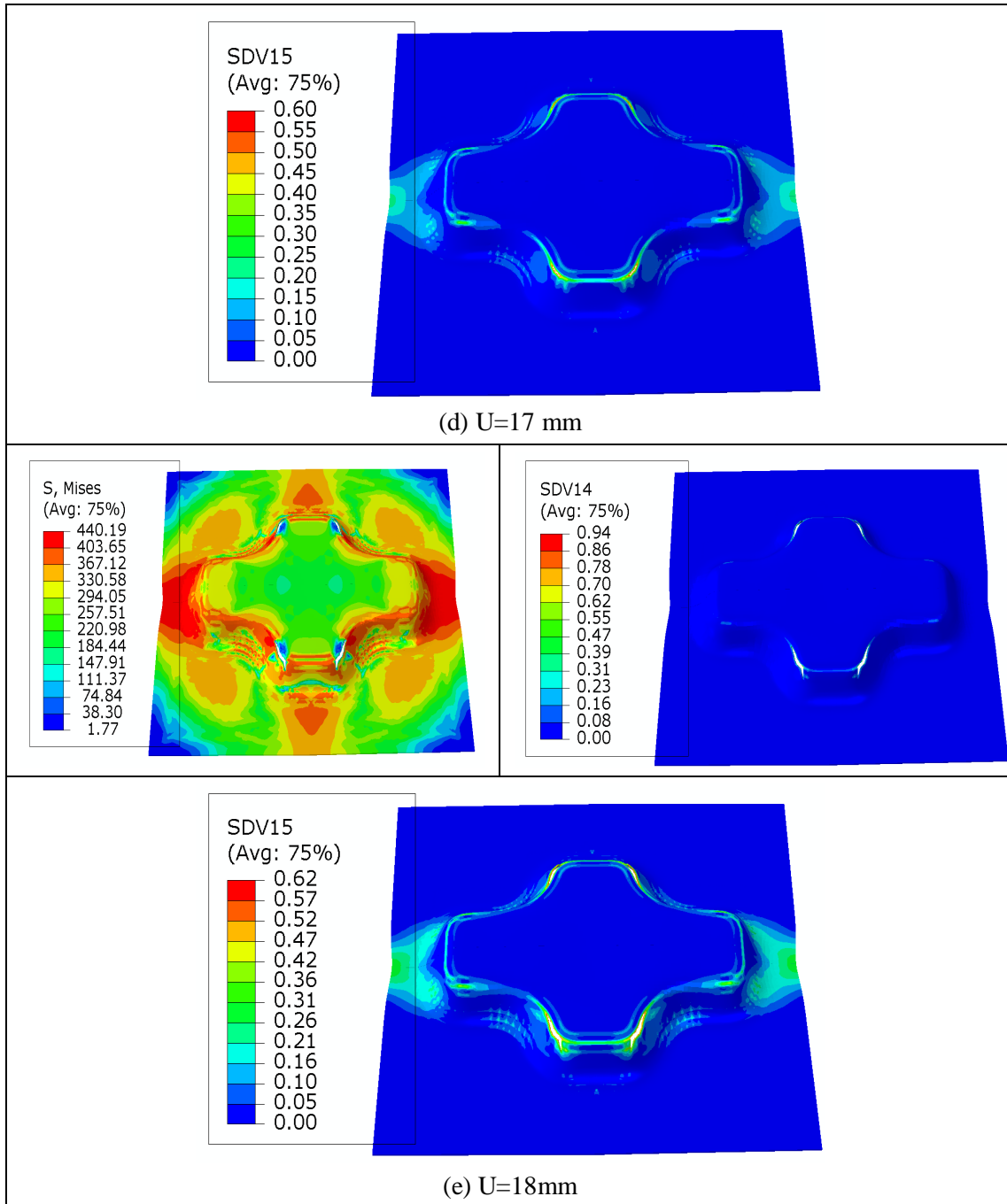


Fig. 4-33. Distributions of von Mises stress, the equivalent plastic strain and the ductile damage for Al7020 at different displacements.

<p>Numerically predicted crack at U = 18.0 mm</p>	<p>Experimentally observed crack at <math>U_{exp} = 18.44</math> mm</p>
---	---

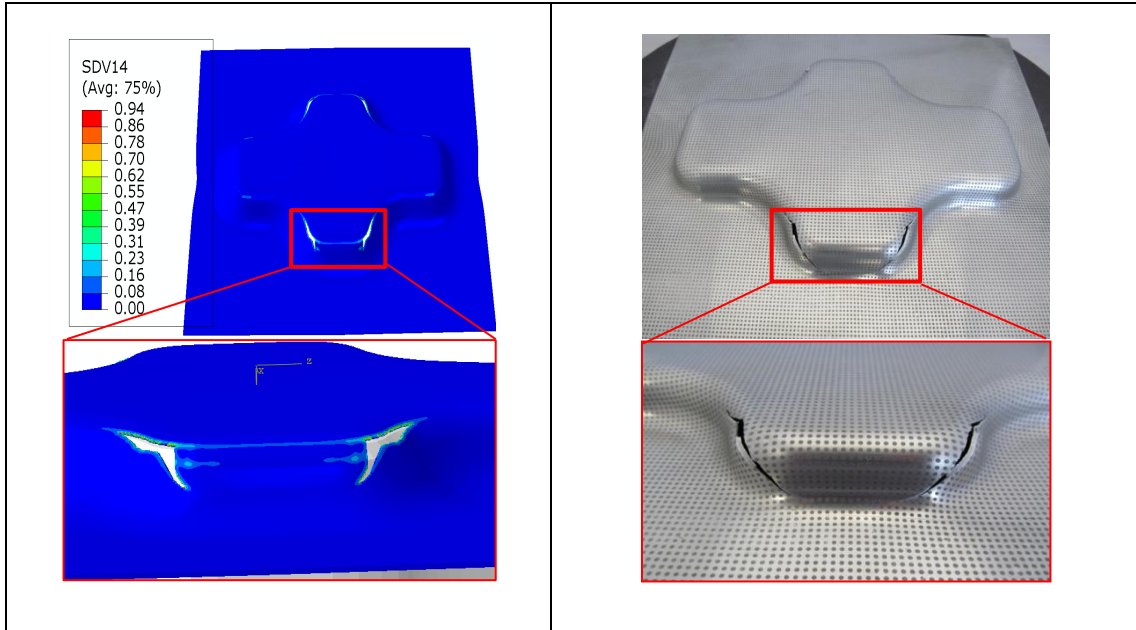
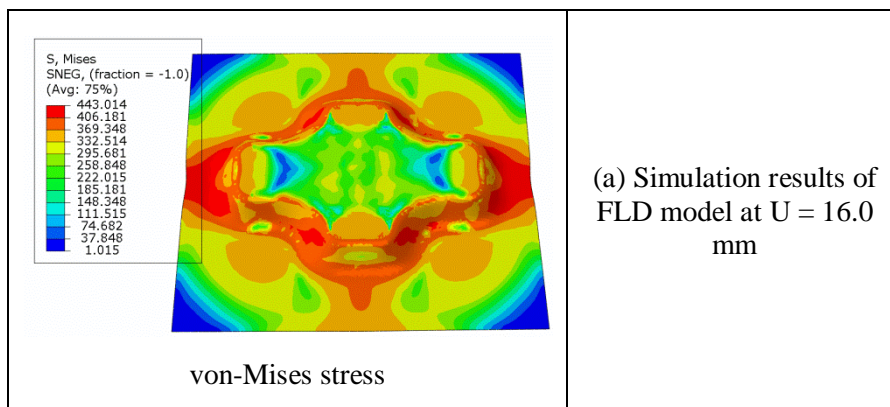
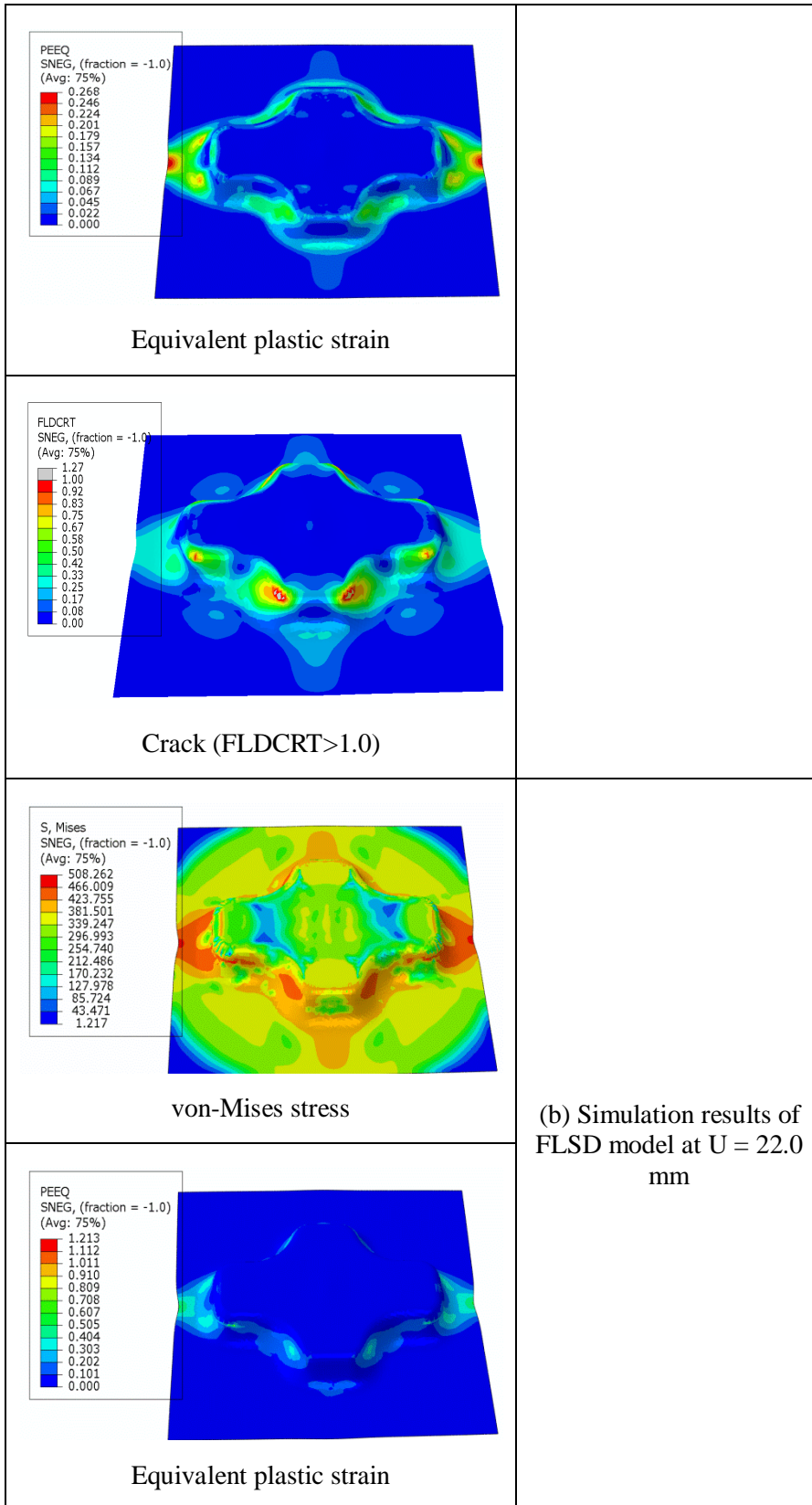


Fig. 4-34. Comparison of the numerical and experimental crack profiles for Al7020.

In Fig.4-34 a comparison between the numerically predicted cracks and the experimentally observed ones is given. Clearly the four experimentally observed cracks are predicted by the fully coupled model. The shape of these numerically predicted cracks are close to the experimentally observed ones. Concerning the punch displacement at fracture we observe a good agreement between the predicted solution ( $U = 18.0$  mm) and the experimentally measured  $U_{exp} = 18.4$  mm.





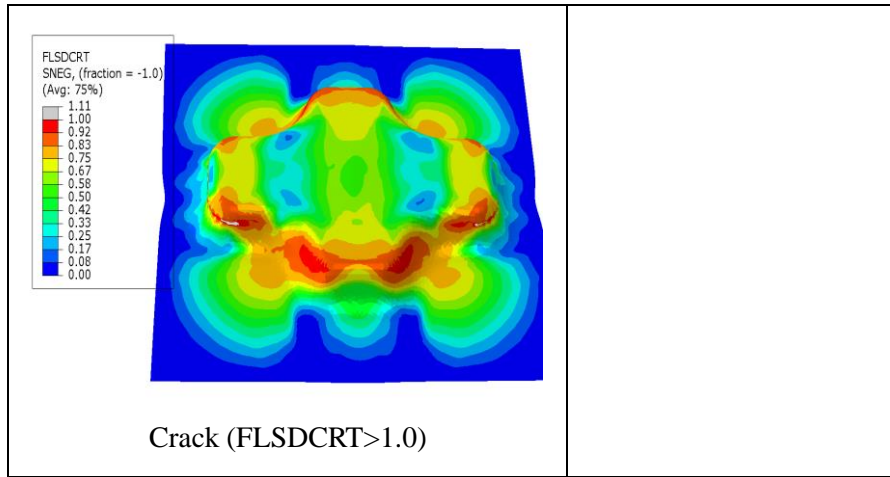
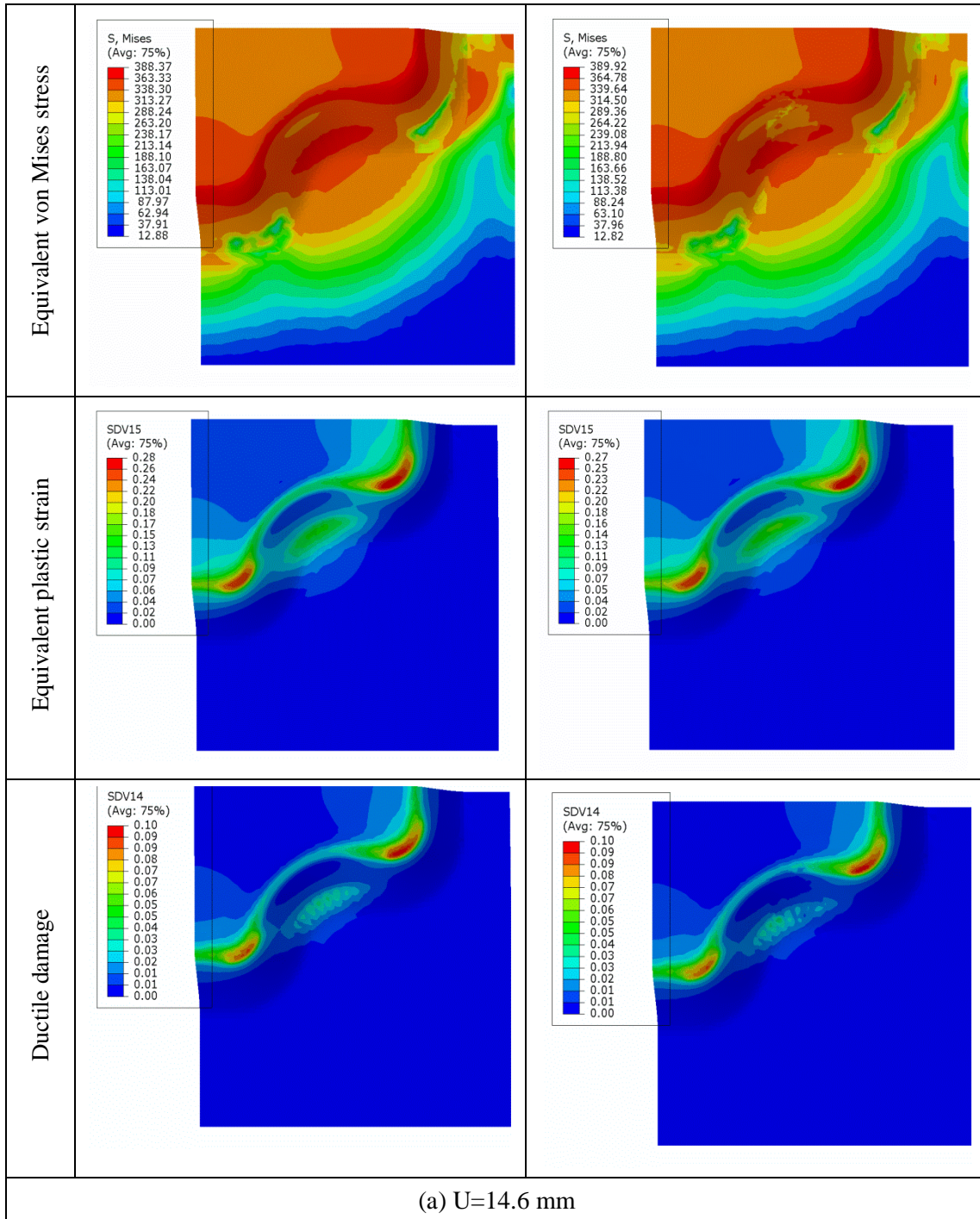


Fig. 4-35. Comparison of CSD tests for Al7020 with (a) FLD and (b) FLSD.

This CSD example has been simulated using the standard model available in ABAQUS to plot the FLD and FLSD curves based on M-K approach using the Swift isotropic hardening rule given in Eq.3-16. The results are summarized in Fig. 4-35 where the distribution of the equivalent von Mises stress, equivalent plastic strain and the FLDCRT and FLSDCRT values are plotted. The FLD model predicts the final fracture at the same place as the experimental response and the CDM coupled model response but at  $U = 16.0$  mm lower than the experimentally observed value  $u = 18.2$  mm (see Fig.4-35a). However, the prediction of the FLSD model is quite different from the experimental responses as well as from the numerical predictions by the CDM and FLD models. As seen in Fig.4-35b the fracture occurs in the opposite corner for a punch displacement  $U=22.0$ mm, much higher than 18.2 mm. It is also worth mentioning that the FLD and FLSD give a maximum stress at the location of the macroscopic cracks in comparison with CDM model which predicts zero stress inside the cracked zone.

**Effect of the yield surface distortion:** To highlight the effect of the yield surface distortion, a series of new simulation are performed using two levels of pre-strain. The first corresponds to 1.0% of the saturated kinematic hardening stress which is  $X_{sat} = 30.0$ MPa , i.e.  $X_{ini} = 0.3$ MPa . The second corresponds to 10.0% of  $X_{sat}$  , i.e. 3.0 MPa. The results are presented in Fig. 4-35 for  $X_{ini} = 0.3$ MPa and in Fig. 4-36 for  $X_{ini} = 3.0$ MPa .

$X_{ini} = 0.3$ MPa	
without distortion	with distortion





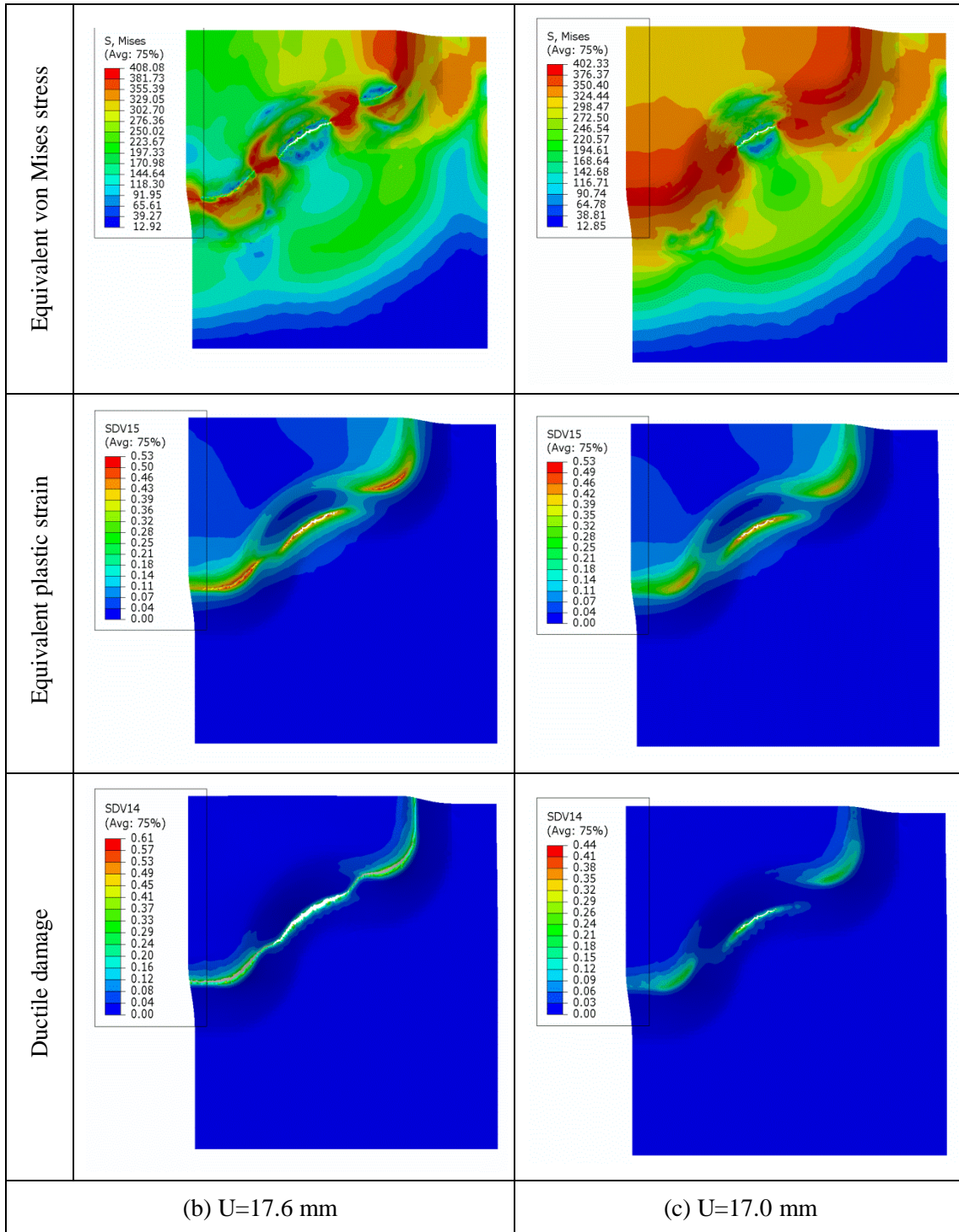
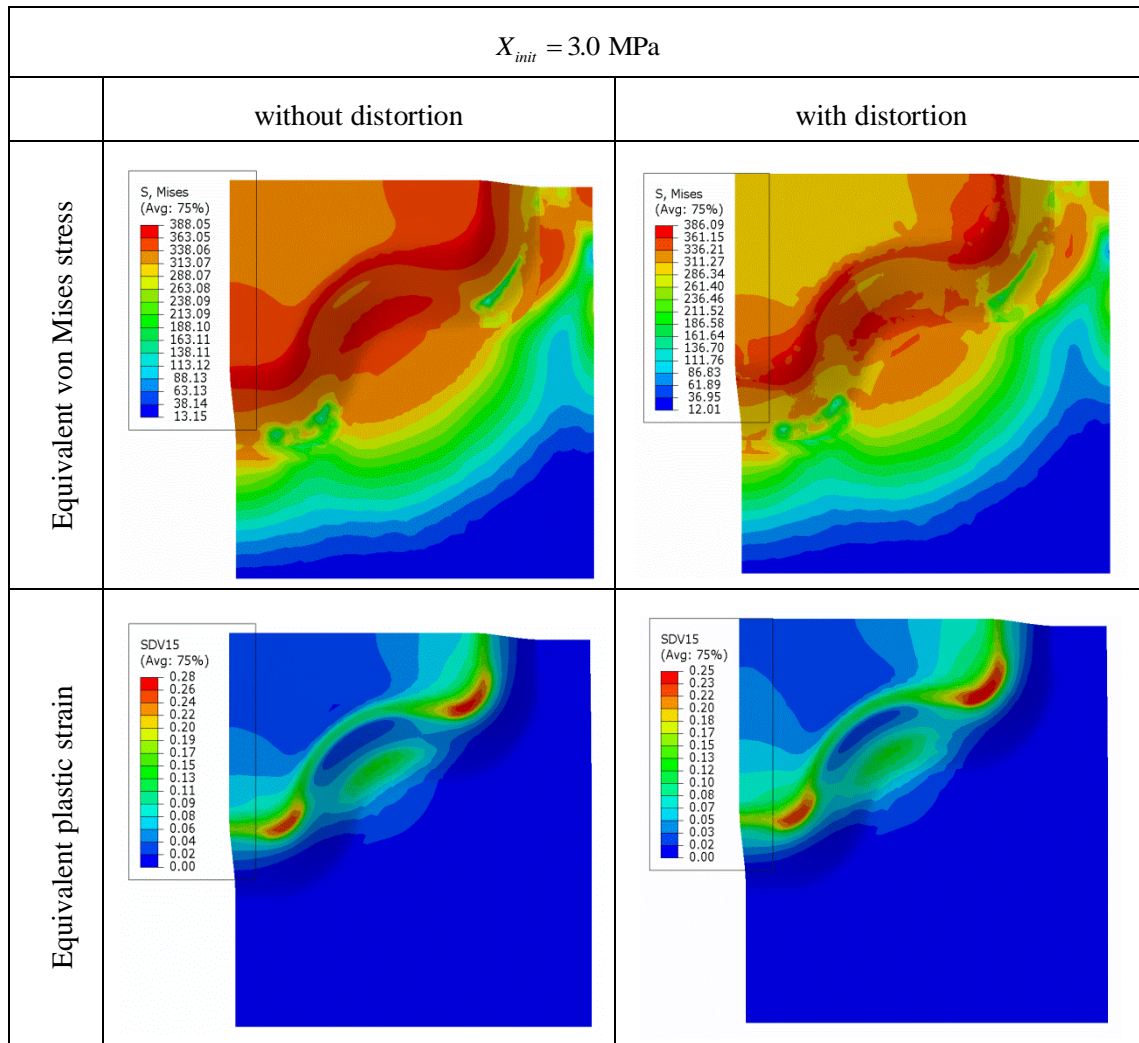


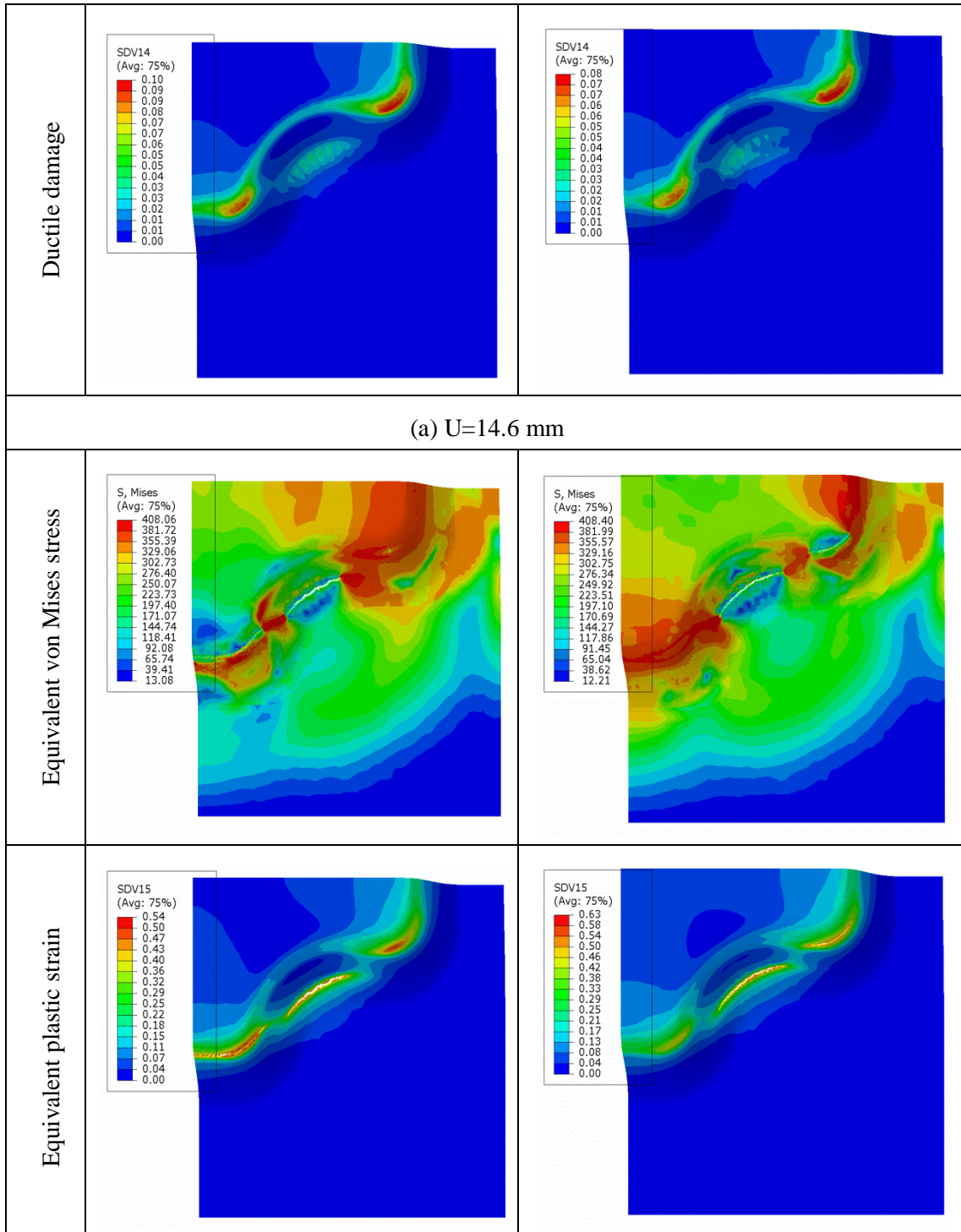
Fig. 4-36. Comparisons between the numerical responses for  $X_{init} = 0.3\text{MPa}$ .

In these figures the equivalent von Mises stress, the equivalent plastic strain and the ductile damage distributions are given for three increasing values of the punch displacement. For the case of  $X_{init} = 0.3\text{MPa}$  (Fig. 4-36) it is observed a difference between the results obtained with or without the distortion effect. This difference increases when the

punch displacement increases. In fact, the difference between the maximum values of stress, equivalent plastic strain and damage are small for  $U = 14.6$  mm as can be seen in Fig.4-36(a). However, the first macroscopic crack appears at internal corner for  $U = 17.0$  mm with distortion effect, while without distortion effect the crack appears simultaneously in internal and external corners for  $U = 17.6$  mm.

Similar remarks can be made for the case with  $X_{init} = 3.0$  MPa shown in Fig.4-37. However, the predicted crack location is quite different from the first case with and without distortion effect. In fact, the macroscopic crack is predicted at the internal corner and one external corner for  $U = 18.8$  mm by the model with distortion; while it is predicted at the internal and another external corners for  $U = 17.6$  mm by the model without distortion effect (Fig. 4-37b).







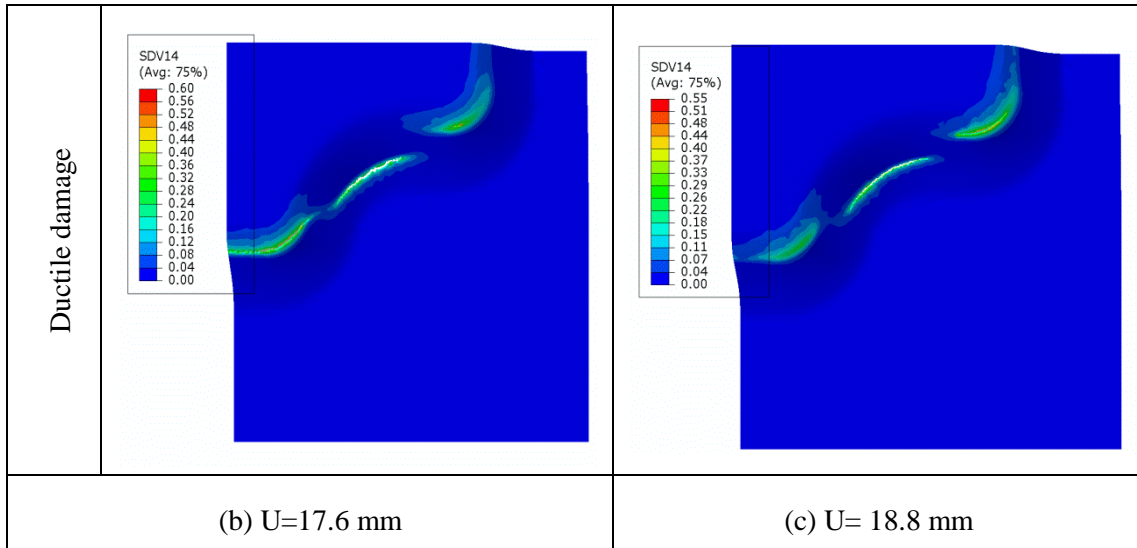


Fig. 4-37 Comparisons between the numerical responses for  $X_{ini} = 3.0$  MPa .

Finally, the Force-displacement curves for the cases with and without distortion effect are shown in Fig.4-38. The results are similar except the case  $X_{ini} = 3.0$  MPa with distortion effect which extends slightly the forming limits.

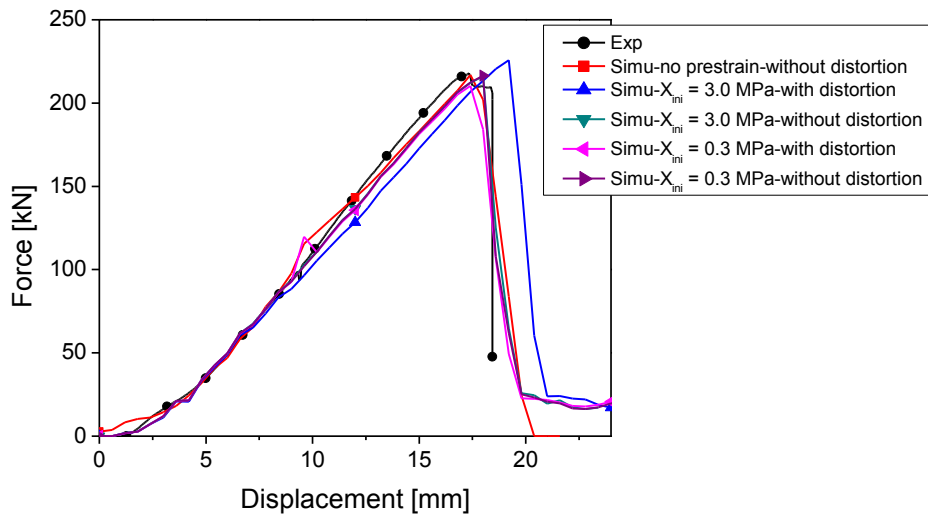


Fig. 4-38. Comparison between the numerical Force-displacement with and without distortion effects.

**CSD simulation for DP1000 and CP1200:** With the same simulation setting as Al7020 and blank holder force 400.0 kN, the CSD tests for DP1000 and CP1200 are simulated with the proposed fully coupled CDM model using the material parameters shown in Table 4-2 and Table 4-4 without yield surface distortion effect.

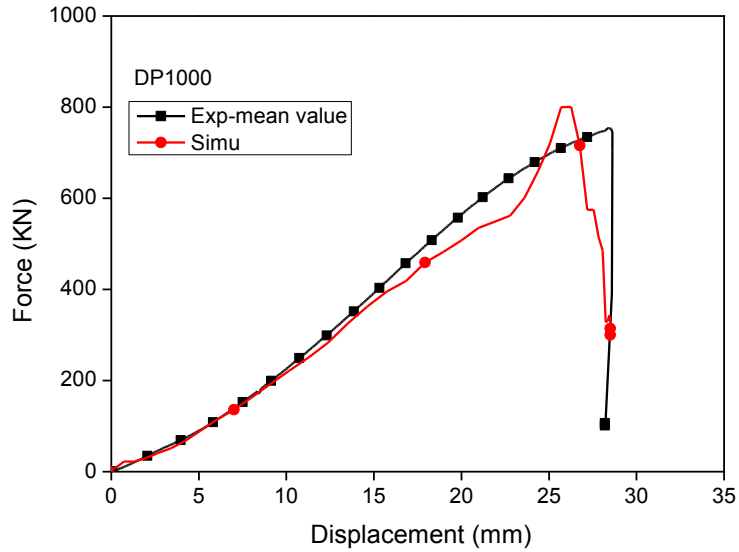


Fig 4-39. Comparison of the force-displacement curves of numerical and experimental responses for CSD tests for DP1000

The comparisons of numerical and experimental force-displacement curves are separately shown in Fig. 4-39 and Fig. 4-40. The model describes relatively well the experimental results including the maximum forces reached for each material. In Fig. 4-41 and 4-42 are given the von Mises stress, ductile damage (SDV14) and accumulated plastic strain (SDV15) distribution during the forming processes for three increasing values of the punch displacement.

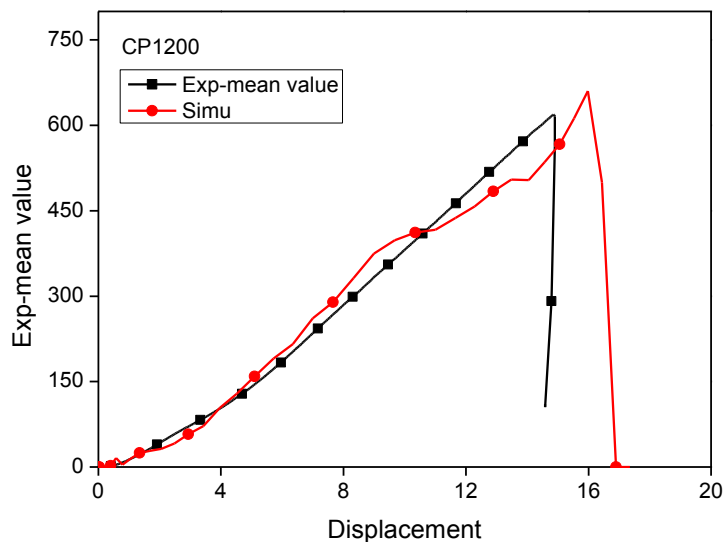
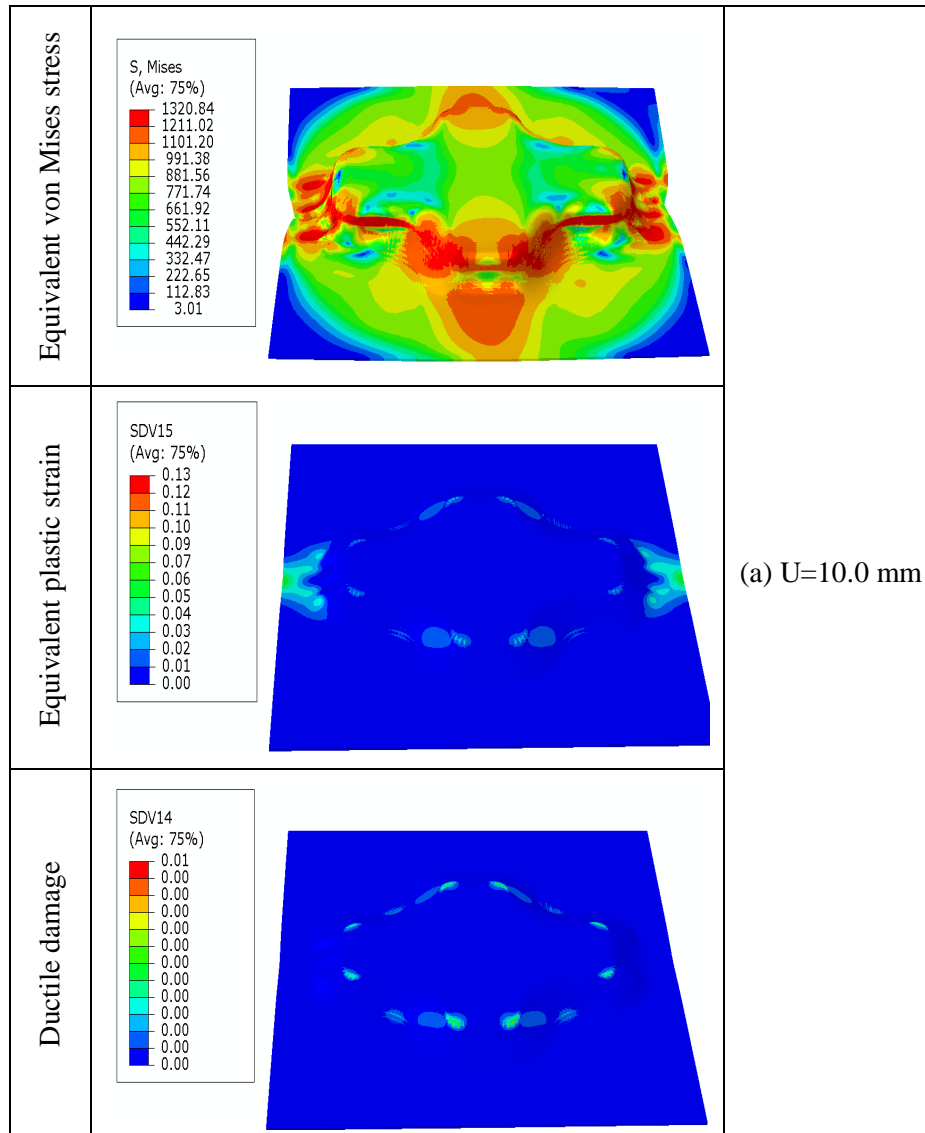
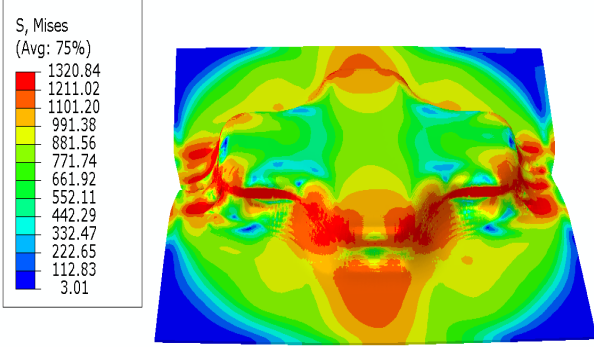
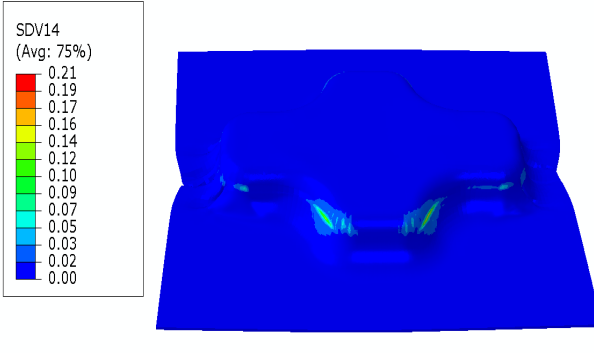
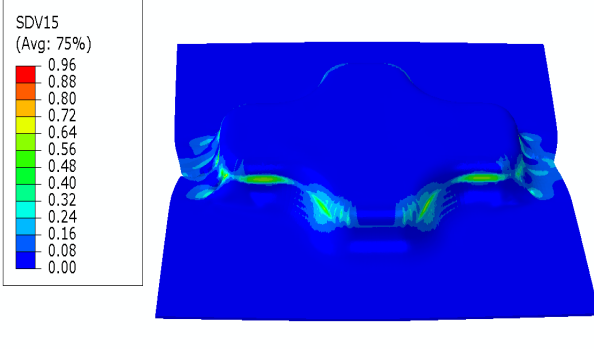
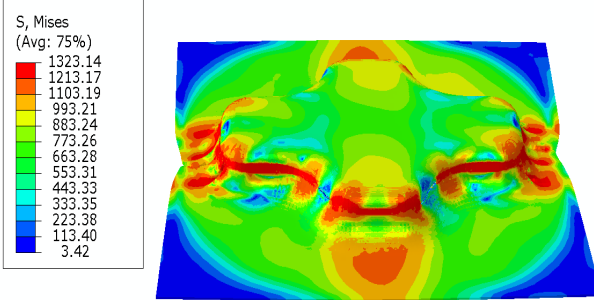


Fig 4-40. Comparison of the force-displacement curves of numerical and experimental responses for CSD tests for CP1200.

For DP1000, no significant damage is observed for  $U = 10.0$  mm (Fig.4-41a). At  $U = 28.0$  mm (i.e. the end of the forming process) significant damage concentrates along the external corner as shown in Fig.4-41c. The same observations can be made for CP1200 where the first cracks are observed at the external corner for  $U = 17.0$  mm (Fig.4-42c). The decrease of the stresses at the location of macroscopic cracks due to the strong damage-behavior coupling is clearly observed for both cases.



Equivalent von Mises stress	 <p>S, Mises (Avg: 75%)</p> <ul style="list-style-type: none"> <li>1320.84</li> <li>1211.02</li> <li>1101.20</li> <li>991.38</li> <li>881.56</li> <li>771.74</li> <li>661.92</li> <li>552.11</li> <li>442.29</li> <li>332.47</li> <li>222.65</li> <li>112.83</li> <li>3.01</li> </ul>	
Equivalent plastic strain	 <p>SDV14 (Avg: 75%)</p> <ul style="list-style-type: none"> <li>0.21</li> <li>0.19</li> <li>0.17</li> <li>0.16</li> <li>0.14</li> <li>0.12</li> <li>0.10</li> <li>0.09</li> <li>0.07</li> <li>0.05</li> <li>0.03</li> <li>0.02</li> <li>0.00</li> </ul>	(b) U=26.0 mm
Ductile damage	 <p>SDV15 (Avg: 75%)</p> <ul style="list-style-type: none"> <li>0.96</li> <li>0.88</li> <li>0.80</li> <li>0.72</li> <li>0.64</li> <li>0.56</li> <li>0.48</li> <li>0.40</li> <li>0.32</li> <li>0.24</li> <li>0.16</li> <li>0.08</li> <li>0.00</li> </ul>	
Equivalent von Mises stress	 <p>S, Mises (Avg: 75%)</p> <ul style="list-style-type: none"> <li>1323.14</li> <li>1213.17</li> <li>1103.19</li> <li>993.21</li> <li>883.24</li> <li>773.26</li> <li>663.28</li> <li>553.31</li> <li>443.33</li> <li>333.35</li> <li>223.38</li> <li>113.40</li> <li>3.42</li> </ul>	(c) U=28.0 mm

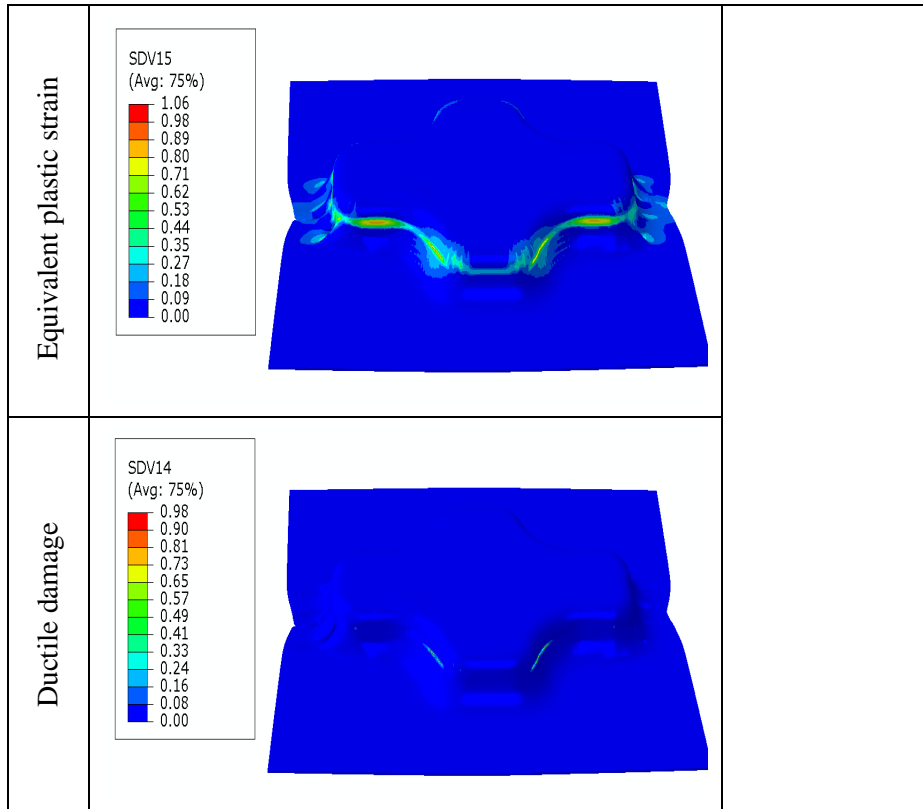
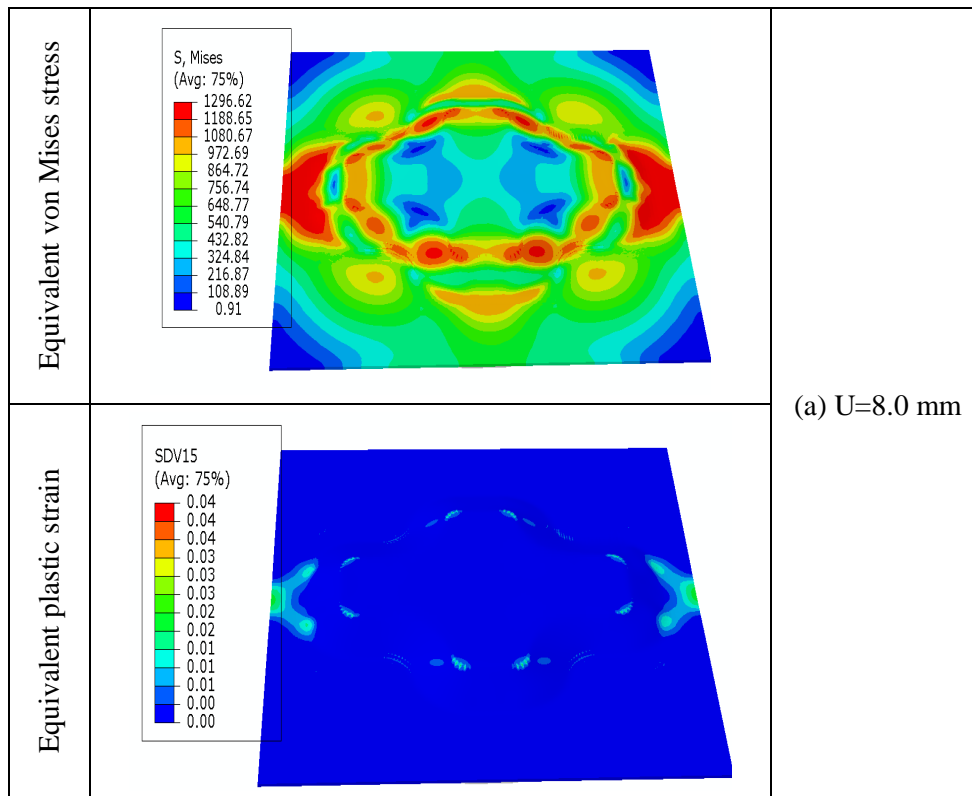
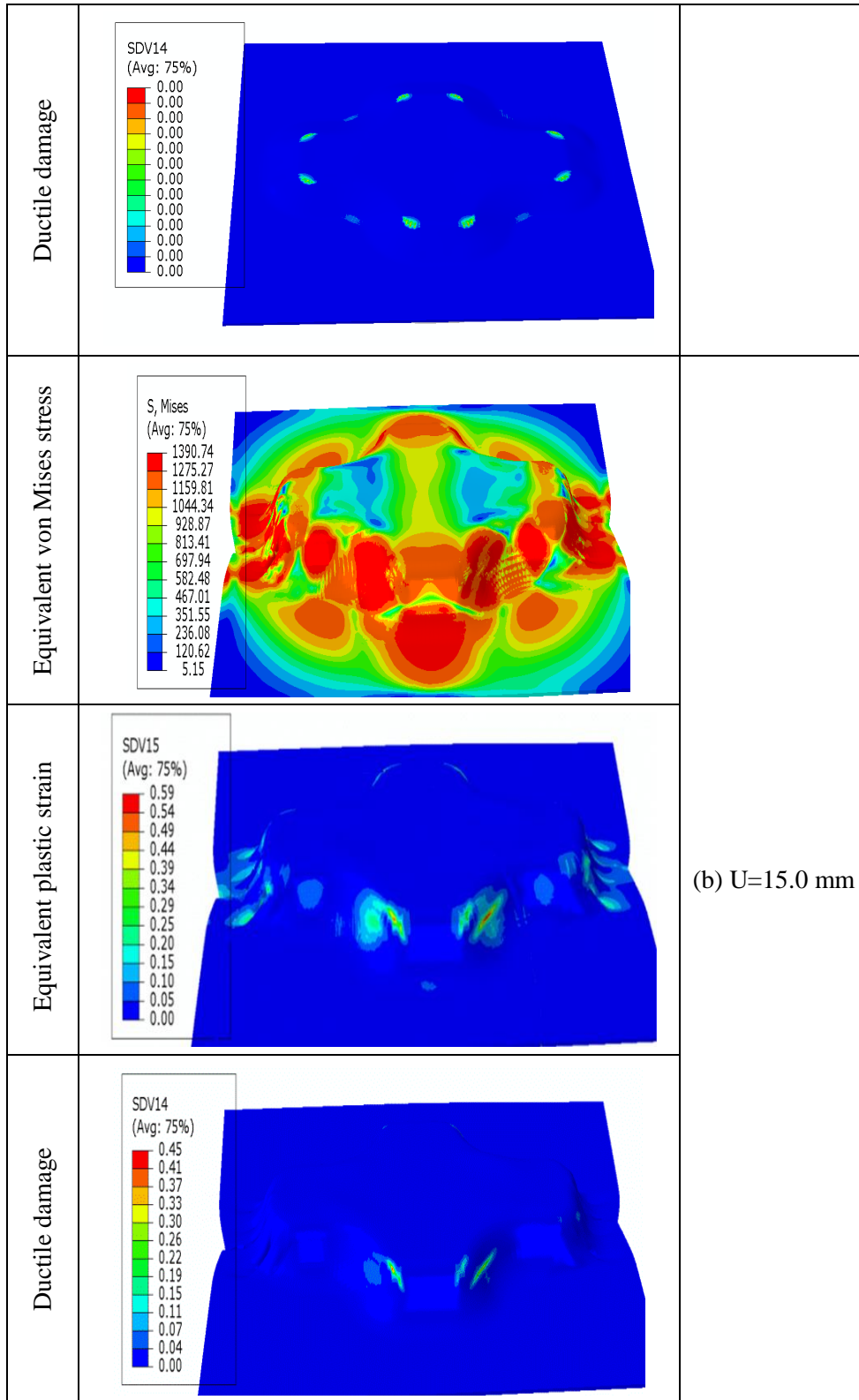


Fig. 4-41. Distribution of the von Mises stress, equivalent plastic strain and the ductile damage at different punch displacements for DP1000.





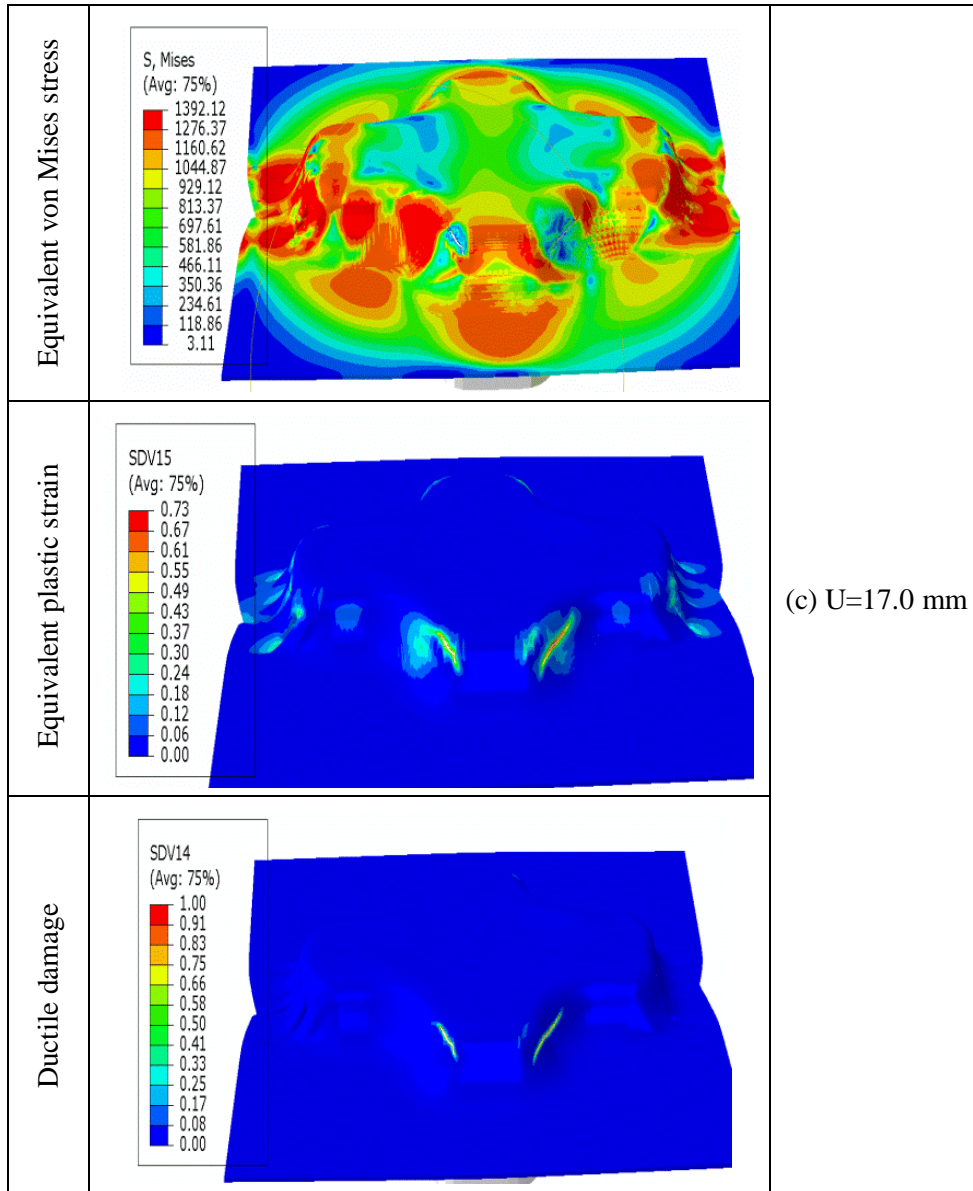


Fig. 4-42. Distribution of the equivalent von Mises stress, equivalent plastic strain and ductile damage at different punch displacements for CP1200.

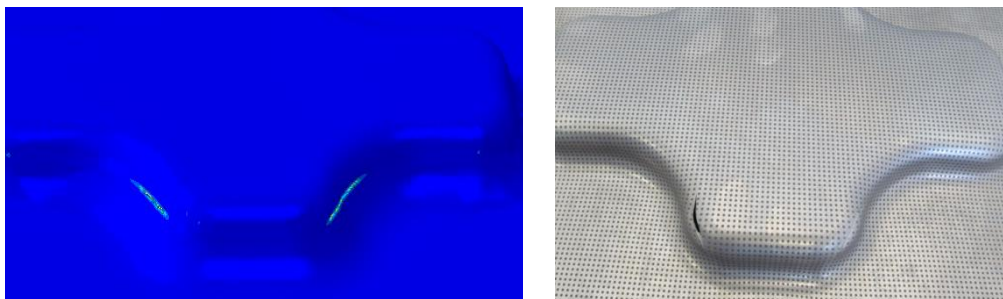


Fig. 4-43. Comparison of the macroscopic cracks between simulation and experimentation for DP1000.

In Fig. 4-43 and Fig. 4-44, the comparisons between the numerically predicted and experimentally observed macroscopic cracks for DP1000 and CP1200 are given. The numerical responses are in agreement with the experimental responses both for cracks location and paths. Failures start in the same critical zone as in the numerical simulations and the cracks evolve along two opposite directions, similar to Al7020. It should be noted that for DP1000 the crack initiation is not symmetric in experiments surely due to the experimental operating mode.

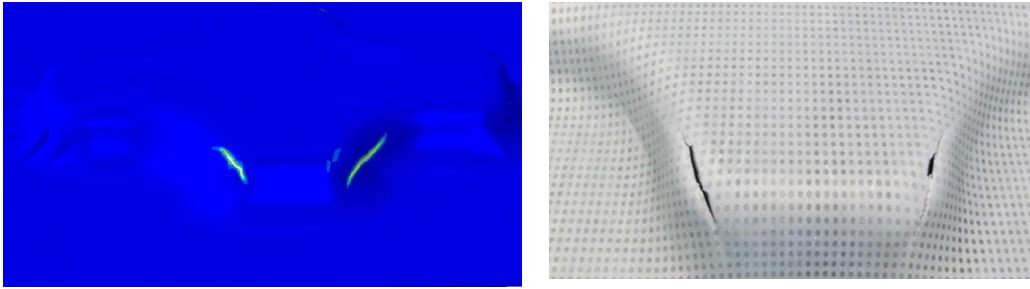
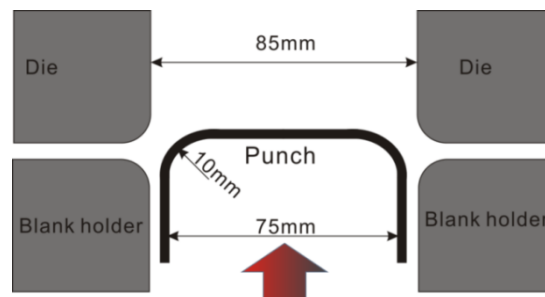


Fig. 4-44 Comparison of the macroscopic cracks form between simulation and experimentation for CP1200.

## IV.6 Rectangular drawing tests (RD)

A simple rectangular draw die is used to draw sheet metal to a certain depth. After load, the draw-in amounts for 4 corners and edges are compared with and without yield surface distortion effect. The experimental setup and geometry of the die and specimen for this test are separately shown in Fig. 4-45. The material Al7020 is chosen for this test. The initial blank is prepared with size of  $130 \times 120 \times 1.5 \text{ mm}^3$ . The friction coefficient is set to be  $\mu = 0.1$ . The maximum drawing depth is 15.0 mm. More details concerning the numerical conditions are given in Table 4-6.



(a)



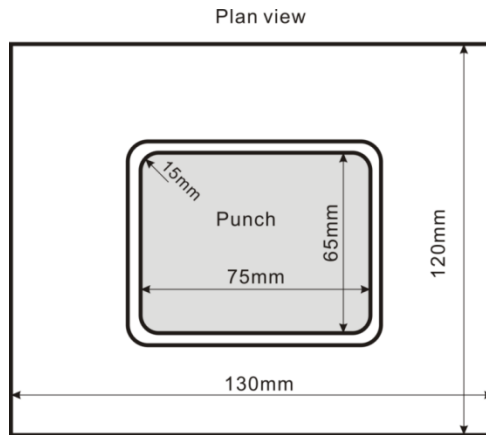


Fig. 4-45 Scheme of the setup of rectangular drawing tests (RD)

Table 4-6 Numerical conditions for RD tests

Blank	
Element type	Reduced intergration solid (C3D8R)
Element size [mm]	0.15×0.15×0.3 (min)
Number of layers in thickness	5
Number of elements	76425
Tools	
Element type	Reduced 4-node shell element (S4R)
Element in radii	12.0
Friction coefficient	0.1
Process parameters	
Punch travel [mm ]	15.0 and 30.0
Punch speed [mm/s]	10.0 mm/s
Blank holder force [kN]	40.0

The half part of the FEM model for RD test and mesh condition of the blank are shown in Fig.4-46. The mesh size in the critical zones of the blank is 0.15 mm, and 1.0 mm in other zones. In the thickness direction, there are 5 elements. The total number of elements is 76425. The element type is C3D8R. The die, the punch and the blank holder are constructed with the reduced 4-node shell elements (S4R).

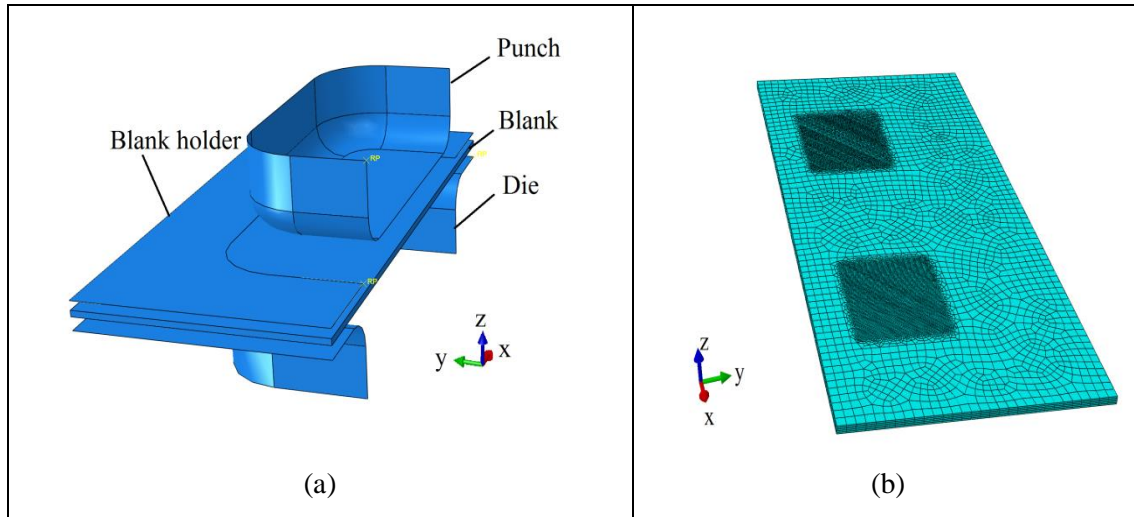


Fig. 4-46 Numerical model for simulation (a) Setup for simulation (b) Blank mesh condition (76425 brick element C3D8R with the minimum mesh size of 0.15mm)

The distributions of the displacement components in two directions, the equivalent von Mises stress, the equivalent plastic strain and the ductile damage inside the formed sheet at punch displacement equal to 15.0 mm are given separately in Fig. 4-47. Both the numerical results with and without yield surface distortion effect are given.

After 15.0 mm drawing of the punch, the draw-in amounts in horizontal direction are 11.39 mm with distortion effect and 11.38 mm without distortion effect. On the other hand, the draw-in amounts in vertical direction are 11.91 mm with distortion effect and 11.92 mm without the distortion effect. The difference of the draw-in shape caused by the yield surface distortion is less than 0.05%.

The Maximum equivalent stress reaches 432.3 MPa, the equivalent plastic strain reaches 27.4% and the ductile damage reaches 8.9% when the yield surface distortion is taken into account. On the other hand, without distortion effect, the Maximum equivalent stress reaches 427.6 MPa, and the equivalent plastic strain and the ductile damage reach 25.4% and 8.0% respectively. The differences of the equivalent plastic strain and the ductile damage do not exceed 7.0% and 10.0%. Note that the ductile damage does not exceed 0.09 at  $U = 15.0$  MPa. No information concerning the thickness distribution is available in this example. From this example no significant differences between the simulations with and without yield surfaces distortion have been observed.

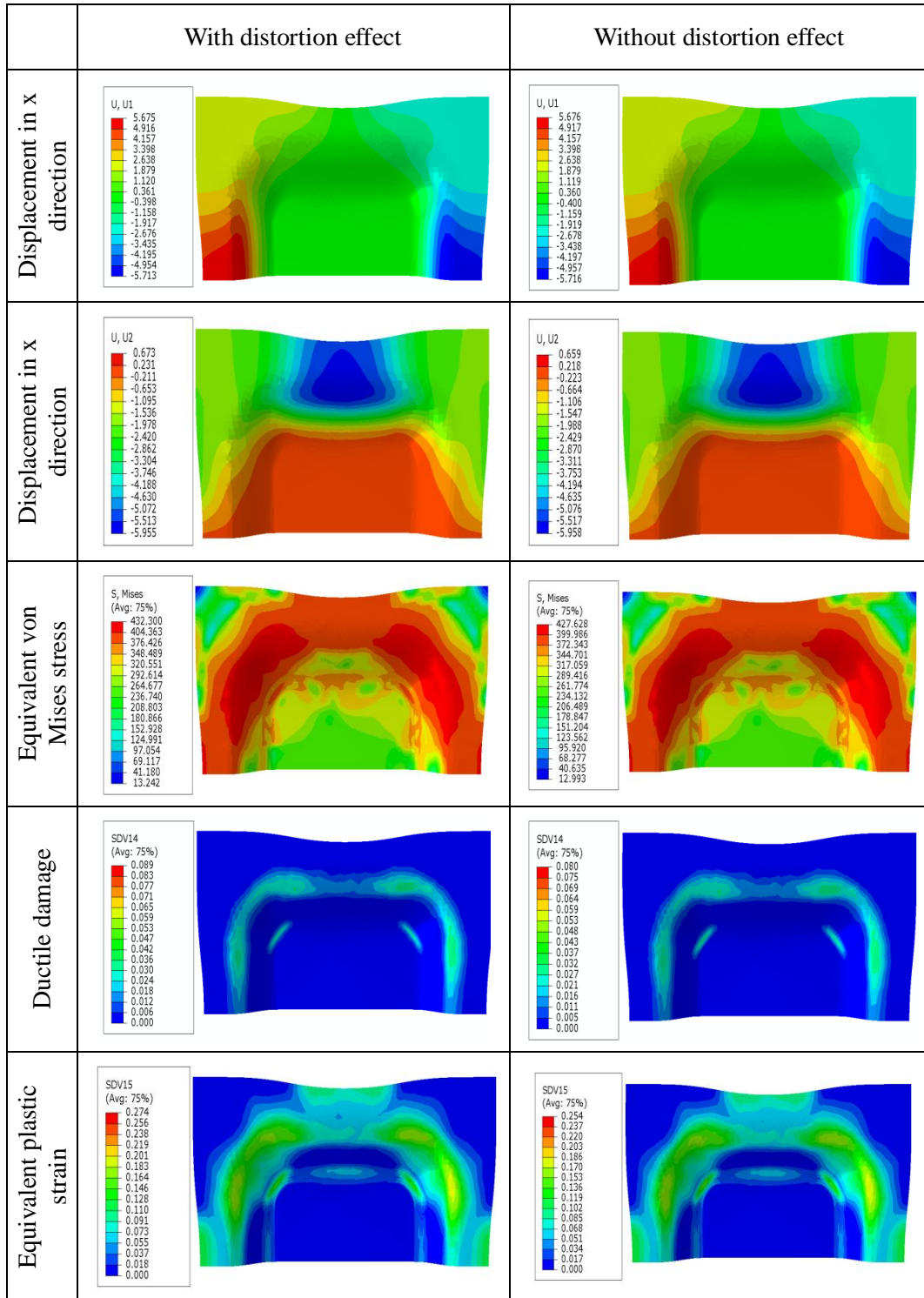


Fig. 4-47 Comparison of the contour of the displacement, strain, stress and ductile damage got from the simulation using with and without distortion effect

To see the fracture occurrence this computation has been continued with distortion effect until a macroscopic cracks are observed at  $U = 21.1$  mm (see Fig.4-48c). The contours of the equivalent plastic strain and ductile damage before and after fracture occurrence are given in

Fig.4-48. As we can find the initial cracks happen at the corner of the drawing part and propagate along the edges.

In Fig.4-49 are shown the location of four Gauss points inside the localization area where the macroscopic crack occurred. In these four points the evolution of the triaxiality ratio versus the equivalent plastic strain is plotted in Fig.4-50a while the evolution of the ductile damage is plotted in Fig.4-50b.

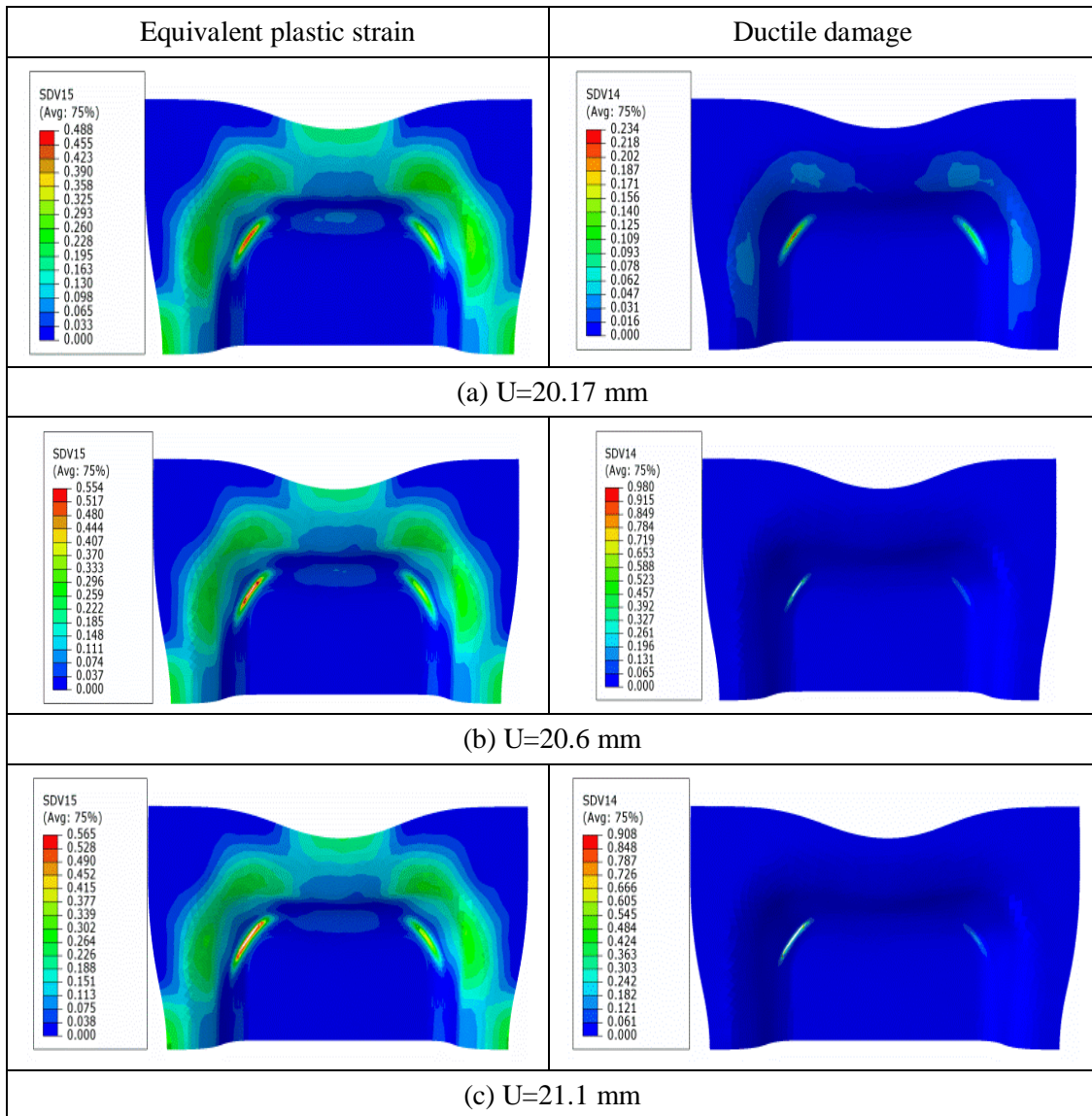


Fig. 4-48. Fracture initiation and propagation for RD simulation with distortion (Al7020).

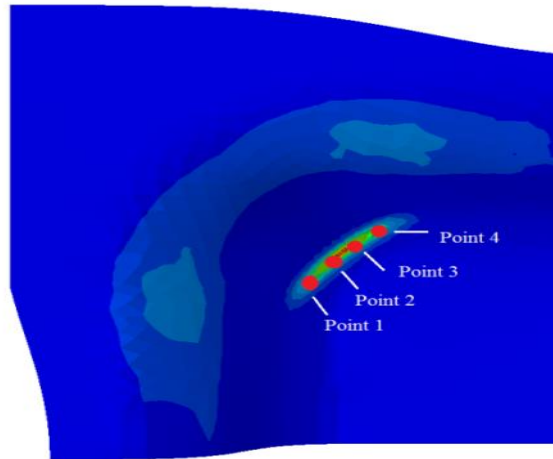


Fig. 4-49. Location of four points inside the fracture zone.

It is observed that the triaxiality ratio of the material in the critical zone is less than zero at the beginning of the loading, which indicates that the material is under shear and compression stress states. With the increasing of the plastic strain, the triaxiality ratio increases and reach around 0.5 until fracture, which indicates the deformation is under tension stress state. The final fracture happens when the equivalent plastic strain is around 0.55 after which the stresses go to zero due to the final fracture.

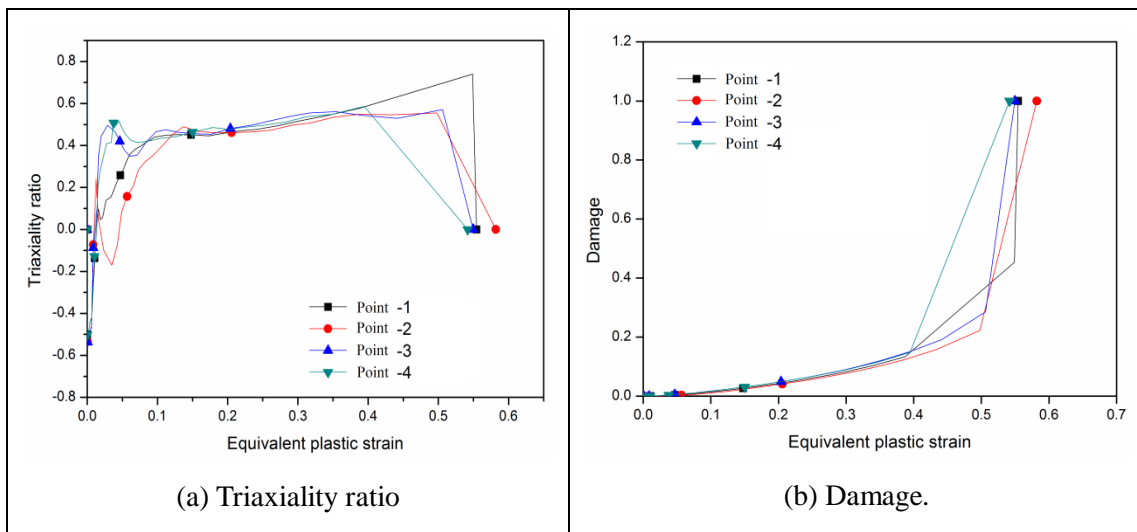


Fig. 4-50. Triaxiality ratio and ductile damage evolutions for the four critical points versus the equivalent plastic strain

## IV.7 Conclusions

In this chapter, the parameters determination and validation of proposed two models are

conducted, including fully coupled CDM model and M-K model. For the parameters identification of fully coupled CDM model, considering the stress states sensitivity, a list of tests including: uniaxial tensile tests, in-plane torsion tests, pre-notched tension tests, simple shear tests and combined loading tests are proposed in order to cover the extensive stress states in terms of triaxiality ratio ( $0.0 \leq \eta \leq 0.57$ ). For the kinematic hardening, in-plane torsion tests have been performed loading-unloading conditions for the Bauschinger effect investigation. Concerning the exist of the microcracks closure effect parameter  $h$  in CDM model, the simple shear tests can help to investigate the contribution of negative part of stress on damage evolution. For the investigation of the yield surfaces distortion, the combined loading tests with tension-shear and shear-tension loading paths are used to investigate the change of the subsequent yield surfaces distortion.

With the help of analytical and inverse methodology, the elastoplasticity parameters, distortion parameters and ductile damage parameters are determined separately. The best values of the material parameters are determined by comparing the output results with the experimental measurements, while minimizing the difference between the numerically predicted and the experimentally observed results.

For the validation tests, cross section deep drawing tests are simulated with fully coupled CDM, FLD model and FLSD model for material Al7020. Through the comparison of the damage initiation and propagation, their capabilities are shown. For other two materials DP1000, CP1200, the simulation results obtained with CDM model well describe the deformation behavior in CSD tests. With the simulation results of Nakazima tests, the numerical forming limit curves based on ductile damage compare with the experimentally determined FLDs and FLSDs for Al7020 and DP1000. Through the comparison of the draw-in amounts and also the stress, strain and ductile damage distributions of the simulation results, the difference with and without yield surfaces distortion consideration are given.

## Conclusions and perspectives

Nowadays, it is well admitted that metal forming simulation requires ‘advanced’ constitutive equations able to describe the main physical phenomena under large plastic strains. This work aims to contribute in this goal by using thermodynamically-consistent non-associative constitutive equations accounting for anisotropic plastic flow, mixed nonlinear isotropic and kinematic hardening, the all fully coupled with isotropic ductile damage. The main contributions of present work consist in taking into account the distortion of the yield surface, the triaxiality ratio and the Lode angle during the loading history and their effects on the hardening and damage occurrence. This goal is justified by the fact that during metal forming the critical zones where high plastic strains and consequently ductile damage localize are subjected to complex loading paths.

The following aspects have been investigated:

- Based on continuum damage mechanics framework the advanced fully coupled constitutive equations are proposed, which take into account the initial and induced anisotropies, isotropic and kinematic hardening as well as isotropic ductile damage. Microcracks closure is introduced to affect damage evolution under a wide range of triaxiality ratios. The introduction of Lode angle parameters (with two formulations) helps to enhance the predictive capabilities of the model. The novelties of the proposed model are the introductions of the Lode angle and the distortion of the yield surfaces during the deformation history. The distortion of the yield surface is described by replacing the usual stress deviator tensor  $\underline{S}$  by a ‘distorted stress’ deviator tensor  $\underline{S}_d$ , which governs the distortion of the yield surfaces.

- The obtained fully coupled constitutive equations have been discretized in the time using appropriate finite difference scheme and in space domain using FEM and implemented into ABAQUS/Explicit FE code.
- In order to assess the capability of the proposed fully coupled CDM model, the obtained numerical results have been compared with the widely used FLD and FLSD curves based on M-K approach for one material (Al7020). Different yield criterion and hardening laws have been used in this analytical model and compared to the predictions of the fully coupled CDM model.
- An experimental data base has been performed during this study. Three metal sheets are chosen as the test materials DP1000, CP1200 and Al7020. Series of proportional and non-proportional loading paths have been used for the identification and validation of the elastoplastic and damage parameters. These tests include: the Uniaxial tensile tests (UT), In-plane torsion tests (IPT), Pre-notched tension tests (PNT), Simple shear tests (SS), Combined loading tests (CL), Nakazima tests (NAK) and Cross section deep-drawing tests (CSD).
- Before the parameters identification, a relatively exhaustive numerical parametric study has been conducted in order to analyse the sensitivity of the model parameters on the macroscopic behavior, including the microcracks closure  $h$ , the distortion parameters and the Lode angle parameters.
- For the identification purpose, an inverse methodology combining MATLAB-based minimization software with ABAQUS FE code through the Python script is used. The best values of the material parameters are determined comparing the output results with the experimental data base by minimizing the objective functions.
- Finally, applications to some sheet metal forming processes were carried out for three materials as: Cross Section Deep drawing tests (CSD) and Nakazima tests (NAK) are simulated with the fully coupled CDM model. Some pre-strain conditions are assumed to test the distortion of the yield surfaces on the plasticity and damage evolution during CSD tests. On the other hand, the FLD and FLSD are also used for failure prediction of the CSD tests with the material Al7020. Through the comparisons of the damage initiation and propagation, the high capability of the fully coupled CDM model is proved.

As is well known, the main objective of any predictive model is to combine the simplicity of numerical implementation with ease of use in order to reproduce as accurately as possible the desired physical phenomena. The proposed model in this work attempts to achieve this by



taking into account the main physical phenomena characteristic of large strains of metallic materials such as various types of hardening, the various initial and induced anisotropies (kinematic hardening, yield surface distortion) and fracture by ductile damage under various complex loading paths. The constitutive equations of the model are derived from the thermodynamics of irreversible processes framework with various couples of state variables. This model is not so complicated to identify and to be used for the simulation of the metal forming processes.

However, further developments are still to be conducted in order to extend the proposed model to cover more general loading conditions. They can be summarized in the following points:

- Mainly in metal sheets the ductile damage can be highly anisotropic. Extension of the present model to include the anisotropy of the ductile damage should be made. This work is done in the LASMIS team by representing the damage through a couple of second-rank tensors namely  $(\underline{d}, \underline{Y})$  [Ngu12, Rajhi14].
- To be free from the dependence of the numerical solution to the discretization aspects, the mechanics of generalized continua should be used. Extension of the present fully local model to the non-local formulation has to be performed in the framework of micromorphic theory [Saanouni12, Saanouni14].
- Some sheet metals forming processes have to be performed under high temperature in order to facilitate their formability. Extension of the present model to the viscoplasticity framework has to be done together with considering the thermal exchanges by adding the heat equations.
- Additional experimental work is still needed to be done in order to cover a wide range of more complex non-proportional loading paths. This is required to facilitate the identification of large number of material parameters entering the advanced constitutive equations which can exceed many tens for the more general version of the model.
- Finally, more industrial tests have to be performed in a wide range of complex forming processes which can help to validate these advanced fully coupled constitutive equations.



---

## Reference

- [Abaqus01] **Abaqus** (2001), *Theory manual*, Version 6.2, Hobbit, Karson & Sorensen.
- [Abbassi10] **Abbassi, F., Pantalé, O., Mistou, S., Zghal, A. and Rakotomalala, R.** (2010), Effect of Ductile Damage Evolution in Sheet Metal Forming: Experimental and Numerical Investigations, *Key Engineering Materials*. 446: 157-169.
- [Abspoel11] **Abspoel, M., Atzema, E.H., Droog, J.M.M., Khandeparkar, T., Scholting, M.E., Schouten, F.J. and Vegter, H.** (2011), Inherent influence of strain path in Nakazima FLC testing, *In: Guttierez, D. (Ed.), Proceedings of the IDDRG 2011 International Conference*, Bilbao, Spain.
- [Arrieux82] **Arrieux, R., Bedrin, C. and Bovin, M.** (1982), Determination of an intrinsic forming limit stress diagram for isotropic sheets, *In: Proceedings of the 12th IDDRG congress, Santa Margherita*, 2: 61–71.
- [Assempour09] **Assempour, A., Hashemi R., Abrinia, K., Ganjiani, M. and Masoumi, E.** (2009), A methodology for prediction of forming limit stress diagrams considering the strain path effect, *Computational Materials Science*, 45(2): 195-204.
- [Badreddine10] **Badreddine, H., Saanouni, K. and Dogui, A.** (2010), On non-associative anisotropic finite plasticity fully coupled with isotropic ductile damage for metal forming, *International Journal of Plasticity*, 26: 1541-1575.
- [Bai08] **Bai, Y. and Wierzbicki, T.** (2008), A new model of metal plasticity and fracture with pressure and lode dependence, *International Journal of Plasticity*, 24(6):1071–1096.
- [Bai08] **Bai, Y. and Wierzbicki, T.** (2008), A new model of metal plasticity and fracture with pressure and Lode dependence, *International Journal of Plasticity*, 24: 1071–1096.
- [Bao04] **Bao, Y. and Wierzbicki, T.** (2004), On fracture locus in the equivalent strain and stress triaxiality space, *Int J Mech Sci*, 46(1): 81–98.
- [Bao04] **Bao, Y., and Wierzbicki, T.** (2004), On fracture locus in the equivalent strain and stress triaxiality space, *International Journal of*

- Mechanical Sciences*, 46: 81–98.
- [Banabic00] **Banabic, D., H. J. Bunge, K. Pohlandt and A. E. Tekkaya** (2000), Formability of metallic materials: plastic anisotropy, formability testing and forming limits, Berlin, Germany, Springer-Verlag.
- [Barlat87] **Barlat, F.** (1987), Crystallographic texture, anisotropic yield surfaces and forming limits of sheet metals, *Materials Science & Engineering*, 91: 55-72.
- [Barlat89] **Barlat, F. and Lian, J.** (1989), Plastic behavior and stretchability of sheet metals. Part I: A yield function for orthotropic sheets under plane stress conditions, *International Journal of Plasticity*, 5: 51–66.
- [Barlat91] **Barlat, F., Lege, D.J. and Brem, J.C.** (1991), A six-component yield function for anisotropic materials, *International Journal of Plasticity*, 7: 693–712.
- [Barlat97] **Barlat, F., Becker, R.C., Brem, J.C., Lege, D.J., Murtha, S.J., Hayashida, Y., Maeda, Y., Yanagawa, M., Chung, K.; Matsui, K., Hattori, S.** (1997), Yielding description for solution strengthened aluminum alloys, *International Journal of Plasticity*, 13(4): 385-401.
- [Barlat11] **Barlat, F., Gracio, J. J., Lee, M.-G., Rauch, E. F. & Vincze, G.** (2011), An alternative to kinematic hardening in classical plasticity. *Int. J. Plast*, **27**: 1309–1327.
- [Bathe81] **Bathe, K.J.** (1981), Finite element procedures in engineering analysis, Prentice Hall.
- [Belytschko01] **Belytschko T., Liu W.K., Moran B.** (2001), Non Linear Finite Elements for Continua and structures, John Wiley & Sons, New York.
- [Besson10] **Besson, J.** (2010). Continuum models of ductile fracture: a review, *International Journal of Damage Mechanics*, 19: 3-52.
- [Bet93] **Betten, J.** (1993), Kontinuumsmechanik: Elasto-, Plasto- und Kriechmechanik. Springer-Verlag, Berlin.
- [Bonnet97] **Bonnet J., Wood R.D.** (1997), Nonlinear Continuum Mechanics for Finite Element analysis, Cambridge University Press, Cambridge.
- [Bonora99] **Bonora, N.** (1999), Identification and measurement of ductile damage parameters, *The Journal of Strain Analysis for Engineering Design*, 34: 463-478.
- [Bow89] **Bowen R.M.** (1989), Introduction to Continuum Mechanics for Engineers, Plenum Press, New York.

- [Bou96] **Boudet R. Chauvin A.** (1996), *Mécanique des Milieux Continus*, Hermès, Paris.
- [Bouchard11] **Bouchard, P.-O., Gachet, J.-M. and Roux, E.** (2011), Ductile damage parameters identification for cold metal forming applications. *THE 14TH INTERNATIONAL ESAFORM CONFERENCE ON MATERIAL FORMING: ESAFORM 2011. AIP Conference Proceedings*, 1353: 47–52.
- [Brown03] **Brown, A.A., Casey, J. and Nikkel Jr., D.J.,** (2003), Experimental conducted in the contest of the strain-space formulation of plasticity. *International Journal of Plasticity*, 19: 1965–2005.
- [Butuc03] **Butuc, M.C., Gracio, J.J., Barata, da and Rocha, A.** (2003), A theoretical study on forming limit diagrams prediction, *Journal of Materials Processing Technology*, 142(3): 714-724.
- [Cal60] **Callen H.B.** (1960), *Thermodynamics*, John Wiley & Sons, New York.
- [Cao13a] **Cao, T.-S., Gaillac, A., Montmitonnet, P. and Bouchard, P.-O.** (2013a), Identification methodology and comparison of phenomenological ductile damage models via hybrid numerical–experimental analysis of fracture experiments conducted on a zirconium alloy, *International Journal of Solids and Structures*, 24: 3984-3999
- [Cao13b] **Cao T.-S., Gaillac A., Montmitonnet, P. and Bouchard, P.-O.** (2013b), On the Development and Identification of Phenomenological Damage Models - Application to Industrial Wire Drawing and Rolling Processes, *Key Engineering Materials*, 554-557: 213.
- [Cha76] **Chadwick P.** (1976), *Continuum Mechanics - Concise Theory and Problems*. G. Allen & Unwin.
- [Chaboche88] **Chaboche, J. L.** (1988), Continuum Damage Mechanics. Parts I and II, *Journal of Applied Mechanics*, 55: 59-72.
- [Cho96] **Cho, H.W. and Dafalias Y.F.,** (1996), Distortional and orientational hardening at large viscoplastic deformations, *International Journal of Plasticity*, 16: 903–925.
- [Chow87] **Chow, C. L. and Wang, J.** (1987), An anisotropic theory of continuum damage mechanics for ductile fracture, *Engineering Fracture Mechanics*, 27: 547–558.
- [Chow88] **Chow, C.L., Wang, J.** (1988), A finite element analysis of continuum

- damage mechanics for ductile fracture, *International Journal of Fracture*, 38: 83–102.
- [Crisfield91] **Crisfield M.A.** (1991), *Non-linear Finite Element Analysis of Solids and Structures Vol. 1: Essentials*, John Wiley & Sons, Chichester.
- [Dafalias85] **Dafalias, Y.F.**, (1985), The plastic spin. *J. Appl. Mech.*, 52: 865–871.
- [Dogui89] **Dogui, A.** (1989), *Plasticité anisotrope en grandes déformations*, Thèse de Doctorat d’Etat, Université Claude Bernard, Lyon ,France.
- [Dudzinski91] **Dudzinski, D. and A. Molinari** (1991). "Perturbation analysis of thermoviscoplastic instabilities in biaxial loading." *International Journal of Solids and Structures*, 27(5): 601-628.
- [Ebnoether13] **Ebnoether, F. and Mohr, D.** (2013), Predicting ductile fracture of low carbon steel sheets: Stress-based versus mixed stress/strain-based Mohr–Coulomb model, *International Journal of Solids and Structures*, 50: 1055-1066.
- [Eggertsen10] **Eggertsen, P. -A., and Mattiasson, K.** (2010), An efficient inverse approach for material hardening parameter identification from a three-point bending test, *Engineering with Computers*, 26: 159-170
- [Eri62] **Eringen A.C.** (1962), *Mechanics of Continuous Media*, McGraw-Hill, New York.
- [Feigenbaum07] **Feigenbaum, H.P., Dafalias, Y.F.** (2007), Directional distortional hardening in metal plasticity within thermodynamics. *International Journal of Solids and Structures*, 44: 7526–7542.
- [Feigenbaum08] **Feigenbaum, H.P., Dafalias, Y.F.** (2008), Simple model for directional distortional hardening in metal plasticity within thermodynamics, *J. Eng. Mech*, 134: 730–738.
- [François01] **François, M.** (2001), A plasticity model with yield surface distortion for non proportional loading. *International Journal of Plasticity*, 17:703–717.
- [Fun65] **Fun, Y.C.** (1965), *Foundation of Slid Mechanics*, Prentice Hall, Englewood Cliffs.
- [Barlat13] **Barlat, F., Ha, J., Grácio, J.J., Lee, M.-G., Rauch, E. F., Vincze, G.** (2013), Extension of homogeneous anisotropic hardening model to cross-loading with latent effects, *International Journal of Plasticity*, 46(0): 130-142.
- [Freudenthal50] **Freudenthal, A.** (1950), *The Inelastic Behavior of Engineering Materials and Structures*. John Wiley & Sons, New York.

- [Ger86] **Germain P.** (1986), *Mécanique*, Vols. I and II, Ellipses, Paris.
- [Gelin94] **Gelin, J.C., Ghouati, O.** (1994), An inverse method for determining viscoplastic properties of aluminum-alloys. *J Mater Process Technol*, 45: 435–40.
- [Ghosh82] **Ghosh, A.K., Hamilton, C.H.** (1982), *Metallurgical Transactions A*, 13A:733
- [Goodwin68] **Goodwin, G. M.** (1968). Application of strain analysis to sheet metal forming problems in the press shop. *Society of Automotive Engineers: Technical paper*, no. 680093.
- [Gur81] **Gurtin, M.E.** (1981), *Introduction to Continuum Mechanics*. Springer.
- [Gurson77] **Gurson, A.L.** (1977), Continuum theory of ductile rupture by void nucleation and growth – Part I. Yield criteria and flow rules for porous ductile media, *Journal of Engineering Materials and Technology*, 99: 2–15.
- [Haddadi06] **Haddadi, H., Bouvier, S., Banu, M., Maier, C., Teodosiu, C.** (2006), Towards an accurate description of the anisotropic behaviour of sheet metals under large plastic deformations: Modelling, numerical analysis and identification. *International Journal of Plasticity*, 22: 2226–2271.
- [Hau02] **Haupt, P.** (2002), *Continuum Mechanics and Theory of Materials*. Springer.
- [Helling86] **Helling, D.E., Miller, A.K., Stout, M.G.** (1986), An experimental investigation of the yield loci of 1100-O aluminum, 70:30 brass, and an overaged 2024 aluminum alloy after various prestrains. *J. Eng. Mat. Tech.* 108: 313–320.
- [Helling87] **Helling, D.E., Miller, A.K.** (1987), The Incorporation of Yield Surface Distortion into a Unified Constitutive Model, Part I, *Acta Mechanica*, 69: 9-23.
- [Hill48] **Hill, R.** (1948), A theory of the yielding and plastic flow of anisotropic metals, *Proc. Roy. Soc. London A*, 193: 281–297.
- [Hol00] **Holzappel, G.** (2000), *Nonlinear Solid Mechanics*. Wiley & Sons.
- [Hughes87] **Hughes, T.J.R.** (1987), *The finite element method*, Prentice Hall.
- [Hun83] **Hunter S.C.,** (1983), *Mechanics of Continuous Media*, Ellis Horwood, Chichester.

- [Ishikawa97] **Ishikawa, H.** (1997), Subsequent yield surface probed from its current center. *Int. J. Plast.* 13: 533–549.
- [Johnson85] **Johnson G.R., Cook W.H.** (1985), Fracture characteristics of three metals subjected to various strains, strain rates, temperatures and pressures, *Engineering Fracture Mechanics*, 21(1): 31–48.
- [Johnson85] **Johnson, G.R., Cook, W.H.** (1985), Fracture characteristics of three metals subjected to various strains, strain rates, temperatures and pressures. *Engineering Fracture Mechanics*, 21 (1): 31–48.
- [Kachanov58] **Kachanov, L.M.** (1958), Time of the rupture process under creep conditions. TVZ Akad. Nauk. S.S.R. Otd, *Tech. Nauk.*, Vol.8.
- [Keeler63] **Keeler, S. P. and W. A. Backofen** (1963). Plastic Instability and fracture in sheets stretched over rigid punches. *Transactions of American Society for Metals*, 56: 25-48.
- [Keeler77] **Keeler, S.P., Brazier S.G.** (1977), Relationship between laboratory material characterization and press-shop formability. *In: Proceedings of Microalloying*, vol. 75, New York, pp. 517–530.
- [Khan09a] **Khan, A. S., Pandey, A., Stoughton, T.** (2010), Evolution of subsequent yield surfaces and elastic constants with finite plastic deformation. Part II: A very high work hardening aluminum alloy (annealed 1100 Al), *International Journal of Plasticity*, 26(10): 1421-1431.
- [Khan10a] **Khan, A.S., Pandey, A., Stoughton, T.** (2010a), Evolution of subsequent yield surfaces and elastic constants with finite plastic deformation. Part II: a very high work hardening aluminium alloy (annealed 1100 Al), *International Journal of Plasticity*, 26: 1421 – 1431.
- [Khan10b] **Khan, A.S., Pandey, A., Stoughton, T.** (2010b), Evolution of subsequent yield surfaces and elastic constants with finite plastic deformation. Part III: yield surface in tension-tension stress space (Al 6061-T6511 and annealed 1100 Al). *International Journal of Plasticity* 26:1432–1441.
- [Khoddam96] **Khoddam, S., Lam, Y.C., Thomson, P.F.** (1996), An inverse computational method for determining the constitutive parameters using the hot torsion test results, *Steel Research International*, 67: 22–25.
- [Kowalsky99] **Kowalsky, U., Ahrens, H., Dinkler, D.** (1999), Distorted yield surfaces modelling by higher order anisotropic hardening tensors,



- Computational Materials Science*, 16: 81–88.
- [Kowalsky99] **Kowalsky, U., Ahrens, H., Dinkler, D.** (1999), Distorted yield surfaces – modelling by higher order anisotropic hardening tensors. *Comput. Mater. Sci.* 16: 81–88.
- [Lemaitre05] **Lemaitre, J. and Desmorat, R.** (2005), *Engineering Damage Mechanics*. Springer.
- [Lemaitre09] **Lemaitre, J., Chaboche, J.L., BENALLAL, A., and Desmorat., R.** (2009), *Mécanique des matériaux solides*, Dunod, Paris, 3ème éditions.
- [Lemaitre85] **Lemaitre, J. and Chaboche, J.L.** (1985). *Mécanique des matériaux solides*, Paris, Dunod.
- [Lemaitre90] **Lemaitre, J., Chaboche, J.L.,** (1990). *Mechanics of Solid Materials*. Cambridge University Press.
- [Lemaitre92] **Lemaitre, J.,** (1992). *A Course on Damage Mechanics*, Springer, Berlin.
- [Lemaitre05] **Lemaitre, J. and Desmorat, R.** (2005). *Engineering Damage Mechanics*. Springer.
- [Lin05] **Lin, J., Liu, Y., and Dean, T.A.** (2005), A Review on Damage Mechanisms, Models and Calibration Methods under Various Deformation Conditions, *International Journal of Damage Mechanics*, 14: 299-319.
- [Lubarda93] **Lubarda, V.A., Krajcinovic, D.** (1993), Damage tensors and the crack density distribution, *International Journal of Solids and Structures* 30, 2859–2877.
- [Man74] **Mandel J.** (1974), *Introduction à la mécanique des milieux continus déformables*, Editions Scientifiques de Pologne, Varsolve.
- [Marciniak67] **Marciniak Z, Kuczynski K.** (1967), Limit strains in the process of stretch-forming sheet metal. *Int J Mech Sci*, 9:609–20.
- [McClintock71] **McClintock, F.A.** (1971), Plasticity aspects of fracture, volume III of *Fracture An Advanced Treatise*, chapter 2, pp. 47–307. Academic Press, New York and London.
- [Menzel05] **Menzel A., Ekh M., Runesson K., Steinmann P.** (2006), A framework for multiplicative elastoplasticity with kinematic hardening coupled to anisotropic damage, *International Journal of Plasticity*, Volume 21, Issue 3, Pages 397-434.

- [Murakami81] **Murakami, S., Ohno, N.** (1981), A continuum theory of creep and creep damage, In: Proceedings of the Third IUTAM Symposium on Creep in Structures , pp. 422–444, Springer, Berlin.
- [Murakami12] **Murakami, S.** (2012), Continuum damage mechanics: A continuum mechanics approach to the analysis of damage and fracture, Springer-Verlag, Dordrecht.
- [Nasim14] **Nasim Larijani, Jim Brouzoulis, Martin Schilke, Magnus Ekh,** (2014), The effect of anisotropy on crack propagation in pearlitic rail steel, *Wear*, Volume 314, Issues 1–2, Pages 57-68.
- [Ngu12] **Nguen D. T** (2012), Anisotropie de l'endommagement et simulation numérique en mise en forme par grandes déformations plastiques, PhD thesis, University of Technology of Troyes, Troyes.
- [Noll58] **Noll, W.** (1958). A mathematical theory of the mechanical behavior of continuous media. *Archive for Rational Mechanics and Analysis*, 2(1): 197-226.
- [Noman10] **Noman, M., Clausmeyer, T., Barthel, C., Svendsen, B., Huetink, J., Riel, M.** (2010), Experimental characterization and modeling of the hardening behavior of the sheet steel LH800, *Materials Science and Engineering A*, 527: 2515–2526.
- [Onate88] **Onate, E., and Kleiber, M.** (1988), Plastic and Viscoplastic Flow of Void Containing Metal - Applications to Axisymmetric Sheet Forming Problem, *Int. J. Num. Meth, In Engng*, 25:237-251.
- [Ortiz83] **Ortiz, M., Popov, E.** (1983), Distortional hardening rules for metals plasticity, *Journal of Engineering Mechanics*, 109: 1042–1057.
- [Ortiz85] **Ortiz, M.** (1985), A constitutive theory for the inelastic behavior of concrete, *Mechanics of Materials*, 4(1): 67–93.
- [Phillips72a] **Phillips, A., Tang, J.L.,** (1972), The effect of loading path on the yield surface at elevated temperatures, *Int. J. Solids Struct.* 8: 463–474.
- [Phillips72b] **Phillips, A., Liu, K., Justusson, J.W.** (1972), An experimental investigation of yield surfaces at elevated temperatures, *Acta Mech*, 14: 119–146.
- [Phillips76] **Phillips, A., Ricciuti, M.** (1976), Fundamental experiments in plasticity and creep of aluminum – extension of previous results, *Int. J. Solids Struct*, 12: 159–171.
- [Phillips79] **Phillips, A., Lee, C.-W.** (1979), Yield surfaces and loading surfaces:

- experiments and recommendations, *Int. J. Solids Struct*, 15: 715–729.
- [Phillips84] **Phillips, A., Lu, W.Y.** (1984), The experimental investigation of yield surfaces and loading surfaces of pure aluminum with stress controlled and strain controlled paths of loading, *ASME J. Eng. Mater. Technol*, 106: 349–354.
- [Pilling85] **Pilling, J.** (1985), Effect of Coalescence on Cavity Growth During Superplastic Deformation, *Materials Science and Technology*, 1: 461–465.
- [Rajhi14] Rajhi, W., Saanouni, K. and Sidhom, H. (2014), Anisotropic ductile damage fully coupled with anisotropic plastic flow: Modeling, experimental validation, and application to metal forming simulation, *International Journal of Damage Mechanics*.
- [Rees84] **Rees, D.W.A.** (1984), A examination of yield surface distortion and translation, *Acta Mech*, 52:15–40.
- [Riel08] **Riel, M.v. and A.H.v.d. Boogaard** (2008): Measurements and calculations on yield surfaces in tension-simple shear experiments, in 7th International Conference and Workshop on Numerical Simulation of 3D Sheet Metal Forming Processes, *Numisheet 2008*, Interlaken, Switzerland. p. 61-66.
- [Rice69] **Rice, J.R., Tracey, D.M.,** (1969), On the ductile enlargement of voids in triaxial stress fields, *Journal of the Mechanics and Physics of Solids*, 17: 201–217.
- [Ridley89] **Ridley, N.** (1989). Cavitations and Superplasticity, In Superplasticity, AGARD Lecture Series No. 168, Essex: Specialised Printing Services Limited, pp. 4.1–4.14.
- [Rousselier09] **Rousselier, G., Barlat, F., Yoon, J.W.** (2009), A novel approach for anisotropic hardening modeling. Part I: Theory and its application to finite element analysis of deep drawing, *Int. J. Plast*, 25: 2383–2409.
- [Saanouni94] **Saanouni, K., Forster, Ch., Ben Hatira, F.** (1994), On the an elastic flow with damage, *Engineering Damage Mechanics*, 3: 140–169.
- [Saanouni03] **Saanouni, K. and Chaboche, J.L.** (2003), Computational damage mechanics. Application to metal forming. Chapter 7 of Vol. 3 “Numerical and Computational methods”, Ed. I. Milne, R.O. Ritchie and B. Karihaloo, ISBN 0-08-043749-4, Elsevier Oxford (UK), p. 321-376.
- [Saanouni03] **Saanouni, K. and Chaboche, J.L.** (2003), Computational damage mechanics. Application to metal forming. Chapter 7 of Vol. 3

- “Numerical and Computational methods”, Ed. I. Milne, R.O. Ritchie and B. Karihaloo, ISBN 0-08-043749-4, Elsevier Oxford (UK), p. 321-376.
- [Saanouni12] **Saanouni, K.** (2012). *Damage Mechanics in Metal Forming: Advanced Modeling and Numerical Simulation*, London: ISTE Ltd; Hoboken, NJ: John Wiley & Sons.
- [Saanouni14] **Saanouni, K., Hamed, M.** (2013), Micromorphic approach for finite gradient-elastoplasticity fully coupled with ductile damage: Formulation and computational aspects, *International Journal of Solids and Structures*, 50(14–15): 2289-2309.
- [Shi13] **Shi, B. and Mosler, J.** (2013), On the macroscopic description of yield surface evolution by means of distortional hardening models: Application to magnesium, *International Journal of Plasticity*, 44: 1-22.
- [Shouler10] **Shouler, D.R., Allwood, J.M.** (2010). Design and use of a novel sample design for formability testing in pure shear, *Journal of Materials Processing Technology*, 210: 1304-1313.
- [Simo98] **Simo J.C., Hughes T.J.R.** (1998), *Computational Inelasticity*, Springer Verlag, New York.
- [Sidoroff73] **Sidoroff, F.** (1973). The geometrical concept of intermediate configuration and elastic-plastic finite strain, *Arch. Mech.*, 25(2): 299-308.
- [Sidoroff01] **Sidoroff, F., Dogui, A.** (2001), some issues about anisotropic elasticplastic models at finite strain, *Int. J. Sol. Str.* 38: 9569-9578.
- [Soyarslan10] Soyarslan, C., Tekkaya, A.E (2010). A damage coupled orthotropic finite plasticity model for sheet metal forming: CDM approach, *Computational Materials Science*, 48: 150-165.
- [Stören75] **Stören S, Rice JR.** (1975), Localized necking in thin sheets, *Journal of Mechanics and Physics of Solids*, 23:421–41.
- [Stoughton04] **Stoughton TB, Zhu X.** (2004), Review of theoretical models of the strain-based FLD and their relevance to the stress-based FLD, *Int J Plasticity*, 20:1463–86.
- [Seweryn98] **Seweryn, A., Mroz, Z.** (1998), On the criterion of damage evolution for variable multiaxial stress states, *International Journal of Solids and Structures*, 35: 1589–1616.
- [Teodosiu95a] **C. Teodosiu, Z. Hu** (1995), Evolution of the intragranular

- microstructure at moderate and large strains: modelling and computational significance, in: S. Shen, P.R. Dawson (Eds.) Proceedings of Numiform'95 on Simulation of Materials Processing: Theory, Methods and Applications, Rotterdam, Balkema, pp. 173–182.
- [Teodosiu95b] **Teodosiu, C., Hu, Z.** (1995), Evolution of the intragranular microstructure at moderate and large strains: modelling and computational significance. In: Shen, S.F., Dawson, P.R. (Eds.), Proceedings of the NUMIFORM' 95. Balkema, Rotterdam, pp. 173–182.
- [Teodosiu98] **Teodosiu C., Hu Z.** (1998), Microstructure in the continuum modelling of plastic anisotropy. In: Roskilde, Denmark (Eds.), Proceedings of the 19th Risø International Symposium on Modelling of Structures and Mechanics of Materials from Microscale to Product, pp. 149–168.
- [Thuillier2011] **Thuillier S., Le Maoût N., Manach P.Y.** (2011), Influence of ductile damage on the bending behaviour of aluminium alloy thin sheets, *Materials & Design*, 32(4): 2049-2057.
- [Thuillier09] **Thuillier S., Manach P.Y.** (2009), Comparison of the work-hardening of metallic sheets using tensile and shear strain paths, *International Journal of Plasticity*, 25(5): 733-751,
- [Unger08] **Unger J, Stiemer M, Brosius A, Svendsen B, Blum H, Kleiner M.** (2008), Inverse error propagation and model identification for coupled dynamic problems with application to electromagnetic metal forming. *International Journal of Solids and Structures*, 45: 442 - 59.
- [Uthaisangsuk08] **V. Uthaisangsuk, U. Prahl, S. Münstermann, W. Bleck** (2008), Experimental and numerical failure criterion for formability prediction in sheet metal forming, *Computational Materials Science*, 43(1): 43-50.
- [Wierzbicki05] **Wierzbicki T, Xue L.** (2005), On the effect of the third invariant of the stress deviator on ductile fracture. Impact and Crashworthiness Lab Report #136, *International Journal of Fracture*, submitted for publication.
- [Wriggers08] **Wriggers P.** (2008), *Nonlinear Finite Element Methods*, Springer Verlag, Berlin.
- [Wu05] **Wu, P.D., MacEwen, S.R., Lloyd, D.J., Jain, M., Tugcu, P., Neale, K.W.** (2005), On pre-straining and the evolution of material anisotropy in sheet metals. *Int. J. Plasticity*, 21: 723–739.

- [Wu91] **Wu, H.C., Yeh, W.C.** (1991), On the experimental determination of yield surfaces and some results of annealed 304 stainless steel, *Int. J. Plast.*, 7: 803–826.
- [Voyiadjis92] **Voyiadjis, G.Z., and Kattan, P.I.** (1992), A plasticity-damage theory for large deformations of solids. Part I: theoretical formulation, *Int. J. Eng. Sci.* 30: 1089–1108.
- [Voyiadjis00] **Voyiadjis, G.Z., Deliktas, B.** (2000), A coupled anisotropic damage model for the inelastic response of composite materials, *Computer Methods in Applied Mechanics and Engineering*, 183: 159–199.
- [Xue05] **Xue L.** (2005), Damage accumulation and fracture initiation in uncracked ductile solids under triaxial loading—Part I: Pressure sensitivity and Lode dependence. Impact and Crashworthiness Lab Report #138, submitted for publication.
- [Yeh06] **Yeh, W.-C., Lin, H.-Y.** (2006), An endochronic model of yield surface accounting for deformation induced anisotropy. *International Journal of Plasticity* 22, 16–38.
- [Yeh96] **Yeh, W.-C., Pan, W.-F.** (1996), An endochronic theory accounting for deformation induced anisotropy of metals under biaxial load. *International Journal of Plasticity*, 12: 987–1004.
- [Yin12] **Yin, Q., Soyarslan, C., Güner, A., Brosius, A., Tekkaya, A.E.** (2012). A cyclic twin bridge shear test for the identification of kinematic hardening parameters, *International Journal of Mechanical Sciences*, 59: 31-43.
- [Yin14] **Qing Yin, Benjamin Zillmann, Sebastian Suttner, Gregory Gerstein, Manfredi Biasutti, A. Erman Tekkaya, Martin F.-X. Wagner, Marion Merklein, Mirko Schaper, Thorsten Halle, Alexander Brosius** (2014), An experimental and numerical investigation of different shear test configurations for sheet metal characterization. *Int. J. Solids Struct.* 51: 1066–1074.
- [Yoshida03] **Yoshida, F., Urabe, M., Hino, R., Toropov, V.V.** (2003). Inverse approach to identification of material parameters of cyclic elasto-plasticity for component layers of a bimetallic sheet, *International Journal of Plasticity*, 19: 2149-2170.
- [Yoshida11] **Yoshida, Y and Ishikawa, T.** (2011). Determination of ductile damage parameters by notched plate tensile test using image analysis, *Materials Research Innovations*, 15: 422-425.
- [Yoshida98] **Yoshida, F., Urabe, M., Toropov, V.V.** (1998). Identification of

- material parameters in constitutive model for sheet metals from cyclic bending tests, *International Journal of Mechanical Sciences*, 40: 237–249.
- [Yue13] **Yue, Z. M., Soyarslan, C., Badreddine, H., Saanouni, K. & Tekkaya, a. E.** (2013), Inverse Identification of CDM Model Parameters for DP1000 Steel Sheets Using a Hybrid Experimental-Numerical Methodology Spanning Various Stress Triaxiality Ratios. *Key Eng. Mater.* 554-557, 2103–2110.
- [Zienkiewicz84] **Zienkiewicz O.C.** (1984), "Flow formulation for numerical solution of forming processes", Numerical analysis of forming processes, John Wiley & Sons Ltd.
- [Zienkiewicz89] **Zienkiewicz O.C. and TAYLOR, R. L.** (1989), "The Finite Element Methode", Vol. I – McGraw Hill.
- [Zienkiewicz91] **Zienkiewicz O.C. and TAYLOR, R. L.** (1991), "The Finite Element Methode", Vol. II – McGraw Hill.





# Résumé extensif en Français

## Introduction

Dans cette étude, un modèle couplé à l'endommagement ductile est proposé, qui tient compte des anisotropies initiales et induites avec écrouissage non linéaire mixte isotrope et cinématique. La fermeture des microfissures et l'angle de Lode sont introduits pour influencer la vitesse d'endommagement dans une large gamme de rapports de triaxialité des contraintes. La distorsion de la surface de charge est décrite par le remplacement de l'habituel tenseur déviateur des contraintes par un tenseur déviateur 'de distorsion', qui régit la distorsion des surfaces de charge. Ce modèle, validé par de nombreux essais, est capable de représenter de nombreux résultats expérimentaux. La mise en œuvre numérique a été réalisée et une série d'études numériques menée pour vérifier le modèle proposé. En outre, une approche MK (Marciniak-Kuczynski) est utilisée pour tracer les courbes limites de formage en déformations CLF (FLD) et en contraintes CLFC (FLSD) afin de comparer la prédiction de la rupture avec le modèle proposé d'endommagement ductile.

La thèse se compose de 4 chapitres.

## Chapitre I Aspects théoriques

### I.1 Formulation d'équations constitutives du modèle élastoplastique couplé à l'endommagement

#### Sélection des variables d'état et des variables effectives

Dans ce chapitre, des équations constitutives élastoplastiques fortement couplées à l'endommagement ductile isotrope sont formulées dans un cadre thermodynamiquement-cohérent. Le couplage fort entre l'écoulement plastique avec écrouissage et l'endommagement ductile est réalisé dans le cadre de l'hypothèse de l'équivalence en énergie totale conduisant à la définition des variables d'état effectives qui sont : l'écoulement élastoplastique  $(\underline{\tilde{\varepsilon}}^e, \underline{\tilde{\sigma}})$ , l'écrouissage cinématique  $(\underline{\tilde{\alpha}}, \underline{\tilde{X}})$  et l'écrouissage isotrope  $(\tilde{r}, \tilde{R})$  :

$$(\underline{\tilde{\varepsilon}}^e = \sqrt{1-d} \underline{\varepsilon}^e, \underline{\tilde{\sigma}} = \frac{\underline{\sigma}}{\sqrt{1-d}}) \quad (1)$$

$$(\tilde{\alpha} = \sqrt{1-d}\alpha, \tilde{X} = \frac{X}{\sqrt{1-d}}) \quad (2)$$

$$(\tilde{r} = \sqrt{1-d^\gamma}r, \tilde{R} = \frac{R}{\sqrt{1-d^\gamma}}) \quad (3)$$

où  $\gamma$  est un paramètre qui exprime l'effet de l'endommagement ductile sur l'érouissage isotrope d'une manière différentes par rapport à l'érouissage cinématique et les modules élastiques [Saanouni12].

### Potentiel d'état et équations d'état

Ces variables effectives sont utilisées dans les potentiels d'état et des dissipations afin de décrire le comportement élastoplastique endommagé. L'énergie libre de Helmholtz  $\psi = \psi(\underline{\varepsilon}^e, \underline{\alpha}, r, d)$ , fonction positive et convexe de toutes les variables d'état dans l'espace des déformations est retenue comme potentiel d'Etat. En supposant que la déformation plastique n'est pas d'effet sur le comportement élastique, le potentiel d'état peut être décomposé de façon additive comme suit (cas isotherme) :

$$\rho\psi(\underline{\varepsilon}^e, \underline{\alpha}, r, d) = \rho\psi^e(\underline{\varepsilon}^e, d) + \rho\psi^p(\underline{\alpha}, r, d) \quad (4)$$

avec

$$\begin{cases} \rho\psi^e(\underline{\varepsilon}^e, d) = \frac{\nu E}{2(1+\nu)(1-2\nu)} (\underline{\varepsilon}^e : \underline{I})^2 (1-d) + \frac{E}{2(1+\nu)} (\underline{\varepsilon}^e : \underline{\varepsilon}^e) (1-d) \\ \rho\psi^p(\underline{\alpha}, r, d) = \frac{1}{3} C \underline{\alpha} : \underline{\alpha} (1-d) + \frac{1}{2} Q r^2 (1-d^\gamma) \end{cases} \quad (5)$$

En supposant que les déformations élastiques sont infinitésimales devant les déformations plastiques, et en utilisant des arguments standard de la thermodynamique des processus irréversibles, les équations d'état suivantes peuvent être obtenues:

$$\underline{\sigma}(\underline{\varepsilon}^e, d) = \underline{\tau}(\underline{\varepsilon}^e, d) = \rho \frac{\partial \Psi}{\partial \underline{\varepsilon}^e} = (1-d)\lambda_e \text{tr}(\underline{\varepsilon}^e) \underline{1} + 2\mu_e (1-d) \underline{\varepsilon}^e \quad (6)$$

$$\underline{X}(\underline{\alpha}, d) = \rho \frac{\partial \Psi}{\partial \underline{\alpha}} = \frac{2}{3} (1-d) C \underline{\alpha} \quad (7)$$

$$R(r, d) = \rho \frac{\partial \Psi}{\partial r} = (1-d^\gamma) Q r \quad (8)$$

$$Y(\underline{\varepsilon}^e, \underline{\alpha}, r, d) = -\rho \frac{\partial \Psi}{\partial d} = Y^e + Y^\alpha + Y^r \quad (9)$$

$$Y^e = \frac{1}{2} \left( \lambda_e (\varepsilon^e : \mathbf{1})^2 + \mu_e \varepsilon^e : \varepsilon^e \right) \quad (10a)$$

$$Y^\alpha = \frac{1}{3} C \underline{\alpha} : \underline{\alpha} \quad (10b)$$

$$Y^r = \frac{1}{2} \gamma d^{r-1} Q r^2 \quad (10c)$$

où  $\mu_e$  et  $\lambda_e$  sont les constantes de Lamé classiques et ( $\lambda_e = \nu E / ((1+\nu)(1-2\nu))$ ,  $\mu_e = E / (2(1+\nu))$ ), tandis que les paramètres  $C$  et  $Q$  sont les modules des écrouissages cinématique et isotrope respectivement.

En tenant compte de la fermeture des microfissures, représentée par le paramètre  $h$ , et son effet sur la croissance d'endommagement, le tenseur des contraintes est spectralement décomposé en parties positives et négatives selon:  $\underline{\sigma} = \langle \underline{\sigma} \rangle_+ + \langle \underline{\sigma} \rangle_-$  où  $\langle \underline{\sigma} \rangle_+ = \sum_{i=1}^3 \langle \sigma_i \rangle \vec{e}_i \otimes \vec{e}_i$  et  $\langle \underline{\sigma} \rangle_- = \underline{\sigma} - \langle \underline{\sigma} \rangle_+$  où  $\sigma_i$  sont les valeurs propres du tenseur  $\underline{\sigma}$  et  $\vec{e}_i$  sont les vecteurs propres associés. La notation  $\langle \cdot \rangle$  indique les parenthèses de Macaulay. Par conséquent, les variables effectives (1) relatives au comportement élastique endommageable sont modifiées et décomposées en parties déviatoriques et hydrostatiques comme suit:

$$\left\{ \begin{array}{l} \tilde{\underline{\varepsilon}}^e = g_e(d) \langle \underline{\varepsilon}^e \rangle_+ + g_e(hd) \langle \underline{\varepsilon}^e \rangle_- \\ \quad = \sqrt{1-d} \left( \langle \underline{\varepsilon}^e \rangle_+ + \frac{1}{3} \langle tr(\underline{\varepsilon}^e) \rangle \mathbf{1} \right) + \sqrt{1-hd} \left( \langle \underline{\varepsilon}^e \rangle_- - \frac{1}{3} \langle -tr(\underline{\varepsilon}^e) \rangle \mathbf{1} \right) \\ \tilde{\underline{\sigma}} = \frac{\langle \underline{\sigma} \rangle_+}{g_e(d)} + \frac{\langle \underline{\sigma} \rangle_-}{g_e(hd)} \\ \quad = \frac{1}{\sqrt{1-d}} \left( \langle \underline{\sigma}^{dev} \rangle_+ + \frac{1}{3} \langle tr(\underline{\sigma}) \rangle \mathbf{1} \right) + \frac{1}{\sqrt{1-hd}} \left( \langle \underline{\sigma}^{dev} \rangle_- - \frac{1}{3} \langle -tr(\underline{\sigma}) \rangle \mathbf{1} \right) \end{array} \right. \quad (11)$$

où  $\underline{e}^e$  désigne la partie déviatorique du tenseur des petites déformations élastiques  $\underline{\varepsilon}^e$  et le paramètre  $h \in [0.0 \ 1.0]$  représente la fermeture des microfissures en compression. En utilisant les variables effectives, définies ci-dessus, dans l'énergie libre de Helmholtz pris comme un potentiel d'Etat, les relations d'état suivantes peuvent être facilement obtenues [Saanouni94, Badreddine10, Saanouni 12] :

$$\underline{\sigma} = 2\mu_e \left[ (1-d) \langle \underline{e}^e \rangle_+ + (1-hd) \langle \underline{e}^e \rangle_- \right] + \lambda_e \left[ (1-d) \langle tr(\underline{\varepsilon}^e) \rangle - (1-hd) \langle -tr(\underline{\varepsilon}^e) \rangle \right] \mathbf{1} \quad (12)$$

$$Y^e = 2\mu_e \left[ \langle \underline{e}^e \rangle_+ : \langle \underline{e}^e \rangle_+ + h \langle \underline{e}^e \rangle_- : \langle \underline{e}^e \rangle_- \right] + \lambda_e \left[ \langle \text{tr}(\underline{\varepsilon}^e) \rangle^2 + h \langle -\text{tr}(\underline{\varepsilon}^e) \rangle^2 \right] \quad (13)$$

### Fonction de charge et potentiel de dissipation : équations d'évolution

Nous introduisons dans le cadre de la plasticité non-associée une fonction de charge  $f$  et un potentiel plastique  $F$  [Badreddine10]. Dans cette étude, un modèle à surface unique est utilisé pour décrire le comportement élastoplastique endommagé en utilisant la même fonction de charge et le potentiel plastique suivant:

$$\begin{cases} f = \frac{\|\underline{S}_d^i - \underline{X}\|_H}{\sqrt{1-d}} - \frac{R}{\sqrt{1-d^\gamma}} - \sigma_y & (a) \\ F = \frac{\|\underline{S}_d^p - \underline{X}\|_H}{\sqrt{1-d}} - \frac{R}{\sqrt{1-d^\gamma}} + \frac{3a}{4(1-d)C} \underline{X} : \underline{X} + \frac{b}{2(1-d)Q} R^2 + \frac{S}{s+1} \left\langle \frac{Y - Y_0}{S(\theta)} \right\rangle^{s+1} \frac{1}{(1-d)^\beta} & (b) \end{cases} \quad (14)$$

$$\|\underline{S}_d^i - \underline{X}\|_H = \sqrt{(\underline{S}_d^i - \underline{X}) : \underline{\underline{H}} : (\underline{S}_d^i - \underline{X})} ; (i = \{c, p\}) \quad (15)$$

$\|\underline{S}_d^i - \underline{X}\|_H$  est la contrainte équivalente anisotrope Hill48 caractérisée par un opérateur anisotrope avec 6 paramètres d'anisotropie:  $F, G, H, L, M$  et  $N$ .  $\sigma_y$  est la limite d'élasticité initiale et  $a$  et  $b$  caractérisent la non-linéarité de l'écrouissage cinématique et isotrope.  $s, s, \beta$  et  $Y_0$  sont des paramètres matériau qui définissent l'évolution de l'endommagement ductile. Afin d'introduire l'angle de Lode  $\theta$  qui influe sensiblement sur l'évolution de l'endommagement, en particulier sous les forts rapport de triaxialité des contraintes, deux formes sont proposées :

$$S(\bar{\theta}) = \begin{cases} \left[ S_0 \left[ c_1 + \frac{\sqrt{3}}{2-\sqrt{3}} c_2 \left( \sec(\bar{\theta} \frac{\pi}{6}) - 1 \right) \right] \right]^{\frac{1}{s}} & \text{Wierzbiki-type} \\ S_0 [c_1 + c_2 \bar{\theta}^2]^{\frac{1}{s}} & \text{Cao-type} \end{cases} \quad (16)$$

$$\bar{\theta} = 1 - 6 \frac{\theta}{\pi} \quad \text{and} \quad \theta = \frac{1}{3} \cos^{-1} \left( \frac{27}{2} \frac{J_3}{\|\underline{\sigma}\|_M^3} \right), \quad J_3 = \det(\underline{\sigma})$$

Les tenseurs déviateurs  $S_d^i$  contrôlent la distorsion de la surface de charge dans deux directions orthogonales et sont définis par:

$$\left\{ \begin{array}{l} \underline{S}_d^c = \underline{S} + \frac{\underline{S}_0 : \underline{S}_0}{2(1-d)X_{11}^c(R/\sqrt{1-d^\gamma} + \sigma_y)} \underline{X} - \frac{\underline{X} : \underline{X}}{2(1-d)X_{12}(R/\sqrt{1-d^\gamma} + \sigma_y)} \underline{S}_0 \quad (a) \\ \underline{S}_d^p = \underline{S} + \frac{\underline{S}_0 : \underline{S}_0}{2(1-d)X_{11}^p(R/\sqrt{1-d^\gamma} + \sigma_y)} \underline{X} \quad (b) \end{array} \right. \quad (17)$$

$$\underline{S}_0 = \underline{S} - \underline{S}_x \quad \text{and} \quad \underline{S}_x = \frac{\underline{S} : \underline{X}}{\underline{X} : \underline{X}} \cdot \underline{X} \quad (18)$$

La surface de charge prend alors une forme d'œuf [Francois01] dont le grand axe est parallèle à la direction du tenseur de l'érouissage cinématique  $\underline{X}$  contrôlée par  $\underline{S}_x$ .  $\underline{S}_0$  contrôle la direction transverse. Les deux paramètres  $X_{11}^c$  et  $X_{11}^p$  différencient l'effet de la distorsion sur la fonction de charge ( $X_{11}$ ) et sur le potentiel plastique. Un nouveau paramètre  $X_{12}$  a été introduit dans  $\underline{S}_d$  pour contrôler la taille transversale de la surface.

En appliquant la règle de normalité généralisée on obtient les variables flux suivants qui définissent l'évolution des phénomènes dissipatifs [Saanouni94, Badreddine10, Saanouni12] :

$$\underline{D}^p = \dot{\lambda} \frac{\partial F}{\partial \underline{\sigma}} = \dot{\lambda} \underline{n}^p \quad \text{with} \quad \underline{n}^p = \frac{\underline{n}^d}{\sqrt{1-d}} : \left[ 1^{dev} + \frac{\underline{X} \otimes \underline{S}_0}{\tilde{X}_{11}^p(R/\sqrt{1-d^\gamma} + \sigma_y)} \right] \quad (19)$$

$$\underline{\alpha} = -\dot{\lambda} \frac{\partial F}{\partial \underline{X}} = \dot{\lambda} \left( \frac{\underline{n}^x}{\sqrt{1-d}} - a\underline{\alpha} \right) \quad \text{and} \quad \underline{n}^x = \underline{n}^d - \frac{1}{(R/\sqrt{1-d^\gamma} + \sigma_y)} \left[ \frac{(\underline{S}_0 : \underline{S}_0)}{2\tilde{X}_{11}^p} \underline{n}^d - \frac{(\underline{S} : \underline{X})(\underline{X} : \underline{n}^d)}{\tilde{X}_{11}^p(\underline{X} : \underline{X})} \underline{S}_0 \right] \quad (20)$$

$$\dot{r} = -\dot{\lambda} \frac{\partial F}{\partial R} = \dot{\lambda} \left( \frac{\underline{n}^i}{\sqrt{1-d^\gamma}} - br \right) \quad \text{with} \quad \underline{n}^i = \frac{(\underline{S}_0 : \underline{S}_0)(\underline{n}^p : \underline{X})}{2\sqrt{1-d}\tilde{X}_{11}^p(R/\sqrt{1-d^\gamma} + \sigma_y)^2} + 1 \quad (21)$$

$$\underline{n}^d = \frac{\underline{H} : (\underline{S}_d^p - \underline{X})}{\|\underline{S}_d^p - \underline{X}\|_H} \quad (22)$$

$$\dot{d} = \dot{\lambda} \frac{\partial F}{\partial Y} = \frac{\dot{\lambda}}{(1-d)^\beta} \left( \frac{\langle Y - Y_0 \rangle}{S(\theta)} \right)^s \quad (23)$$

Le multiplicateur plastique  $\dot{\lambda}$  peut être déterminé à partir de la condition de cohérence  $\dot{f}^p = 0$  si  $f^p = 0$ , toutefois, il sera gardé comme la principale inconnue à chaque point d'intégration de chaque élément fini. Ce modèle est mis en œuvre dans ABAQUS / Explicit © code aux éléments finis à travers la routine de l'utilisateur VUMAT. Ce sous-programme est développé en utilisant un algorithme itératif numérique purement implicite d'intégration [Saanouni03, Badreddine10, Saanouni12].

## I.2 Courbes limites de formage pour les tôles (CLF)

### A propos la construction CLF

Pour la détermination expérimentale de la CLF, les essais de Nakazima et de Marciniak sont les plus communément utilisées. Les deux essais peuvent être effectués sur machine d'essai de Erichsen.

### Une brève description de l'approche M-K

L'approche Marciniak - Kuczynski (MK) est basée sur la croissance d'un défaut initial comme inhomogénéité sous la forme d'une bande étroite inclinée d'un angle ( $\varphi^0$ ) par rapport à l'axe principal (Fig. 1-8). En Plasticité rigide, l'état de contraintes planes et l'écroutissage isotrope du matériau sont supposés. Le défaut de géométrie dans la zone  $b$  est caractérisé par un rapport  $f^0$  des épaisseurs :

$$f^0 = e_b / e_a \quad (24)$$

où  $e_b^0$  et  $e_a^0$  représentent l'épaisseur initiale dans la zone  $b$  et la zone  $a$ . Le repère  $(x, y, z)$  défini les axes de laminage, transversal et normal de la plaque, tandis que les directions 1, 2 et 3 représentent les directions des contraintes principales dans la région homogène. Dans la zone de la rainure,  $n$  et  $t$  représentent le sens normal et longitudinal de la rainure.

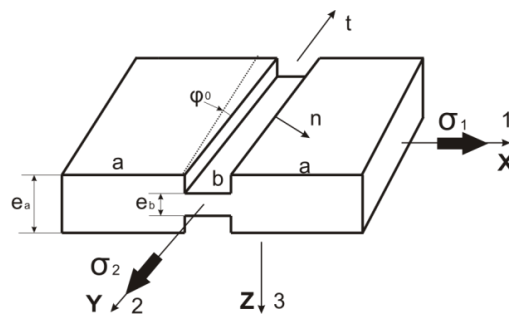


Fig. 1. Schématisation de l'approche M-K.

La condition d'équilibre qui indique l'équilibre des forces conduit aux équations suivantes:

$$\sigma_{nm}^a e_a = \sigma_{nm}^b e_b, \sigma_{nt}^a e_a = \sigma_{nt}^b e_b \quad (25)$$

La condition de continuité suppose que la vitesse des déformations est identique dans les deux régions :

$$d\varepsilon_n^a = d\varepsilon_n^b \quad (26)$$

Les équations d'équilibre donnent:

$$\begin{aligned} f \sigma_{nn}^b &= \sigma_{nn}^a \\ f \sigma_{nt}^b &= \sigma_{nt}^a \end{aligned} \quad (27)$$

où  $f = e_b / e_a$  est le rapport des épaisseurs actuelles donné par:

$$f = f^0 \cdot \exp(\varepsilon_{zz}^b - \varepsilon_{zz}^a) \quad (28)$$

Finalement la contrainte et le taux des déformations s'expriment par les deux équations non linéaires suivantes avec deux inconnues :

$$\begin{cases} F_1(d\bar{\varepsilon}_b, \sigma_{tt}^b) = \bar{\sigma}^b - \bar{\sigma}_{YF}^b = 0 \\ F_2(d\bar{\varepsilon}_b, \sigma_{tt}^b) = d\varepsilon_{tt}^a - d\varepsilon_{tt}^b = 0 \end{cases} \quad (29)$$

### Définition de la striction locale

Le système (1-97) peut être résolu itérativement avec la méthode de Newton–Raphson pour calculer les deux inconnues  $d\bar{\varepsilon}_b$  et  $\sigma_{tt}^b$ . Le critère M-K suppose que la localisation de l'écoulement plastique se produit lorsque l'incrément de la déformation équivalente  $d\bar{\varepsilon}_b$  est 10 fois plus grand que  $d\bar{\varepsilon}_a$  dans la zone homogène. Alors, les composantes  $(\varepsilon_{xx}^a, \varepsilon_{yy}^a)$  accumulées dans la zone homogène sont les déformations limites. L'analyse est répétée pour différentes valeurs de  $\varphi^0$  (compris entre  $0^\circ$  et  $90^\circ$ ) et la courbe limite est obtenue après réduction au minimum de la courbe  $\varepsilon_{xx}^a$  en fonction de  $\varphi^0$ .

## Chapitre II Aspects numériques

### II.1 application numérique du modèle proposé

#### Programme d'intégration locale: calcul des variables d'état

Quel que soit le schéma global de la résolution utilisée, nous devons calculer les opérateurs élémentaires que sont la matrice et les vecteurs caractérisant le problème d'évolution, qui sont définis par les intégrales de volume ou de surface pour chaque élément de référence. Ce calcul passe par la connaissance de toutes les variables d'état qui sont décrites par les équations constitutives. Pour résoudre ces équations, le schéma de prédiction élastique et correction plastique est utilisé.

$$\begin{aligned}
 f_{n+1} &= \frac{\|\underline{S}_{d(n+1)}^c - \underline{X}_{n+1}\|_H}{\sqrt{1-d_{n+1}}} - \frac{R_{n+1}}{\sqrt{1-d_{n+1}^\gamma}} - \sigma_y = 0 & (a) \\
 \|\underline{S}_{d(n+1)}^k - \underline{X}_{n+1}\|_H &= \sqrt{(\underline{S}_{d(n+1)}^k - \underline{X}_{n+1}) : \underline{H} : (\underline{S}_{d(n+1)}^k - \underline{X}_{n+1})} \quad k \in \{c, p\} & (b) \\
 \underline{S}_{d(n+1)}^c &= \underline{S}_{n+1} + \frac{\underline{S}_{0(n+1)} : \underline{S}_{0(n+1)}}{2(1-d_{n+1})X_{l1}^c(R_{n+1}/\sqrt{1-d_{n+1}^\gamma} + \sigma_y)} \underline{X}_{n+1} \\
 &\quad - \frac{\underline{X}_{n+1} : \underline{X}_{n+1}}{2(1-d_{n+1})X_{l2}^c(R_{n+1}/\sqrt{1-d_{n+1}^\gamma} + \sigma_y)} \underline{S}_{0(n+1)} & (c) \\
 \underline{S}_{d(n+1)}^p &= \underline{S}_{n+1} + \frac{\underline{S}_{0(n+1)} : \underline{S}_{0(n+1)}}{2(1-d_{n+1})X_{l1}^p(R_{n+1}/\sqrt{1-d_{n+1}^\gamma} + \sigma_y)} \underline{X}_{n+1} \quad , \quad \underline{S}_{0(n+1)} = \underline{S}_{n+1} - \frac{\underline{S}_{n+1} : \underline{X}_{n+1}}{\underline{X}_{n+1} : \underline{X}_{n+1}} \underline{X}_{n+1} & (d) \\
 \underline{S}_{n+1} &= \underline{\sigma}_{n+1} - \frac{1}{3} \text{tr}(\underline{\sigma}_{n+1}) \underline{1} & (e) \\
 \underline{\sigma}_{n+1} &= 2\mu_e \left[ (1-d_{n+1}) \langle \underline{\varepsilon}_{n+1}^e \rangle_+ + (1-hd_{n+1}) \langle \underline{\varepsilon}_{n+1}^e \rangle_- \right] & (f) \\
 &\quad + \lambda_e \left[ (1-d_{n+1}) \langle \text{tr}(\underline{\varepsilon}_{n+1}^e) \rangle - (1-hd_{n+1}) \langle -\text{tr}(\underline{\varepsilon}_{n+1}^e) \rangle \right] \underline{1} & (g) \\
 \underline{X}_{n+1} &= \frac{2}{3} (1-d_{n+1}) C \underline{\alpha}_{n+1} & (h) \\
 R_{n+1} &= (1-d_{n+1}^\gamma) Q r_{n+1} & (i) \\
 \underline{\varepsilon}_{n+1}^p - \underline{\varepsilon}_n^p - \Delta \lambda \underline{n}_{n+1}^p &= 0 & (j) \\
 g_\alpha &= \begin{cases} \underline{\alpha}_{n+1} - \frac{1}{(1+a\Delta\lambda)} \left( \Delta\lambda \frac{n_{n+1}^x}{\sqrt{1-d_{n+1}}} + \underline{\alpha}_n \right) = 0 & \text{Forward Euler} \\ \underline{\alpha}_{n+1} - \underline{\alpha}_n e^{-a\Delta\lambda} - \frac{n_{n+1}^x}{a\sqrt{1-d_{n+1}}} (1 - e^{-a\Delta\lambda}) = 0 & \text{Asymptotic} \end{cases} & (k) \\
 g_r &= \begin{cases} r_{n+1} - \frac{1}{(1+b\Delta\lambda)} \left( \Delta\lambda \frac{n_{n+1}^i}{\sqrt{1-d_{n+1}^\gamma}} + r_n \right) = 0 & \text{Forward Euler} \\ r_{n+1} - r_n e^{-b\Delta\lambda} - \frac{n_{n+1}^i}{b\sqrt{1-d_{n+1}^\gamma}} (1 - e^{-b\Delta\lambda}) = 0 & \text{Asymptotic} \end{cases} & (l) \\
 \underline{n}_{n+1}^p &= \frac{n_{n+1}^d}{\sqrt{1-d_{n+1}}} : \left[ \underline{1}^{dev} + \frac{\underline{X}_{n+1} \otimes \underline{S}_{0(n+1)}}{(1-d_{n+1})X_{l1}^p(R_{n+1}/\sqrt{1-d_{n+1}^\gamma} + \sigma_y)} \right] & (m) \\
 \underline{n}_{n+1}^x &= \underline{n}_{n+1}^d - \frac{\left[ \frac{(\underline{S}_{0(n+1)} : \underline{S}_{0(n+1)}) \underline{n}_{n+1}^d}{2} - \frac{(\underline{S}_{n+1} : \underline{X}_{n+1})(\underline{X}_{n+1} : \underline{n}_{n+1}^d)}{(\underline{X}_{n+1} : \underline{X}_{n+1})} \underline{S}_0 \right]}{(1-d_{n+1})X_{l1}^p(R_{n+1}/\sqrt{1-d_{n+1}^\gamma} + \sigma_y)} & (n) \\
 n_{n+1}^i &= \frac{(\underline{S}_{0(n+1)} : \underline{S}_{0(n+1)}) (n_{n+1}^d : \underline{X}_{n+1})}{2(1-d_{n+1})^{3/2} X_{l1}^p(R_{n+1}/\sqrt{1-d_{n+1}^\gamma} + \sigma_y)^2} + 1 & (o) \\
 \underline{n}_{n+1}^d &= \frac{\underline{H} : (\underline{S}_{d(n+1)}^p - \underline{X}_{n+1})}{\|\underline{S}_{d(n+1)}^p - \underline{X}_{n+1}\|_H} & (p) \\
 d_{n+1} - d_n - \frac{\Delta\lambda}{(1-d_{n+1})^\beta} \left( \frac{\langle Y_{n+1} - Y_0 \rangle}{S(\bar{\theta}_{n+1})} \right)^s &= 0 & (q) \\
 S(\bar{\theta}_{n+1}) &= \begin{cases} \left[ S_0 \left[ c_1 + \frac{\sqrt{3}}{2 - \sqrt{3}} c_2 \sec \left( (\bar{\theta}_{n+1} - \frac{\pi}{6}) - 1 \right) \right] \right]^{-1/s} & \text{Wierzbicki type} \\ \left[ S_0 \left[ c_1 + c_2 \bar{\theta}_{n+1}^2 \right] \right]^{-1/s} & \text{Cao type} \end{cases} \quad , \quad \bar{\theta}_{n+1} = 1 - 6 \frac{\theta_{n+1}}{\pi} & (r) \\
 \theta_{n+1} &= \frac{1}{3} \cos^{-1} \left( \frac{27}{2} \frac{J_{3(n+1)}}{\|\underline{\sigma}_{n+1}\|_M^3} \right) \quad \text{where} \quad \|\underline{\sigma}_{n+1}\|_M = \sqrt{\frac{3}{2} \underline{S}_{n+1} : \underline{S}_{n+1}} \quad \text{and} \quad J_{3(n+1)} = \det(\underline{S}_{n+1}) & (s)
 \end{aligned}$$

Ces équations discrétisées par des schémas aux différences finies appropriés sont résumées par (30). En fait la discrétisation repose sur la combinaison de deux schémas :



- La Téta-méthode purement implicite pour les équations gouvernant la déformation plastique et l'endommagement
- La méthode asymptotique pour les équations gouvernant l'érouissage isotrope et l'érouissage cinématique

De plus amples détails peuvent être trouvés dans (Badreddine 10, Saanouni12). Nous nous contentons de donner ici la synthèse de toutes les équations écrite à l'instant  $t_{n+1}$  qui est le temps de fin d'un intervalle de temps typique résultant de la discrétisation du temps. Ces équations sont rassemblées dans (30).

### Prédiction élastique :

On suppose que l'accroissement de la déformation totale  $\Delta \underline{\varepsilon}$  est complètement élastique :

$$\begin{cases} \Delta \underline{\varepsilon}^p = 0 \\ \Delta \underline{\alpha} = 0 \\ \Delta r = 0 \\ \Delta d = 0 \end{cases} \Rightarrow \begin{cases} \underline{\varepsilon}_{n+1}^p = \underline{\varepsilon}_n^p \\ \underline{\alpha}_{n+1} = \underline{\alpha}_n \\ r_{n+1} = r_n \\ d_{n+1} = d_n \end{cases} \quad (31)$$

Ainsi, la contrainte « essai » peut être obtenue :

$$\underline{\sigma}_{n+1}^* = 2\mu_e \left[ (1-d_n) \langle \underline{\varepsilon}_{n+1}^e \rangle_+ + (1-hd_n) \langle \underline{\varepsilon}_{n+1}^e \rangle_- \right] + \lambda_e \left[ (1-d_n) \langle \text{tr}(\underline{\varepsilon}_{n+1}^e) \rangle - (1-hd_n) \langle -\text{tr}(\underline{\varepsilon}_{n+1}^e) \rangle \right] \underline{1} \quad (32)$$

$$\underline{S}_{n+1}^* = \underline{\sigma}_{n+1}^* - \text{tr}(\underline{\sigma}_{n+1}^*) \underline{I} \quad (33)$$

$$\underline{e}_{n+1}^{e*} = \underline{\varepsilon}_{n+1}^{e*} - \frac{1}{3} \text{tr}(\underline{\varepsilon}_{n+1}^{e*}) \underline{I} \quad (34)$$

$$\underline{S}_{0(n+1)}^* = \underline{S}_{(n+1)}^* - \underline{S}_{x(n+1)}^* \quad \text{and} \quad \underline{S}_{x(n+1)}^* = \frac{\underline{S}_{(n+1)}^* : \underline{X}_n}{\underline{X}_n : \underline{X}_n} \cdot \underline{X}_n \quad (35)$$

$$\underline{S}_{d(n+1)}^{c*} = \underline{S}_{(n+1)}^* + \frac{\underline{S}_{0(n+1)}^* : \underline{S}_{0(n+1)}^*}{2(1-d_n)X_{l1}^c(R_{n+1}/\sqrt{1-d_n'} + \sigma_y)} \underline{X}_n - \frac{\underline{X}_n : \underline{X}_n}{2(1-d_n)X_{l2}(R_n/\sqrt{1-d_n'} + \sigma_y)} \underline{S}_{0(n+1)}^* \quad (36)$$

Le critère d'écoulement correspondant à cet état essai est alors donné par :

$$f_{n+1}^*(\underline{\sigma}_{n+1}^*, \underline{X}_n, R_n, d_n) = \frac{\| \underline{S}_{d(n+1)}^{c*} - \underline{X}_n \|_H}{\sqrt{1-d_n}} - \frac{R_n}{\sqrt{1-d_n'}} - \sigma_y \quad (37)$$

Si  $f_{n+1}^*(\underline{\sigma}_{n+1}^*, \underline{X}_n, R_n, d_n) < 0$ , donc l'hypothèse de solution élastique est correcte, et la solution du problème est la suivante :

$$\underline{\sigma}_{n+1} = \underline{\sigma}_{n+1}^*, \quad \underline{\varepsilon}_{n+1}^p = \underline{\varepsilon}_n^p, \quad \underline{X}_{n+1} = \underline{X}_n, \quad \underline{\alpha}_{n+1} = \underline{\alpha}_n, \quad R_{n+1} = R_n, \quad r_{n+1} = r_n \quad \text{et} \quad Y_{n+1} = Y_n, \quad d_{n+1} = d_n \quad (38)$$

### Correction plastique :

Si  $f_{n+1}^*(\underline{\sigma}_{n+1}, \underline{X}_n, R_n, d_n) > 0$  alors la solution du problème est plastique et on doit corriger les variables « essai » pour garantir que  $f_{n+1}(\Delta\lambda, \underline{n}_{n+1}^p, d_{n+1}) = 0$ . Cela revient à résoudre les équations (30) après réduction du nombre d'équations pour économiser le temps CPU conduisant au système suivant :

$$\left\{ \begin{array}{l} f(\Delta\lambda, \underline{n}_{n+1}^p, d_{n+1}) = \frac{\| \underline{S}_{n+1}^d(\Delta\lambda, d_{n+1}, \underline{\sigma}_{n+1}, \underline{X}_{n+1}) - \underline{X}_{n+1} \|_H}{\sqrt{1-d_{n+1}}} - \frac{R_{n+1}(\Delta\lambda, d_{n+1})}{\sqrt{1-d_{n+1}^\gamma}} - \sigma_y = 0 \\ g(\Delta\lambda, \underline{n}_{n+1}^p, d_{n+1}) = d_{n+1} - d_n - \frac{\Delta\lambda}{(1-d_{n+1})^\beta} \left\langle \frac{Y_{n+1}^*(\Delta\lambda, d_{n+1}, \underline{\sigma}_{n+1}, \underline{X}_{n+1}) - Y_0}{S(\theta)_{n+1}} \right\rangle^s = 0 \\ \wp(\Delta\lambda, \underline{n}_{n+1}^p, d_{n+1}) = \underline{n}_{n+1}^p - \frac{\underline{n}_{d(n+1)}}{\sqrt{1-d_{n+1}}} : \left[ \mathbf{1}^{dev} + \frac{\underline{X}_{n+1} \otimes \underline{S}_{0(n+1)}}{(1-d_{n+1})X_{I1}(R_{n+1}/\sqrt{1-d_{n+1}} + \sigma_y)} \right] = 0 \end{array} \right. \quad (39)$$

Ce système est résolu grâce à la discrétisation par la méthode de Newton-Raphson. Plus de détails au sujet de la solution en 3D et en 2D contraintes planes sont présentés dans II.1.3.

## Chapitre III : Aspects expérimentaux et étude paramétrique

### III.1 Procédure expérimentale et les résultats

Une étude expérimentale a été menée sur des tôles minces en trois matériaux : deux aciers DP1000 et CP1200 et un aluminium A17020. Une série d'essais a été effectuée afin d'étalonner et de valider les modèles proposés. Divers essais uni axiaux de traction sur éprouvettes lisses (UT), de torsion (IPT), de tension sur éprouvettes pré-entaillées (PNT), de cisaillement simple (SS), des essais avec chargements combinés (CL), des essais Nakazima (NAK) et des essais d'emboutissage profond d'un embouti cruciforme (CSD).

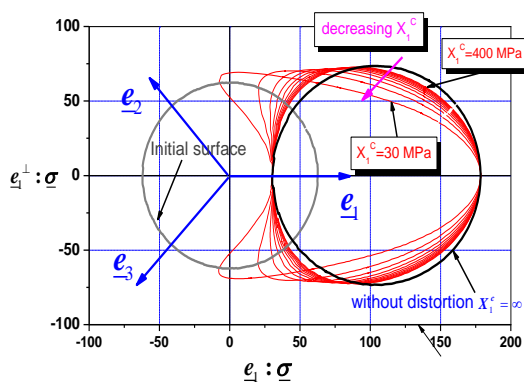
### III.2 Etude paramétrique et identification des modèles proposés

Avant de déterminer les paramètres matériaux intervenant dans les équations du modèle, une étude paramétrique sur la sensibilité de la réponse du modèle aux divers paramètres est menée. La sensibilité aux valeurs de plusieurs paramètres a été faite en détail dans plusieurs publications (voir par exemple Saanouni 10). Ici nous nous limitons à l'étude de sensibilité sur les nouveaux paramètres introduits pour décrire la distorsion de la surface de charge et les paramètres relatifs à l'effet de l'angle de Lode sur la vitesse d'endommagement.

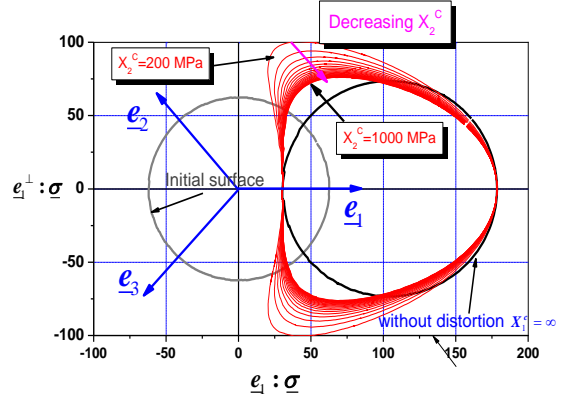
#### Effets des paramètres de distorsion sur les surfaces des charges

La Fig. 2 compare la surface de charge initiale aux surfaces de charge après 5% de  $\varepsilon_{eq}^p$  dans

différents espaces des contraintes : le plan déviatorique ( $\pi$ -plane), le plan des contraintes principales ( $\sigma_1, \sigma_2$ ) et le plan de tension – cisaillement plan ( $\frac{3}{2}e_1 : \sigma, \sqrt{3}e_3 : \sigma$ ). Il est constaté que le paramètre  $X_{11}^c$  commande le rapport de distorsion de la surface de charge, mais ne change pas sa taille ; alors que  $X_{12}$  commande la taille transversale des surfaces de charge orthogonalement à la direction de chargement. La décroissance de  $X_{12}$  entraine une croissance de la taille de la surface de charge.

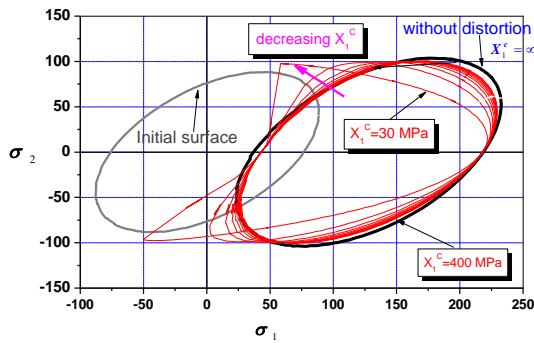


(a) Effet du paramètre  $X_1^c$  ( $X_2^c = \infty$ ).

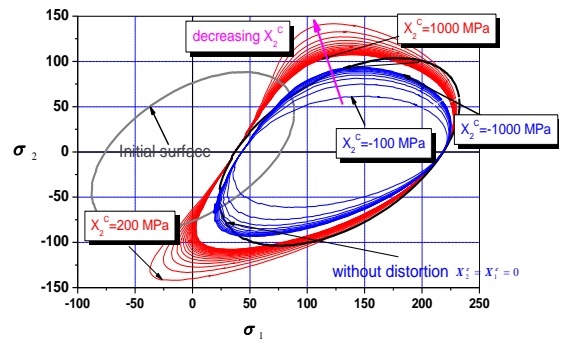


(b) Effet du paramètre  $X_2^c$  ( $X_1^c = 100$ ).

le plan déviatorique ( $\pi$ -plane)

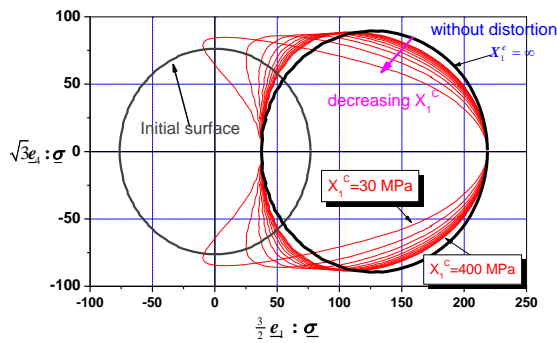


(c) Effet du paramètre  $X_1^c$  ( $X_2^c = \infty$ ).

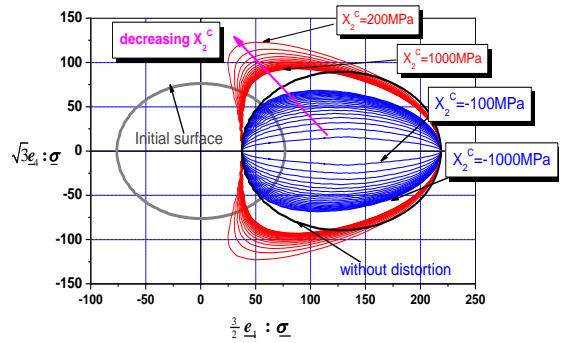


(d) Effet du paramètre  $X_2^c$  ( $X_1^c = 100$ ).

le plan des contraintes principales ( $\sigma_1, \sigma_2$ ).



(e) Effet du paramètre  $X_1^c$  ( $X_2^c = \infty$ ).



(f) Effet du paramètre  $X_2^c$  ( $X_1^c = 100$ ).

le plan de tension – cisaillement plan ( $\frac{3}{2}e_1 : \underline{\sigma}$ ,  $\sqrt{3}e_4 : \underline{\sigma}$ ).

Fig. 2. Influence des paramètres de distorsion  $X_1^c$  et  $X_2^c$  sur les évolutions de la surface de charge.

### Effet des paramètres de distorsion sur l'évolution de l'endommagement

Dans la Fig.3, la contrainte équivalente est tracée pour différentes valeurs des paramètres de distorsion ( $X_{11}^c$ ,  $X_{11}^p$ ,  $X_{12}$ ). En comparant les courbes avec et sans distorsion, on constate que la baisse de  $X_{11}^c$  entraîne l'amplification de la distorsion et la rupture est retardée en augmentant le stade de saturation de l'écroutissage. On remarque aussi que le paramètre  $X_{11}^p$  n'affecte pas la limite d'élasticité, mais influence l'évolution de l'écroutissage. Quand  $X_{12}$  est positif, la surface de charge se dilate, mais quand le durcissement augmente, la courbe contrainte-déformation coïncide à nouveau avec les courbes d'origine. D'autre part, quand  $X_{12}$  est négatif, la surface de charge décroît progressivement.

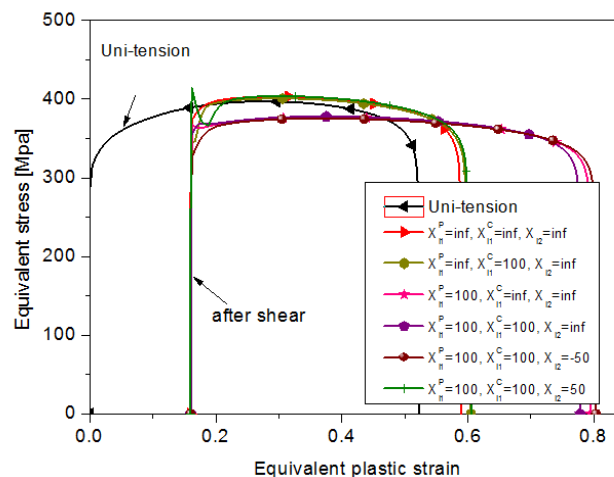


Fig. 3. Effet des paramètres de distorsion sur les courbes de contrainte équivalente déformation plastique après 12 % de pré-contrainte

**Effet de l'angle de Lode et rapport de triaxialité des contraintes sur l'évolution de l'endommagement.**

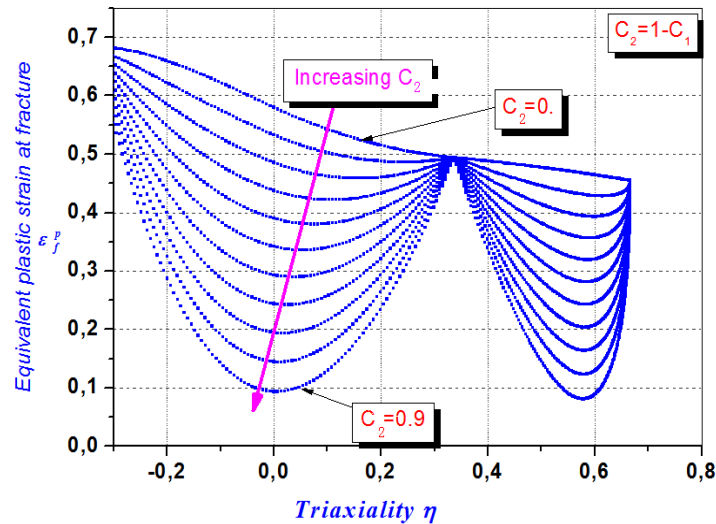


Fig. 4. Locus de fracture dans le plan de l'état de stress pour le type proposé évolution de l'endommagement.

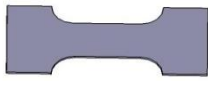

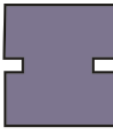
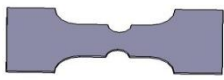

La contribution de l'angle de Lode de  $s(\bar{\theta})$  pour le modèle de Wierzbicki et le modèle de Cao sur l'évolution de l'endommagement pour ( $c_1 = 1$  et  $c_2 = 0$ ) est maintenant étudiée. Il se trouve que ces deux formes donnent approximativement les mêmes valeurs avec la modification des paramètres de Lode, de sorte que ces deux formes peuvent être considérées comme identiques. Dans la Fig.4 les déformations plastiques équivalentes à la rupture sont tracées en fonction du rapport de triaxialité avec ( $c_1 + c_2 = 1$ ). Ces résultats ont montré que la déformation à la rupture n'est pas une fonction monotone décroissante de la triaxialité des contraintes lorsque le paramètre Lode est considéré. Pour les fortes valeur de triaxialité des contraintes, où le mécanisme de croissance sphérique des cavités joue un rôle majeur dans le processus d'évolution des dommages, la déformation plastique équivalente diminue avec l'augmentation du rapport de triaxialité des contraintes. Dans la plage de  $0 \leq \eta \leq 0.33$  et  $0.57 \leq \eta \leq 0.66$  la déformation plastique équivalente à la rupture augmente avec l'augmentation du rapport de la triaxialité, qui est en bon accord avec les résultats expérimentaux [Bao04].

## Chapitre IV Identification et validation des modèles proposés

### IV.1 La méthodologie d'identification du modèle couplé

Une méthode inverse est utilisée pour l'identification des paramètres du modèle sur un matériau donné. Cette méthode d'identification inverse combine le script Python, le logiciel ABAQUS avec un programme d'optimisation basé sur MATLAB. Le Tableau 1 synthétise les essais utilisés pour identifier les différents groupes de paramètres intervenant dans le modèle fortement couplé.

Tableau 1. Différents essais pour identifier différents groupes de paramètres

		Type d'essais	Paramètres	Nombre	Méthodologie
Elastoplasticité	UT		$E, \nu, \sigma_y, F, G, H, L, M, N$	9	Analytique
	IPT		$C, a, Q, b$	4	Inverse
Distorsion	CL		$X_{11}^C, X_{11}^P, X_{12}$	3	Analytique
Endommagement	PNT		$S, s, \beta, Y_0$	4	Inverse
	SS		$h$	1	Inverse

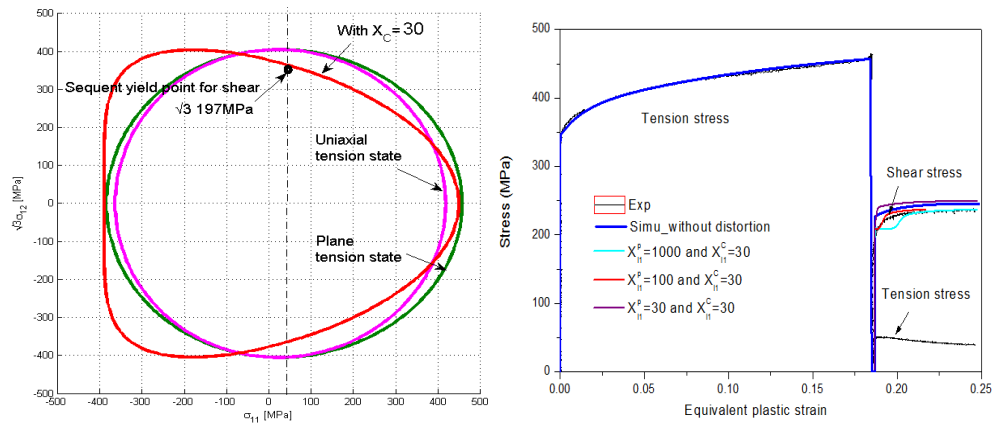
Pour les essais UT, les paramètres d'élasticité ( $E, \nu$ ), et  $\sigma_y$  sont obtenus directement, et avec le paramètre de Lankford  $r_\theta^L$  dans trois directions, les paramètres d'anisotropie de Hill48 sont déterminées avec l'approche analytique. Les paramètres d'érouissage mixte sont déterminés avec les réponses expérimentales IPT et UT par la méthode inverse. Les valeurs optimales des paramètres matériaux du modèle proposé sont résumées dans le Tableau 2.

Tableau 2. Paramètres d'élastoplasticité obtenus à partir de résultats UT et TBT

	$E$ (GPa)	$\nu$	$\sigma_y$ (MPa)	$Q$ (MPa)	$b$	$C$ (MPa)	$a$	$F$	$G$	$H$	$L$	$M$	$N$
DP 1000	208.0	0.3	809.0	4000.0	13.0	32000.0	150. 0	0.525	0.546	0.455	1.5	1.5	1.67
CP 1200	207.0	0.3	980.0	5848.0	37.0	37000.0	507. 0	0.567	0.610	0.389	1.5	1.5	1.37
AL 7020	69.8	0.3	322.0	675.0	8.0	2260.0	75.0	0.631	0.634	0.366	1.5	1.5	1.4

### Identification des paramètres de distorsion

Les essais CL servent à calibrer les paramètres de distorsion  $X_{11}^C$  et  $X_{11}^P$  par un essai de tension-cisaillement avec une certaine déformation plastique équivalente. Selon les besoins, le  $X_{12}$  sera déterminé.



(a) Surface de charge (b) Courbe d'écoulement pour tension- cisaillement

Fig. 5. Evolution du comportement après 18% de pré-tension pour Al7020.

Pour l'alliage Al7020, la valeur de la déformation plastique équivalente de pré-tension est de 18.% (Fig.5). Après 18,0% de pré-tension, les contraintes de cisaillement sont de 197.0 MPa, tandis que le résultat simulé (sans l'effet de distorsion de la surface) est de 220.0 MPa. La valeur de  $X_{II}^c$  peut être déterminée dans l'espace des tension-cisaillement avec la diminution de la limite d'élasticité (comme représenté sur la Fig.5). Quand  $X_{II}^c$  est égal à 30.0 MPa, la surface de charge couvre la valeur expérimentale  $\sqrt{3} \times 197$  MPa. La valeur optimale de  $X_{II}^p$  qui contrôle l'écoulement est choisie à 100.0 MPa.

### Identification des paramètres d'endommagement ductile

Pour la détermination des paramètres d'endommagement ( $S$ ,  $s$ ,  $\beta$ ,  $Y_0$ ,  $h$ ), les essais PNT et SS conduits jusqu'à la rupture finale sont utilisés. Cela permet de suivre le développement de l'endommagement ductile sous différents trajets de chargement caractérisés par différents rapports de triaxialité des contraintes.

Les réponses numériques des essais de PNT en termes de courbes force-déplacement sont utilisées comme courbes de références pour identifier les paramètres. Le tableau 3 présente les valeurs optimales de tous les paramètres identifiés.

Tableau 3. Paramètres d'endommagement résultant d'essais PNT et SS.

	<b>S(MPa)</b>	<b>s</b>	<b><math>\beta</math></b>	<b><math>\gamma</math></b>	<b><math>Y_0</math>(MPa)</b>	<b>h</b>
DP1000	12.5	1.15	2.5	4	2.0	0.25
CP1200	10.2	1.31	1.98	4	2.0	0.21
Al7020	4.50	1.48	3.4	4	0.0	0.3

### Détermination des paramètres de l'approche M-K pour Al7020

Pour cette étude le modèle d'érouissage isotrope de Swift est considéré. Les paramètres déterminés sont indiqués dans le tableau 3-17. La Fig. 3-67 montre la comparaison entre les courbes réelles de contrainte vraie expérimentales et numériques, montrant un bon accord avant la striction. Les courbes CLF et CLFC déterminées par la procédure M-K sont indiquées dans la Fig. 6.

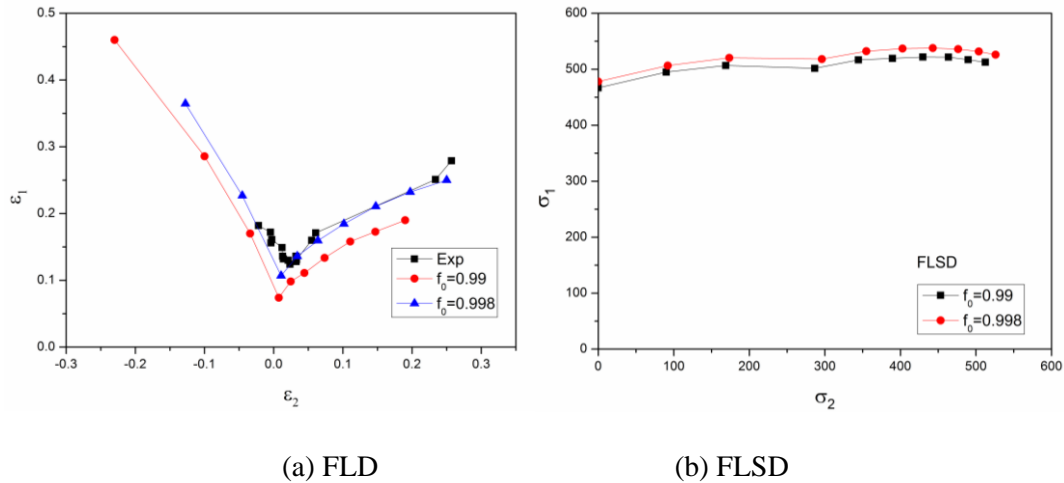


Fig. 6. FLDs et FLSDs expérimentales et théoriques pour Al7020

### IV.3 Simulation Nakazima avec modèle CDM

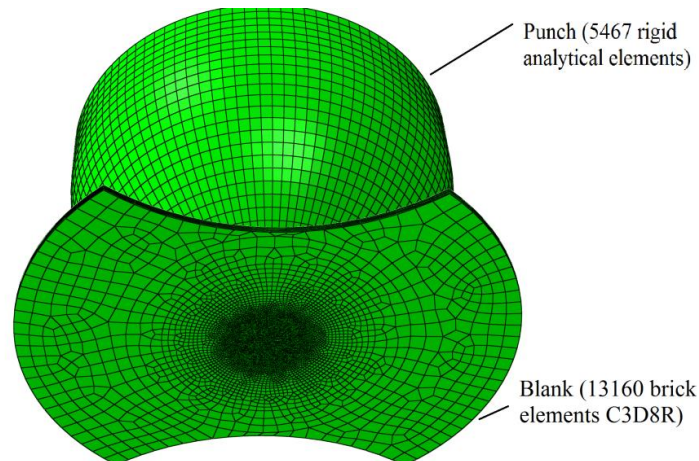


Fig. 7. Maillage des composants de l'essai Nakazima N°4.

Un exemple de modèle de la géométrie pour  $r^N = 65.0$  mm est représenté Fig. 7. L'élément de brique C3D8R est utilisé pour construire l'ébauche. Dans la zone critique, la taille minimale de 0.15 mm de maille est utilisée, de sorte qu'il doit être de 10 éléments de la



section d'épaisseur. Le numéro de l'élément total est de 13160. Le poinçon se déplace verticalement avec une vitesse de 10.0 mm/s. Lorsque les contacts du poinçon de l'ébauche, les modèles de friction avec des coefficients de frottement 0.05 seront utilisés. La simulation va s'arrêter jusqu'à la rupture finale se produit sur le flan

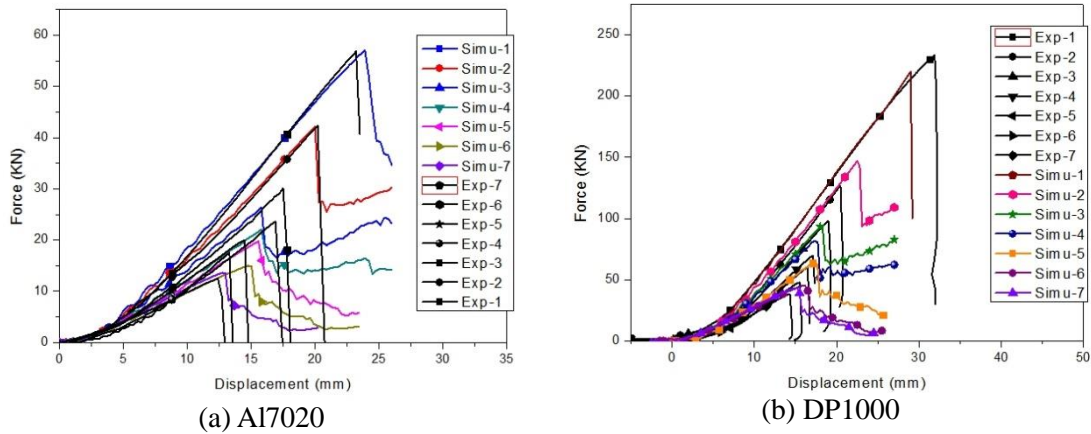


Fig. 8. Comparaison des courbes Force-Déplacement entre les réponses expérimentales et simulées.

Les comparaisons des courbes force-déplacement expérimentales et numériques pour AI7020 et DP1000 sont présentées Fig. 8. Dans la Fig. 9 nous donnons des comparaisons quantitatives entre les valeurs expérimentales et numériques relatives aux essais NAK.

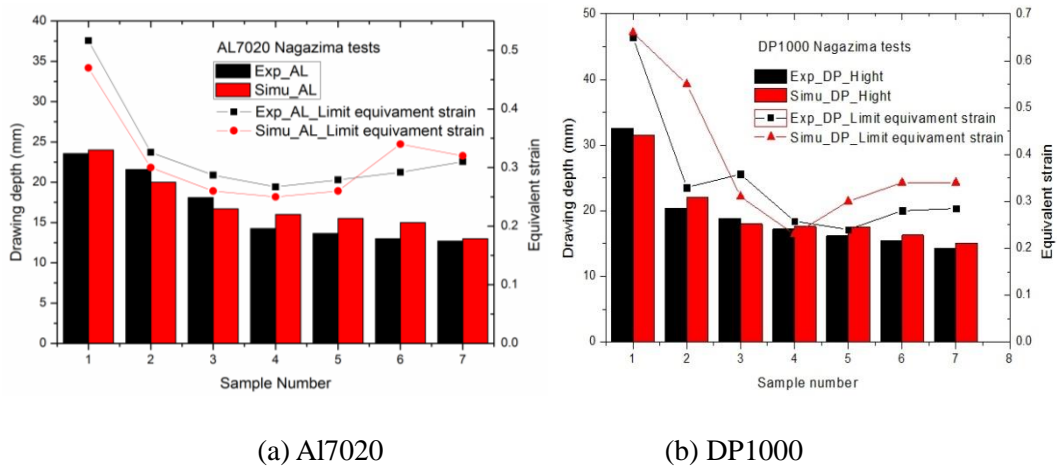


Fig. 9. Comparaison des déplacements et déformations plastiques équivalentes de

(a) AI7020, (b) DP1000 pour les essais NAK.

#### IV.4 Essais d'emboutissage

Les essais CSD des trois matériaux sont également simulés dans ABAQUS/Explicit avec le

modèle couplé pour prévoir leurs limites de formage. Pour Al7020; Les CLF et CLFC obtenues avec l'approche MK sont également utilisés pour comparaison avec les prévisions du modèle couplé. Pour la clarté de la présentation du modèle géométrique seule la moitié du procédé est présentée sur la Fig. 10 alors que le modèle complet est modélisé par EF comme le montre la Fig. 11. L'élément solide hexaédrique C3D8R à 8 nœuds est utilisé pour mailler la tôle avec une taille des mailles de 0,15 mm dans les zones critiques donnant un total de 675615 éléments solides.

### **Simulation de l'essai d'emboutissage en croix avec les trois nuances de matériaux : Al7020, DP1000 and CP1200**

Des simulations de l'essai d'emboutissage profond en forme de croix, ont été réalisées avec les trois nuances de matériaux étudiés : Al7020, DP1000 and CP1200 afin de prédire leurs limites de formabilité. Ces simulations ont été effectuées en utilisant les paramètres matériaux identifiées du modèle de comportement couplée à l'endommagement ductile et elles ont été conduites avec le code E.F. ABAQUS/Explicit. Particulièrement pour le matériaux Al7020, une comparaison avec des simulations utilisant un modèle standard d'ABAQUS défini par une approche non couplé utilisant les courbes limites de formage (dans l'espace des déformations FLD et des contraintes FLSD ) ayant été construites numériquement en utilisant la méthode classique MK. Dans la Fig.10 est présenté l'assemblage du modèle E.F. de l'essai en croix (notons qu'uniment la moitié du modèle a été illustrée pour des raisons de clarté). Les paramètres de maillage utilisé pour la tôle sont présentés dans la Fig. 11.

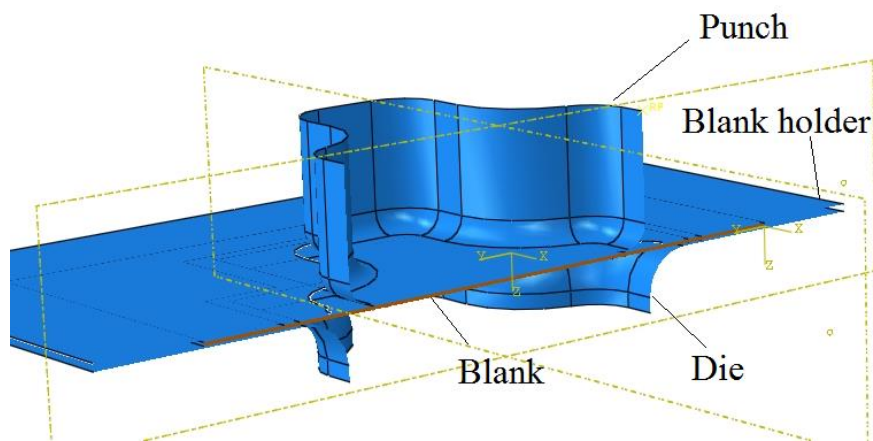


Fig. 10. Model E.F. de l'essai d'emboutissage en croix.

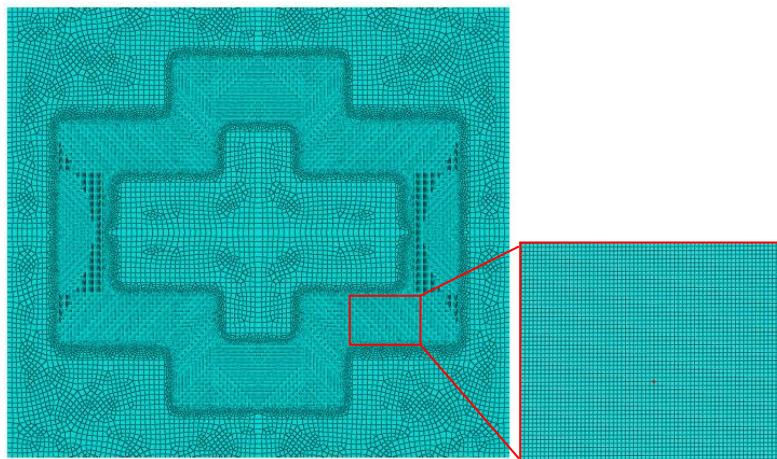


Fig. 11. Propriétés du Maillage de la tôle de l'essai d'emboutissage en croix (157860 hexaédrique C3D8R avec une taille de  $0.15 \times 0.15 \text{ mm}^2$  dans la zone critique).

Pour l'Al7020, la force de serre-flan est réglée pour atteindre une valeur maxi de l'ordre de 120 kN. La comparaison des courbes expérimentales et numériques en termes de force-déplacement est représentée sur la Fig. 12. Cette figure montre un bon accord entre la prédiction numérique du modèle et l'expérimentation. Dans la Fig.13 sont présentés les trajets de fissures macroscopiques obtenues numériquement et expérimentalement. On peut voir qu'aussi bien la forme que le lieu de la fissure prédite numériquement sont quasi similaires avec les résultats expérimentaux. Sur la Fig.13 on observe 4 fissures qui s'amorcent d'une façon parfaitement symétrique sur les 4 coins de la partie la moins élancé de la croix et se développent exactement au niveau de l'arrondi du poinçon.

Pour les matériaux DP1000 et CP1200 les simulations de l'essai d'emboutissage en croix ont été réalisées uniquement avec le modèle de comportement couplé à l'endommagement et avec les mêmes paramètres de maillage (donné dans la Fig.11). Il est à signaler que l'effort de serre-flan utilisé dans ce cas est de l'ordre de 400.0 kN. Les comparaisons des courbes expérimentales et numériques en termes de force-déplacement sont présentées dans la Fig. 15. Cette figure montre également un bon accord entre résultats expérimentaux et numériques pour les deux matériaux DP1000 et CP1200 .

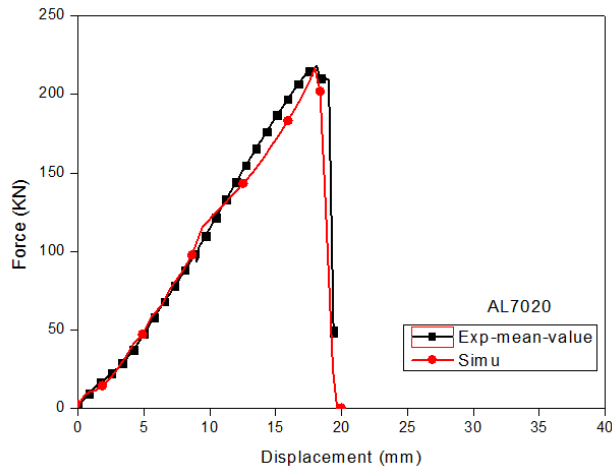


Fig. 12. Comparaison des courbes expérimentale et numérique en termes de force-déplacement obtenues avec l'essai d'emboutissage en croix avec l' Al7020.

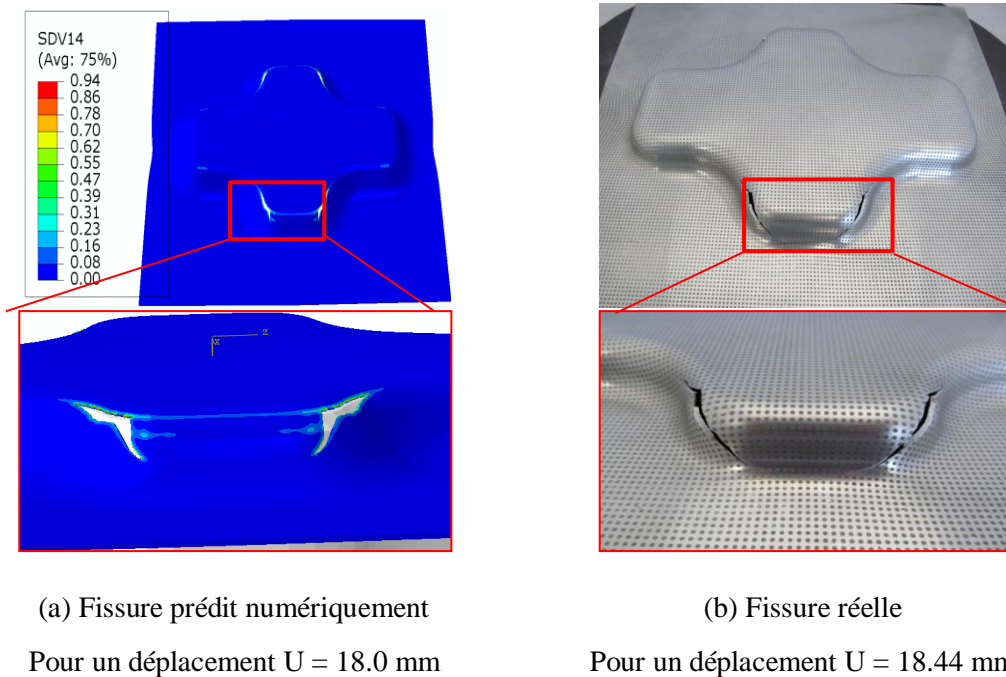
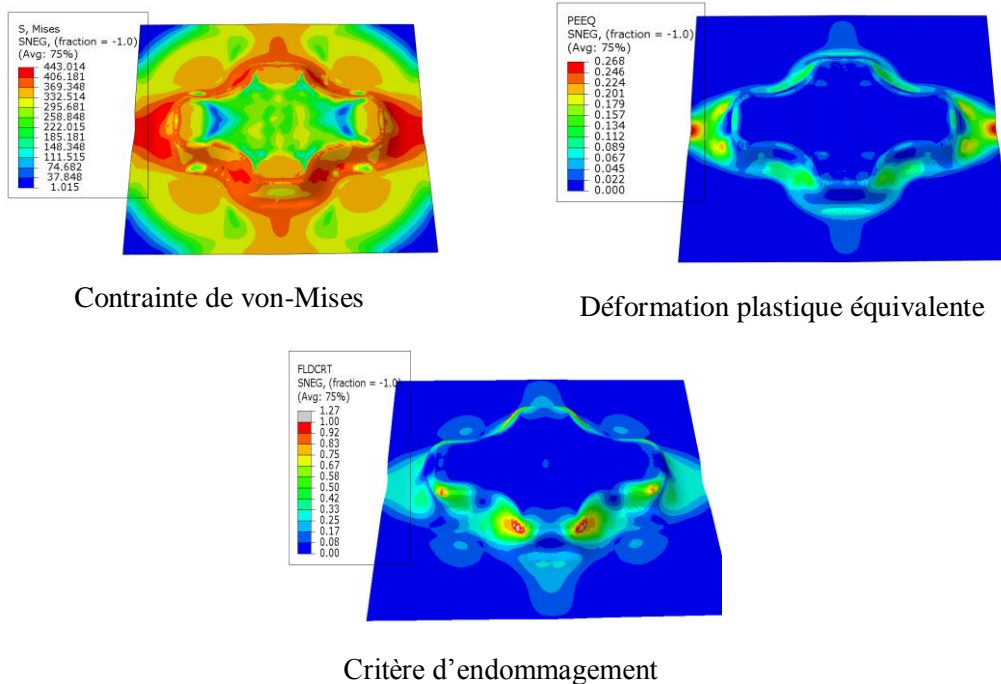


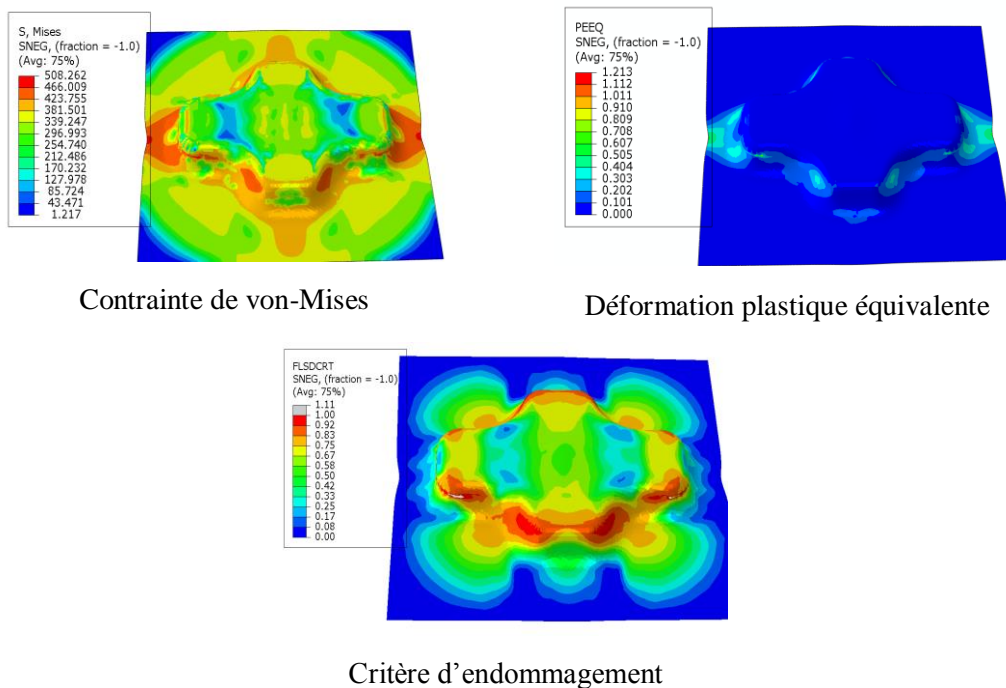
Fig. 13. Comparaison des trajets de fissure numérique et expérimentale pour l'essai d'emboutissage en croix avec l'Al7020.

La Fig.14 donne la répartition de la contrainte de Mises, de la déformation plastique équivalente ainsi que le critère d'endommagement pour les deux approches utilisant les courbes limites de formage (FLD et FLSD). D'après cette figure nous pouvons constater que l'approche avec FLD prédit une fissure précoce avec un déplacement  $U=16\text{mm}$  (plus faible que le déplacement mesuré expérimentalement  $U=18.44\text{ mm}$ ) par contre elle donne une bonne estimation du lieu de l'amorçage. En ce qui concerne l'approche utilisant la FLSD,

nous constatons à partir de la Fig.14b que l'amorce survient très tardivement pour un déplacement  $U=22.0$  mm et que le lieu de l'amorce se trouve sur l'autre partie de la croix (partie la plus élancé) .



(a) Résultats de simulation utilisant un modèle standard d'ABAQUS avec la courbe FLD. Le critère de rupture prédit un amorçage de fissure pour un déplacement  $U = 16.0$  mm



(b) Résultats de simulation utilisant un modèle standard d'ABAQUS avec la courbe FLSD. Le critère de rupture prédit un amorçage de fissure pour un déplacement  $U = 22.0$  mm



Fig.14. Comparaison des résultats de simulation de l'essai d'emboutissage en croix avec un modèle utilisant les FLD et FLSD.

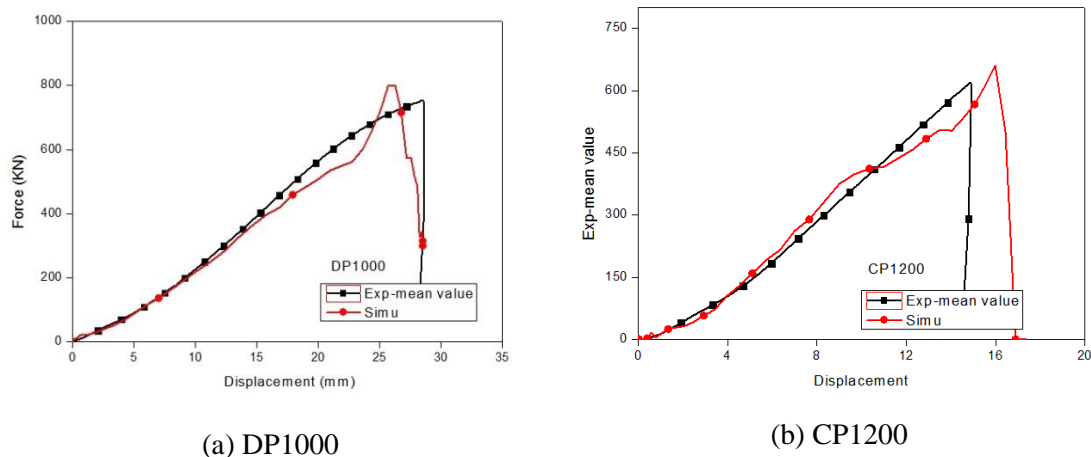


Fig 15. Comparaison des courbes numériques et expérimentales en termes de force-déplacement obtenues avec l'essai d'emboutissage en croix et avec les matériaux DP1000 et CP1200.

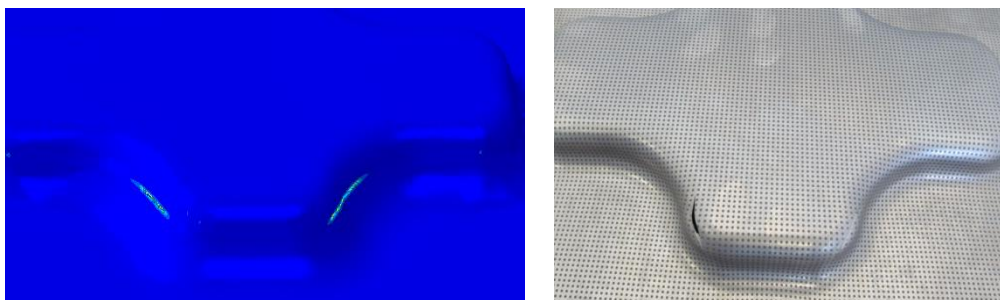


Fig. 16. Comparaison du trajet de fissure expérimental et numérique obtenu avec le modèle couplé à l'endommagement pour le DP1000.

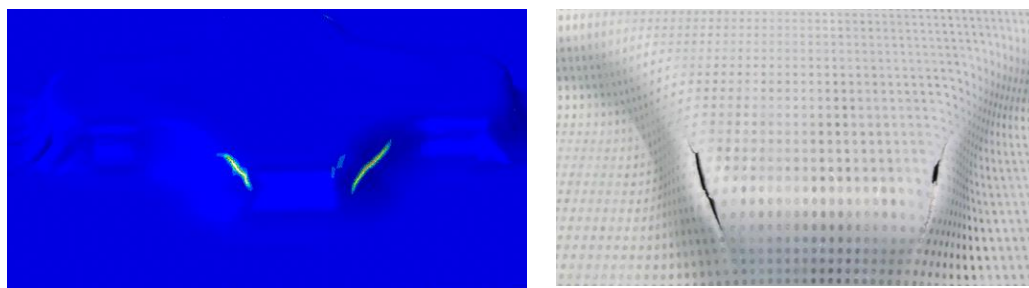


Fig. 17. Comparaison du trajet de fissure expérimental et numérique obtenu avec le modèle couplé à l'endommagement pour le CP1200.

## Conclusions et perspectives

Les principales contributions de ce travail concernent la prise en compte, pour la simulation des procédés de mise en forme des tôles minces, de la distorsion de la surface de charge, du

taux de triaxialité, de l'angle de Lode, de l'histoire de chargement et l'analyse de leurs effets sur les évolutions de l'ensemble variables décrivant l'état mécanique et plus particulièrement sur l'endommagement. Cet objectif est motivé par le fait que les zones critiques qui se développent lors de la mise en forme d'une tôle et où apparaissent des déformations plastiques élevées et par conséquent des dommages ductile localisé, sont les lieux de trajets de chargement loin d'être monotones et proportionnels.

Beaucoup de travail reste à faire afin d'étendre le modèle proposé d'une part pour l'appliqué sur des trajets de chargement non proportionnels divers et variés et d'une autre part pour couvrir d'autre aspects plus généraux, tels que: l'anisotropie de l'endommagement, la prise en compte de la non localité de l'endommagement dans le cadre d'une formulation Micromorphe, la viscoplasticité dans le cadre d'une formulation thermomécanique couplé... Cette extension nécessite bien entendu le développement d'une base de données expérimentale assez complète permettant de couvrir des trajets de chargements plus complexes. Cette base de données servira à alimenter la méthodologie d'identification des paramètres du modèle de comportement qui dans sa version la plus générale contiendra des dizaines de paramètres.

Afin de valider toute cette modélisation avancée il primordiale de mettre en œuvre une panoplie d'essais de mise en forme couvrant une grande partie des procédés industriels complexes .





# Umfangreiche zusammengefasst in Deutch

## Einführung:

In dieser Arbeit wird ein vollständiges, gekoppeltes, duktils Schädigungsmodell vorgeschlagen, welche die anfängliche- und induzierte Anisotropie der Fließfläche sowie die isotrope und kinematische Verfestigung berücksichtigt. Ebenfalls wird in diesem Modell die Mikrorisssschließung betrachtet, um die Formänderungsgrenze bei niedrigem Triaxialitätsverhältnis zu erhalten. Der Lode-Winkel-Parameter nimmt drei Formen in die Gleichung der Schädigungsentwicklung ein, um den Einfluss der Umformgrenzen bei positiver und negativer Triaxialität zu erhalten. Das vorgeschlagene Modell kann viele bestehende Umformprozesse wiedergeben und wurde durch weitere Versuchreihe überprüft. Die Umsetzung des vorgeschlagenen Bruchmodells erfolgte numerisch und wurde anhand von numerischen Versuchsreihen auf die Gültigkeit überprüft. Darüber hinaus wird ein MK-Ansatz entwickelt, um den Vergleich zwischen FLDs, FLSDs und duktilen Schädigung hinsichtlich der Vorhersage des Bruchversagens zu erhalten.

## Kapitel I Theoretische Aspekte

### I.2 Formulierung der vorgeschlagenen voll gekoppelten Modell

#### Auswahl der Zustandsvariablen und effektiven Zustandsvariablen

In dieser Studie wurde ein elastoplastische Stoffgesetz, welches vollständig mit einer isotropen, duktilen Schädigung und einem thermodynamischen Stoffgesetz [Saanouni94, Badreddine10, Saanouni12] gekoppelt ist, vorgeschlagen. Theoretische, numerische und applikative Aspekte der vollständigen, gekoppelten Formulierungen sind in [Saanouni12] zu finden. Im Rahmen dieser Arbeit wird vollständiges gekoppeltes Modell zur Beschreibung der verzerrten Fließfläche in [Saanouni12], welches auf das oben beschriebenen François 'Modell basiert, verwendet und erweitert. Es werden folgenden Paare von Zustandsvariablen verwendet: (i)  $(\underline{\epsilon}^e, \underline{\sigma})$  für das elastoplastische Fließen; (ii)  $(\underline{\alpha}, \underline{X})$  für die kinematische Verfestigung, welche die Fließfläche beschreibt; (iii)  $(r, R)$  für die isotrope Verfestigung, die den veränderten Radius der Fließfläche darstellt und (iv)  $(d, Y)$ , welche die isotrope, duktile Schädigung darstellt [Lemaitre85, Saanouni12]. Die Verzerrung der Fließfläche während der Verformung wird durch Spannungstensoren beschrieben, wobei der Spannungsdeviator  $\underline{S}$

durch eine "verzerrte Spannung"  $\underline{S}_d$  ersetzen wird [François01]. Diese wird als neue thermodynamische Kraft angesehen und ist lediglich eine Funktion der vorhandenen Variablen. Es sei darauf hingewiesen, dass die Schädigungsvariable einen Wert zwischen 0 und 1 ist. Ist ein vollständiger Bruch des RVEs (repräsentatives Volumeelement) erreicht, so entspricht der Wert  $d = d_c = 1$ . Die stark Kopplung zwischen der plastischen Verfestigung und der duktilen Schädigung wurde als Gesamtenergieäquivalenz angenommen [Saanouni94, Saanouni12], zusammenhängend mit der Definition der effektiven Zustandsvariablen  $(\underline{\tilde{\varepsilon}}^e, \underline{\tilde{\sigma}})$ ,  $(\underline{\tilde{\alpha}}, \underline{\tilde{X}})$  und  $(\underline{\tilde{r}}, \underline{\tilde{R}})$ . Daraus ergeben sich zwei Funktionen der Schädigungseffekte:

$$(\underline{\tilde{\varepsilon}}^e = \sqrt{1-d} \underline{\varepsilon}^e, \quad \underline{\tilde{\sigma}} = \frac{\underline{\sigma}}{\sqrt{1-d}}) \quad (1)$$

$$(\underline{\tilde{\alpha}} = \sqrt{1-d} \underline{\alpha}, \quad \underline{\tilde{X}} = \frac{\underline{X}}{\sqrt{1-d}}) \quad (2)$$

$$(\underline{\tilde{r}} = \sqrt{1-d^\gamma} \underline{r}, \quad \underline{\tilde{R}} = \frac{\underline{R}}{\sqrt{1-d^\gamma}}) \quad (3)$$

wobei  $\gamma$  ein Parameter für die Wirkung der duktilen Schädigung isotroper Verfestigung ist, welcher vergleichbar mit der kinematische Verfestigung und elastischen Modulen [Saanouni12] steht.

### Zustandspotential und Zustandsgleichungen

Diese oben gewählten effektiven Variablen werden als Zustands- und Dissipationspotentiale verwendet, um das beschädigte elastoplastischen Verhalten zu beschreiben. Die Helmholtz freie Energie  $\psi(\underline{\varepsilon}^e, \underline{\alpha}, r, d)$ , die positive und konvexe Funktion aller Zustandsgrößen im dem Dehnungsraum wird als ein Zustandpotenzial genommen. Es wird hier angenommen, dass die elastische Dehnung relativ klein ist als im Vergleich zu der plastischen Verformung, so dass:  $\underline{\bar{D}} = \underline{\bar{\varepsilon}}^{el} + \underline{\bar{D}}^p$  gilt. Unter der Annahme, daß die plastische Verformung keine Auswirkung auf das elastische Verhalten hat, kann das Zustandpotential additiv zerlegt werden (isothermer Fall):

$$\rho\psi(\underline{\varepsilon}^e, \underline{\alpha}, r, d) = \rho\psi^e(\underline{\varepsilon}^e, d) + \rho\psi^p(\underline{\alpha}, r, d) \quad (4)$$

mit

$$\begin{cases} \rho\psi^e(\underline{\varepsilon}^e, d) = \frac{\nu E}{2(1+\nu)(1-2\nu)} (\underline{\varepsilon}^e : \underline{1})^2 (1-d) + \frac{E}{2(1+\nu)} (\underline{\varepsilon}^e : \underline{\varepsilon}^e) (1-d) \\ \rho\psi^p(\underline{\alpha}, r, d) = \frac{1}{3} C \underline{\alpha} : \underline{\alpha} (1-d) + \frac{1}{2} Q r^2 (1-d^\gamma) \end{cases} \quad (5)$$

Nach der reversiblen, elastischen Verformung und der Nicht-Dissipation Hypothese wird die freie Helmholtz Energie  $\psi$  als eine isotrope Funktion, mit kleiner elastischer Dehnung und inkompressiblen Verformungsannahmen vorausgesetzt, sodass folgende Zustandsgleichungen gilt:

$$\underline{\sigma}(\underline{\varepsilon}^e, d) = \underline{\tau}(\underline{\varepsilon}^e, d) = \rho \frac{\partial \psi}{\partial \underline{\varepsilon}^e} = (1-d) \lambda_e \text{tr}(\underline{\varepsilon}^e) \underline{1} + 2\mu_e (1-d) \underline{\varepsilon}^e \quad (6)$$

$$\underline{X}(\underline{\alpha}, d) = \rho \frac{\partial \psi}{\partial \underline{\alpha}} = \frac{2}{3} (1-d) C \underline{\alpha} \quad (7)$$

$$R(r, d) = \rho \frac{\partial \psi}{\partial r} = (1-d^\gamma) Q r \quad (8)$$

$$Y(\underline{\varepsilon}^e, \underline{\alpha}, r, d) = -\rho \frac{\partial \psi}{\partial d} = Y^e + Y^\alpha + Y^r \quad (9)$$

$$Y^e = \frac{1}{2} \left( \lambda_e (\underline{\varepsilon}^e : \underline{1})^2 + \mu_e \underline{\varepsilon}^e : \underline{\varepsilon}^e \right) \quad (10a)$$

$$Y^\alpha = \frac{1}{3} C \underline{\alpha} : \underline{\alpha} \quad (10b)$$

$$Y^r = \frac{1}{2} \gamma d^{\gamma-1} Q r^2 \quad (10c)$$

wobei  $\mu_e$  und  $\lambda_e$  die klassischen Lamé-Konstanten ( $\lambda_e = \nu E / ((1+\nu)(1-2\nu))$ ,  $\mu_e = E / (2(1+\nu))$ ). Die Parameter  $C$  und  $Q$  entspricht die kinematische und isotrope Verfestigung des Moduls.

Dies kann erreicht werden, indem die Spannungs- und Dehngensoren in positive und negative Anteile zerlegt werden. Hierfür wird jeder symmetrischer Tensor zweiter Stufe  $\underline{T}$  mit  $\underline{T}^{dev} = \underline{T} - T^S \underline{1}$  als deviatorischen Teil betrachten.  $T^S = \frac{1}{3} \text{tr}(\underline{T})$  ist der Mittelwert,  $\underline{1}$  ist der Tensor zweiter Stufe. Die additiven Zerlegung dieses Tensor in positive und negative Anteilen  $\underline{T} = \langle \underline{T} \rangle_+ + \langle \underline{T} \rangle_-$  entspricht  $\langle \underline{T} \rangle_+ = \sum_{i=1}^3 \langle T_i \rangle \bar{e}_i \otimes \bar{e}_i$  und  $\langle \underline{T} \rangle_- = \underline{T} - \langle \underline{T} \rangle_+$  wobei  $\langle T_i \rangle$  der  $i^{\text{th}}$

Eigenwert des Tensors  $\underline{\tau}$  und  $\vec{e}_i$  die zugehörige Eigenvektor ist. Die Notation  $\langle x \rangle$  gibt nur den positiven Wert der Notation  $x$  i.e.  $\langle x \rangle = x$  wenn  $x > 0$  und  $\langle x \rangle = 0$  wenn  $x \leq 0$  wieder. Dementsprechend wird der Effekt der duktilen Schädigung des elastischen Verhaltens der effektiven Variablen der Gleichung (1) beschrieben, modifiziert und in deviatorische und hydrostatischen Teile wie folgend zerlegt:

$$\left\{ \begin{aligned} \tilde{\underline{\varepsilon}}^e &= g_e(d) \langle \underline{\varepsilon}^e \rangle_+ + g_e(hd) \langle \underline{\varepsilon}^e \rangle_- \\ &= \sqrt{1-d} \left( \langle \underline{\varepsilon}^e \rangle_+ + \frac{1}{3} \langle tr(\underline{\varepsilon}^e) \rangle_{\perp} \right) + \sqrt{1-hd} \left( \langle \underline{\varepsilon}^e \rangle_- - \frac{1}{3} \langle -tr(\underline{\varepsilon}^e) \rangle_{\perp} \right) \\ \tilde{\underline{\sigma}} &= \frac{\langle \underline{\sigma} \rangle_+}{g_e(d)} + \frac{\langle \underline{\sigma} \rangle_-}{g_e(hd)} \\ &= \frac{1}{\sqrt{1-d}} \left( \langle \underline{\sigma}^{dev} \rangle_+ + \frac{1}{3} \langle tr(\underline{\sigma}) \rangle_{\perp} \right) + \frac{1}{\sqrt{1-hd}} \left( \langle \underline{\sigma}^{dev} \rangle_- - \frac{1}{3} \langle -tr(\underline{\sigma}) \rangle_{\perp} \right) \end{aligned} \right. \quad (11)$$

wobei  $\underline{e}^e$  für den deviatorischen Teil kleinet elastischet Verzerrungstensor  $\underline{\varepsilon}^e$  steht und der Parameter  $h \in [0.0 \ 1.0]$  als Rissschließungsparameter für Mikrorisse darstellt.

Durch die Verwendung der effektiven Dehnungsvariablen, wie zuvor in der Helmholtz freie Energie definiert ist und als Zustandspotenzial genommen wird, ergeben folglich die neue Ausdrücke für  $\underline{\sigma}$  und  $Y^e$  [Saanouni94, Saanouni12]:

$$\underline{\sigma} = 2\mu_e \left[ (1-d) \langle \underline{e}^e \rangle_+ + (1-hd) \langle \underline{e}^e \rangle_- \right] + \lambda_e \left[ (1-d) \langle tr(\underline{\varepsilon}^e) \rangle - (1-hd) \langle -tr(\underline{\varepsilon}^e) \rangle \right]_{\perp} \quad (12)$$

$$Y^e = 2\mu_e \left[ \langle \underline{e}^e \rangle_+ : \langle \underline{e}^e \rangle_+ + h \langle \underline{e}^e \rangle_- : \langle \underline{e}^e \rangle_- \right] + \lambda_e \left[ \langle tr(\underline{\varepsilon}^e) \rangle^2 + h \langle -tr(\underline{\varepsilon}^e) \rangle^2 \right] \quad (13)$$

Aus der Gleichung (1-74) geht hervor, dass der Mikrorissschließungsparameter  $h$  die elastische Schädigungskraft  $Y^e$  bei Drucklast reduziert, wenn  $h < 1$  ist und wenn keine Druckbelastung vorherrscht  $h = 0$  gilt Dies ist der einfachste Weg, um die Schädigungsrate unter Zug und Druckbelastung zu unterscheiden (siehe Kapitel III).

### Fließfunktion, Dissipationpotenzial und Evolutionsgleichungen

Es wird eine nicht-assoziative Plastizität verwendet und eine Fließfunktion  $f$  und ein plastisches Potential  $F$ , welches beide eine positive und konvexe Funktion im Spannungsraum annimmt und aus der Beziehungen der Evolution die Normalitätsregel gilt. In dieser Studie wird ein einzelnes Flächenmodell verwendet, um das beschädigte elastoplastische Verhalten mit der gleichen Fließfunktion und plastischenPotential zu

beschreiben:

$$\begin{cases} f = \frac{\|\underline{S}_d^c - \underline{X}\|_H}{\sqrt{1-d}} - \frac{R}{\sqrt{1-d^\gamma}} - \sigma_y & (a) \\ F = \frac{\|\underline{S}_d^p - \underline{X}\|_H}{\sqrt{1-d}} - \frac{R}{\sqrt{1-d^\gamma}} + \frac{3a}{4(1-d)C} \underline{X} : \underline{X} + \frac{b}{2(1-d)Q} R^2 + \frac{S}{s+1} \left\langle \frac{Y - Y_0}{S(\theta)} \right\rangle^{s+1} \frac{1}{(1-d)^\beta} & (b) \end{cases} \quad (14)$$

$$\|\underline{S}_d^i - \underline{X}\| = \sqrt{(\underline{S}_d^i - \underline{X}) : \underline{H} : (\underline{S}_d^i - \underline{X})} \quad ; \quad (i = \{c, p\}) \quad (15)$$

Es konnte bei vielen duktilen Werkstoffen beobachtet werden, dass die Duktilität empfindlich gegenüber den Spannungszuständen ist, die durch die Spannungsinvarianten dargestellt werden. Insbesondere der Lode-Winkel ( $\bar{\theta} = \frac{27}{2} \frac{J_3}{\sigma_{eq}^3}$ ) hat einen großen Einfluss auf die Duktilität des Werkstoffs, wie in [Wierzbicki05, Cao13] beschrieben wurde. Ein einfacher Weg, um dieser Abhängigkeit anzunehmen, ist, dass  $S$  eine Funktion von  $\bar{\theta}$  (Gleichung 16).

$$S(\bar{\theta}) = \begin{cases} \left[ S_0 \left[ c_1 + \frac{\sqrt{3}}{2 - \sqrt{3}} c_2 \left( \sec(\bar{\theta} \frac{\pi}{6}) - 1 \right) \right] \right]^{\frac{1}{s}} & \text{Wierzbicki-type} \\ S_0 [c_1 + c_2 \bar{\theta}^2]^{\frac{1}{s}} & \text{Cao-type} \end{cases} \quad (16)$$

$$\bar{\theta} = 1 - 6 \frac{\theta}{\pi} \quad \text{and} \quad \theta = \frac{1}{3} \cos^{-1} \left( \frac{27}{2} \frac{J_3}{\|\underline{\sigma}\|_M^3} \right) \quad , \quad J_3 = \det(\underline{\sigma})$$

wobei das  $\underline{S}_d$  hier vom François Modell unterscheidet. Ein neuer Term wird eingeführt, um die Schnittgröße (senkrecht zur Belastungsrichtung) der nachfolgenden Fließfläche zu regeln (siehe Teil III.2.2.1):

$$\begin{cases} \underline{S}_d^c = \underline{S} + \frac{\underline{S}_0 : \underline{S}_0}{2(1-d)X_{11}^c (R/\sqrt{1-d^\gamma} + \sigma_y)} \underline{X} - \frac{\underline{X} : \underline{X}}{2(1-d)X_{12} (R/\sqrt{1-d^\gamma} + \sigma_y)} \underline{S}_0 & (a) \\ \underline{S}_d^p = \underline{S} + \frac{\underline{S}_0 : \underline{S}_0}{2(1-d)X_{11}^p (R/\sqrt{1-d^\gamma} + \sigma_y)} \underline{X} & (b) \end{cases} \quad (17)$$

$$\underline{S}_0 = \underline{S} - \underline{S}_x \quad \text{and} \quad \underline{S}_x = \frac{\underline{S} : \underline{X}}{\underline{X} : \underline{X}} \cdot \underline{X} \quad (18)$$

$\underline{S}$  wird in  $\underline{S}_x$  kollinear zu  $\underline{X}$  und seine orthogonale Teil  $\underline{S}_0$  zerlegt.  $X_{11}$  hat die selbe Bedeutung wie in François Modell und hilft bei der Einstellung des Verzerrungsverhältnisses

nachfolgenden Fließfläche. Zwei Formen der  $X_{II}^c$  und  $X_{II}^p$  ersetzt  $X_{II}$  separat von Fließfunktion und Dissipationalfunktion. Ein neuer Parameter  $X_{I2}$  wurde in  $\underline{S}_d$  eingeführt, um die Quergröße der anschließenden Fließfläche regeln. Die Anwendung des bekannten Normalitätregels führt zu folgenden Fließvariablen, die die Entwicklung der dissipativen Phänomene definiert:

$$\dot{\underline{\varepsilon}}^p = \dot{\lambda} \frac{\partial F}{\partial \underline{\sigma}} = \dot{\lambda} \underline{n}^p \quad \text{with} \quad \underline{n}^p = \frac{\underline{n}^d}{\sqrt{1-d}} : \left[ 1^{dev} + \frac{\underline{X} \otimes \underline{S}_0}{\tilde{X}_{II}^p (R/\sqrt{1-d^\gamma} + \sigma_y)} \right] \quad (19)$$

$$\dot{\underline{\alpha}} = -\dot{\lambda} \frac{\partial F}{\partial \underline{X}} = \dot{\lambda} \left( \frac{\underline{n}^x}{\sqrt{1-d}} - a\underline{\alpha} \right) \text{ and } \underline{n}^x = \underline{n}^d - \frac{1}{(R/\sqrt{1-d^\gamma} + \sigma_y)} \left[ \frac{(\underline{S}_0 : \underline{S}_0)}{2\tilde{X}_{II}^p} \underline{n}^d - \frac{(\underline{S} : \underline{X})(\underline{X} : \underline{n}^d)}{\tilde{X}_{II}^p (\underline{X} : \underline{X})} \underline{S}_0 \right] \quad (20)$$

$$\dot{r} = -\dot{\lambda} \frac{\partial F}{\partial R} = \dot{\lambda} \left( \frac{n^i}{\sqrt{1-d^\gamma}} - br \right) \quad \text{with} \quad n^i = \frac{(\underline{S}_0 : \underline{S}_0)(\underline{n}^p : \underline{X})}{2\sqrt{1-d} \tilde{X}_{II}^p (R/\sqrt{1-d^\gamma} + \sigma_y)^2} + 1 \quad (21)$$

$$\underline{n}^d = \frac{\underline{H} : (\underline{S}_d^p - \underline{X})}{\| \underline{S}_d^p - \underline{X} \|_H} \quad (22)$$

$$\dot{d} = \dot{\lambda} \frac{\partial F}{\partial Y} = \frac{\dot{\lambda}}{(1-d)^\beta} \left( \frac{\langle Y - Y_0 \rangle}{S(\theta)} \right)^s \quad (23)$$

Der plastische Multiplikator  $\dot{\lambda}$  kann aus der Konsistenzbedingung  $\dot{f} = 0$  bestimmt werden, wenn  $f = 0$  ist [Saanouni94, Badreddine10, Saanouni12], jedoch gilt er an jedem Integrationspunkt jedes Finite-Elemente als Unbekannt und mit Hilfe der FE berechnet wird. Dieses Modell wird in ABAQUS / Explicit © Finite-Elemente-Code durch die ein VUMAT-Code implementiert (siehe nächstes Kapitel II).

### I.3 Grenzformänderungskurven für die Blechumformung (FLCs)

Für die experimentelle Bestimmung der FLD, zählt der Nakazima Versuch – und der Marciniak-Versuch zu den häufigsten verwendeten Methoden. Beide Versuche können auf zwei Erichsen Blechprüfmaschine durchgeführt werden. Die Nakazima Versuch ist wahrscheinlich das am häufigsten verwendete Verfahren, da das Marciniak Verfahren ist aufwendiger bei der Ausführung ist.

#### Eine kurze Beschreibung des M-K-Ansatz

Marciniak Kuczynski-Modell (M-K) basiert auf das Wachstum von anfänglichen Defekten

und Inhomogenitäten in Form von schmalen Bändern und mit einem orientierten Winkel ( $\varphi^0$ ), welcher auf die Hauptachse ausgerichtet ist. Starre Plastizität, ebenen Spannungszustand und isotropen Verfestigung am Werkstoff kann angenommen werden. Eine detaillierte Beschreibung des theoretischen MK-Ansatzes ist in Fig. 1-8 schematisch dargestellt und wird in vielen Publikationen [Marciniak67, Barata89] verwendet. Die Defektgeometrie in der Zone *B* wird durch das Dickenverhältnis gekennzeichnet

$$f^0 = e_b / e_a \quad (24)$$

wobei  $e_b^0$  und  $e_a^0$  die Ausgangsdicke in zone *b* und zone *a* separat darstellt. Die *x*, *y*, *z* Achsen entsprechen der walz, quer-und senkrechten Richtungen der Folie, während 1, 2 und 3 die Hauptspannungen und Belastungsrichtungen in der homogenen Region ist. In der Nutzone stellt  $\vec{n}$  und  $\vec{t}$  die normale und die Längsrichtung der Nut dar.

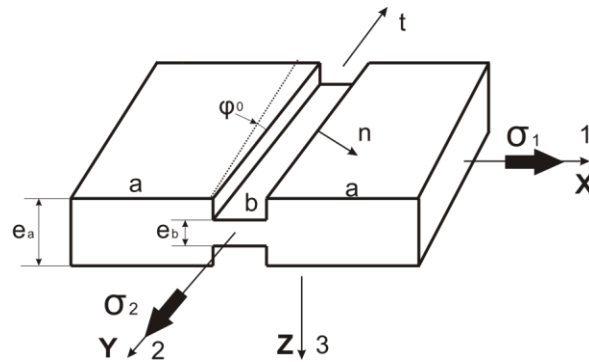


Fig. 1. Anfangsbedingungen für die M-K-Ansatz.

Um das Vergleichsdehngsinkrement  $d\bar{\varepsilon}_b$  und den Spannungswert in Längsrichtung der Nut  $\sigma_{tt}^b$  zu berechnen, wird die Kraftgleichgewichtsbedingung und Kompatibilitätgleichungen an beiden Regionen angenommen. Aus der Gleichgewichtsbedingung, die das Kräftegleichgewicht angibt, gelten die folgenden Gleichungen:

$$\sigma_{mm}^a e_a = \sigma_{mm}^b e_b, \sigma_{nt}^a e_a = \sigma_{nt}^b e_b \quad (25)$$

Die Kompatibilitätsregel setzt voraus, dass die Dehnung in Richtung der Einschnürung bei beiden Regionen identisch ist:

$$d\varepsilon_{tt}^a = d\varepsilon_{tt}^b \quad (26)$$

Die Gleichgewichtsgleichungen kann reduziert werden in:

$$\begin{aligned} f \sigma_{mm}^b &= \sigma_{mm}^a \\ f \sigma_{nt}^b &= \sigma_{nt}^a \end{aligned} \quad (27)$$

wobei  $f = e_b / e_a$  die Inhomogenitätsfaktor ist und wie folgt beschrieben wird:

$$f = f^0 \cdot \exp(\varepsilon_{zz}^b - \varepsilon_{zz}^a) \quad (28)$$

Mit der obigen Bedingung, kann sowohl der Fließspannungswert in Normalenrichtung als auch die Scherfließspannung in der Nut berechnet werden. Wird die Spannungsmatrix in das Hauptbezugssystem  $[\sigma]_{xyz}$  transportiert, kann die Fließfunktion für die Auswertung der Vergleichsfließspannung  $\bar{\sigma}_{YF}^b$  verwendet werden. Aufgrund der Verfestigungsregel  $\bar{\sigma} = f_{HR}(\bar{\varepsilon}^b)$  und Fließregel  $\bar{\sigma} = f_{HR}(\bar{\varepsilon}^b)$  kann  $[d\varepsilon^b]_{xyz}$  bestimmt werden.

Durch die folgenden zwei nichtlineare Gleichungen mit zwei Unveränderlichen kann  $d\bar{\varepsilon}_b$  und  $\sigma_n^b$  ausgedrückt werden als:

$$\begin{cases} F_1(d\bar{\varepsilon}_b, \sigma_n^b) = \bar{\sigma}^b - \bar{\sigma}_{YF}^b = 0 \\ F_2(d\bar{\varepsilon}_b, \sigma_n^b) = d\varepsilon_n^a - d\varepsilon_n^b = 0 \end{cases} \quad (29)$$

### Lokale Einschnürung Definition

Mit der Newton-Raphson-Methode kann  $d\bar{\varepsilon}_b$  und  $\sigma_n^b$  bestimmt werden kann. Hierbei wird beim M-K Einschnürungskriterium angenommen, dass das lokale plastische Fließen eintritt, wenn die Vergleichsspannungsinkrement  $d\bar{\varepsilon}_b$  im Scherband das 10fache größer ist als  $d\bar{\varepsilon}_a$  in der homogenen Zone. In diesem Moment sind akkumulieren die entsprechenden Dehnungen  $(\varepsilon_{xx}^a, \varepsilon_{yy}^a)$  in der homogenen Zone. Die Analyse wird für verschiedene Werte von  $\varphi^0$  (zwischen  $0^\circ$  und  $90^\circ$ ) wiederholt, sodass der Grenzpunkt auf der FLD nach der Minimierung der  $\varepsilon_{xx}^a - \varphi^0$ . Kurve bestimmt werden kann.

## Chapter II Numerische Aspekte

### II.1 Numerische Umsetzung des vorgeschlagenen Modells

#### Lokale Integrationsschema: Zustandsgrößen Berechnung

Weiterhin wird das globale Auflösungsschema verwendet, müssen wir die elementaren Operatoren, die Matrix oder die Charakterisierung der IBVP Vektoren, die durch die Integrale der Volumen-oder Oberflächen für jedes Referenzelement definiert werden, sind zu berechnen. In Abschnitt I.2.3 formulierten wir mehrere Sorten von Elastoplastizität konstitutive Gleichung voll mit duktilen Schaden gekoppelt. In allen Fällen angesprochen, werden wir uns



nicht assoziative konstitutiven Gleichungen mit einzigartigen Fließfunktion und unelastisch Potential mit quadratischen Vergleichsspannungen, kinematischen und isotropen Mischung Härten, und rein isotropen duktilen Schädigung ohne induzierte Volumenänderung beschränken.

**Erste Prognose:**

Es wird zunächst angenommen, dass das gesamte Deformationinkrement völlig elastisch ist:

$$\begin{cases} \Delta \underline{\varepsilon}^p = 0 \\ \Delta \underline{\alpha} = 0 \\ \Delta r = 0 \\ \Delta d = 0 \end{cases} \Rightarrow \begin{cases} \underline{\varepsilon}_{n+1}^p = \underline{\varepsilon}_n^p \\ \underline{\alpha}_{n+1} = \underline{\alpha}_n \\ r_{n+1} = r_n \\ d_{n+1} = d_n \end{cases} \quad (30)$$

Daraus ergibt sich für die sogenannte Prüfspannung:

$$\underline{\sigma}_{n+1}^* = 2\mu_e \left[ (1-d_n) \langle \underline{\varepsilon}_{n+1}^e \rangle_+ + (1-hd_n) \langle \underline{\varepsilon}_{n+1}^e \rangle_- \right] + \lambda_e \left[ (1-d_n) \langle tr(\underline{\varepsilon}_{n+1}^e) \rangle - (1-hd_n) \langle -tr(\underline{\varepsilon}_{n+1}^e) \rangle \right] \underline{1} \quad (31)$$

$$\underline{S}_{n+1}^* = \underline{\sigma}_{n+1}^* - tr(\underline{\sigma}_{n+1}^*) \underline{I} \quad (32)$$

$$\underline{e}_{n+1}^{e*} = \underline{\varepsilon}_{n+1}^{e*} - \frac{1}{3} tr(\underline{\varepsilon}_{n+1}^{e*}) \underline{I} \quad (33)$$

$$\underline{S}_{0(n+1)}^* = \underline{S}_{(n+1)}^* - \underline{S}_{x(n+1)}^* \quad \text{und} \quad \underline{S}_{x(n+1)}^* = \frac{\underline{S}_{(n+1)}^* : \underline{X}_n}{\underline{X}_n : \underline{X}_n} \cdot \underline{X}_n \quad (34)$$

$$\underline{S}_{d(n+1)}^{c*} = \underline{S}_{n+1}^* + \frac{\underline{S}_{0(n+1)}^* : \underline{S}_{0(n+1)}^*}{2X_{11}^c(R_{n+1} / \sqrt{1-d_n^y} + \sigma_y)} \underline{X}_n - \frac{\underline{X}_n : \underline{X}_n}{2X_{12}(R_n / \sqrt{1-d_n^y} + \sigma_y)} \underline{S}_{0(n+1)}^* \quad (35)$$

Anschließend werden diese Zustandsgrößen in die Fließfunktion importiert:

$$f_{n+1}^*(\underline{\sigma}_{n+1}^*, \underline{X}_n, R_n, d_n) = \frac{\|\underline{S}_{d(n+1)}^* - \underline{X}_n\|_H}{\sqrt{1-d_n}} - \frac{R_n}{\sqrt{1-d_n^y}} - \sigma_{y_n} = 0 \quad (36)$$

Wenn  $f_{n+1}^*(\underline{\sigma}_{n+1}^*, \underline{X}_n, R_n, d_n) < 0$ , gilt die Annahme, dass die elastische Belastung richtig ist.

Daraus ergeben sich folgende Lösungen:

$$\begin{cases} \underline{\sigma}_{n+1} = \underline{\sigma}_{n+1}^*, & \underline{\varepsilon}_{n+1}^p = \underline{\varepsilon}_n^p & (a) \\ \underline{X}_{n+1} = \underline{X}_n, & \underline{\alpha}_{n+1} = \underline{\alpha}_n & (b) \\ R_{n+1} = R_n, & r_{n+1} = r_n & (c) \\ Y_{n+1} = Y_n, & d_{n+1} = d_n & (d) \end{cases} \quad (37)$$

Andernfalls, wenn  $f_{n+1}^*(\underline{\sigma}_{n+1}^*, \underline{X}_n, R_n, d_n) > 0$ , so ist die Lösung nicht elastisch. Hierbei ist es erforderlich für  $\underline{\sigma}, \underline{X}, Y, R, D$  eine plastische Korrektur einzuführen, damit sichergestellt werden kann, dass folgende Gleichung gilt:

$$f_{n+1}(\underline{\sigma}_{n+1}, \underline{X}_{n+1}, Y_{n+1}, R_{n+1}, d_{n+1}) = 0 \quad (38)$$

### Plastische Korrektur:

Die Gleichung (2-28) beinhaltet viele nichtlineare Gleichungen für die Elastoplastizität, die verzerrende Verfestigung und auch die isotrope duktile Schädigung. Um die Effizienz der Berechnung zu erhöhen, die es notwendig, die Größen des Systems zu reduzieren:

$$\left\{ \begin{array}{l} f(\Delta\lambda, \underline{n}_{n+1}^p, d_{n+1}) = \frac{\|\underline{S}_{n+1}^d(\Delta\lambda, \underline{n}_{n+1}^p, d_{n+1}) - \underline{X}_{n+1}\|_H}{\sqrt{1-d_{n+1}}} - \frac{R_{n+1}(\Delta\lambda, d_{n+1})}{\sqrt{1-d_{n+1}^y}} - \sigma_y = 0 \\ g(\Delta\lambda, \underline{n}_{n+1}^p, d_{n+1}) = d_{n+1} - d_n - \frac{\Delta\lambda}{(1-d_{n+1})^\beta} \left\langle \frac{Y_{n+1}^*(\Delta\lambda, \underline{n}_{n+1}^p, d_{n+1}) - Y_0}{S(\theta)_{n+1}} \right\rangle^s = 0 \\ \wp(\Delta\lambda, \underline{n}_{n+1}^p, d_{n+1}) = \underline{n}_{n+1}^p - \frac{\underline{n}_{d(n+1)}}{\sqrt{1-d_{n+1}}} : \left[ \mathbf{1}^{dev} + \frac{\underline{X}_{n+1} \otimes \underline{S}_{0(n+1)}}{(1-d_{n+1})X_{I1}(R_{n+1} / \sqrt{1-d_{n+1}^y} + \sigma_y)} \right] = 0 \end{array} \right. \quad (39)$$

Mit Hilfe der tensoriellen Diskretisierung des Newton-Raphson-Verfahrens kann das System reduziert werden. Die Werkstoffkomponenten der Jacobi-Matrix in Gl. (2-13) sind im Anhang zu finden. Sobald die Korrekturgrößen  $\delta\lambda_{n+1}^k, \delta d_{n+1}^k, (\delta \underline{n}_{n+1}^p)^k$  eine Konvergenz an der Iteration (k) erreicht, sollen alle Zustandsvariablen aktualisiert werden. Wenn  $d_{n+1} \geq 1$ , ist, dann ist der Bruch erreicht. Für ebene Spannungszustände wird eine neue Gleichung  $\mathfrak{Z}(\Delta\lambda, d_{n+1}, \underline{n}_{n+1}^p, \underline{\varepsilon}_{n+1}^{33})$  in die Gleichungen 2-42 ergänzt.

## Kapitel III Experimentelle Aspekte und Parameterstudie von zwei Modellen

### III.2 Versuchsdurchführung und Ergebnisse

In diesem Kapitel werden die experimentellen Versuche bei drei Blechwerkstoffen vorgestellt. Es werden eine Reihe von Versuchen durchgeführt, um die Kalibrierung und Validierung der vorgeschlagenen Modelle zu erhalten. Das Formänderungsvermögen der drei Werkstoffe wird mithilfe von unterschiedlichen Deformationsszenarien bestimmt: Einachsigen Zugversuch (UT), ebener Torsionsversuch (IPT), Kerbzugversuche (PNT), Scherzugversuche (SS), Orthogonal Belastungsversuche (CL), Nakazimaversuch (NAK), Tiefziehversuch (CSD). Alle Versuchsergebnisse sind in Abschnitt III. 2.3 zu finden.

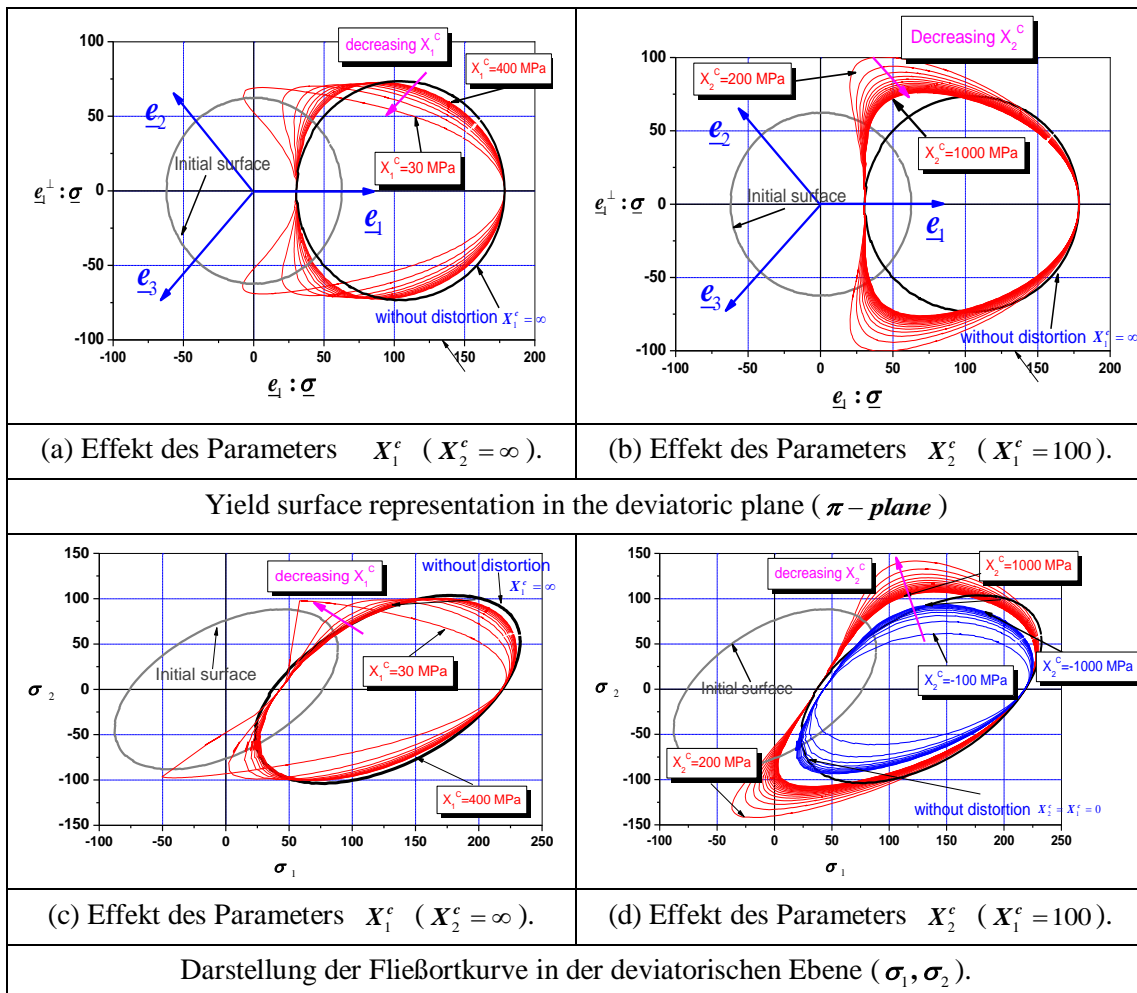
### III.3 Parametrische Untersuchung und Identifikation der vorgeschlagenen Modelle

Vor der Berechnung der Eingangsparameter sollte eine Studie über die Empfindlichkeit der

Parameter gegenüber dem makroskopischen Verhalten untersucht werden, um das Modell besser verstehen zu können. In dem vorgeschlagenen Modell werden neue Parameter eingeführt: Mikroriss-schließungsfaktor  $h$ , Verzerrungsparameter und ein neuer Term  $S(\bar{\theta})$ , welcher verwendet wird, um die Lode Parameter  $\bar{\theta}$  bei der Schädigungsentwicklung zu erhalten. In den nächsten Abschnitten werden die neuen Parameter kurz beschrieben.

### Distorsionsisomere Parametereinfluss auf nachfolgende Fließfläche

Um den Einfluss des Verzerrungsparameters auf das vorgeschlagenen Modells zu untersuchen, wird ein isotropes Werkstoffverhalten mit den Parameter in Tabelle 3-5 betrachtet. Das Fig. 3-40 vergleicht die Anfangsoberfläche ohne Verzerrung der Fließflächen nach 5%  $\varepsilon_{eq}^p$ , die Spannungen in verschiedenen Räumen bzw. in deviatorischen Hauptspannungsebene und die Spannung in der Scherebene.



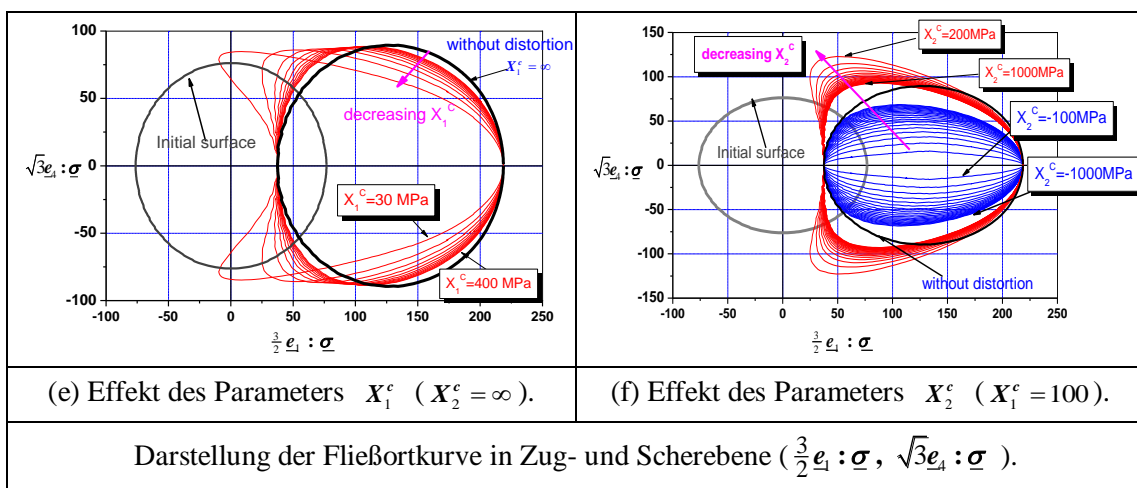


Fig. 2. Darstellung der Spannungsoberfläche für verschiedene Räume: Effekt der Verzerrungsparameter  $X_1^c$  und  $X_2^c$

### Einfluss des verzerrten Parameters auf die Schädigungsentwicklung

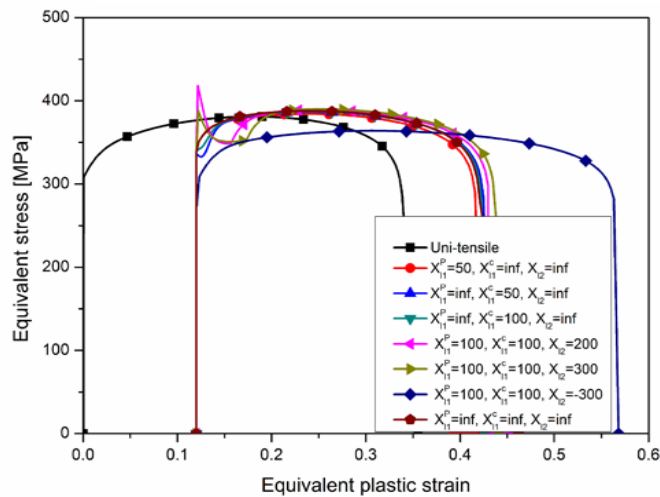


Fig.3. Einfluss des distortionalen Parameters auf die Vergleichsspannung-plastische Dehnungskurven nach 12% Vordehnung.

In Fig.3, wird die nachfolgende Vergleichsspannung mit verschiedenen Verzerrungswert aufgetragen ( $X_{11}^c, X_{11}^p, X_{12}$ ). Durch einen Vergleich der nachfolgenden Spannungslinien zwischen den Ergebnissen mit und ohne Verzerrungseffekt kann gezeigt werden, dass sich  $X_{11}^c$  erhöht, das Verzerrungsverhältnis abnimmt und das Versagen früher eintritt. Ebenso auch die das Stagnation-Stadium der Kaltverfestigung.  $X_{11}^p$  hat kein Einfluss auf die Streckgrenze, jedoch einen Einfluss auf die Verfestigungsevolution. Wenn  $X_{12}$  positiv ist, vergrößert sich die nachfolgende Fließortkurve. Aber wenn die Verfestigung erhöht wird, stimmt die

Spannung-Dehnung-Kurve wieder mit den ursprünglichen Kurven überein. Andernfalls, wenn  $X_{12}$  negativ ist, wird die Fließortkurve sich dauerhaft verringern.

### Wirkung der Triaxialität und Lode-Winkel auf die Schädensevolution

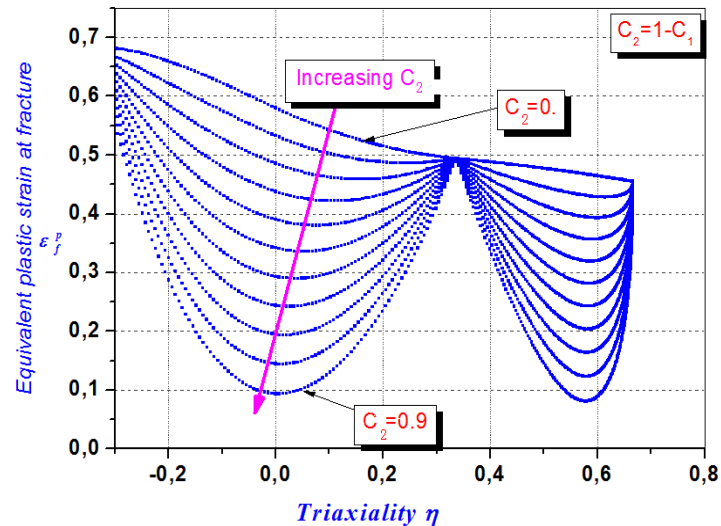


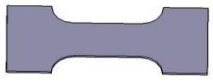

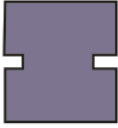

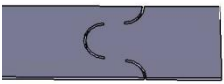
Fig. 4. Fracture Locus in ebenen Spannungszustand für vorgeschlagene Art Schädigungsentwicklung.

Die Beiträge der Ader zu  $S(\bar{\theta})$  Parameter für Wierzbicki und neue vorgeschlagene Form der Schäden Entwicklungen werden mit ( $c_1 = 1$  und  $c_2 = 0$ ) verglichen. Es wird festgestellt, dass diese beiden Formen geben, in der Nähe die gleichen Werte mit wechselnden Gangparameter, so dass diese beiden Formen können als gleich betrachtet werden. In Fig.4 die äquivalenten plastischen Dehnungen Bruch sind gegenüber dem Triaxialität Verhältnis aufgetragen mit ( $c_1 + c_2 = 1$ ). Diese Ergebnisse haben gezeigt, dass die Bruchdehnung ist eine monoton abnehmende Funktion des Druckes Triaxialität wenn der Parameter Ader eingeführt. Für hohe Belastungen Triaxialität Verhältnis, wobei die sphärischen Hohlraum Wachstumsmechanismus spielt eine wichtige Rolle bei der Schädigung Evolutionsprozesses nimmt die entsprechende plastische Verformung mit der Zunahme der Belastung Triaxialität Verhältnis. Jedoch im Bereich von  $0 \leq \eta \leq 0.33$  und  $0.57 \leq \eta \leq 0.66$  die entsprechende plastische Verformung beim Bruch mit der Zunahme der Belastung Triaxialität Verhältnis, was in guter Übereinstimmung mit den Testergebnissen [Bao04] ist. Die Abhängigkeit von Druck und Lode Winkel der Schäden können durch die Parameter  $c_1$  und  $c_2$  eingestellt werden.

## Kapitel IV Identifizierung und Validierung der vorgeschlagenen Modelle

### IV.2 Die Identifizierung Methodik der CDM-Modell

Tabelle 1. Experimentelle Proben und deren Materialparameter.

		Probenform	Parameter	Anzahl der Parameter	Methodology
Elastoplastisch	UT		$E, \nu, \sigma_y,$ $F, G, H, L, M, N$	9	Direkt (analytisch)
	IPT		$C, a, Q, b$	4	Invers
Distortion	CL		$X_{11}^C, X_{11}^P, X_{12}$	3	Direkt (analytisch)
Schädigung	PNT		$S, s, \beta, Y_0$	4	Invers
	SS		$h$	1	Invers

In dieser Studie wurden die Werkstoffe DP1000, CP1200 und Al7020 gewählt und die inverse Methodik in Tabelle 1 für die Parameteridentifikation verwendet. Diese inverse Identifikation erfolgt durch die Verwendung eines MATLAB-basierten Minimierungscodes, welches das Python-Skript in ABAQUS liest und optimiert. Das Optimierungsprogramm vergleicht die experimentellen mit den numerischen Ergebnissen und minimiert den Bereich der Zielfunktion, sodass ein optimaler Parametersatz gefunden werden kann. Mehr Details über die inverse Methode, den Aufbau und die Überprüfung sind im Anhang B zu finden.

#### IV.2.1 Identifikation der Elastoplastizitätsparameter

Aus dem UT-Versuch werden die Elastizitätsparameter ( $E, \nu$ ) und Fließgrenze  $\sigma_y$  direkt ermittelt. Mit dem Lankford Parameter  $r_\theta^L$  in drei Richtungen (Fig. 3-8) und der Gleichung 3-9 werden die Anisotropie-Parameter nach Hill48 analytisch bestimmt. Die kombinierten Verfestigungsparameter werden aus den Ergebnissen IPT und UT Versuchen invers ermittelt.

Die ermittelten Werkstoffparameter des vorgeschlagenen Modells sind in Tabelle 2 zusammengefasst.

Tabelle 2. die generierten Parameter aus dem UT und TBT Versuch.

	$E$ (GPa)	$\nu$	$\sigma_y$ (MPa)	$Q$ (MPa)	$b$	$C$ (MPa)	$a$	$F$	$G$	$H$	$L$	$M$	$N$
DP 1000	208.0	0.3	809.0	4000.0	13.0	32000.0	150. 0	0.525	0.546	0.455	1.5	1.5	1.67
CP 1200	207.0	0.3	980.0	5848.0	37.0	37000.0	507. 0	0.567	0.610	0.389	1.5	1.5	1.37
AL 7020	69.8	0.3	322.0	675.0	8.0	2260.0	75.0	0.631	0.634	0.366	1.5	1.5	1.4

### Identifikation des Distortion-Parameter

Die Strategie des CL-Versuchs dient dazu, die Verzerrungsparameter  $X_{II}^C$  und  $X_{II}^P$  durch einen Scherzugversuch mit einem entsprechenden plastischen Verformung zu kalibrieren. Die Validierung erfolgt durch weitere Schub- und Scherzugversuchen mit unterschiedlicher Zugrichtungen. Nach Bedarf, soll geprüft, ob  $X_{I2}$  festgelegt wird oder nicht. Bei Al7020 beträgt die Vorzugs-Vergleichsdehnung 18.0 % (Fig. 5).

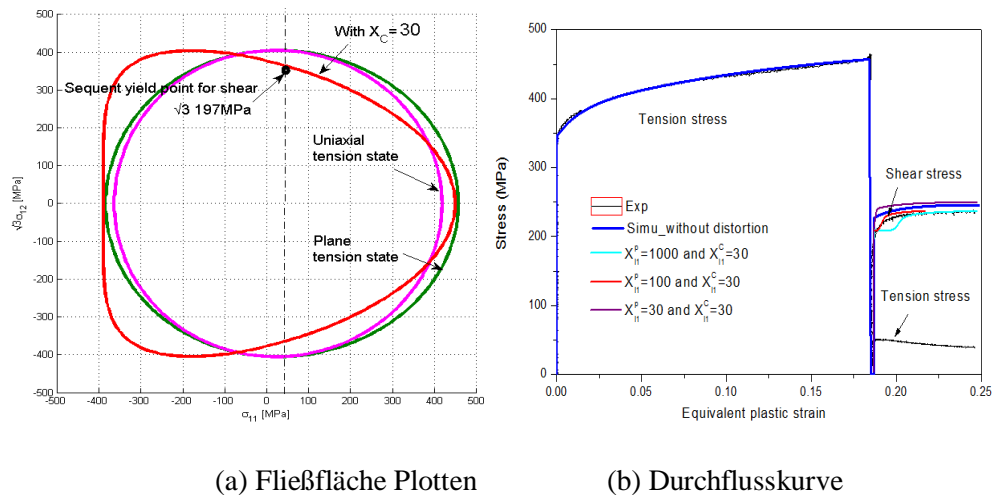


Fig. 5. Nachfolgende Verhalten Nach 18.0% Vorspannung für Al7020.

### Identifizierung der duktilen Schädigungsparameter

Die numerischen Ergebnisse (globale Kräfte über die lokalen Punktverschiebungen) der PNT Versuche werden mit den experimentellen Ergebnissen über das Optimierungsprogramm verglichen. Die Einfluss der anderen Schädigungsparameter ( $S$ ,  $s$ ,  $\beta$ ,  $h$ ) und Schädigungsentwicklung sind nicht gleich. Eine ausführliche Beschreibung der Einflüsse auf die Schädigungsentwicklung sind in [Saanouni12] zu finden. Mit Hilfe der inversen Methode,

welche den Fehler der Zielfunktionen bei einzelnen Simulation minimiert und mit der Methode der kleinsten Quadrate ausgewertet, kann das optimale Parameterset ( $S, s, \beta, h$ ) nach vielen Optimierungszyklen bestimmt werden in Tabelle 3, der auch die Parameter dargestellt ( $\gamma, Y_0$ ) bekam mit analytischen Ansätzen.

Tabelle 3. Schädigungsparameter aus dem PNT-und SS-Versuch.

	$S$ (MPa)	$s$	$\beta$	$\gamma$	$Y_0$ (MPa)	$h$
DP1000	12.5	1.15	2.5	4	2.0	0.25
CP1200	10.2	1.31	1.98	4	2.0	0.21
Al7020	4.50	1.48	3.4	4	0.0	0.3

### IV.3 Parameterbestimmung des MK-Ansatzes für Al7020

In der Studie wird das Fließverhalten nach Swift betrachtet. Die Parameter sind in Tabelle 3-17 angegeben. Fig. 3-67 wird ein Vergleich zwischen den experimentellen und numerischen wahre Spannung- wahr Dehnungskurve gezeigt. Eine gute Übereinstimmung der Kurven vor dem Einschnürungsbereich konnte erzielt werden. Die ermittelten FLD und FLSD Kurven sind in Fig.4-17 dargestellt.

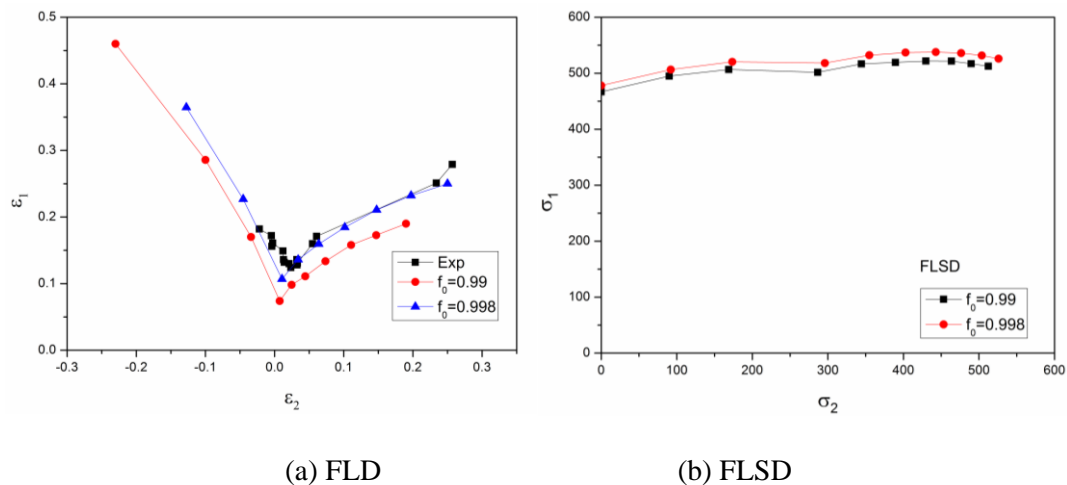


Fig.6. Experimentelle und theoretische Flds und FLSDs mit dem MK-Ansatz bei Al7020.

### Nakazima testet Simulation mit CDM-Modell

C3D8R-Elemente werden bei der Modellierung der Probe verwendet. In der kritischen Zone beträgt die minimale Vernetzunggröße 0.15 mm, sodass 10 Elemente in dem Dickenrichtugen ergeben. Die Gesamtelementzahl betrug 13168. Der Stempel bewegt sich vertikal mit einer Geschwindigkeit von 10 mm/s. An den Kontaktflächen wurde das Reibungsmodelle mit



Reibungskoeffizienten von 0.05 verwendet. Die Simulation wird angehalten, sobald ein endgültiger Bruch auf der Probe auftritt.

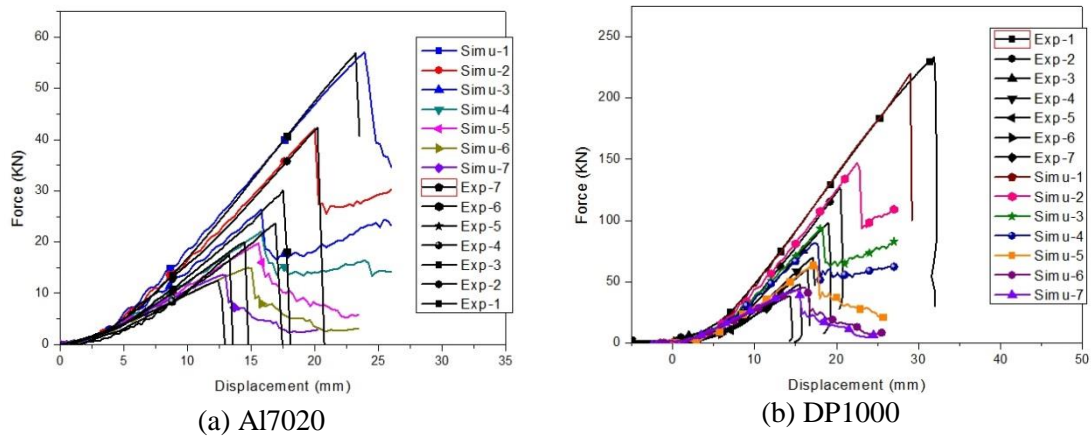


Fig. 7. Vergleich der experimentellen und simulativen Kraft-Wegkurven.

Einen Vergleich zwischen den experimentellen und numerischen Kraft-Weg-Verläufen bei Al7020 und DP1000 sind im Fig. 4-19 dargestellt. In Fig. 4-20 sind die beiden NAK Simulationsergebnisse bei Al7020 und DP1000 dargestellt, darunter auch die Angaben der Maximalwerte und der Vergleichsdehnung beim Ziehtiefen.

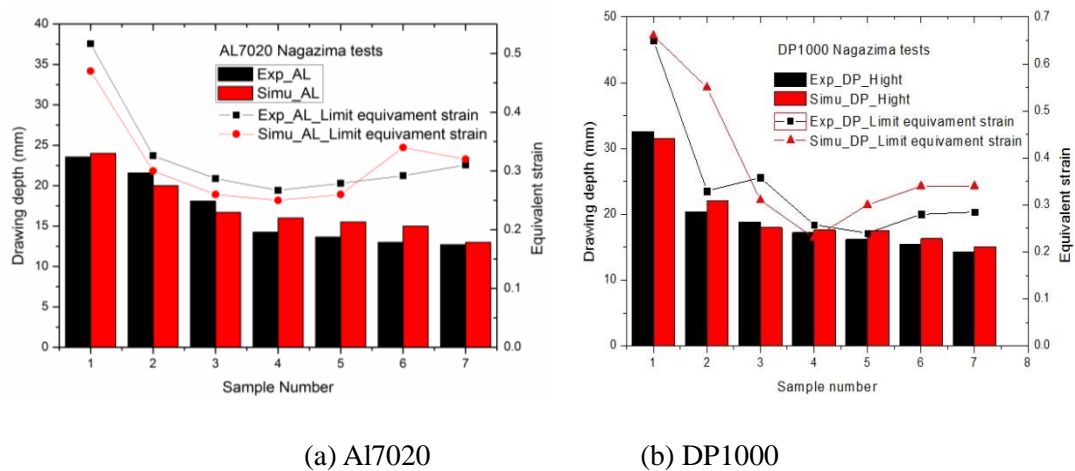


Fig.8. Vergleich der Genzverschiebung und plastische Vergleichsdehnung bei (a) Al7020, (b) DP1000.

Nach der Simulation des gesamten NAK-Versuchs kann die Grenzformänderungskurve mit entsprechenden Schädigungswerten generiert werden, um den Unterschied mit FLD Kurven in Fig. 4-27 bei Al7020 und DP1000 vergleichen zu können. Der kritische Schädigungswert  $d$  wird mit 0.1, 0.5 und 1.0 separat definiert.

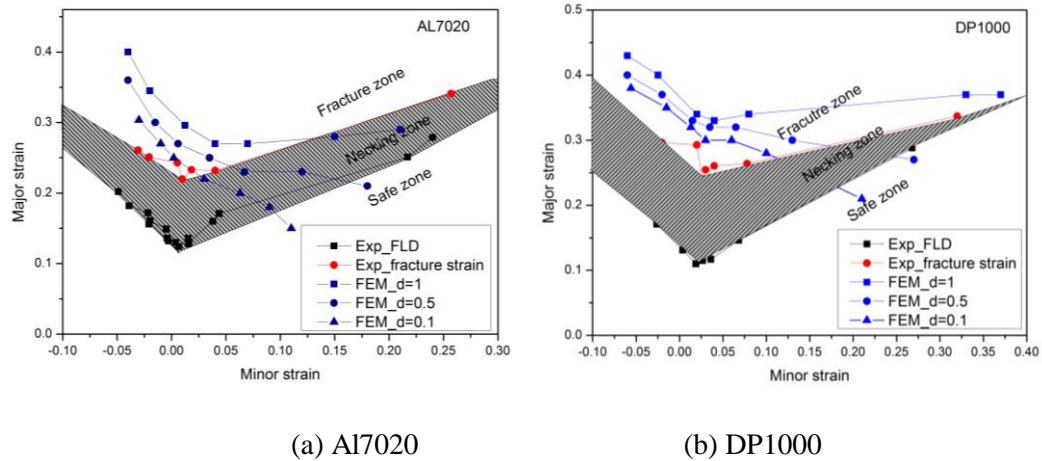


Fig. 9. Vergleich der numerischen FLCs und der experimentellen FLCs

### Cross section deep drawing tests

Der Cross-Section Tiefziehversuch (CSD) wurde bei drei Werkstoffe mit ABAQUS / Explicit und dem CDM-Modell simuliert, um die Umformgrenzen vorhersagen zu können. Für den Werkstoff Al7020 wurde die FLD und FLSD mit MK-Ansatz verwendet, um es mit der CDM-Methode zu vergleichen. Die simulierte Geometrie (um die Modellstruktur zu erkennen, wird nur die Hälfte der Geometrie betrachtet) und die angenommenen FE-Netzungen sind in Fig. 4-28 und Fig. 4-29 dargestellt. Um die Randbedingung zu vermeiden, wird die vollständige Probe in der Simulation modelliert. C3D8R-Elemente werden bei der Modellierung der Probe verwendet. Die Vernetzunggröße im kritischen Bereich beträgt 0.15 mm (in Fig.4-28). Daraus ergeben sich insgesamt 675.615 Acht-Knoten-Elemente.

#### CSD-Simulation für Al7020

Für den Werkstoff Al7020 beträgt die Niederhaltekraft 120 kN. Der Vergleich zwischen experimentellen und numerischen Kraft-Weg-Kurven ist in Fig. 10 dargestellt. In Fig. 11 ist der Vergleich zwischen der numerischen und experimentellen Rissentwicklung wiedergeben. Es konnte gezeigt werden, dass der numerische, vorhergesagte Riss in Übereinstimmung mit den experimentellen Ergebnissen steht. In Experiment beginnt das Versagen ebenfalls in der Ecke des Querschnitts. Mit der gleichen Simulationseinstellung und einer Niederhaltekraft von 400 kN wurde das CDM-Modell für die CSD-Tests vorgeschlagen und bei den Werkstoff DP1000 und CP1200 simuliert. Der Vergleich der numerischen und experimentellen Kraft-Weg-Verläufe ist in Fig. 13 gezeigt. Die Kraft-Weg-Kurve stimmen gut mit den experimentellen Ergebnissen überein. In Fig. 14 und Fig. 15 wird der Unterschied zwischen der numerischen und experimentellen Rissentwicklungen bei DP1000 und CP1200

wiedergegeben.

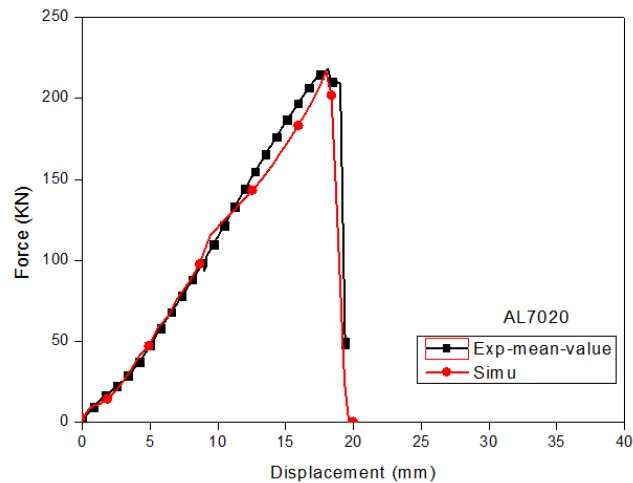


Fig. 10. Vergleich der Kraft-Weg-Kurven Kurven zwischen Simulation und Experiment bei CSD-Tests.

Numerisch vorhergesagt Riss bei  $U = 18.0$  mm

Experimentell beobachtet Riss bei  $U_{\text{exp}} = 18.44$  mm

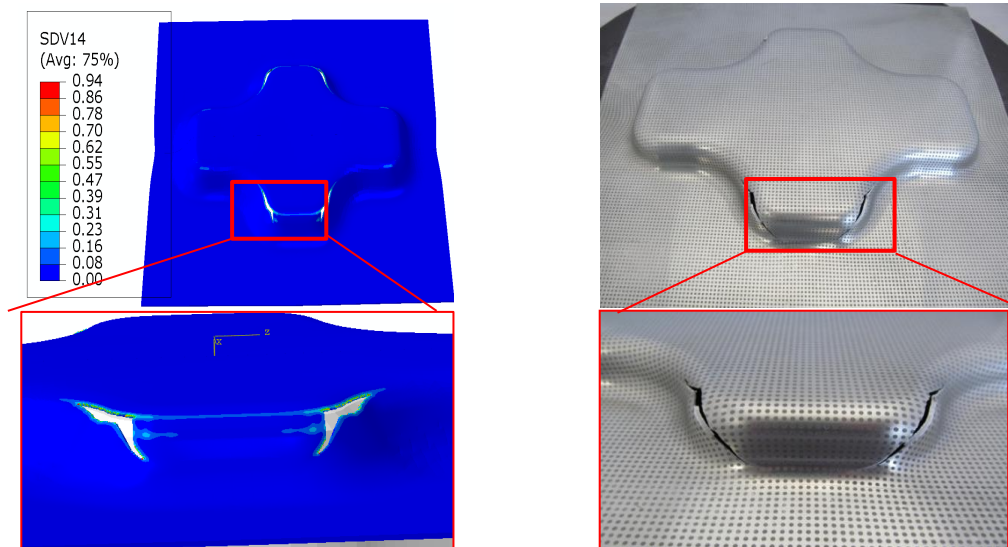
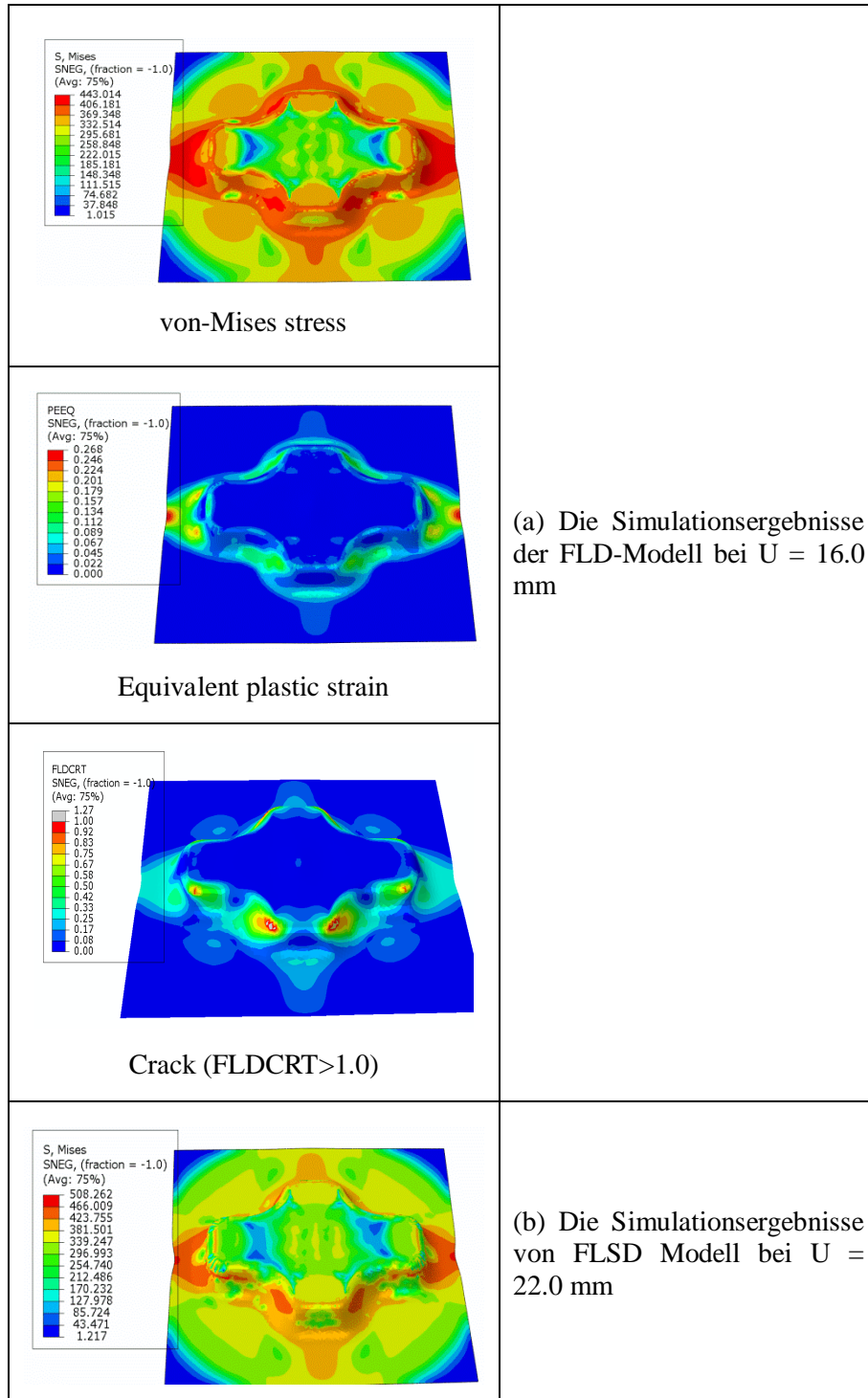


Fig. 11. Vergleich der numerischen und experimentellen Rissprofile für Al7020.

Neben den CDM-Modellen wird auch der Umformprozess mit isotroper Verfestigung gekoppelt mit der FLD und FLSD (basiert auf den MK-Ansatz) simuliert. In Fig. 12 ist die Fehlerverteilung nach dem Riss bei den drei Versagenskriterien, vollständig gekoppelt CDM, FLD und FLSD, abgebildet. Durch den Vergleich mit den Ergebnissen der CDM, zeigt die FLD-Methode eine unterschätzte Schädigungsinitiierung, jedoch eine genaue Position des

Risses. Dagegen zeigt die FLSD Methode, dass die Schädigungsinitiierung bei  $U = 28$  mm erfolgt, wobei die Formbarkeit überschätzt wird und der Riss am dicken breiten Ecke auftritt, was nicht mit den experimentellen Ergebnissen übereinstimmt. Die Position der Rissinitiierung befindet sich an der breiten Ecke, welche auch nicht identisch ist mit echtem Profil im Experiment.



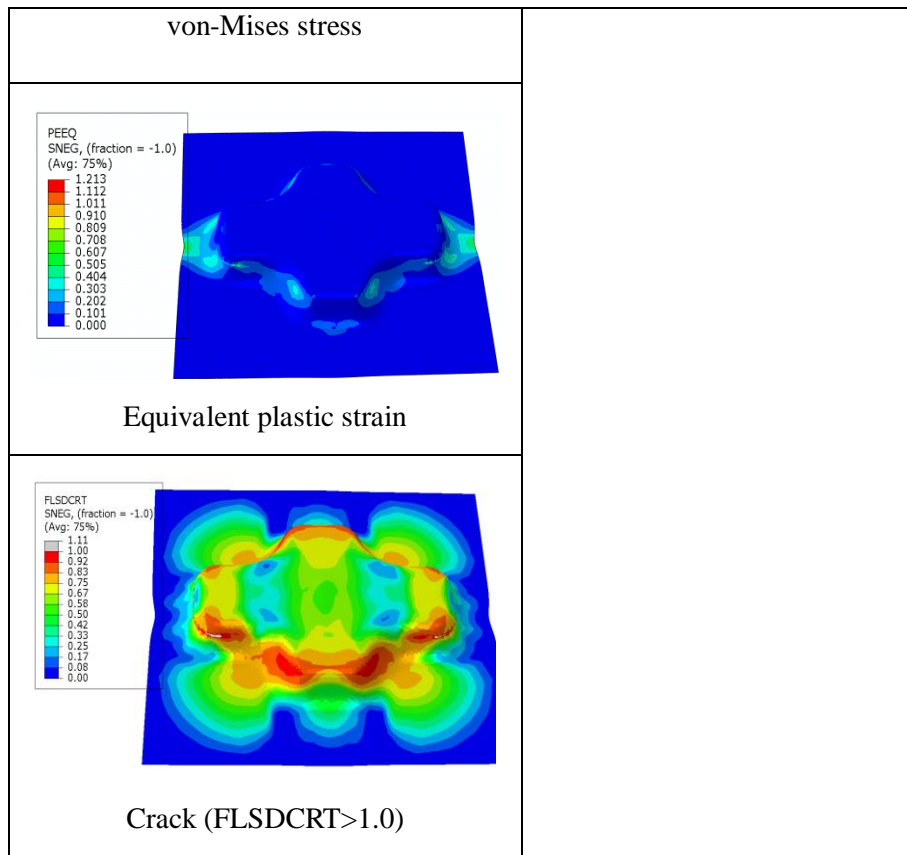


Fig. 12. Vergleich der CSD-Tests für Al7020 mit (a) FLD und (b) FLSD.

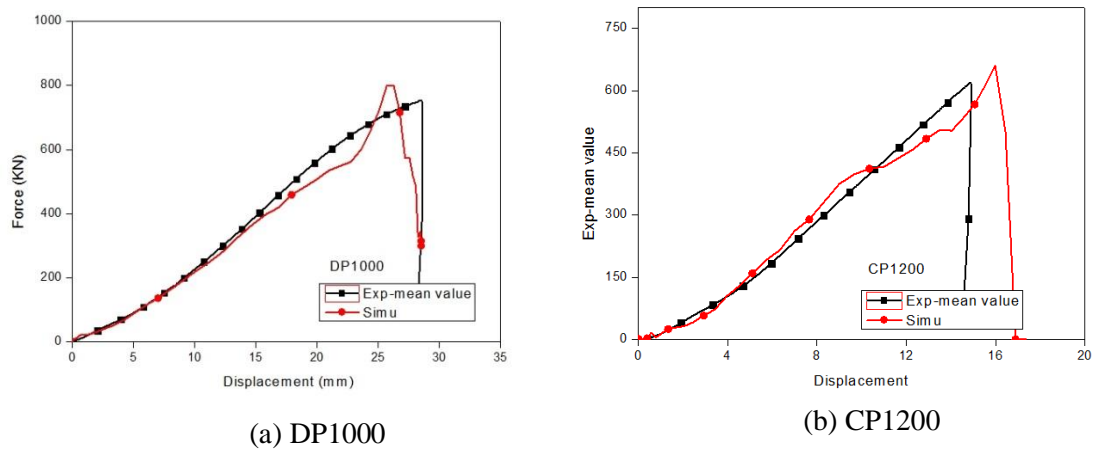


Fig 13. Vergleich der Kraft-Weg-Kurven zwischen Simulation und Experiment beim CSD-Tests.

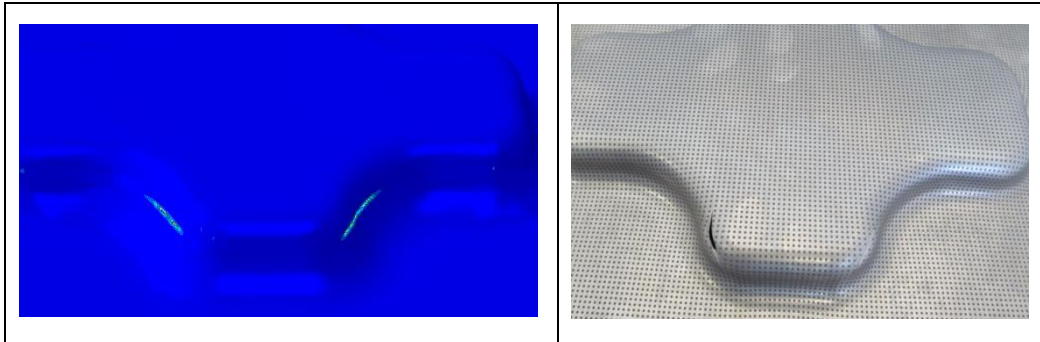


Fig. 14. Vergleich des Rissbereichs zwischen Simulation und Experiment beim DP1000.

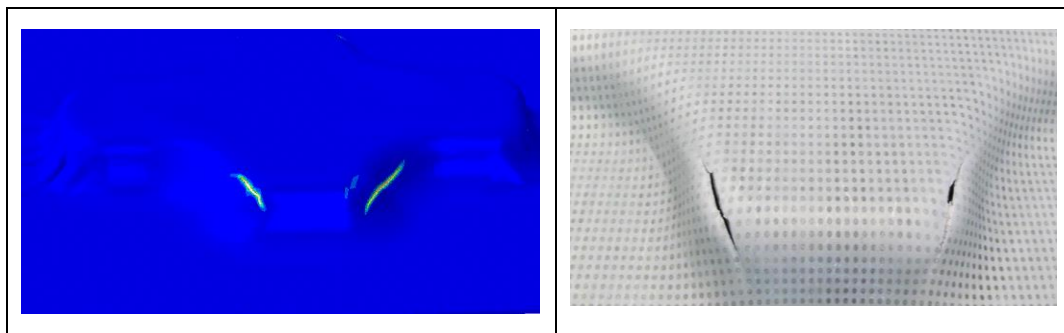


Fig. 15. Vergleich des Rissbereichs zwischen Simulation und Experiment beim CP1200.

### **Schlussfolgerungen und Perspektiven**

In der vorliegenden Arbeit wird gezeigt, dass die Verzerrung, die Fließortkurvefläche, die Triaxialität und der Lode-Winkels während der Belastungsgeschichte eine besondere Auswirkung auf die Werkstoffverfestigung und auf Initiierung der Schädigung haben. Dieses Ziel wird durch die Tatsache, dass während der Umformtechnik, die kritischen Zonen, in denen hohe plastische Dehnungen und damit duktilen localize Schäden an komplexen Belastungspfade unterzogen gerechtfertigt.

Weitere Entwicklungen sind noch zu, um das vorgeschlagene Modell zu erweitern, um mehr allgemeine Belastungsbedingungen durchgeführt werden, zu decken. Sie können in den folgenden Punkten zusammenfassen: Anisotrope duktilen Schaden; Erweiterung der vorliegenden vollständig lokales Modell der nicht-lokalen Formulierung, die im Rahmen der micromorphic Theorie durchgeführt werden; Erweiterung des vorliegenden Modells auf die Viskoplastizität Rahmen muss zusammen mit Berücksichtigung der Wärmeaustausch, indem die Wärmeleichungen durchgeführt werden; Weitere experimentelle Arbeit noch benötigt wird, um eine breite Palette von komplexen nichtproportionale Belastung Wege decken geführt werden. Dies ist erforderlich, um die Identifizierung einer großen Anzahl von Eingabe die erweiterten konstitutiven Gleichungen, die viele Zehn für die allgemeine Version des

Modells übersteigen können Materialparameter facilitate.

Schließlich haben mehr industrielle Tests, um in einer Vielzahl von komplexen Bildungsprozesse, die helfen, diese erweiterten vollständig gekoppelten Stoffgesetze zu überprüfen durchgeführt werden.





## Appendix A

The hybrid experimental-numerical methodology used in this paper belongs to the inverse approach category, where certain input data is deduced from the comparison between the experimental results and numerical simulation results. Here, the relevant information from experiments can be the displacement-load responses or full-field surface measurements with optical measurement system. The inverse method here is narrowed to the optimization of the material parameters including hardening parameters and damage parameters. The basic principle of inverse methodology is almost the same, which is to search the minimum error value between simulation and experiment responses.

$$g(x_i) = \frac{1}{N} \sum_{n=1}^N W_n \left( \frac{f_n(x_i) - F_n(x_i)}{Z_{area}} \right)^2 \quad (\text{A-1})$$

where  $g(x_i)$  is the objective function expressed in terms of weighted least square form,  $x_i$  is the parameter needed to be optimized,  $N$  denotes the total number of observations (sample points),  $f_n(x_i)$  is the simulation force response,  $F_n(x_i)$  is the objective experimental response,  $Z_{area} = \sigma_y \varpi$  is residual scale factor,  $\varpi$  denotes the size of loading cross section surface,  $W_n$  is the weighting factors, equal to  $1/N$  here, which means the even weighting factors. For damage parameter identification, six experimental data in the form of Force-Point displacement related to local 1.0 mm, 4.0 mm away from the notched axis of three PNT tests are proposed to identify the damage parameters ( $S, s, \beta$ ), so  $N$  value, here is 6.

In this study, in order to minimize the objective function, the Trust Region reflective method is used, which suits itself to nonlinear least square optimization problem. The optimization process involves the approximate solution of a large linear system based on the method of preconditioned conjugate gradients. The identification procedure requires the definition of bounds for each parameter, namely  $x_i^{min}, x_i^{max}$ . With the help of the normalized function  $\xi_i^n$  (its bound should be in (0, 1)), the actual value for each unknown parameter can be created, as shown below:

$$x_i^{n+1} = x_i^{\min} + (x_i^{\max} - x_i^{\min}) \cdot \xi_i^{n+1} \quad (\text{A-2})$$

The global criteria of the convergence are that the numerical results must satisfy the following conditions:

$$g(x_i) < \theta_{total} \quad (\text{A-3})$$

where  $\theta_{total}$  is the limit tolerance between the simulation and experiment force.

The whole optimization process works based on a set of MATLAB code which is written linking ABAQUS/Explicit solver. With ABAQUS script language python, the objective data can be read from the objective file. The optimization process can be divided in six stages, which includes: operate the ABAQUS simulation, read global data, compare the results with the experimental measurements, build and minimize the objective function, optimize parameters and update the input file. The detail of the optimization process is shown in Fig. 3-48. The verification of the developed optimization scheme is given below.

The verification study depends on uniaxial tension of a single finite element which is free of the mesh size effects. The analytical expression for the damage development for this stress state is given in Equation A4. Initially, the test is run for a known parameter set of  $E = 200000$  MPa and  $\nu = 0.3$ ,  $\sigma_y = 900$  MPa,  $K = 100$  and  $(S, s, \beta)$  as  $(0.5, 1.0, 3.0)$  and the response is recorded, the  $(x_i^{\min}, x_i^{\max})$  here are chosen to be  $(0\sim 1, 0\sim 3, 0\sim 5)$  for  $(S, s, \beta)$  with empirical assumption. Then, the target damage parameters can be identified with different sets of initial values.

$$D = 1 - \left[ 1 - \left( \frac{1+\nu}{3ES} \right)^s \frac{\beta+1}{(2s+1)K} \left[ (\sigma_y + K\alpha)^{2s+1} - \sigma_y^{2s+1} \right] \right]^{\frac{1}{\beta+1}} \quad (\text{A-4})$$

In order to show the importance of initial value for the convergence, two comparable examples with different initial set of values are given. The convergence pattern with initial set of  $(S, s, \beta) = (0.75, 0.4, 2.2)$  are given in Fig.A1. As it is seen, the scheme locates the optimum value after 14 iterations. The situation for initial set of  $(S, s, \beta) = (0.3, 1.2, 2.8)$  is shown in Fig. A2. It can be found that after 300 iterations the final parameter set comes to  $(0.55, 1.5, 3)$ , and arrives the optimum value after more than 1000 iterations, but it can be seen that the error between the experimental numerical results can be negligible (less than 1%) compared with initial error after 10 iterations, so this inverse method is applicable for the

parameter identification.

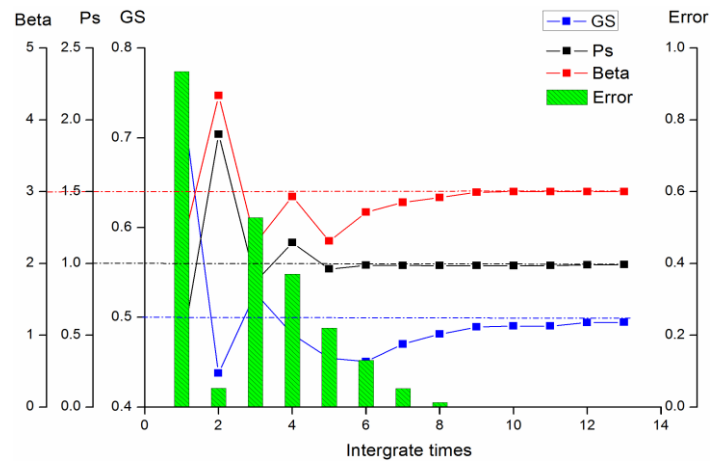


Fig. A1. The parameters convergence process with initial set of  $(S, s, \beta) = (0.75, 0.4, 2.2)$

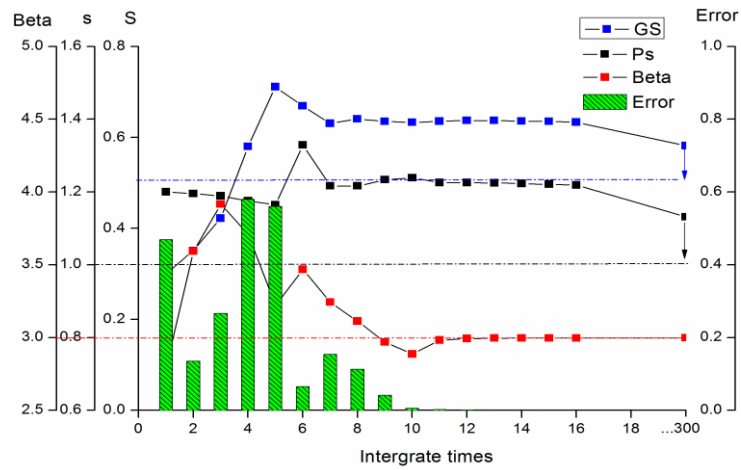


Fig. A2. The parameters convergence process with initial set of  $(S, s, \beta) = (0.3, 1.2, 2.8)$

# Zhenming YUE

## Doctorat : Systèmes Mécaniques et Matériaux

### Année 2014

#### Prédiction de l'endommagement ductile en formage de tôles minces

L'objectif de ce travail est de proposer un modèle de comportement avec endommagement ductile pour la simulation des procédés de mise en forme de tôles minces qui peut bien représenter le comportement des matériaux sous des trajets de chargement complexes en grandes déformations plastiques. Basées sur la thermodynamique des processus irréversibles, les équations du comportement couplé à l'endommagement tiennent compte des anisotropies initiales et induites, de l'écroutissage isotrope et cinématique et de l'endommagement isotrope ductile. Les effets de fermeture des microfissures, de triaxialité des contraintes et de l'angle de Lode sont introduits pour influencer l'évolution de l'endommagement sous une large gamme de triaxialité des contraintes. La distorsion de la surface de charge est introduite via un tenseur déviateur qui gouverne la distorsion de la surface de charge. A des fins de comparaison, les courbes limites de formage sont tracées basées sur l'approche M-K. Des essais sont conduits sur trois matériaux pour les besoins d'identification et de validation des modèles proposés. L'identification utilise un couplage entre le code ABAQUS et un programme MATLAB via un script en langage Python. Après l'implémentation numérique du modèle dans ABAQUS/Explicite et une étude paramétrique systématique, plusieurs procédés de mise en forme de structures minces sont simulés. Des comparaisons expériences-calculs montrent les performances prédictives de la modélisation proposée.

**Mots clés :** endommagement, mécanique de l'(milieux continus) - anisotropie - élastoplasticité - simulation par ordinateur - tôle, propriétés mécaniques.

#### Ductile Damage Prediction in Sheet Metal Forming Processes

The objective of this work is to propose a "highly" predictive material model for sheet metal forming simulation which can well represent the sheet material behavior with damage under complex loading paths and large plastic strains. Based on the thermodynamics of irreversible processes framework, the advanced fully coupled constitutive equations are proposed taking into account the initial and induced anisotropies, isotropic and kinematic hardening as well as the isotropic ductile damage. The microcracks closure, the stress triaxiality and the Lode angle effects are introduced to influence the damage rate under a wide range of triaxiality ratios. The distortion of the yield surface is described by replacing the usual stress deviator tensor by a 'distorted stress' deviator tensor, which governs the distortion of the yield surfaces. For comparisons, the FLD and FLSD models based on M-K approach are developed.

A series of experiments for three materials are conducted for the identification and validation of the proposed models. For the parameters identification of the fully coupled CDM model, an inverse methodology combining MATLAB-based minimization software with ABAQUS FE code through the Python script is used. After the implementation of the model in ABAQUS/Explicit and a systematic parametric study, various sheet metal forming processes have been numerically simulated. At last, through the comparisons between experimental and numerical results including the ductile damage initiation and propagation, the high capability of the fully coupled CDM model is proved.

**Keywords:** continuum damage mechanics – anisotropy - elastoplasticity - computer simulation - sheet-metal, mechanical properties.

Thèse réalisée en partenariat entre :

